CARBON MOLECULAR SIEVE DENSE FILM MEMBRANES FOR ETHYLENE/ETHANE SEPARATIONS

A Dissertation
Presented to
The Academic Faculty

By

Meha Rungta

In Partial Fulfillment
Of the Requirements for the Degree
Doctor of Philosophy in the
School of Chemical & Biomolecular Engineering

Georgia Institute of Technology

December 2012

CARBON MOLECULAR SIEVE DENSE FILM MEMBRANES FOR ETHYLENE/ETHANE SEPARATIONS

Approved by:

Dr. William J. Koros, Advisor
School of Chemical & Biomolecular Engineering
Georgia Institute of Technology

Dr. Christopher W. Jones
School of Chemical & Biomolecular Engineering
Georgia Institute of Technology

Dr. David Sholl
School of Chemical & Biomolecular Engineering
Georgia Institute of Technology

Dr. David Bucknall
School of Materials Science & Engineering
Georgia Institute of Technology

Mr. Mark Brayden
Hydrocarbons R&D
The Dow Chemical Company

Date Approved: October 8, 2012

Dedicated to

My Parents and

My Advisor, Dr. William J. Koros

ACKNOWLEDGEMENTS

My graduate school experience at Georgia Tech has been absolutely incredible. First and foremost, I would like to acknowledge my advisor, Dr. Koros. He has been a mentor, a parent and a friend to me, and I cannot thank him enough for everything. His enthusiasm, relentless energy, dedication, and work ethic will always continue to inspire me in my personal and professional life.

Funding support from The Dow Chemical Company is greatly appreciated. Mr. Mark Brayden and Mr. Marcos Martinez have been truly amazing collaborators. I'd like to express my gratitude to Mark and Marcos for their wisdom and infinite support.

I am also grateful to my committee members, Dr. Christopher Jones, Dr. David Sholl and Dr. David Bucknall for technical input and feedback related to my thesis.

The entire Koros Group has been a pleasure to work with. I have to especially thank Liren Xu for the endless discussions, his dedication, and the fun times over the last four years. I am thankful to Dr. J.R. Johnson and Dr. Oguz Karvan for their immense technical support as well as for all the office fun. I'd also like to thank Chen Zhang for his contributions to the advanced membranes section of my dissertation.

I consider myself fortunate to have always been blessed with the most incredible friends, who have stood by me through thick and thin. I would like to thank each one of them as I could never do justice if I were to start taking names.

Last, but not the least, I will always remain indebted to my family for just about anything and everything. I could never thank my parents enough for their unconditional love and support, for making me what I am today, and for always believing in me. Thank you.

TABLE OF CONTENTS

LIST OF TABLES

LIST OF FIGURES

SUMMARY

Olefin/paraffin separations using cryogenic distillation are extremely energy and cost intensive processes in the petrochemical industry, accounting for nearly 0.15 Quads of energy consumption annually. Augmenting distillation processes with energy efficient separations such as membranes, adsorption, extraction etc. have been proposed by several researchers to achieve significant cost and energy savings. The specific focus here is on ethylene/ethane (C_2H_4/C_2H_6) separations. The application of membranes to C_2H_4/C_2H_6 separations remains challenging owing to the low selectivity or instability of C_2H_4/C_2H_6 separation membranes reported in the literature. Carbon molecular sieve (CMS) membranes, formed via the high temperature pyrolysis of polymeric precursor membranes, have shown the potential to surpass the polymeric upper bound for several gas separations such as O_2/N_2, CO_2/CH_4 etc. In addition, they have also demonstrated the ability to perform stably at high feed pressures up to 1000 psi. These combined attributes made them an interesting option to evaluate for C_2H_4/C_2H_6 separation. The overarching goal of this work was thus to develop CMS membranes for use in C_2H_4/C_2H_6 separation.

In collaboration with The Dow Chemical Company, two projects focused on addressing the fundamental and practical aspects of CMS membrane development, primarily for supplementing the C_2-splitter (C_2H_4/C_2H_6), while also considering other potential applications in the petrochemical industry. The specific focus of the current work was to define the material science options to fabricate novel, high performing ethylene/ethane separation CMS dense film membranes by identifying and optimizing key parameters to tune the CMS micro-morphology. Homogeneous dense films were

used to develop fundamental and theoretical knowledge, and to extract intrinsic CMS characteristics, transport properties, and structure-performance relationships.

Three polymer precursors: Matrimid®, 6FDA-DAM and 6FDA:BPDA-DAM were used as precursors to CMS membranes for C_2H_4/C_2H_6 separation. The polymeric C_2H_4/C_2H_6 upper bound line was established as a basis against which to compare CMS performance. CMS dense film membranes were successfully fabricated by pyrolyzing the precursor polymer materials, and showed attractive C_2H_4/C_2H_6 separation performance far exceeding the polymeric upper bound line. Performance optimization for CMS derived from each precursor was achieved by way of tuning pyrolysis conditions such as the pyrolysis temperature, heating rate, pyrolysis atmosphere etc. The evolution in C_2H_4/C_2H_6 separation performance with the pyrolysis parameters was explained with respect to the CMS schematic pore structures and hypothetical pore distributions. Further, semi-quantitative diffusion size pore distributions were constructed by studying the transport performance of a range of different penetrant gases as molecular sized probes of the CMS pore structure. This, in conjunction with separation performance data, provided critical insights into the structure-performance relationships of the CMS materials.

An unexpected physical aging phenomenon was discovered in CMS membranes, resulting in time-dependent performance behavior. Analogous to physical aging in glassy polymeric membranes, CMS membrane physical aging exhibited dependence on factors such as the starting precursor material, separation layer thickness, storage conditions, history etc. This finding adds another controlling factor to CMS performance besides the CMS fabrication parameters.

The effects of testing conditions, i.e. the testing temperature, pressure and feed composition on C_2H_4/C_2H_6 separation performance of CMS dense films were also analyzed. These studies were useful not just in predicting the membrane behavior from

a practical stand-point, but also in a fundamental understanding of the nature of CMS membrane separation. The study helped clarify why CMS membranes outperform polymeric membrane performance, as well as allowed comparison between CMS derived from different precursors and processing conditions. The pressure dependence study demonstrated that the application of membranes to C_2H_4/C_2H_6 separation may be more meaningful as debottlenecking applications rather than as stand-alone processes, since the expected product purity achievable using currently available membranes is limited. Finally, the effects on C_2H_4/C_2H_6 separation in the presence of binary gas mixture were also assessed to get a more realistic measure of the CMS performance resulting from competition and bulk flow effects. In addition to experimental analysis, modeling work to predict multicomponent transport in CMS membranes was also carried out.

While the current study focuses on CMS dense films owing to their simple geometry that allow fundamental analysis, considerations related to translation to the practically useful CMS hollow fiber form were also presented based on Liren Xu's work in the Koros Group. Considering the combined effects of substructure collapse resulting from intense heat treatment during pyrolysis, physical aging and CMS separation performance, 6FDA:BPDA-DAM was found to be the most preferred precursor for CMS fabrication for C_2H_4/C_2H_6 separation in this study. The current work thus establishes a framework for guiding research ultimately aimed at providing a convenient, potentially scalable hollow fiber membrane formation technology for C_2H_4/C_2H_6 separation.

CHAPTER 1

INTRODUCTION

1.1. Olefin/Paraffin Technology Overview

Ethylene and propylene are the two most important feed stocks in the petrochemical industry [1]. The global ethylene production capacity in 2009 was 133 million tons per year (tpy), up nearly 5% from 127 million tpy in 2008 [2]. Propylene demand is growing much more rapidly with the global propylene production capacity being 85 million tpy in 2009 [3, 4]. Global ethylene demand is dominated by polyethylene, the world's largest used polymer, while that for propylene is driven by polypropylene. In addition, organic chemicals such as ethylene dichloride, ethylene oxide, ethyl benzene etc. are also significant consumers of ethylene, while propylene is used to derive acrylonitrile, propylene oxide, cumene etc. [3-5]. Figure 1.1 below gives a general overview of olefin/paraffin technology in the petrochemical industry.

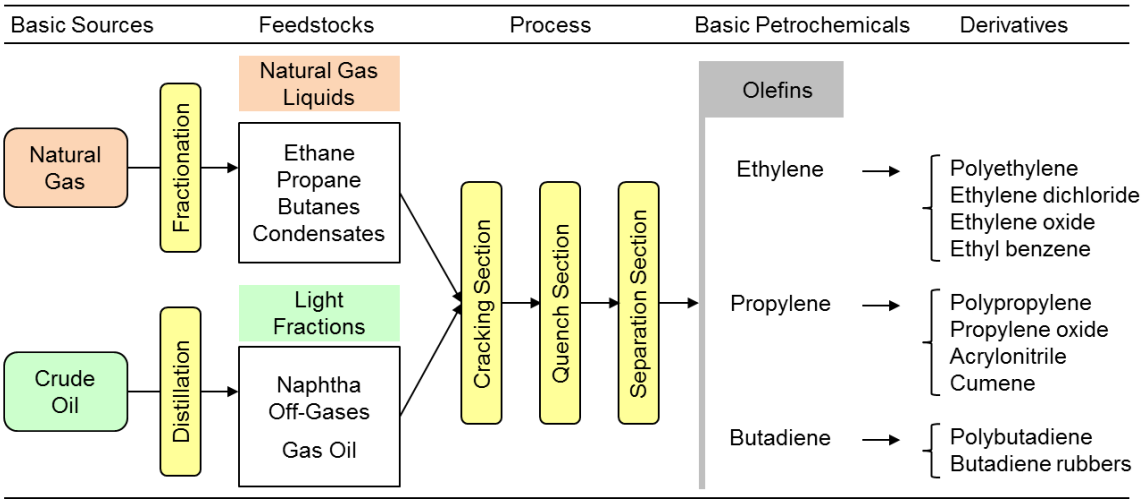

Figure 1.1: Overview of olefin/paraffin technology [6]

Ethylene is produced commercially from petroleum and natural gas sources, propylene being an important by-product of ethylene production [3]. Ethylene production from hydrocarbon sources (ethane, propane, butane, naphtha etc.) consists of four basic operations: thermal cracking, quenching, gas compression/treatment and purification/separation [5, 7-9]. The first step is the thermal cracking of the hydrocarbon feed stock at high temperature resulting in C1-C12 fractions. The cracking reactions are abruptly terminated by rapidly cooling and quenching the furnace effluents. The cracked gas is then compressed to high pressure to separate the heavy oil fraction from the lighter fraction, stripped of acid gases, and dried to make it moisture-free. The gaseous fraction is fed to a series of columns (demethanizer, deethanizer, depropanizer, debutanizer etc.), where various components are separated by liquefaction and fractionation, along with further purification of various components after catalytically/selectively hydrogenating dienes to olefins. The relative sequence of the columns (for example, demethanizer first, deethanizer first, depropanizer first etc.) as well as the process location and regime for hydrogenation of acetylenic compounds to

olefins varies from plant to plant. The separation of olefins from paraffins is the last step in the process.

1.2. Olefin/Paraffin Separations

Olefin/paraffin separations in the petrochemical industry are currently carried out by high pressure distillation operations, which are extremely energy intensive and estimated to consume nearly 0.15 Quads of energy annually [9, 10]. The close boiling points of olefins and paraffins make them very hard to separate, thus requiring aggressive conditions with high reflux ratios and large columns with 120-180 trays. For example, a typical C2-splitter may be ~70 m high and 5 m in diameter, being operated under sub-ambient conditions of -20 to -30°C and 20 bar pressure [10-13]. Figure 1.2 shows a simple schematic of distillation operations typically involved in olefins production.

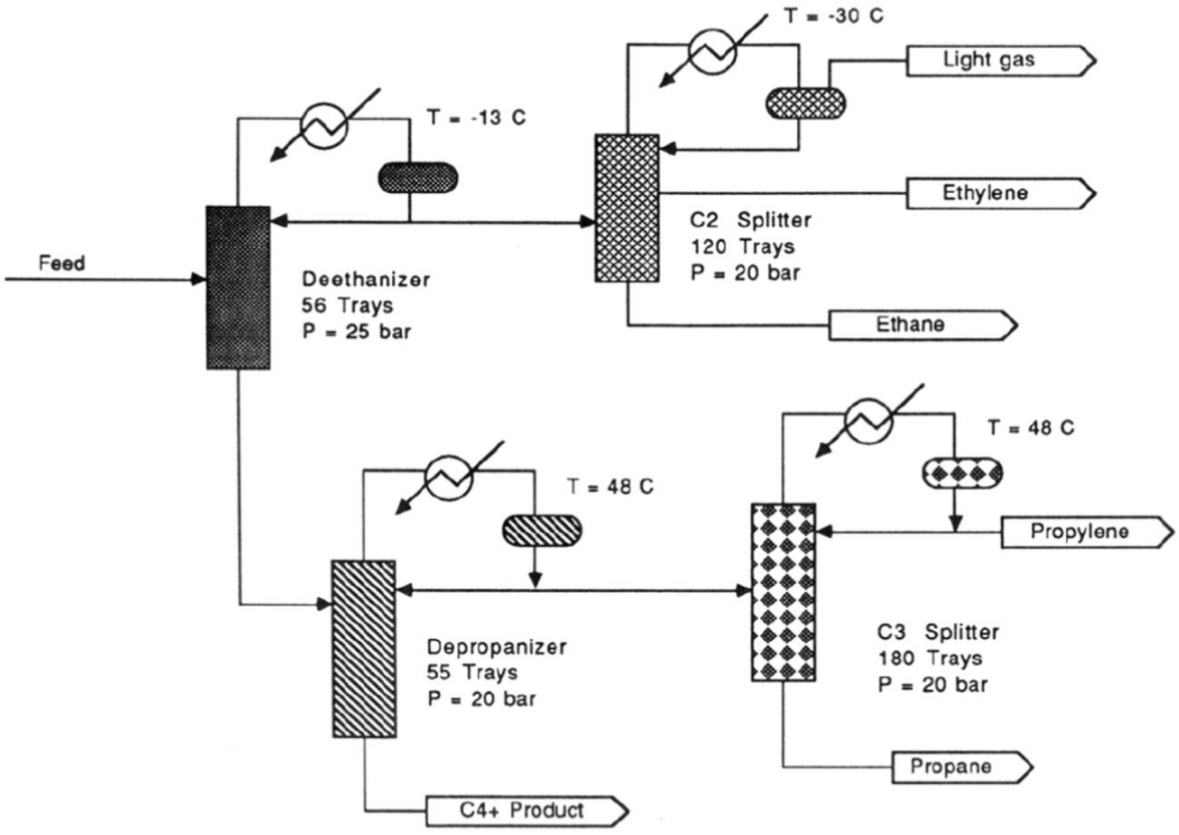

Figure 1.2: Typical distillation process for olefin/paraffin separation [10]

Owing to the cost and complexity of distillation operations in the petrochemical industry, alternative less energy intensive separation technologies, such as membranes, adsorption, extraction, have been important areas of research. While these technologies may not, in the near future, have the potential to stand alone, augmenting distillation operations with these advanced processes to form energy-efficient hybrid systems can still result in significant savings [11-15]. A recent DOE report estimates potential energy savings on the order of $6x10^{12}$ Btu/yr for ethylene/ethane separation and $13x10^{12}$ Btu/yr for propylene/propane separation by using hybrid membrane-distillation operations [11].

1.3. Membrane Technology Overview

Membranes physically separate a feed mixture into two streams by allowing one (or more) component(s) to pass through (permeate) while retaining the remaining component(s) (retentate), and can offer an attractive alternative to energy-intensive traditional thermally-driven processes such as distillation [1, 15-17]. Membranes are already used in mainstream seawater desalination processes and are over ten times more efficient than thermal operations in this application [1]. Gas separation membranes have become increasingly important over the years and commercially attractive in many industrial applications, with a large majority of sales remaining in air separations, hydrogen separations and natural gas treatment [1, 16, 18]. A large growth potential exists for gas separation membranes in the refinery/petrochemical areas, and the rapidly growing natural gas industries [1, 18]. Figure 1.3 shows a breakdown of the predicted gas separation membrane market in 2020 [1].

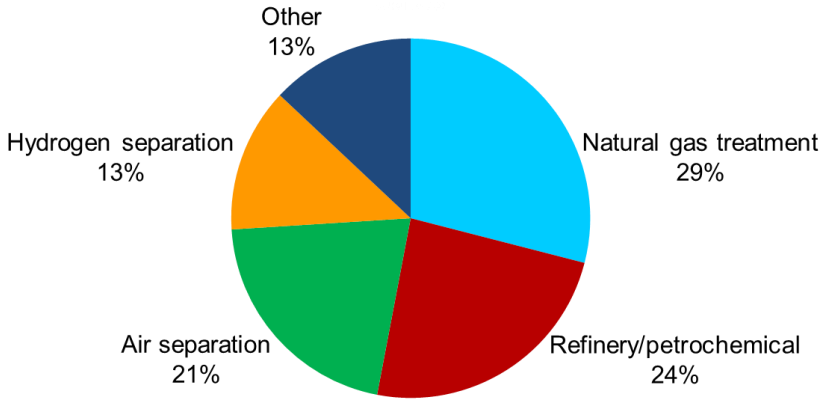

Figure 1.3: % breakdown of membrane market predicted in 2020 (predicted total market of 760 million in 2020) [1]

The petrochemical industry presents vast untapped opportunities for membrane separations. For example, membranes may be promising in several debottlenecking and retrofitting applications including separation of olefins from their respective paraffins (ethylene/ethane, propylene/propane etc.), separation of olefins from paraffins (ethylene+propylene/methane+ethane+propane), hydrogen removal, removal of impurities like acetylene, methyl-acetylene (MA) and propadiene (PD) etc. While some discussion towards the end will be centered on these different possible applications, the main focus of this thesis is ethylene/ethane (C_2H_4/C_2H_6) separation.

The greatest challenges for application of membranes to the C_2H_4/C_2H_6 pair is their lack of selectivity owing to the similar size and physical properties of C_2H_4 and C_2H_6, their narrow range of useful operating conditions under aggressive feeds that can significantly diminish membrane performance, and their high costs [1, 15, 16, 18]. Figure 1.4 summarizes the key elements that must essentially be integrated to introduce any new type of membrane process.

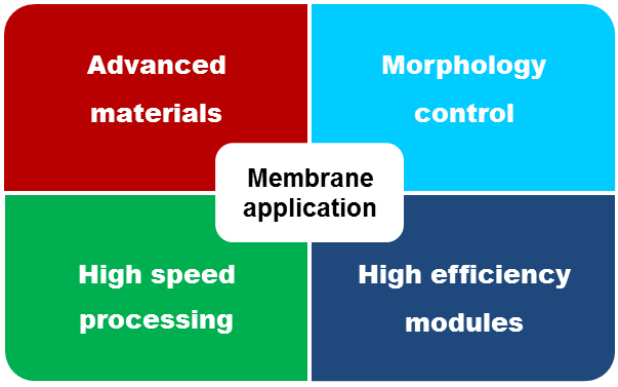

Figure 1.4: Enabling elements for membrane technology advancement [16]

Investigating advanced membrane materials with tunable capabilities is a first key step in developing membranes for (C_2H_4/C_2H_6) separations. Currently explored membrane materials are either excessively expensively, or lack the separation performance or the stability required to successfully implement hybrid membrane-distillation concepts [19]. Conventional polymeric membranes being limited by a trade-off between their productivity (permeability) and efficiency (selectivity), commonly referred to as the "upper bound", cannot achieve the permeability vs. selectivity combinations sufficient for practical C_2H_4/C_2H_6 separations (see Figure 1.5) [20-22]. In addition, polymeric membrane stability under aggressive, highly condensable hydrocarbon feeds can be a serious issue, with membrane swelling (plasticization) and a corresponding selectivity loss occurring even for the most rigid polymers [17, 19, 23, 24]. These concerns have directed significant research to the development of advanced membrane materials for C_2H_4/C_2H_6separations.

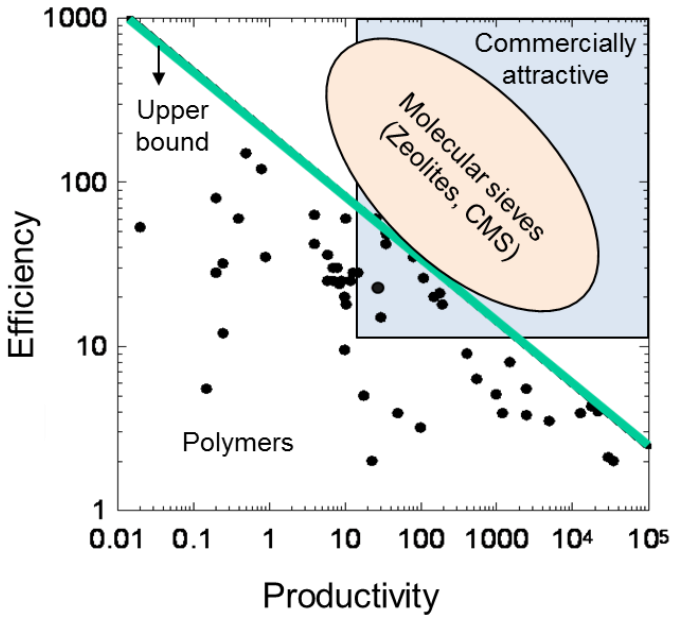

Figure 1.5: Hypothetical polymeric upper bound and capability of molecular sieve membranes to surpass the upper bound

A widely investigated class of membranes for olefin/paraffin separations is facilitated transport membranes. Facilitated membranes consist of clusters of ions (for example silver ions) that selectively bind with the olefin (C_2H_4) favoring its transport across the membrane. They have shown exceptional C_2H_4/C_2H_6 selectivity; however, the intrinsic instability of these membranes makes them questionable for practical applications [10, 12, 25-30].

Molecular sieving inorganic materials such as zeolites and carbon molecular sieve membranes with rigid pore structures may have the ability to overcome the polymeric upper bound (Figure 1.5) since they can very effectively discriminate between subtle size and shape differences of molecules [22, 31]. In the case of zeolite membranes however, their brittle nature as well as the difficulty in fabricating a sufficiently coherent and robust membrane on a large scale makes it hard to justify their use based on expensive fabrication costs.

Carbon molecular sieve (CMS) membranes, formed by the high temperature pyrolysis of polymeric materials under controlled conditions [32-34], have shown separation performance surpassing the polymeric upper bound for a variety of gas pairs such as O_2/N_2, CO_2/CH_4 etc. [22]. Additionally, because of their rigid structure, they do not undergo plasticization under high pressure condensable feeds such as CO_2 and hydrocarbons [24]. These combined attributes make them an exciting option to evaluate for C_2H_4/C_2H_6 separations

Creation, characterization and a thorough fundamental analysis of CMS membranes for C_2H_4/C_2H_6 separation may be best achieved in the simple homogeneous dense film configuration in order to extract intrinsic material properties. While this is important, it is only the first key element needed. Development of high efficiency modules with large surface area per unit volume is necessary for the emergence of large scale operations [16]. In most gas separation operations, membranes are used in the

hollow fiber configuration to meet these requirements. Hollow fiber modules offer much higher surface areas per unit volume compared to other membrane configurations such as plate and frame units, spiral wound membranes etc. and can contain up to 10,000 m^2/m^3 in each module [16]. It is thus critical to develop C_2H_4/C_2H_6 separation CMS membranes in the hollow fiber configuration as well. Specifically for CMS membranes, while studies on homogeneous dense films are crucial for fundamental knowledge, hollow fibers are practically preferred because they are more robust and offer greater flexibility in handling. In fact, although more brittle compared to polymeric membranes, CMS hollow fiber membranes have demonstrated the ability to perform stably up to 1000 psi natural gas feed pressures [24]. Hence, a focused study on development of CMS hollow fiber membranes for C_2H_4/C_2H_6 separation is a second important element from a practical stand point.

Development of sophisticated capability to control the transport properties by tailoring the membrane morphology at multiple levels is another important factor in the emergence of materials [16]. This may include both the microscopic and macroscopic membrane morphology. At the microscopic level, the pore structure of CMS membranes must be effectively tuned to target a particular separation. For example, CMS membranes effective in O_2/N_2 separation may not necessarily be ideal for C_2H_4/C_2H_6 separation. Several tuning parameters such as the choice of the starting polymer, pretreatment on the polymer precursor prior to pyrolysis, the pyrolysis conditions, and any post-treatment on the fabricated CMS can be used to tailor the separation properties of CMS membranes [22, 35-37]. The effects of such microscopic tuning on C_2H_4/C_2H_6 separation may be studied in the CMS dense film configuration enabling insights into structure-performance relationships, and carefully translated to the hollow fiber form. Besides tuning the internal pore structure of CMS membranes to achieve high intrinsic separation performance, control of the macroscopic morphology is also essential. This

becomes especially important in the industrially viable hollow fiber configuration. It has been found that the porous substructure of the starting asymmetric polymeric hollow fiber may collapse due to excessive heat treatment [23]. As a result the ultra-thin separation layer of the starting precursor fiber ends up in a very thick and dense separation layer, which drastically reduces the flux. High flux is essential from a practical stand point since it directly affects membrane area and cost. Hence, controlling the macroscopic fiber morphology and investigating ways to overcome this substructure collapse is critical for CMS application in C_2H_4/C_2H_6 separation.

Last but not the least, the development of manufacturing methods to rapidly link the three elements into economical devices with minimal defects is a critical factor for commercial large-scale membrane systems [16]. Economic feasibility may currently be one of the biggest hurdles to CMS membrane production and implementation. Scale-up and high speed processing capability is necessary to achieve cost-competitiveness. Complicated fabrication techniques can drastically increase membrane cost and may not be feasible for scale-up. For example, use of a vacuum environment as well as multiple treatment steps can rapidly increase costs. Polymeric membranes are state of the art and cost ~\$10-20 per m^2, whereas CMS membranes are estimated to cost \$50-100 per m^2 [37]. While olefin/paraffin applications, where use of polymeric membranes may be impractical, could justify higher membrane costs, in order to make CMS competitive, simple, reproducible, and easily-scalable fabrication techniques must still be addressed [19, 37]. Additionally, practical module construction, tube-sheet and sealing aspects in realistic devices at the temperatures of interest must also be considered.

The four key elements described above have been addressed following a two-pronged approach to investigate CMS membranes for C_2H_4/C_2H_6 separation. In collaboration with The Dow Chemical Company, two projects address both the fundamental and practical aspects of CMS membrane development, primarily for

supplementing the C_2-splitter (C_2H_4/C_2H_6), while also considering other potential applications in the petrochemical industry. The overarching goal of my thesis project is to define the material science options to fabricate novel, high performing C_2H_4/C_2H_6 separation CMS dense film membranes by identifying and optimizing key parameters to tune the CMS micro-morphology. Homogeneous dense films are being used in this work to develop fundamental and theoretical knowledge, and to extract intrinsic CMS characteristics, transport properties, and structure-performance relationships. This work intends to establish a basis for guiding research ultimately aimed at providing a convenient, potentially scalable hollow fiber membrane formation technology for C_2H_4/C_2H_6 separation. Liren Xu's project in the Koros Group focuses on translating insights from the current CMS dense film project to engineer CMS membranes for C_2H_4/C_2H_6 separation in the hollow fiber configuration. His work addresses defect-free asymmetric precursor hollow fiber spinning and corresponding CMS fabrication, control of the fiber morphology, and development and testing of CMS modules. It also considers practical aspects of membrane integration into current distillation operations.

The following section outlines the specific research objectives of this dissertation.

1.4. Research Objectives

1. Analysis of different polymers as precursors to CMS dense film membranes for C_2H_4/C_2H_6 separation.

The intrinsic polymer precursor properties can significantly affect the properties of the resulting CMS membrane; hence choosing the appropriate starting material for CMS fabrication and assessing its viability in C_2H_4/C_2H_6 separation is a first crucial step. This step includes defining a basis against which to compare CMS performance, identifying and testing the performance of the precursor materials for C_2H_4/C_2H_6 separation, as well as preliminary fabrication and testing of CMS membranes formed from the respective precursor materials.

2. Analysis of the effects of pyrolysis parameters on C_2H_4/C_2H_6 separation, and structure-performance evaluation of CMS dense film membranes.

The pore structure of carbon molecular sieve materials may be tailored to obtain the desired properties for a specific separation by controlling several parameters in the CMS fabrication process. In this study, the effects of several pyrolysis parameters such as the heating protocol and pyrolysis atmosphere on the CMS microstructure and performance have been investigated. The evolution in C_2H_4/C_2H_6 separation performance with pyrolysis parameters has been considered with respect to the CMS schematic pore structures and hypothetical critical pore size distributions. This information has been used to achieve optimum CMS fabrication conditions for C_2H_4/C_2H_6 separation. Several techniques such as gas permeation and sorption, density and pore volume measurement from sorption, wide angle x-ray diffraction (WAXD), elemental

analysis, thermogravimetric analysis (TGA) coupled with fourier transform infrared spectroscopy (FTIR) etc. were used to characterize the CMS materials. Traditional characterization techniques were found inconclusive in interpreting CMS performance based on its morphology. In the current work, a method based on measuring the transport properties of different sized gases as molecular scale probes for the CMS ultramicropores was developed to infer pore structure of the engineered CMS membranes. This, in conjunction with separation performance data, provides critical insights into the structure-performance relationships of the engineered CMS materials.

3. Analysis of the effects of testing temperature, pressure and feed composition on C_2H_4/C_2H_6 separation of CMS dense film membranes.

Characterizing the effects of temperature, pressure and feed composition on CMS performance is important not just from a practical stand-point but also for a fundamental understanding of the nature of CMS membrane separation. The effects of temperature on CMS transport were evaluated by varying the testing temperature between 25-50°C. Transport and thermodynamics fundamentals were applied to elucidate how CMS membranes can outperform polymeric membrane performance, as well as to compare between CMS formed from different precursors and processing conditions. The pressure dependence of C_2H_4 and C_2H_6 transport in the CMS was studied. Finally, the effects on C_2H_4 and C_2H_6 transport in the presence of binary gas mixture was assessed to get a more realistic measure of the CMS performance resulting from competition and bulk flow effects. In addition to experimental analysis, modeling work to predict multicomponent transport in CMS membranes was also carried out.

1.5. Dissertation Organization

Following this introductory chapter there are six additional chapters. Chapter 2 provides the essential background and theory to facilitate understanding of the work presented in this dissertation, as well as a literature review on CMS. Chapter 3 describes the materials, experimental procedures, equipment and characterization techniques used in this work. Chapters 4-6 form the main body chapters, corresponding to the three research objectives for this dissertation as stated in the previous section, and present and discuss the results of this work. Chapter 7 summarizes the key findings of this work and recommends several areas for future research in the field. Finally, several appendices provide supplemental information.

1.6. References

[1] Baker RW. Future directions of membrane gas separation technology. Ind Eng Chem Res. 2002;41(6):1393-411.

[2] True WR. OGJ Focus: Global ethylene production continues advance in 2009. Oil Gas J. 2010;108(27):34-8.

[3] http://www.dow.com/productsafety/finder/.

[4] http://www.plastemart.com/upload/literature/Global_demand_of_ethylene.asp.

[5] http://www.chemsystems.com/reports/search/docs/abstracts/0405-7-abs.pdf.

[6] http://www.lyondellbasell.com/index.htm.

[7] Abedi AA. Economic analysis of a new gas to ethylene technology. Texas A&M University, Master of Science, 2007.

[8] Falqi FH. The miracle of petrochemicals - Olefins industry: An in-depth look at steam crackers. Boca Raton: Universal Publishers 2009.

[9] Worrell E, Phylipsen D, Einstein D, Martin N. Energy use and energy intensity of the U.S. chemical industry. Berkeley: Ernest Orlando Lawrence Berkeley National Laboratory, University of California; 2000.

[10] Eldridge RB. Olefin paraffin separation technology - A review. Ind Eng Chem Res. 1993;32(10):2208-12.

[11] Gottschlich DE, Roberts DL. Energy minimization of separation processes using conventional/membrane hybrid systems: US Department of Energy; 1990.

[12] Merkel T, Blanc R, Zeid J, Suwarlim A, Firat B, Wijmans S, et al. Separation of olefin/paraffin mixtures with carrier facilitated membranes: US Department of Energy; 2007.

[13] Caballero JA, Grossmann IE, Keyvani M, Lenz ES. Design of hybrid distillation-vapor membrane separation systems. Ind Eng Chem Res. 2009;48(20):9151-62.

[14] Ozokwelu D. Hybrid separations/distillation technology: Research opportunities for energy and emissions reduction: US Department of Energy; 2005.

[15] Robinson S, Jubin R, Choate B. Materials for separation technologies: Energy and emission reduction opportunities: US Department of Energy; 2005.

[16] Koros WJ. Evolving beyond the thermal age of separation processes: Membranes can lead the way. AIChE J. 2004;50(10):2326-34.

[17] Vu DQ. Formation and characterization of asymmetric carbon molecular sieve and mixed matrix membranes for natural gas purification. The University of Texas at Austin, Doctor of Philosophy, 2001.

[18] Koros WJ, Mahajan R. Pushing the limits on possibilities for large scale gas separation: Which strategies? J Membrane Sci. 2000;175(2):181-96.

[19] Rungta M, Xu L, Koros WJ. Carbon molecular sieve dense film membranes derived from Matrimid® for ethylene/ethane separation. Carbon. 2012;50(4):1488-502.

[20] Robeson LM. Correlation of separation factor versus permeability for polymeric membranes. J Membrane Sci. 1991;62(2):165-85.

[21] Robeson LM. The upper bound revisited. J Membrane Sci. 2008;320(1-2):390-400.

[22] Steel KM. Carbon membranes for challenging gas separations. The University of Texas at Austin, Doctor of Philosophy, 2000.

[23] Xu L, Rungta M, Koros WJ. Matrimid® derived carbon molecular sieve hollow fiber membranes for ethylene/ethane separation. J Membrane Sci. 2011;380(1-2):138-47.

[24] Vu DQ, Koros WJ, Miller SJ. High pressure CO_2/CH_4 separation using carbon molecular sieve hollow fiber membranes. Ind Eng Chem Res. 2002;41(3):367-80.

[25] Azhin M, Kaghazchi T, Rahmani M. A review on olefin/paraffin separation using reversible chemical complexation technology. J Ind Eng Chem. 2008;14(5):622-38.

[26] Faiz R, Li K. Olefin/paraffin separation using membrane based facilitated transport/chemical absorption techniques. Chem Eng Sci. 2012;73:261-84.

[27] Pinnau I, Toy LG. Solid polymer electrolyte composite membranes for olefin/paraffin separation. J Membrane Sci. 2001;184(1):39-48.

[28] Ho WS, Dalrymple DC. Facilitated transport of olefins in Ag^+-containing polymer membranes. J Membrane Sci. 1994;91(1-2):13-25.

[29] Teramoto M, Shimizu S, Matsuyama H, Matsumiya N. Ethylene/ethane separation and concentration by hollow fiber facilitated transport membrane module with permeation of silver nitrate solution. Sep Purif Technol. 2005;44(1):19-29.

[30] Teramoto M, Takeuchi N, Maki T, Matsuyama H. Ethylene/ethane separation by facilitated transport membrane accompanied by permeation of aqueous silver nitrate solution. Sep Purif Technol. 2002;28(2):117-24.

[31] Singh A. Membrane materials with enhanced selectivity: An entropic interpretation. The University of Texas at Austin, Doctor of Philosophy, 1997.

[32] Marsh H. Introduction to carbon science: Butterworths; 1989.

[33] Pierson. Handbook of carbon, graphite, diamond, and fullerenes NY: Noyes Publication 1993.

[34] Jenkins GM, Kawamura K. Polymeric carbons - Carbon fiber, glass and char. London: Cambridge University Press 1976.

[35] Williams PJ. Analysis of factors influencing the performance of CMS membranes for gas separation. Georgia Institute of Technology, Doctor of Philosophy, 2006.

[36] Ismail AF, Saufi SM. Fabrication of carbon membranes for gas separation - A review. Carbon. 2004;42(2):241-59.

[37] Kiyono M. Carbon molecular sieve membranes for natural gas separations. Georgia Institute of Technology, Doctor of Philosophy, 2010.

CHAPTER 2

BACKGROUND AND THEORY

2.1. Overview

This chapter provides essential background, theory and terminology pertinent to this work. A brief background on pyrolytic carbon forms and the structure of carbon molecular sieve (CMS) membranes is included in Section 2.2. Section 2.3 outlines fundamental gas transport theory in membranes including permeation, sorption and diffusion of gases in both polymeric and carbon molecular sieve membranes. Finally, a review of carbon molecular sieve membrane production and factors affecting its formation and transport properties has been described in Section 2.4.

2.2. Pyrolytic Carbon and Carbon Molecular Sieve Membranes

Pyrolysis of carbonaceous precursor materials typically yields either coke or char. Coke comes from precursors that pass through a liquid phase on pyrolysis and form graphitizable carbons. Char is formed from precursors that do not fuse during pyrolysis and form non-graphitizable carbons [1-3].

Figure 2.1 shows the structure of hexagonal graphite with layers or lamellae of carbon atoms arranged parallel to each other and lying above each other with an AB-AB-AB sequence. Carbon forms can be derived from such a model and the structure of both graphitizable (anisotropic) and non-graphitizable (isotropic) carbons is based on graphite, albeit in very defective forms [1, 2].

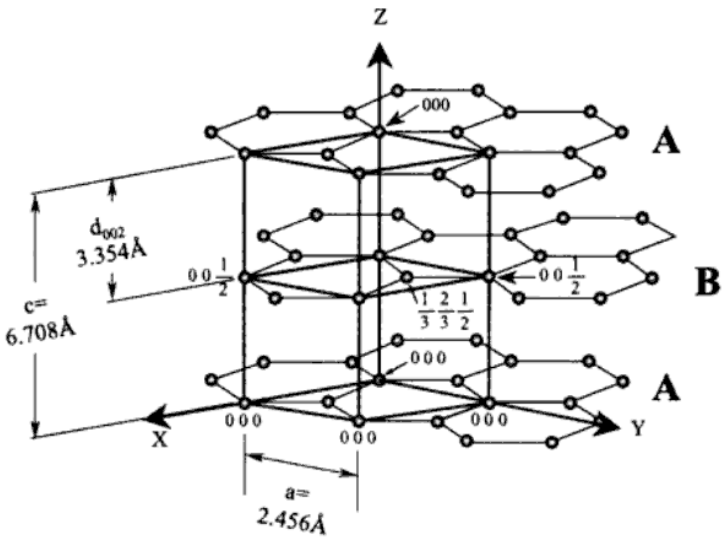

Figure 2.1: Crystal structure of graphite with AB stacking [2]

Anisotropic carbons have essentially approximate parallel arrangements of lamellae which subsequently assume increased order on heat treatment to give graphitic material [1]. Isotropic carbons, on the other hand, have lamellae arranged randomly, bent twisted and imperfect, with some parallel arrangement over short range, and remain in the amorphous form. The arrangement of carbon atoms within the lamellae is not perfect and there could also be heteroatoms like hydrogen, oxygen, nitrogen, sulfur, bonded into the lamellae. Holes resulting due to displacements from true lattice configurations and the irregular stacking arrangements of the lamellae contribute to porosity in the material [1]. Two-dimensional cartoon representations of anisotropic and isotropic carbon forms are shown in Figure 2.2.

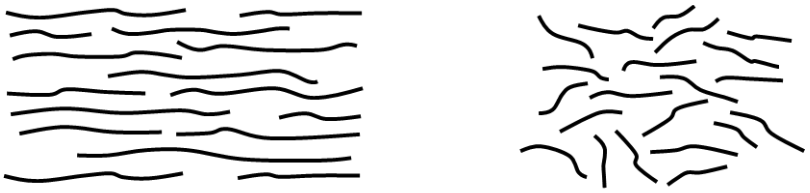

(i) (ii)

Figure 2.2: Two-dimensional drawings of carbon lamellae to illustrate structure in (i) anisotropic and (ii) isotropic carbons [1]

Carbon molecular sieve (CMS) membranes for gas separation are derived from the high temperature pyrolysis of polymeric precursor materials under controlled conditions, resulting in a turbostratic ribbon-like structure with very little long range order, and are considered essentially isotropic, with material properties as described above [1, 3]. They are amorphous materials comprised of disordered and highly disoriented, sp^2 hybridized condensed hexagonal sheets, with pores formed from packing imperfections. Figure 2.3 illustrates the structure of CMS membranes.

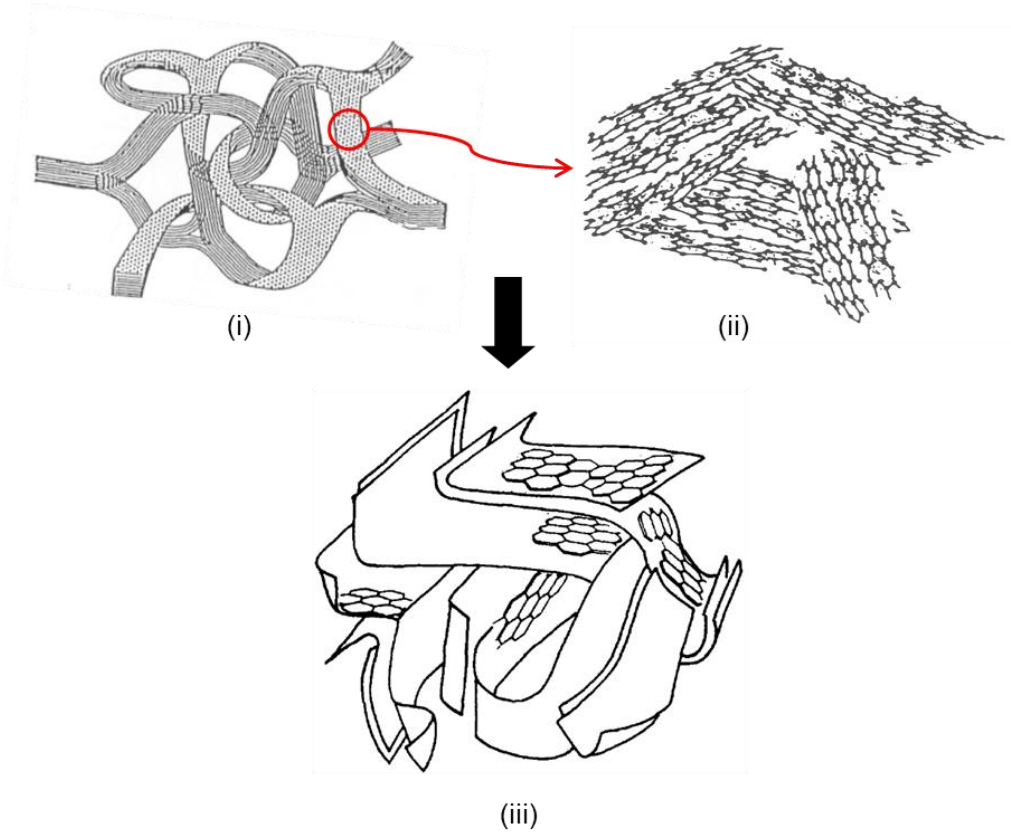

Figure 2.3: Structure of pyrolytic CMS membranes (i) turbostratic ribbon-like matrix [2] (ii) disordered sp^2 hybridized condensed hexagonal sheets [3] (iii) overall structure schematic [4]

An idealized pore structure can be described as slit-like (Figure 2.4) and can be represented by a bimodal pore size distribution with larger pores (~ 6-20 Å) called micropores connected by smaller pore windows called ultramicropores (< 6 Å) [5, 6]. This combination of micropores and ultramicropores allows CMS membranes to achieve both high permeability and high selectivity via a molecular sieving effect.

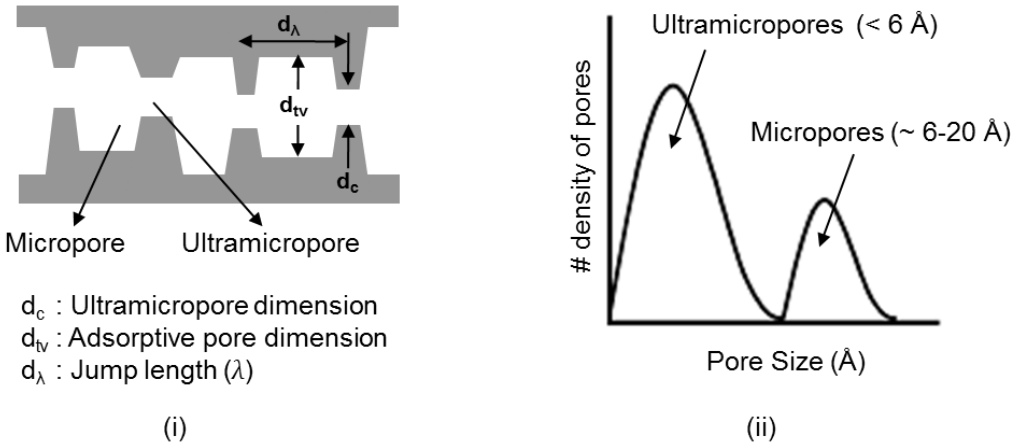

Figure 2.4: Cartoon representation of CMS membrane showing (i) Ideal "slit-like" pore structure [5] and (ii) Bimodal distribution of pores [5]

The disordered structure of CMS materials is different from zeolites. While CMS are amorphous materials having a wide pore size distribution, zeolites are crystalline materials with well-defined pore structures. For example, the crystal structure of zeolite 4A has been well characterized [7]. It consists of different cavity dimensions which may be determined by x-ray diffraction, while the critical dimensions may be determined by gas transport. For example, in the sorbed state a gas molecule resides in the 11.2 Å cavities, but to make a diffusive jump it must jump through the 3.8 Å constrictions. CMS materials, on the other hand, because of their amorphous nature are hard to characterize, especially the critical ultramicropore distributions. Traditional materials characterization techniques such as x-ray diffraction (XRD), high resolution microscopy, positron annihilation lifetime spectroscopy etc. fail to conclusively characterize CMS materials [5, 8-12]. Gas sorption measurements on the other hand provide information regarding the larger micropores [5, 10, 13, 14], but cannot completely elucidate the critical ultramicropore size distribution responsible for molecular sieving. The difficulties in characterizing CMS materials will be discussed in Chapter 5 and a method to infer the

CMS structure by investigating the transport properties of different sized gas molecules as molecular sized probes will be presented.

2.3. Fundamentals of Gas Transport in Membranes

A gas separation membrane functions as a selective barrier material. A feed gas mixture contacts the upstream side of the membrane, one (or more) components selectively pass through the membrane, resulting in a permeate stream on the downstream side of the membrane and the enrichment of the rejected species on the retentate side of the membrane. Several mechanisms can lead to selective transport through gas separation membranes: (i) Knudsen diffusion transport, (ii) selective surface adsorption with surface diffusion, (iii) molecular sieving transport and (iv) sorption-diffusion transport [15, 16], as shown in Figure 2.5.

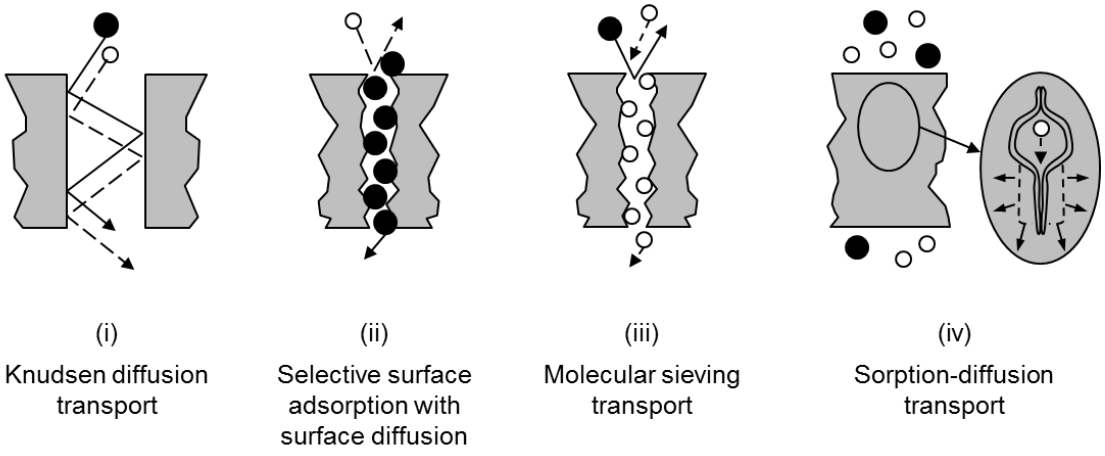

Figure 2.5: General mechanisms for selective gas transport through membranes [15, 16]

In porous membranes, the pore size and the mean free path for diffusion of the penetrant at a given temperature and pressure govern the transport process. When the pore radius is much larger than the mean free path of the penetrant molecules, viscous flow occurs with no discrimination between the penetrants [15]. When the pore size is reduced to a point smaller than the mean free path of the molecules, gas transport takes place by a Knudsen diffusion mechanism, and discrimination between penetrants can be possible based on their molecular weights [17] as,

$$\alpha_{A/B} = \sqrt{\frac{M_A}{M_B}} \tag{2.1}$$

where, $\alpha_{A/B}$ represents the selectivity of component A over B. It is evident from Equation 2.1 that selectivities resulting from Knudsen diffusion transport are generally fairly low for molecules of similar molecular weight such as O_2/N_2, C_2H_4/C_2H_6 etc.

Selective adsorption separation occurs when certain species are preferentially adsorbed into the membrane while excluding the other components, followed by surface diffusion of the adsorbed species across the membrane from one sorbed site to the next [15]. The separation efficiency is driven by the physicochemical nature of the pore surface and the pore size. For example, Rao & Sircar [18-20] developed selective surface flow membranes based on this mechanism for separating low sorbing hydrogen from highly adsorptive hydrocarbon streams.

Molecular sieving transport occurs when penetrant molecules are separated based on size using the pore structure of the membranes. Diffusion through the critical pores requires molecules to overcome repulsion from the pore walls, and even small changes in size can result in significant differences in the activation energy required for

diffusion. Hence, size-selective molecular sieving allows passage of the smallest molecule(s) through the membrane resulting in effective separation [5, 15, 16].

In the sorption-diffusion transport process, the size (diffusivity) and condensability (solubility) selective factors interact to determine which component(s) pass through the membrane the fastest [15]. For example, in non-porous polymeric membranes, gas transport takes place by a sorption-diffusion mechanism. Mechanisms for gas transport can be very different at temperatures below and above the glass-transition temperature (T_g) of the polymer, i.e. depending on whether the polymer is in a rubbery state (above T_g) or glassy state (below T_g) [21], as shown in Figure 2.6.

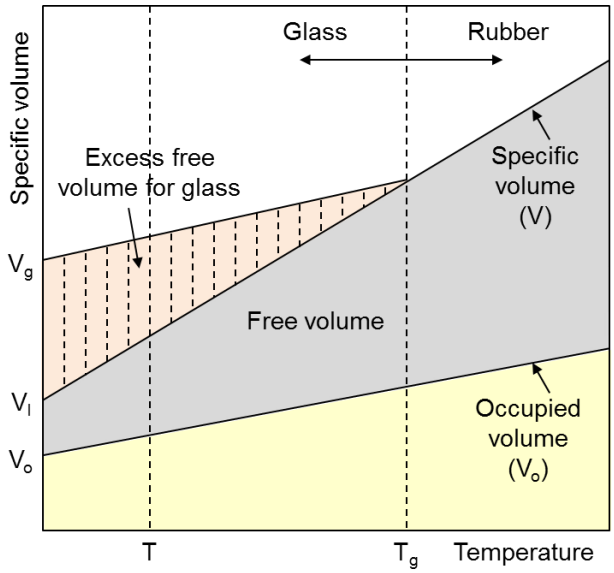

Figure 2.6: Specific volume behavior of amorphous polymers as a function of temperature [22]

The differences in the transport behavior of rubbery and glassy polymers are due to the fact that the latter are not in a state of true thermodynamic equilibrium. Rubbery polymers have flexible chains with very short relaxation times, and sorption is the

dominating factor in gas transport. In other words, highly condensable gases sorb preferentially in the rubbery polymer matrix and thus permeate faster. By comparison, glassy polymers have rigid chains with longer relaxation times. Penetrant molecules can potentially sit in "holes" with different intrinsic diffusion mobilities depending on the kinetic diameter of the gas as well as polymer chain packing and mobility [21].

Gas transport in CMS membranes relies on a combination of size and shape (diffusivity) and condensability (solubility) of the components in the CMS matrix, and is modeled based on the sorption-diffusion mechanism [5, 12, 23]. Micropores provide sorption sites for the gas molecules and long diffusion jump lengths, resulting in high permeability. Gas transport takes place by a hopping mechanism from one sorption site to the next, driven by a concentration gradient between the upstream and the downstream side. The critical ultramicropores on the other hand restrict diffusion, requiring the penetrant molecules to overcome repulsive interactions from the pore walls. This allows effective discrimination between similar sized gas molecules via a molecular sieving effect [5, 12, 23]. Thus the combination of micropores and ultramicropores allow CMS membranes to achieve both high permeability and high selectivity [5, 8, 24].

The following sub-sections discuss essential theory and terminology for membranes-based gas separation.

2.3.1. Permeation

As mentioned above, gas transport in polymeric and CMS membranes is described by a sorption-diffusion model, wherein gas molecules sorb at the upstream face of the membrane, diffuse through the membrane under a chemical potential gradient, and desorb at the downstream side [22]. It is assumed that the fluid on either

side of the membrane is in equilibrium with the membrane material at the gas-membrane interface. Additionally, the sorption-diffusion model assumes that there is a pressure drop across the membrane but the pressure within the membrane is constant at the high pressure (upstream) value. The driving force based on the chemical potential gradient across the membrane is expressed as a concentration gradient [25]. These assumptions are illustrated in Figure 2.7 below.

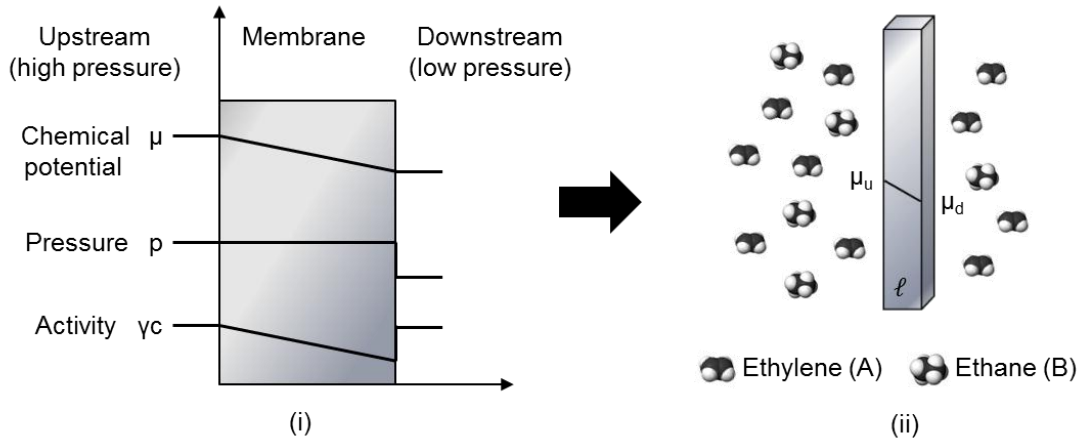

Figure 2.7: Sorption diffusion model (i) Schematic representation of assumptions in solution-diffusion membrane transport [25], (ii) Schematic representation of ethylene/ethane separation by the solution-diffusion process

Membrane performance is characterized by two main parameters: 'permeability', a measure of the membrane's intrinsic productivity, and 'selectivity', a measure of the membrane's separation efficiency [22, 26]. The permeability (P_A) of a component A is expressed as the steady-state flux of A across the membrane (N_A) normalized by the partial pressure difference across the membrane (Δp_A) and the membrane thickness (ℓ).

$$P_A = \frac{N_A \, \ell}{\Delta p_A} \tag{2.2}$$

In the case of homogeneous dense film membranes, the membrane thickness can be determined fairly easily. However, for asymmetric membranes, the exact thickness of the separation layer cannot be determined. The productivity of asymmetric membranes is thus represented in terms of permeance, as defined in Equation 2.3.

$$\frac{P_A}{\ell} = \frac{N_A}{\Delta p_A} \tag{2.3}$$

In membrane literature, the permeation term is often reported in a variety of units. In the work, for consistency, permeability and permeance are reported in the units of Barrer and Gas Permeance Unit (GPU) respectively, as defined in Table 2.1.

Table 2.1: Units for permeability and permeance

Permeability	Permeance
$1 \text{ Barrer} = 10^{-10} \frac{\text{cc(STP)}.\text{ cm}}{\text{cm}^2.\ \text{s}\ .\text{cmHg}}$	$1 \text{ GPU} = 10^{-6} \frac{\text{cc(STP)}}{\text{cm}^2.\ \text{s}\ .\text{cmHg}}$

Figure 2.8 shows a cartoon representation of polymeric and CMS membranes in the dense film and the asymmetric hollow fiber configuration.

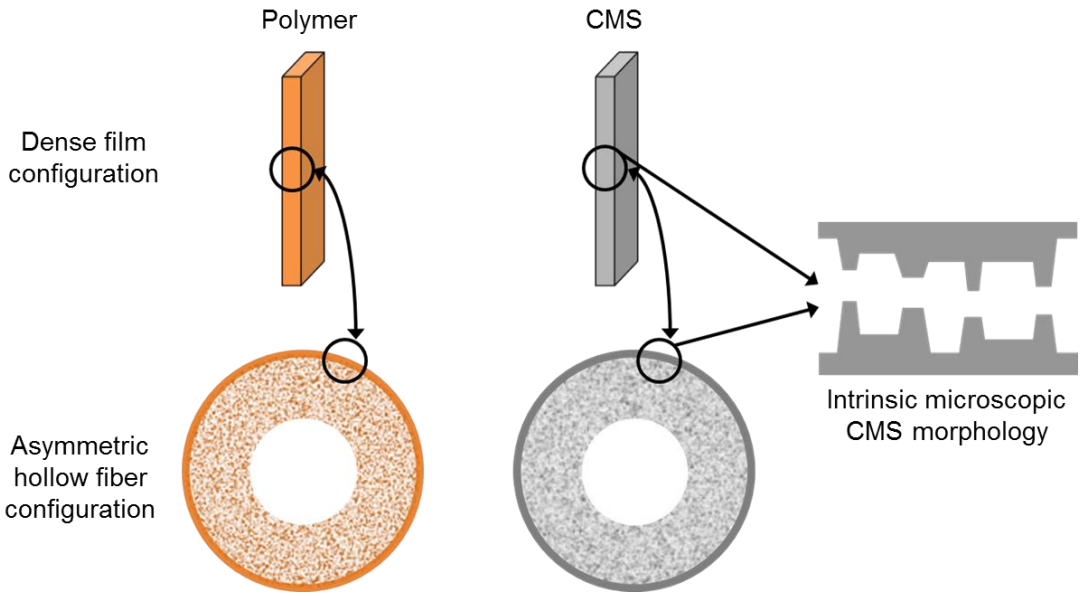

Figure 2.8: Representation of dense film and asymmetric hollow fiber membrane configurations in polymeric and CMS membranes

Based on the sorption-diffusion model, the permeability (P_A) of component A can further be represented as a product of a kinetic factor, i.e. the average diffusion coefficient ($\overline{D}_A$), and a thermodynamic factor, i.e. the average sorption coefficient ($\overline{S}_A$) [21, 22]. This relationship can be derived by representing the flux (N_A), in the absence of any bulk flow effect, using Fick's first law of diffusion [17, 22] as shown in Equation 2.4.

$$N_A = -D_A \frac{dC_A}{dx} \tag{2.4}$$

where, C_A represents the concentration of A in the membrane. The effects of bulk flow on the overall transport flux and the corresponding modified flux equations have been discussed in detail in Chapter 6.

Substituting Equation 2.4 in Equation 2.2 above gives an expression for permeability as shown in Equation 2.5.

$$P_A = \frac{N_A \ell}{\Delta p_A} = -D_A \frac{dC_A}{dx} \frac{\ell}{\Delta p_A} \tag{2.5}$$

Equation 2.5 can be integrated with the following boundary conditions across the membranes: $C_A = C_{A,u}$ at $x = 0$ (upstream face of the membrane at pressure $p_A = p_{A,u}$) and $C_A = C_{A,d} = 0$ at $x = \ell$ (downstream face of the membrane under vacuum i.e. $p_A = p_{A,d} = 0$). Thus,

$$\int_0^{\ell} \frac{P_A}{\ell} dx = -\int_{C_{A,u}}^{C_{A,d}} D_A(C_A) \frac{dC_A}{\Delta p_A} \tag{2.6}$$

$$P_A = -\int_{C_{A,u}}^{C_{A,d}} \frac{D_A(C_A)\, dC_A}{(C_{A,u} - C_{A,d})} \frac{(C_{A,u} - C_{A,d})}{\Delta p_A} \tag{2.7}$$

The right hand side of equation 2.7 is simplified by introducing the mean transport diffusion coefficient ($\overline{D}_A$) and the mean sorption coefficient ($\overline{\mathbb{S}}_A$) as defined in Equations 2.8 and 2.9 respectively [12, 21, 22].

$$\overline{D}_A = \frac{\int_{C_{A,u}}^{C_{A,d}} D_A(C_A)\, dC_A}{\int_{C_{A,u}}^{C_{A,d}} dC_A} = -\int_{C_{A,u}}^{C_{A,d}} \frac{D_A(C_A)\, dC_A}{(C_{A,u} - C_{A,d})} \tag{2.8}$$

$$\overline{\mathbb{S}}_A = \frac{\int_{C_{A,u}}^{C_{A,d}} dC_A}{\int_{p_{A,u}}^{p_{A,d}} dp_A} = \frac{(C_{A,u} - C_{A,d})}{\Delta p_A} \tag{2.9}$$

Substituting Equations 2.8 and 2.9 in Equation 2.7, the permeability of component A can be represented as a product of its mean diffusion and sorption coefficients.

$$P_A = \overline{D}_A \overline{\mathbb{S}}_A \tag{2.10}$$

The efficiency of a membrane in separating components of a gas mixture is given by the separation factor, defined as the ratio of the permeate-side mole fractions (y) of the fast gas (A) versus the slow gas (B) over the feed-side mole fractions (x) of the fast gas (A) versus the slow gas (B) [22].

$$\alpha_{A/B} = \frac{(y_A/y_B)_{permeate}}{(x_A/x_B)_{feed}} \tag{2.11}$$

When the pressure on the permeate (downstream) side is negligible compared to the upstream pressure, as in the current study where the downstream is maintained under vacuum, and for pure component feeds, the separation factor is known as the ideal permselectivity, and can be represented as a ratio of the fast gas and slow gas permeabilities. From Equation 2.10, the permselectivity can further be represented as a product of diffusion and sorption selectivities [22].

$$\alpha_{A/B} = \frac{P_A}{P_B} = \left(\frac{\overline{D}_A}{\overline{D}_B}\right)\left(\frac{\overline{S}_A}{\overline{S}_B}\right) \quad (2.12)$$

The membrane selectivity is thus dependent on a kinetic and a thermodynamic selection factor. Membrane materials may be tailored to increase the permselectivity by optimizing these two characteristics. The diffusion selectivity is dependent on the size and shape of the gases, while the sorption selectivity is dependent on the relative condensabilities of the gases and their interactions with the membrane material [27]. In the case of C_2H_4/C_2H_6 separation, owing to the similar condensabilities and critical temperatures of the penetrants, the sorption selectivity offers little room for tailoring (unless the membrane is functionalized), and high diffusion selectivity may be required to achieve useful selectivity in Equation 2.12. In this regard, molecular sieving materials like CMS and zeolites having rigid pore walls, as opposed to flexible chains in polymeric membranes, may be a key factor enabling effective discrimination between similar sized molecules to achieve high selectivity [8].

In commercial applications, the permeability and selectivity of the membrane material must be balanced to achieve a practical optimum since there is usually a trade-off between the two performance parameters [5, 26, 28-31].

2.3.2. Sorption

The sorption coefficient of a gas A describes the amount or concentration of gas (C_A) taken up by the membrane material at a given pressure (p_A) at equilibrium as represented in Equation 2.13 [22]. It depends on the condensability of the gas and its interactions with the membrane material.

$$\mathbb{S}_A = \frac{C_A}{p_A} \tag{2.13}$$

In glassy polymers, the dual mode sorption model [21, 22] offers a satisfactory description of equilibrium gas sorption and penetrant concentration dependence. This model postulates that a gas sorbed in a glassy polymer consists of two distinct molecular populations: (i) molecules sorbed in the polymer by an ordinary dissolution process in the dense polymer matrix, similar to that above T_g (as in the case of rubbery polymers), and (ii) molecules sorbed in a limited number of holes or microvoids in the polymer matrix corresponding to the unrelaxed excess free volume in glassy polymers. The concentration of molecules sorbed in the well-packed regions (C_{DA}) is related to the penetrant equilibrium pressure (p_A) by Henry's law isotherm:

$$C_{DA} = k_{DA} p_A \tag{2.14}$$

where, k_{DA} is the Henry's law constant. The concentration of molecules dissolved in packing disruptions, or so-called holes or microvoids, (C_{HA}) is related to p_A by the Langmuir isotherm:

$$C_{HA} = \frac{C'_{HA} b_A p_A}{1 + b_A p_A} \tag{2.15}$$

where, C'_{HA} is the Langmuir saturation constant and b_A is the Langmuir affinity constant. Local equilibrium is assumed to exist between the two molecular populations.

The total concentration of dissolved penetrant at a given pressure and temperature is given as the sum of Equations 2.14 and 2.15 (Figure 2.9).

$$C_A = C_{DA} + C_{HA} = k_{DA}p_A + \frac{C'_{HA}b_A p_A}{1 + b_A p_A} \tag{2.16}$$

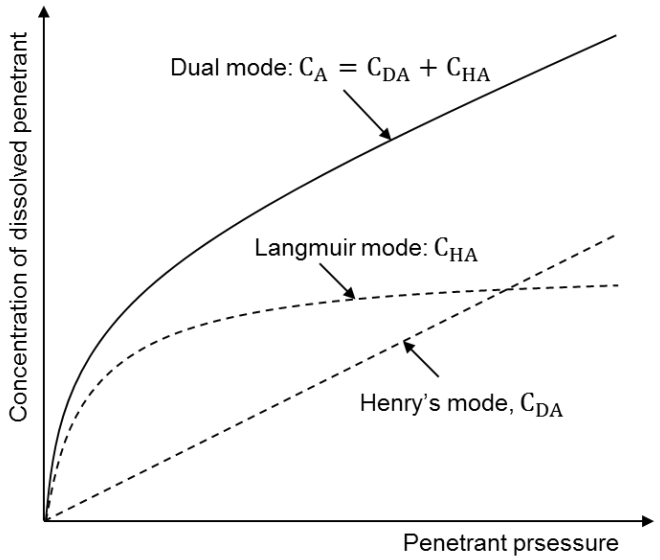

Figure 2.9: Sorption isotherms

For molecular sieving materials, such as zeolites and CMS, with a finite number of sorption sites and rigid saturable capacities, the Langmuir isotherm is typically used to describe gas sorption [5, 32]:

$$C_A = C_{HA} = \frac{C'_{HA}b_A p_A}{1 + b_A p_A} \tag{2.17}$$

In CMS membranes, the majority of the penetrant molecules are sorbed into the larger pores (micropores) [5] characterized by dimension d_{tv} in Figure 2.10, since the repulsive interaction energy of the molecule sorbed into the larger pores is lower than that of sitting in the critical pore windows of dimension d_c. The Langmuir isotherm accounts for site saturation, the rate of sorption being proportional to the product of the penetrant concentration in the gas phase and the amount of available sorption sites, which reaches dynamic equilibrium with the desorption rate. The Langmuir isotherm, albeit simple, offers a useful visualization of sorption process in CMS [32].

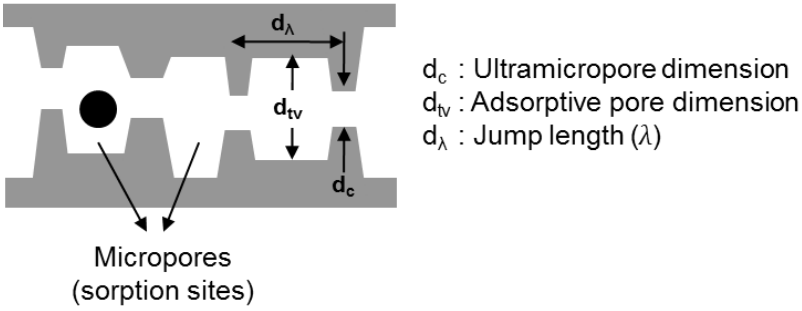

Figure 2.10: Schematic representation of sorption sites in CMS membranes [5]

In highly porous molecular sieving materials, such as CMS, with high surface area, the concentration dependence of transport properties may be significant and can depend on the adsorbate loading. It is useful to define a fractional site saturation factor (θ_A), based on the Langmuir isotherm model, to account for uptake of gas A by the CMS membrane material [32, 33]. Thus,

$$\theta_A = \frac{C_A}{C'_{HA}} = \frac{b_A p_A}{1 + b_A p_A} \tag{2.18}$$

In case of multi-component mixtures, competitive sorption factors come into play, with both species contending for the same sorption sites, and for each component (i) in the mixture, similar expressions can be derived based on Langmuir sorption model in CMS membranes.

$$C_i = C_{Hi} = \frac{C'_{Hi} b_i p_i}{1 + \sum b_i p_i} \tag{2.19}$$

2.3.3. Diffusion

The diffusion coefficient is a measure of the mobility of the gas penetrant through the membrane. In polymeric and CMS membranes, gas molecules diffuse through the membrane in the direction of a concentration gradient by making random jumps from site to site. Quantitatively, the diffusion coefficient of a penetrant A is a function of the frequency of jumps that the molecule makes (f_A) and the average diffusion jump length (λ_A) [21].

$$D_A = \frac{f_A \lambda_A{}^2}{6} \tag{2.20}$$

In polymeric membranes, the diffusion coefficient is a function of the penetrant size, the packing and mobility of the polymer chains and the cohesive energy [27, 34]. It is envisioned that polymer matrices exhibit fluctuating 'gaps' that are continuously

created and redistributed by thermally stimulated polymer chain segmental motions. A transient gap of sufficient size adjacent to a sorbed penetrant enables an actual diffusive step by the penetrant [21, 22]. Figure 2.11 shows a schematic representation of the diffusion process in polymers. The size and frequency of the jumps differs for different-sized penetrants because of their different sizes and condensabilities in the polymer matrix, thus resulting in different diffusion rates.

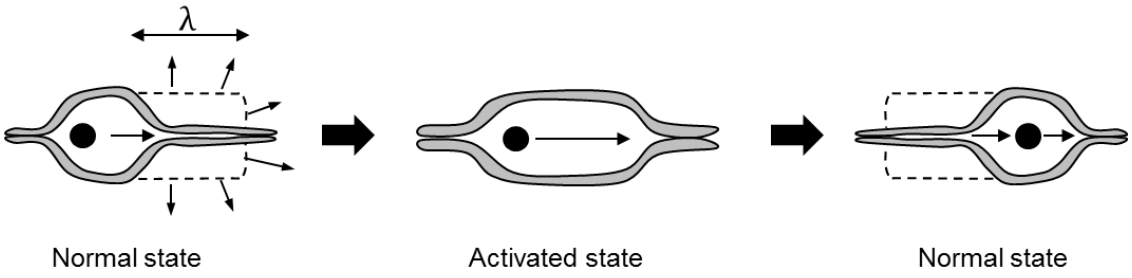

Figure 2.11: Conceptual depiction of a diffusion step in a polymeric membrane [21, 22]

The diffusion mechanism in molecular sieving materials, with rigid pore structures, is somewhat different from polymers. The diffusion rate depends on the sizes and shapes of the gas molecules and the critical ultramicropore dimensions. The diffusion process is envisioned to occur when a gas molecule makes a diffusive jump from one sorption site (micropore) to the next by making a jump through a narrow pore window (ultramicropore) [5, 8, 32], as shown in Figure 2.12.

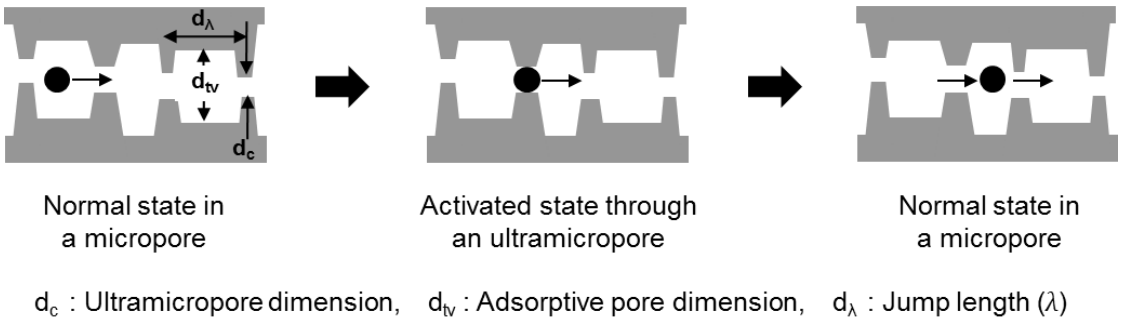

Figure 2.12: Conceptual depiction of diffusion in CMS membranes

In doing so, a gas molecule needs to overcome the repulsive interaction energy from the rigid ultramicropore walls. Molecular sieving ultramicropores can very effectively separate similar sized gas molecules since even small changes in size can result in considerable differences in the activation energy required to make a diffusive jump. This is referred to as 'energetic selectivity' [8]. In addition, unlike polymers which have flexible chains, the rigid ultramicropore walls of the CMS can very effectively discriminate between the shapes of similar sized molecules and restrict several degrees of freedom of rotation and internal vibration of the rejected molecule. This is referred to as 'entropic selectivity' [8]. This unique feature allows molecular sieving materials to outperform the polymeric membrane performance [35].

In CMS membranes, although the average transport (Fickian) diffusivity ($\overline{D}$) is commonly used to characterize diffusion, it can be strongly concentration-dependent. This can be particularly significant for highly adsorbing species. To account for this concentration dependence, it is often useful to evaluate molecular sieving behavior based on a thermodynamically corrected concentration-independent diffusivity (Maxwell-Stefan diffusivity) by accounting for the amount of gas taken up by the membrane [7, 32] as follows:

$$\mathrm{D} = Đ\frac{\mathrm{d}\,\ln p}{\mathrm{d}\,\ln C(p)} \tag{2.21}$$

where, D is the transport diffusivity, $Đ$ is the Maxwell-Stefan diffusivity and represents the diffusion coefficient at zero loading, p is the gas phase equilibrium pressure and $\mathrm{C}(\mathrm{p})$ is the gas uptake by the membrane material. Using the Langmuir isotherm model in Equation 2.21, the following relationship is obtained for gas A:

$$\mathrm{D_A} = \frac{Đ_A}{1-\theta_A} \tag{2.22}$$

where, θ_A is the fractional site saturation factor [33] as defined in Equation 2.18.

Since the diffusion coefficient obtained from permeation and sorption measurements represents an average transport (Fickian) diffusivity ($\overline{\mathrm{D}}_\mathrm{A}$), it is useful to relate the corrected diffusivity ($Đ_A$) to the average transport diffusivity. This can be done by appropriately averaging the local transport diffusivity ($\mathrm{D_A}$) by integrating over a certain concentration ($\mathrm{C_A}$) within the membrane to the membrane downstream, in this case maintained under vacuum. Thus, from Equations 2.8, 2.18 and 2.22 we get

$$\overline{\mathrm{D}}_\mathrm{A} = \frac{\int_{C_A}^{0} \mathrm{D_A}\,\mathrm{dC_A}}{\int_{C_A}^{0} \mathrm{dC_A}} \approx \frac{\int_{\theta_A}^{0} \frac{Đ_A}{(1-\theta_A)}\,\mathrm{d}\theta_A}{\int_{\theta_A}^{0} \mathrm{d}\theta_A} = \frac{Đ_A}{\theta_A}\ln\left(\frac{1}{1-\theta_A}\right) \tag{2.23}$$

2.3.4. Temperature Dependence of Diffusion, Sorption and Permeation

As described above, usefully selective diffusion of a gas penetrant through either polymeric or CMS membranes occurs by an activated process. The diffusion coefficient increases with temperature following an Arrhenius-type equation (Equation 2.24). The thermodynamic sorption coefficient decreases with temperature following a van't-Hoff-type equation (Equation 2.25) [21, 22, 36].

$$D = D_o \exp\left(-\frac{E_D}{RT}\right) \tag{2.24}$$

$$\mathbb{S} = \mathbb{S}_o \exp\left(-\frac{H_{\mathbb{S}}}{RT}\right) \tag{2.25}$$

where, D_o and $\mathbb{S}_o$ are the pre-exponential factors for diffusion and sorption respectively, E_D is the apparent activation energy for diffusion, $H_{\mathbb{S}}$ is the apparent heat of sorption, R is the universal gas constant, and T is the absolute temperature.

Since permeability is a product of the diffusion and sorption coefficients, Equations 2.24 and 2.25 can be combined to express permeability in an Arrhenius-type equation [12, 22, 36]:

$$P = \overline{D}_A \overline{\mathbb{S}}_A = D_o \exp\left(-\frac{E_D}{RT}\right) \mathbb{S}_o \exp\left(-\frac{H_{\mathbb{S}}}{RT}\right) = P_o \exp\left(-\frac{E_P}{RT}\right) \tag{2.26}$$

which gives,

$$P_o = D_o \mathbb{S}_o \tag{2.27}$$

$$E_P = E_D + H_{\mathbb{S}} \tag{2.28}$$

where, P_o is the pre-exponential factor for permeation and E_P is the apparent activation energy for permeation.

The temperature dependence of permeability is typically less pronounced than that of diffusion, because the activation energy of permeation is lower than for diffusion due to the negative heat of sorption. The increase in diffusivity generally outweighs the decrease in the sorption coefficient, thereby resulting in an increase in permeability with temperature. Selectivity, on the other hand, decreases with temperature since in most cases an increase in temperature results in a greater increase in the permeability of the slower gas.

2.3.5. Energetic and Entropic Contributions to Diffusion Selectivity

As described in the previous section, diffusion coefficient increases with temperature according to an Arrhenius relationship (Equation 2.24). The overall diffusion selectivity comprises of an "energetic selection" factor and an "entropic selection" factor [8, 35, 37]. While the activation energy of diffusion (E_D) corresponds to the energetic factor, the pre-exponential factor for diffusion (D_o) includes an entropic factor. The Eyring theory of rate processes [38] has been used to describe D_o based on transition state theory as

$$D_o = e\lambda^2 \frac{kT}{h} \exp\left(\frac{S_D}{R}\right) \tag{2.29}$$

where, λ is the average diffusive jump length, S_D is the activation entropy of diffusion, k is Boltzmann's constant, and h is Planck's constant [35, 37, 38] . Note that the S used for entropy is different from the $\mathbb{S}$ used for the sorption coefficient. For a gas pair A and B of similar size, the jump length λ in a CMS may be considered essentially equivalent for both penetrants [35, 37]. The diffusion selectivity is thus obtained from Equation 2.24 and 2.29 as

$$\begin{aligned} \frac{D_A}{D_B} &= \frac{D_{oA}}{D_{oB}} \exp\left(-\frac{E_{DA} - E_{DB}}{RT}\right) \\ &= \exp\left(\frac{S_{DA} - S_{DB}}{R}\right) \exp\left(-\frac{E_{DA} - E_{DB}}{RT}\right) \\ &= \underbrace{\exp\left(\frac{\Delta S_{DA,B}}{R}\right)}_{\substack{\text{Entropic} \\ \text{Selectivity}}} \underbrace{\exp\left(-\frac{\Delta E_{DA,B}}{RT}\right)}_{\substack{\text{Energetic} \\ \text{Selecitivity}}} \end{aligned} \tag{2.30}$$

From transition state theory, the diffusion coefficient can also be represented in terms of the partition function as

$$D = \lambda^2 \left(\frac{kT}{h}\right) \frac{F^{\neq}}{F} \exp\left(\frac{-E_D}{RT}\right) \tag{2.31}$$

where, $F = F_{trans}.F_{rot}.F_{vib}$ is the partition function of a gas molecule in the sorbed (assumed as normal) state, and $F^{\neq}$ is its partition function in the activated or transition

state [35, 37]. The normal and transition states for polymeric membranes [21, 22] and CMS membranes [35] are illustrated respectively in Figures 2.11 and 2.12 above. $F^{\neq}$ does not contain the translational degree of freedom in the direction of diffusion and this is accounted for by the factor $\left(\frac{kT}{h}\right)$. Combining Equations 2.29, 2.30 and 2.31 we get the "entropic selectivity" as

$$\exp\left(\frac{\Delta S_{D_{A,B}}}{R}\right) = \frac{D_{oA}}{D_{oB}} = \frac{(F^{\neq}/F)_A}{(F^{\neq}/F)_B} \tag{2.32}$$

Singh and Koros [8, 35] have discussed the importance of entropic selectivity in molecular sieving materials such as zeolites and CMS. In the case of CMS membranes, a gas molecule is in the normal state when it sits in a micropore, and the transition state occurs as it passes through the ultramicropore window. The ultramicropores in CMS membranes are analogous to the selective window openings in zeolites and can restrict the rotational and internal vibrational degrees of freedom of one molecule compared to the other, thus allowing very subtle discrimination between small size, shape and configurational differences of molecules. This enables CMS membranes to achieve a high degree of entropic selectivity, which is typically lacking in polymeric membranes comprising flexible chains. This capability can be especially useful in the separation of similar sized gas molecules like C_2H_4 and C_2H_6.

2.4. Formation of Carbon Molecular Sieve Membranes

As mentioned in Section 2.1, carbon molecular sieve (CMS) membranes are produced by the pyrolysis of polymer precursor materials under controlled environments. The pyrolysis process is usually carried out slowly in a vacuum, inert or reducing environment, over a range of temperature depending on the starting polymer and may extend to 1300°C. The carbonization process in polymers is quite intricate and complex, and several reactions may take place at the same time such as cleavage, dehydrogenation, condensation, isomerization etc. [2, 39, 40]. The early stages of carbonization involve cleavage of bonds within the macromolecular system to give free radicals. Details of collapse of the macromolecular system are not fully understood although the early stages of carbonization involve the elimination of small molecules as volatile material in the form of water, methanol, methane, carbon dioxide etc. Such eliminations generate microporosity within the rigid macromolecular system and, at the same time, radicals generated at surfaces combine with each other or extract hydrogen from the system. The carbonization process is thus a simultaneous process of elimination of small molecules and the subsequent re-arrangements of carbon atoms to form more stable six-membered rings of disordered carbon lamellae. Around 550°C, depending on the system, all of the aliphatic carbon is converted to aromatic C-H, resulting in the final CMS residue with over 85% carbon [1].

As explained in Section 2.1, the gas separation performance in CMS membranes is controlled by its pore size distribution and critical ultramicropores. Several key parameters can be used to tailor the pore structure of CMS membranes, namely the starting polymer precursor, pre-treatment conditions, pyrolysis conditions (i.e. the heating protocol and pyrolysis atmosphere), and the post-treatment conditions etc. A review on the effects of these factors is presented below.

2.4.1. Polymer Precursor

The choice of the polymer precursor is the first important factor in CMS membrane fabrication. In 1983 Koresh & Soffer [41] pioneered the production of defect-free CMS membranes from cellulose hollow fibers. They showed that polymers suitable as precursors for CMS membrane production should not melt or flow before they decompose. A variety of thermosetting polymers including cellulose derivatives [41], poly(vinylidene)-based polymers [42], phenolic resin [43-45], polyfurfuryl alcohol [46, 47], polyacrylonitrile [48] and polyimides [5, 12, 49-52] have since been used in CMS membrane fabrication. Polyimides have been the preferred precursor for many researchers owing to high glass transition temperature, processability, mechanical strength and good intrinsic separation performance [49, 50, 53]. Williams & Koros [49] and Saufi & Ismail [53] provide a review of different precursors for CMS membrane fabrication.

The intrinsic properties of the starting polymer such as its chemical structure, fractional free volume (FFV) and chain mobility, glass transition temperature, as well as the composition and amount of volatile products evolved during pyrolysis all affect the final CMS properties [49, 54, 55]. Williams [24] elucidated the effect of the fractional free volume of the starting polymer in CMS fabrication. He used two polyimides 6FDA-6FpDA and 6FDA-6FmDA as precursors, with the only difference being the location of the aromatic linkage in the diamine resulting in a difference in free volumes but not in the atomic composition or pyrolysis by-products. CMS membranes produced from these precursors under identical pyrolysis conditions illustrate the effect of the intrinsic precursor free volume on resulting CMS properties. 6FDA-6FpDA has a FFV~0.190 while 6FDA:6FmDA has a FFV~0.175. The separation performance of CMS membranes derived from the precursors showed that 6FDA:6FpDA-derived CMS had higher

permeabilities and diffusivities compared to 6FDA-6FmDA-derived CMS. These results were attributed to the differences in FFV of the starting polymers.

Park et al. [11] analyzed the effects of microstructural changes of a series of aromatic polyimides on the gas permeation properties of their resultant CMS membranes fabricated using identical pyrolysis conditions. They synthesized three copolyimides using a common dianhydride and diamines with a different number of methyl substituent groups. The introduction of methyl substituent groups in the polymer backbone increases the FFV of the polymer. Additionally, the weight loss due to pyrolysis, analyzed using thermogravimetric analysis also increased with the introduction of more methyl substituents. Consequently, the permeabilities of He, CO_2, O_2 and N_2 in the resulting CMS membranes were also found to increase with an increase in the number of methyl substituent groups.

Steel & Koros [5] produced CMS dense films using a commercial polyimide Matrimid® and an in-house polyimide 6FDA:BPDA-DAM. These polymers were pyrolyzed at two pyrolysis temperatures, 550°C and 800°C, using identical pyrolysis conditions under a vacuum environment. At both temperatures, their results showed that Matrimid®-based CMS membranes were more selective and less permeable compared to 6FDA:BPDA-DAM-based CMS. This is primarily due to the different chemical structures of the two polyimides. 6FDA:BPDA-DAM consists of bulky -CF_3 groups that hinder packing of the polymer chains leading to a higher fractional free volume compared to Matrimid®. CMS derived from a higher FFV polymer precursor leads to a more open structure with higher permeability. In addition, while Matrimid® evolves volatiles such as CO, CO_2 aniline etc., 6FDA:BPDA-DAM also evolves fluorinated compounds, such as CHF_3 and trace HF, leading to higher microporosity which apparently contributes to a more permeable CMS structure. Vu & Koros [6] reported a similar trend for CMS hollow fibers fabricated from these two polyimides.

These studies indicate that the choice of the starting polymer indeed affects the resulting CMS properties and the intrinsic polymer properties may be somewhat preserved in the membrane structure after thermal decomposition. Choosing an appropriate starting material is hence critical to fabricate CMS membranes for a particular gas separation. In this study, three polyimides Matrimid®, 6FDA:BPDA-DAM and 6FDA-DAM have been chosen as starting materials to derive CMS membranes for ethylene/ethane separation. Preliminary investigation of the three precursors and their viability in forming CMS membranes for C_2H_4/C_2H_6 separation will be discussed in Chapter 3. Differences in the separation properties and morphology of CMS membranes resulting from the 3 precursors has also been analyzed and individual optimization of the pyrolysis conditions for each precursor has been explored for C_2H_4/C_2H_6 separation.

2.4.2. Pre-treatment of Polymer Precursor

Polymeric membranes are often subject to pre-treatment prior to pyrolysis. Pre-treatment of precursors has been shown to alter the chain packing or chain segmental mobility of the polymer, which can significantly affect the structural organization of the membrane during pyrolysis. This step may be used to ensure the stability of the precursor in order to preserve its morphology during pyrolysis and/or to enhance the uniformity of pore formation during pyrolysis [49, 53]. Several pre-treatments have been used to condition the polymer precursor prior to pyrolysis.

Pre-treatment of precursors has been shown to alter the chain packing or chain segmental mobility of the polymer which can significantly affect the structural organization of the membrane during pyrolysis. Precursor pre-treatment stabilizes the structure of the precursor, acts to maintain the molecular structure of the carbon chains, and/or enhances the uniformity of pore formation during pyrolysis [56]. Thermo-

stabilization and pre-oxidation of the polymer precursor prior to pyrolysis is a commonly used pre-treatment method. Pre-oxidation can form crosslinks in the polymer structure thus increasing the thermal stability of the precursor. For example, Kusuki et al. [57] and Okamoto et al. [58] found that it was necessary to stabilize hollow fibers based on BPDA and aromatic diamines by heating in air at 400°C for 30 min prior to pyrolysis, in order to prevent softening and collapse and to maintain the asymmetric morphology of the fibers during pyrolysis. Similarly, David & Ismail [48] have shown that the thermal stability of PAN hollow fiber membranes was improved when the precursors were heated to 250°C in air or oxygen for 30 min. Oxidative pre-treatment conditions must be optimized for a given precursor to improve CMS membrane properties for a particular application. For example, Centeno & Fuertes [42] analyzed the effect of oxidative pre-treatment in air at 150-200°C for up to 2.5 days before carbonization on the performance of supported poly(vinylidene chloride-co-vinyl chloride)-based CMS membranes. Their results show that CMS membranes derived from oxidation at 200°C for 6 hours showed a decreased permeability but increase in selectivity, while those treated at 150°C for 2.5 days had increased permeability and decreased selectivity, indicating the need for oxidative pre-treatment optimization

In many cases, a non-solvent or chemical reagent may be used to modify the precursor prior to pyrolysis. For example, Tin et al. [56] carried out modification on the starting polyimide using chemical cross-linking and methanol pre-treatment. They investigated the effect of non-solvent pre-treatment of the precursor prior to pyrolysis. Matrimid® and P-84 precursor films were soaked in methanol, ethanol, propanol or butanol for 1 day and air-dried prior to pyrolysis. The resulting CMS membranes showed an increase in selectivity compared to CMS derived from the untreated precursor. Tin et al. [56] suggest that the function of non-solvent pre-treatment is to weaken the

intermolecular interactions, allowing structural reorganization of the carbon chains during pyrolysis, leading to smaller pores.

Tin et al. [59] also carried out room temperature chemical cross-linking modification on Matrimid® by immersing the films in a 10-w/v% solution of p-xylenediamine in methanol for 1-7 days and pyrolyzed the cross-linked Matrimid® under vacuum at 800°C. Their results indicate a decrease in the permeability of the resulting CMS with increasing cross-linking density with a selectivity maximum at 1 day cross-linked Matrimid®. Xiao et al. [60] carried out bromination on Matrimid® polyimide, thereby increasing the polymer chain rigidity, FFV and glass transition temperature of the starting material, prior to carbonization to produce carbon membranes,. Their results indicate that CMS dense films derived from brominated Matrimid® using 550°C pyrolysis under vacuum show a higher permeability along with competitive selectivity compared to its untreated counterpart.

For the purpose of this study, pre-treatment of polymer precursor dense films was not explored. The aim of this work is to study the intrinsic properties of the membranes and to investigate economical ways for high selectivity CMS membrane fabrication. Additional pre-treatment steps add to both the complexity and cost of CMS production. Pre-oxidation of polymer precursors prior to pyrolysis was explored in the hollow fiber configuration by Liren Xu in the Koros Group, and was found to improve the morphology (asymmetry) of 6FDA:BPDA-DAM-derived CMS fibers. However, while pre-treatment to stabilize the precursor may not be necessary in case of 6F-precursors studied in this work it may be required to prevent collapse and loss of asymmetry in Matrimid® hollow fibers during pyrolysis in order to achieve commercially attractive productivities. These pre-treatment options to improve the hollow fiber performance are being investigated in the Koros Group.

2.4.3. Pyrolysis Conditions

Pyrolysis is a process in which a suitable precursor is heated in a controlled atmosphere to the pyrolysis temperature via a ramp/soak process and held (soaked) at the final pyrolysis temperature for a sufficient time. The pore structure of the resulting CMS, consisting of micropores connected by ultramicropores (Figure 2.4), can thus be controlled selectively by adjusting the various process parameters. The most important parameters are the final pyrolysis temperature, ramp rate, thermal soak time and the pyrolysis atmosphere. The general effects of these parameters on the final CMS properties have been discussed below.

2.4.3.1. Pyrolysis Temperature

Pyrolysis temperature refers to the highest temperature to which the precursor is heated during the pyrolysis process. The pyrolysis temperature is chosen to lie above the decomposition temperature for the polymer but below the graphitization temperature, typically in the range of ~500-1000°C [1, 3]. Conventional wisdom holds that an increase in pyrolysis temperature typically results in more compact CMS with smaller average pore sizes, lower permeability and, in general, higher selectivity.

Suda & Haraya [12] prepared CMS dense films from polyimide Kapton® by pyrolysis at three temperatures: 600°C, 800°C and 1000°C, under a vacuum environment using a ramp rate of 10°C/min. Their results showed a decrease in the permeability of He, H_2, CO_2 and O_2, with an increase in the selectivity for several gas pairs. They analyzed pore size changes as a function of pyrolysis temperature using sorption measurements, and concluded that with increasing temperature, both the limiting pore size and the pore volume decrease. Moreover, they reported that the pore size distribution became sharper with a significant reduction in the portion of larger

pores. This explains the loss of permeability with pyrolysis temperature, with a greater reduction for larger gases compared to smaller resulting in permselectivity increases.

Steel & Koros [5, 61] reported a decrease in both O_2 and CO_2 permeability along with an increase in O_2/N_2 and CO_2/CH_4 selectivity in going from a pyrolysis temperature of 550°C to 800°C under vacuum for CMS membranes derived from Matrimid® and 6FDA:BPDA-DAM, as shown in Figure 2.13.

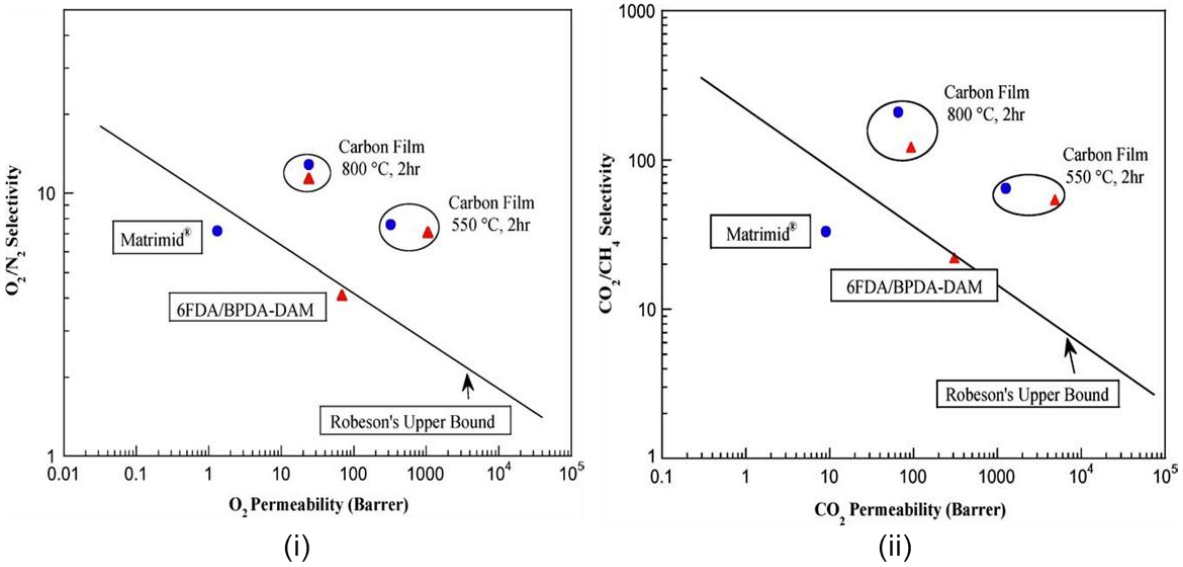

Figure 2.13: Effect of final pyrolysis temperature on (i) O_2/N_2 separation and (ii) CO_2/CH_4 separation [5, 61]

For C_3H_6/C_3H_8 separation, on the other hand, Steel & Koros [5, 61] reported a further drop in the C_3H_6 permeability as well as the C_3H_6/C_3H_8 selectivity for the 800°C CMS, as shown in Figure 2.14. In fact, for CMS films derived from Matrimid®, 500°C was found to be an attractive pyrolysis temperature for C_3H_6/C_3H_8 separation, while the performance for both the 550°C and 800°C CMS lie below the C_3H_6/C_3H_8 polymeric upper bound.

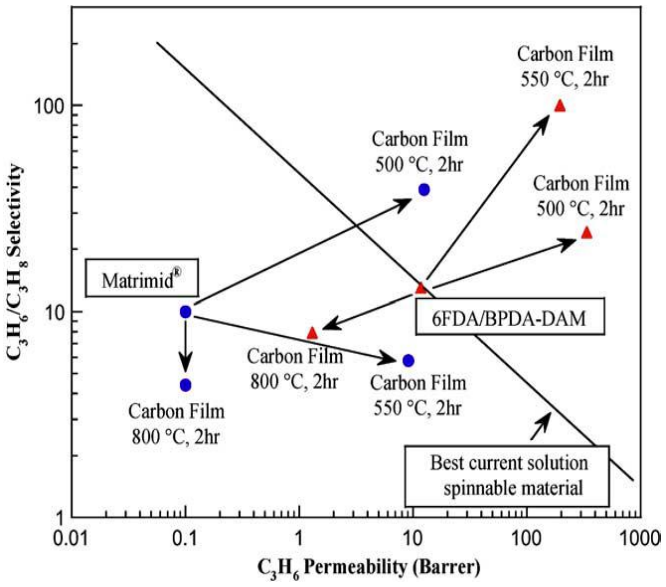

Figure 2.14: Effect of final pyrolysis temperature on C_3H_6/C_3H_8 separation [5, 61]

These performance trends have been explained by Steel & Koros [5, 61] on the basis of changes in the hypothetical CMS ultramicropore distributions with the pyrolysis temperature, which will be discussed in detail later in this work. These studies clearly show that the optimum pyrolysis temperature depends on the starting polymer and the targeted separation.

2.4.3.2. Ramp Rate

The ramp rates used for pyrolysis generally determine the rate of evolution of volatile by-products from the polymer matrix during carbonization and the total pyrolysis time, and can consequently affect the pore structure of the CMS and the resulting transport properties [49]. Suda & Haraya [12] varied the ramp rate of pyrolysis from 1.33-13.3°C/min and reported a decrease in the permeability of several gases: He, H_2, CO_2 and O_2, with decreasing ramp rates for CMS dense films made by pyrolyzing Kapton® at 1000°C in an argon atmosphere. This trend has been attributed to a slower rate of by-product evolution at lower heating rates as well as an increase in the total pyrolysis time that allows for pore sintering, thus leading to a smaller average pore size and consequently a lower permeability.

2.4.3.3. Soak Time

Soak time refers to the total time held at the final pyrolysis temperature. It may be used to fine-tune the transport properties of CMS membranes at a particular pyrolysis temperature [49, 53]. It is believed that increasing the soak time leads to microstructural rearrangements and pore sintering, typically resulting in reduced pore sizes and thereby a decrease in the CMS permeability.

For example, Kim et al. [55] studied the effect of short thermal soak times, 0, 30 and 60 min, on BTDA-ODA polyimide pyrolyzed at 700°C in an argon atmosphere. They reported a loss in permeability for He, CO_2, O_2 and N_2 with increasing soak time, as well as an increase in the He/N_2, CO_2/N_2 and O_2/N_2 selectivities.

Steel & Koros [5, 61] investigated the effects of longer soak times: 2 and 8 hours, on the pyrolysis of Matrimid® and 6FDA:BPDA-DAM precursors at 550°C and 800°C under vacuum. In in all cases they reported a decrease in permeability for O_2, N_2, CO_2

and CH_4 and a corresponding increase in O_2/N_2 and CO_2/CH_4 selectivity with an increase in the soak time. The effect of soak time may however be a complex function of several other parameters. As shown in Figure 2.15(i), for CO_2/CH_4 separation, Matrimid® derived CMS films show a decrease in CO_2 permeability and an increase in CO_2/CH_4 selectivity for 550°C pyrolysis in going from a 2 hour to 8 hour soak time. At 800°C however, soak time however has little effect on selectivity but the CO_2 permeability for 8 hour soak is drastically reduced compared to a 2 hour soak. For 6FDA:BPDA-DAM CMS, the effect of increase in soak time at 800°C is even less pronounced (Figure 2.15(ii)). The soak time may thus need optimization based on the precursor of choice, the gas pair under consideration as well as the final pyrolysis temperature, besides other impacting factors.

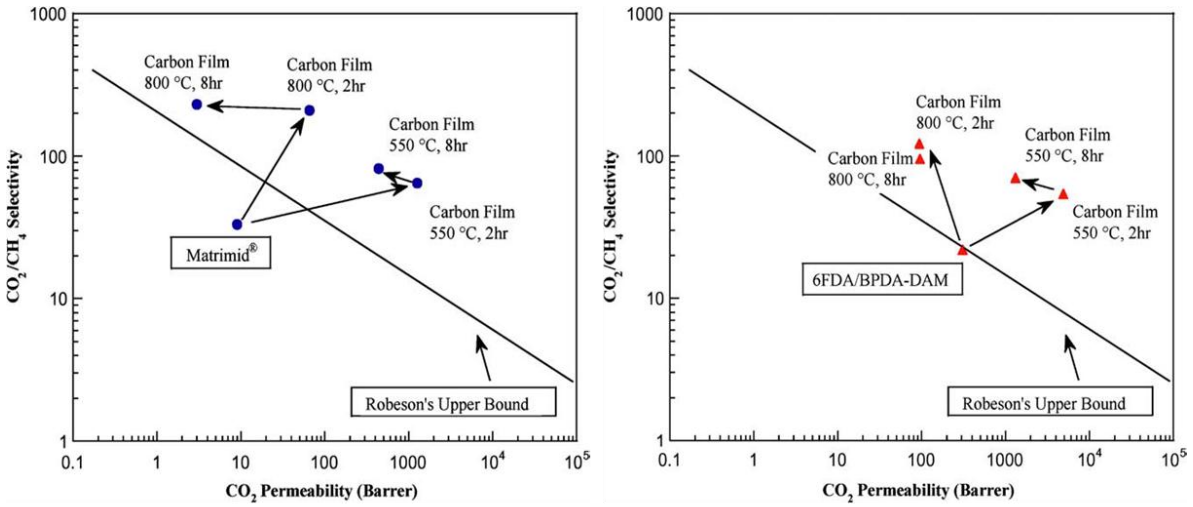

(i) (ii)

Figure 2.15: Effect of thermal soak time on (i) O_2/N_2 separation and (ii) CO_2/CH_4 separation [5, 61]

2.4.3.4. Pyrolysis Atmosphere

The pyrolysis atmosphere must be controlled in order to prevent undesired burn-off and chemical damage of the membrane precursor during pyrolysis. Pyrolysis can be carried out in either a vacuum or inert environment. Vacuum pyrolysis is reported to yield more selective but less permeable CMS than inert pyrolysis. In the case of inert pyrolysis, one must consider the flow rate, pressure etc. The effect of pyrolysis atmosphere has been investigated by several researchers.

Suda & Haraya [12] formed CMS dense films from Kapton® by pyrolysis at 1000°C under vacuum and in inert argon atmosphere. Their results indicate little difference in the permeation properties of membranes formed under vacuum and inert argon atmospheres. Geiszler & Koros [62, 63] also did a detailed study on the effect of pyrolysis atmosphere on the separation performance of asymmetric CMS hollow fibers formed from 6FDA:BPDA-DAM polyimide. Their fibers were pyrolyzed under vacuum (0.01-0.03 mtorr), helium and argon atmospheres with gas flow rates of 20 and 200 sccm. For the higher inert flow rate, Geiszler & Koros [62, 63] reported a higher O_2 permeance and lower O_2/N_2 selectivity for CMS produced from inert pyrolysis compared to vacuum. A similar phenomenon was reported by Vu [6] for CO_2/CH_4 separation using CMS derived from Matrimid® hollow fibers. For an inert flow rate of 20 sccm however, Geiszler & Koros [62, 63] reported a drop in permeance below that of vacuum, with the selectivity remaining unchanged in the error range. Geiszler [62, 63] suggested that inert pyrolysis may change the mechanism of the carbonization reaction by changing the gas phase heat and mass transfer rates compared to vacuum. At higher flow rates, the rate of carbonization may be accelerated and enhanced convective mass transfer of large chunks of pyrolysis by-products away from the membrane surface may result in a more open and porous CMS matrix, thus resulting in higher permeance and lower selectivity.

At lower flow rates however, the volatile by-products may further decompose and deposit on the membrane surface or pores, thus resulting in reduced permeance. It seems likely that the effect of pyrolysis atmosphere may be related to the properties of the precursor and the temperature profile used for pyrolysis.

In order to understand the differences between pyrolysis in vacuum and inert gas environments, Williams [24] hypothesized that the oxygen content during pyrolysis can affect the resulting transport properties of the CMS membranes. He used the term 'total oxygen exposure factor' to describe the total moles of oxygen available for reaction during pyrolysis. At elevated temperatures during pyrolysis, the oxygen present in the inert gas tends to selectively chemisorb at the ultramicropore sites, which have been shown to be ~17 times more reactive than the basal plane, thus allowing for carefully tuned separation performances [64]. This process was termed 'oxygen doping'. Figure 2.16 shows a cartoon representation of the oxygen doping process.

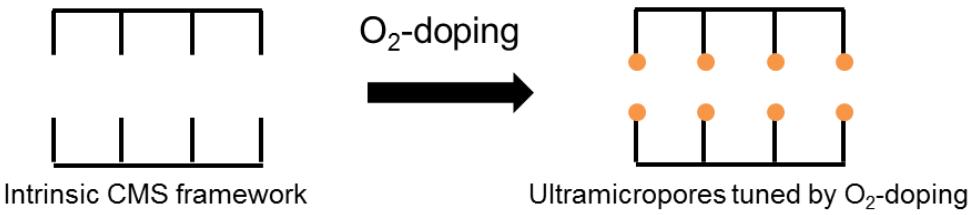

Figure 2.16: Cartoon representation of oxygen doping process in CMS

Kiyono et al. [31, 65] carried out a detailed analysis of the above hypothesis to demonstrate that the oxygen concentration present during pyrolysis is critical. As shown in Figure 2.17(i) the CO_2/CH_4 separation performance of 6FDA:BPDA-DAM CMS dense

films pyrolyzed at 550°C can be controlled by carefully tuning the oxygen concentration in the inert gas during pyrolysis.

The oxygen doping process must be used cautiously since it may require optimization based on the starting polymer, the pyrolysis profile as well as the gas separation under consideration. For example, Kiyono et al. [31, 66] demonstrated that for Matrimid® dense films (Figure 2.17(ii)), the oxygen doping process was not very useful at 550°C for CO_2/CH_4 separation and a reduced pyrolysis temperature of 500°C was required to make use of the oxygen doping process.

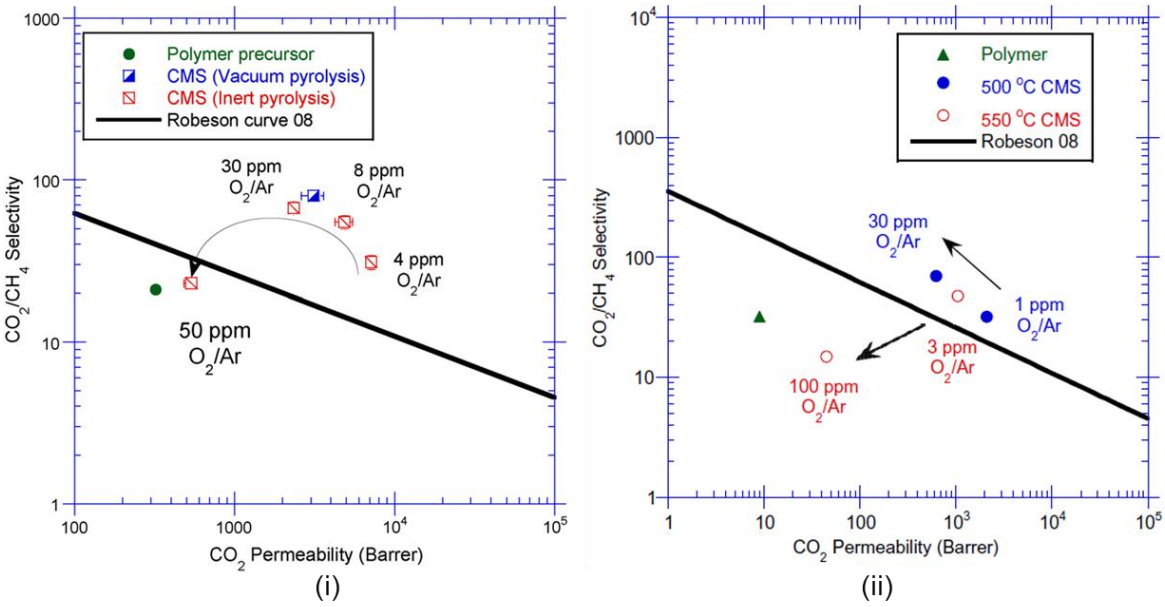

Figure 2.17: Effect of pyrolysis atmosphere (oxygen doping) on the CO_2/CH_4 separation performance of CMS derived from (i) 6FDA:BPDA-DAM and (ii) Matrimid® [64, 66]

Some researchers have used statistical analysis based on a factorial design of experiments considering a main factor and two-factor interactions in order to analyze the influence of pyrolysis parameters on the transport properties of CMS membranes. Such

studies are useful in evaluating the effectiveness of varying different pyrolysis factors on the formation of CMS membranes. For example, Su & Lua [67] showed that the final pyrolysis temperature in general has the strongest effect on the transport properties of their CMS membranes for He, CO_2, O_2 and N_2 transport, while the carbonization . Steel [5] concluded that the pyrolysis temperature and polymer precursor are the most important parameters to be considered and may be used to tailor the structure of the CMS material so that desired transport properties may be obtained for a particular separation. Thus such studies are useful in understanding the significance of different pyrolysis parameters on CMS transport properties; however, extensive experimentation is still necessary to optimize performance.

This work considers the detailed effects of various pyrolysis conditions on C_2H_4/C_2H_6 separation performance of the CMS membranes. As is clear from the above discussion, the effects of the various pyrolysis parameters can be complex and unique to the system under consideration; hence, optimization of the pyrolysis conditions in the context of C_2H_4/C_2H_6 separation will be discussed in Chapter 5 for all three precursors Matrimid®, 6FDA:BPDA-DAM and 6FDA-DAM. Additionally, changes in the CMS morphology have been correlated to the resulting separation performance in order to elucidate structure-performance relationship of the engineered CMS membranes.

2.4.4. Post-treatment of Carbon Molecular Sieve Membrane

Post-treatment processes may be used to tailor the separation performance of CMS membranes by finely adjusting its pore dimensions and pore size distribution. Several common post-treatment techniques include post-oxidation, chemical vapor deposition and coating. Coating techniques may be used to repair cracks and defects in

the membrane, while others have used it to counteract the decrease in performance in the membranes over time.

Low temperature post-oxidation is often used to increase the pore-size in CMS membranes, and researchers have used different techniques to achieve this. Soffer et al. [68] treated hollow fiber CMS membranes derived from cellulose precursors at 400°C in air for 15 min to increase the fiber permeance. Kusakabe et al. [69] produced supported CMS membranes from BPDA-ODA polyimide and post-treated the CMS at 300°C in oxygen for 3 hours. This increased permeance by an order of magnitude without significantly affecting selectivity, and this was attributed to an increase in pore volume without broadening the pore size distribution.

Chemical vapor deposition techniques have often been used to improve the separation performance of CMS membranes. Soffer et al. [70] developed a method for improving CMS selectivity by the chemical vapor deposition of hydrocarbon gases in the pore system of the CMS. Similarly, Hayashi et al. [71] prepared supported CMS membranes derived from BPDA-ODA polyimide and modified the resulting CMS membrane by CVD using a propylene carbon source at 650°C. At a pyrolysis temp of 700°C, CVD modification was found effective in increasing the CO_2/N_2 and O_2/N_2 selectivity by narrowing the pore structure.

Several coating techniques on the other hand have been used by researchers to overcome cracks or defects present in the CMS membrane after pyrolysis or to counteract the adverse effects of factors such as humidity on the membrane performance over time. It has been found that water molecules can sorb on the micropore walls of the CMS thus resulting in reduced performance over time. Such problems can be overcome by coating the membrane with a highly permeable and hydrophobic film which does not prohibitively reduce the flux of the membrane. As

demonstrated by several researchers, the resulting carbon composite membrane shows greater resistance to humidity while retaining good performance [31, 69, 72].

While simple post-treatment methods such as post-oxidation may be useful in tuning the CMS properties, more complicated techniques can add to the number of steps in CMS fabrication and increase costs significantly when weighed against the resulting improvement in performance. Hence the use of such complicated post-treatment methods has been avoided in this work. A simple method of post-pyrolysis oxygen doping has been used to tune the performance of 6FDA-based CMS membranes produced in this work, since it can be carried out as a final step during the pyrolysis process itself, without the need of any additional steps. The concept of post-pyrolysis oxygen doping was recently developed by Dr. Rachana Singh in the Koros Group for O_2/N_2 separation. It involves exposing the CMS membrane to trace amounts of oxygen by briefly taking it to a temperature higher than the final pyrolysis temperature. This allows selective doping of the ultramicropore edges to tune the CMS selectivity, somewhat similar to the oxygen doping concept that was described earlier. Of course, excessive amounts of oxygen would have a similar impact as post-oxidation and can enlarge the pore sizes. Detailed discussion of post-pyrolysis oxygen-doping is presented later in this work.

2.5. References

[1] Marsh H. Introduction to carbon science: Butterworths; 1989.

[2] Pierson. Handbook of carbon, graphite, diamond, and fullerenes NY: Noyes Publication 1993.

[3] Jenkins GM, Kawamura K. Polymeric carbons - Carbon fiber, glass and char. London: Cambridge University Press 1976.

[4] Stoeckli HF. Microporous carbons and their characterization: The present state of the art. Carbon. 1990;28(1):1-6.

[5] Steel KM. Carbon membranes for challenging gas separations. The University of Texas at Austin, Doctor of Philosophy, 2000.

[6] Vu DQ. Formation and characterization of asymmetric carbon molecular sieve and mixed matrix membranes for natural gas purification. The University of Texas at Austin, Doctor of Philosophy, 2001.

[7] Breck DW. Zeolite molecular sieves. New York: Wiley & Sons; 1974.

[8] Singh A. Membrane materials with enhanced selectivity: An entropic interpretation. The University of Texas at Austin, Doctor of Philosophy, 1997.

[9] Fu YJ, Liao KS, Hu CC, Lee KR, Lai JY. Development and characterization of micropores in carbon molecular sieve membrane for gas separation. Micropor Mesopor Mat. 2011;143(1):78-86.

[10] Steel KM, Koros WJ. Investigation of porosity of carbon materials and related effects on gas separation properties. Carbon. 2003;41(2):253-66.

[11] Park HB, Kim YK, Lee JM, Lee SY, Lee YM. Relationship between chemical structure of aromatic polyimides and gas permeation properties of their carbon molecular sieve membranes. J Membrane Sci. 2004;229(1-2):117-27.

[12] Suda H, Haraya K. Gas permeation through micropores of carbon molecular sieve membranes derived from Kapton polyimide. J Phys Chem B. 1997;101(20):3988-94.

[13] Campo MC, Magalhaes FD, Mendes A. Comparative study between a CMS membrane and a CMS adsorbent: Part I-Morphology, adsorption equilibrium and kinetics. J Membrane Sci. 2010;346(1):15-25.

[14] Chen J, Loo LS, Wang K, Do DD. The structural characterization of a CMS membrane using Ar sorption and permeation. J Membrane Sci. 2009;335(1-2):1-4.

[15] Koros WJ. Membranes: Learning a lesson from nature. Chemical Engineering Progress. 1995;91(10):68-81.

[16] Koros WJ, Fleming GK. Membrane-based gas separation. J Membrane Sci. 1993;83(1):1-80.

[17] Hines AL, Maddox RN. Mass transfer fundamentals and applications: Englewood Cliffs, New Jersey: Prentice Hall; 1985.

[18] Rao MB, Sircar S. Nanoporous carbon membranes for separation of gas-mixtures by selective surface flow. J Membrane Sci. 1993;85(3):253-64.

[19] Rao MB, Sircar S. Nanoporous carbon membrane for gas separation. Gas Purification & Separation. 1993;7(4):279-84.

[20] Rao MB, Sircar S. Performance and pore characterization of nanoporous carbon membranes for gas separation. J Membrane Sci. 1996;110(1):109-18.

[21] Koros WJ. Barrier polymers and structures. Washington DC: American Chemical Society 1990.

[22] Koros WJ. Transport properties. In: Mark HM. Encyclopedia of polymer science and technology. 3ed: Wiley-Interscience 2004.

[23] Ismail AF, David LIB. A review on the latest development of carbon membranes for gas separation. J Membrane Sci. 2001;193(1):1-18.

[24] Williams PJ. Analysis of factors influencing the performance of CMS membranes for gas separation. Georgia Institute of Technology, Doctor of Philosophy, 2006.

[25] Wijmans JG, Baker RW. The solution-diffusion model - A review. J Membrane Sci. 1995;107(1-2):1-21.

[26] Baker RW. Membrane technology and applications. New York: McGraw-Hill; 2000.

[27] van Krevelen DW. Properties of polymers. 3 ed: Elsevier Science; 1997.

[28] Baker RW. Future directions of membrane gas separation technology. Ind Eng Chem Res. 2002;41(6):1393-411.

[29] Robeson LM. Correlation of separation factor versus permeability for polymeric membranes. J Membrane Sci. 1991;62(2):165-85.

[30] Robeson LM. The upper bound revisited. J Membrane Sci. 2008;320(1-2):390-400.

[31] Kiyono M. Carbon molecular sieve membranes for natural gas separations. Georgia Institute of Technology, Doctor of Philosophy, 2010.

[32] Karger J, Ruthven DM. Diffusion in zeolites and other microporous solids. New York: John Wiley & Sons Inc.; 1991.

[33] Higashi K, Ito H, Oshi J. Surface diffusion phenomena in gaseous diffusion. I. Surface diffusion of pure gas. J At Energy Soc Jpn. 1963;5:846-53.

[34] Crank J, Park GS. Diffusion in polymers. New York: Academic Press; 1968.

[35] Singh A, Koros WJ. Significance of entropic selectivity for advanced gas separation membranes. Ind Eng Chem Res. 1996;35(4):1231-4.

[36] Das M. Membranes for olefin/paraffin separations. Georgia Institute of Technology, Doctor of Philosophy, 2009.

[37] Singh-Ghosal A, Koros WJ. Energetic and entropic contributions to mobility selectivity in glassy polymers for gas separation membranes. Ind Eng Chem Res. 1999;38(10):3647-54.

[38] Glasstone S, Laidler KJ, Eyring H. The Theory of Rate Processes. 1st ed. New York: McGraw-Hill Book Co., Inc. 1941.

[39] Hatori H, Yamada Y, Shiraishi M, Yoshihara M, Kimura T. The mechanism of polyimide pyrolysis in the early stage. Carbon. 1996;34(2):201-8.

[40] Ehlers GFL, Fisch KR, Powell WR. Thermal degradation of polymers with phenylene units in the chain. IV. Aromatic polyamides and polyimides. J Polymer Sci Part A: Polymer Chemistry. 1970;8(12):3511-27.

[41] Koresh J, Soffer A. A Molecular-sieve carbon membrane for continuous process gas separation. Carbon. 1984;22(2):225-.

[42] Centeno TA, Fuertes AB. Carbon molecular sieve gas separation membranes based on poly(vinylidene chloride-co-vinyl chloride). Carbon. 2000;38(7):1067-73.

[43] Fuertes AB, Menendez I. Separation of hydrocarbon gas mixtures using phenolic resin-based carbon membranes. Sep Purif Technol. 2002;28(1):29-41.

[44] Wei W, Hu HQ, You LB, Chen GH. Preparation of carbon molecular sieve membrane from phenol-formaldehyde Novolac resin. Carbon. 2002;40(3):465-7.

[45] Centeno TA, Fuertes AB. Supported carbon molecular sieve membranes based on a phenolic resin. J Membrane Sci. 1999;160(2):201-11.

[46] Acharya M, Foley HC. Spray-coating of nanoporous carbon membranes for air separation. J Membrane Sci. 1999;161(1-2):1-5.

[47] Acharya M, Raich BA, Foley HC, Harold MP, Lerou JJ. Metal-supported carbogenic molecular sieve membranes: Synthesis and applications. Ind Eng Chem Res. 1997;36(8):2924-30.

[48] Ismail AF, David LIB. Influence of the thermastabilization process and soak time during pyrolysis process on the polyacrylonitrile carbon membranes for O-2/N-2 separation. J Membrane Sci. 2003;213(1-2):285-91.

[49] Williams PJ, Koros WJ. Gas separation by carbon membranes. In: Li NN, Fane AG, Winston Ho WS, Matsura T. Advanced membrane technology and applications. New Jersey: John Wiley & Sons Inc. 2008.

[50] Jones CW, Koros WJ. Carbon Molecular-sieve gas separation membranes .1. Preparation and characterization based on polyimide precursors. Carbon. 1994;32(8):1419-25.

[51] Fuertes AB, Nevskaia DM, Centeno TA. Carbon composite membranes from Matrimid (R) and Kapton (R) polyimides for gas separation. Micropor Mesopor Mat. 1999;33(1-3):115-25.

[52] Barsema JN, Klijnstra SD, Balster JH, van der Vegt NFA, Koops GH, Wessling M. Intermediate polymer to carbon gas separation membranes based on Matrimid PI. J Membrane Sci. 2004;238(1-2):93-102.

[53] Ismail AF, Saufi SM. Fabrication of carbon membranes for gas separation - a review. Carbon. 2004;42(2):241-59.

[54] Kim YK, Lee JM, Park HB, Lee YM. The gas separation properties of carbon molecular sieve membranes derived from polyimides having carboxylic acid groups. J Membrane Sci. 2004;235(1-2):139-46.

[55] Kim YK, Park HB, Lee YM. Preparation and characterization of carbon molecular sieve membranes derived from BTDA-ODA polyimide and their gas separation properties. J Membrane Sci. 2005;255(1-2):265-73.

[56] Tin PS, Chung TS, Hill AJ. Advanced fabrication of carbon molecular sieve membranes by nonsolvent pretreatment of precursor polymers. Ind Eng Chem Res. 2004;43(20):6476-83.

[57] Kusuki Y, Shimazaki H, Tanihara N, Nakanishi S, Yoshinaga T. Gas permeation properties and characterization of asymmetric carbon membranes prepared by pyrolyzing asymmetric polyimide hollow fiber membrane. J Membrane Sci. 1997;134(2):245-53.

[58] Okamoto K, Kawamura S, Yoshino M, Kita H, Hirayama Y, Tanihara N, et al. Olefin/paraffin separation through carbonized membranes derived from an asymmetric polyimide hollow fiber membrane. Ind Eng Chem Res. 1999;38(11):4424-32.

[59] Tin PS, Chung TS, Kawi S, Guiver M. Novel approaches to fabricate carbon molecular sieve membranes based on chemical modified and solvent treated polyimides. Micropor Mesopor Mat. 2004;73(3).

[60] Xiao YC, Dai Y, Chung TS, Guiver MD. Effects of brominating matrimid polyimide on the physical and gas transport properties of derived carbon membranes. Macromolecules. 2005;38(24):10042-9.

[61] Steel KM, Koros WJ. An investigation of the effects of pyrolysis parameters on gas separation properties of carbon materials. Carbon. 2005;43(9):1843-56.

[62] Geiszler V. Polyimide precursors for carbon molecular sieve membranes. University of Texas at Austin, Doctor of Philosophy, 1997.

[63] Geiszler VC, Koros WJ. Effects of polyimide pyrolysis conditions on carbon molecular sieve membrane properties. Ind Eng Chem Res. 1996;35(9):2999-3003.

[64] Grisdale RO. The properties of carbon contacts. J Appl Phys. 1953;24(10):1288-96.

[65] Kiyono M, Williams PJ, Koros WJ. Effect of pyrolysis atmosphere on separation performance of carbon molecular sieve membranes. J Membrane Sci. 2010;359(1-2):2-10.

[66] Kiyono M, Williams PJ, Koros WJ. Effect of polymer precursors on carbon molecular sieve structure and separation performance properties. Carbon. 2010;48(15):4432-41.

[67] Su J, Lua AC. Influence of carbonisation parameters on the transport properties of carbon membranes by statistical analysis. J Membrane Sci. 2006;278(1-2):335-43.

[68] Koresh JE, Soffer A. The carbon molecular-sieve membranes - General properties and the permeability of CH4/H2 mixture. Separ Sci Technol. 1987;22(2-3):973-82.

[69] Kusakabe K, Yamamoto M, Morooka S. Gas permeation and micropore structure of carbon molecular sieving membranes modified by oxidation. J Membrane Sci. 1998;149(1):59-67.

[70] Soffer A, Azariah M, Amar A, Cohen H, Golub D, Saguee S, et al., inventors; Rotem Industries Ltd., assignee. Method of improving the selectivity of carbon membranes by chemical vapor deposition. United States. 1997.

[71] Hayashi J, Mizuta H, Yamamoto M, Kusakabe K, Morooka S. Pore size control of carbonized BPDA-pp'ODA polyimide membrane by chemical vapor deposition of carbon. J Membrane Sci. 1997;124(2):243-51.

[72] Jones CW, Koros WJ. Carbon composite membranes - A solution to adverse humidity effects. Ind Eng Chem Res. 1995;34(1):164-7.

CHAPTER 3

MATERIALS AND EXPERIMENTAL PROCEDURES

3.1. Overview

This chapter contains a description of the different materials and experimental procedures used in this work. Section 3.2 discusses the polymers used and gases tested. Section 3.3 describes membrane formation methods, both polymeric and carbon molecular sieve. Finally Section 3.4 outlines the various techniques used to characterize the membranes.

3.2. Materials

3.2.1. Polymer

As mentioned previously, polyimides have been shown to be the preferred class of polymers as precursors to carbon molecular sieve membrane formation for gas separation. Three polyimides were used in this work: BTDA-DAPI a commercial polyimide obtained under the tradename Matrimid® 5218 in the form of a yellow powder (Huntsman International LLC), and two in-house polymers 6FDA-DAM and 6FDA:BPDA(1:1)-DAM synthesized using standard procedure [1, 2]. The chemical structures and chemical names of the polymers are shown in Figure 3.1 below and the molecular weights of the polymers are shown in Table 3.1.

Figure 3.1: Chemical structures and chemical names of polymers used in this work

Precursor	Chemical Structure
Matrimid® (BTDA-DAPI)	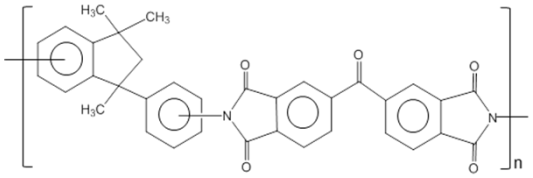 BTDA: 3,3',4,4'-benzophenone tetracarboxylic dianhydride DAPI: 5(6)-amino-1-(4'-aminophenyl)-1,3-trimethylindane
6FDA-DAM	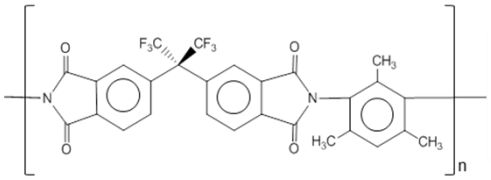 6FDA: 4,4′-(hexafluoroisopropylidene) diphthalic anhydride DAM: 2,4,6,-trimethyl-1,3-phenylene diamine
6FDA:BPDA-DAM (X=1, Y=1)	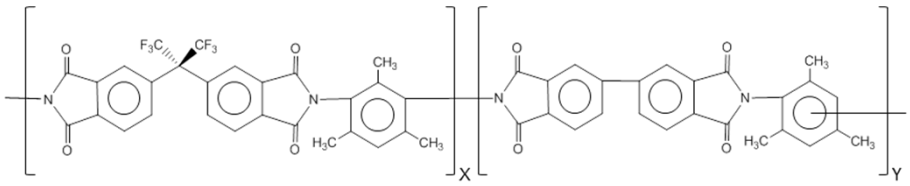 6FDA: 4,4′-(hexafluoroisopropylidene) diphthalic anhydride BPDA: 3,3′-4,4′-biphenyl tetracarboxylic acid dianhydride DAM: 2,4,6,-trimethyl-1,3-phenylene diamine

Table 3.1: Molecular weight and polydispersity index of polymers used in this work

Precursor	M_w Dalton	M_w/M_n
Matrimid®	71,200	3.6
6FDA-DAM	165,000	1.9
6FDA:BPDA-DAM	160,000	1.8

The three polymers are designated as follows throughout the work for convenience: P1 - Matrimid®, P2 - 6FDA-DAM, P3 - 6FDA:BPDA-DAM.

3.2.2. Gases

C_2H_4 and C_2H_6 (CP Grade, Airgas) were used for pure gas permeation and sorption measurements in order to evaluate the intrinsic separation performance of the fabricated polymeric and CMS membranes for C_2H_4/C_2H_6 separation. Additionally, a binary mixture containing 63.2 mol% C_2H_4 and 36.8 mol% C_2H_6 (Praxair) was used for mixed gas permeation measurements.

Other gases used to characterize polymeric and CMS membranes include He (UHP Grade Airgas), Ne (Research Grade, Praxair), Ar (UHP Grade, Airgas), Kr (Research Grade, Praxair), Xe (Research Grade, Praxair), H_2 (UHP Grade, Airgas) O_2 (UHP Grade, Airgas), N_2 (UHP Grade, Airgas), CO_2 (Research Grade, Airgas), CH_4 (Research Grade, Airgas) C_3H_6 (Research Grade, Airgas), C_3H_8 (Research Grade, Airgas), and SF_6 (CP Grade Airgas).

Different grades of argon were used as pyrolysis inert gas. These include Ultra High Purity Ar (UHP Grade, Airgas) and specialty gases containing 1.08, 10.1, 28.8 and 49.1 ppm O_2 in Ar (Praxair).

3.3. Membrane Formation

3.3.1. Polymer Dense Film Membrane Formation

The polymer powder was first dried in a vacuum oven at 120°C for at least 12 hours to remove moisture. The dried powder was dissolved in dichloromethane (≥99.8% purity, Sigma-Aldrich) to form a 3-5 wt% polymer solution in a 40 ml vial (Fisher Scientific) and placed on a roller for at least 6 hours for mixing. The polymer solution was then used to prepare polymer dense films by a solution casting method at room temperature as shown in Figure 3.2. The entire set up for solution casting was contained inside a glove bag (Cole Parmer) in a fume hood as follows: A leveled stage was placed in the glove bag to ensure a flat and uniform surface and Teflon® disk was used as the casting substrate. The polymer solution vial, a 30 ml syringe with a Millex®-RH 0.45 micron PTFE filter (Micropore Corporation), a crystallization dish (VWR), as well as two jars containing excess dichloromethane were all placed inside the glove bag prior to casting. The glove bag was then sealed, purged with nitrogen, and allowed to saturate with dichloromethane by waiting at least 3 hours before casting. The polymer solution was then transferred from the vial to the syringe and slowly drawn through the PTFE filter onto the Teflon® disk. The set up was covered with the crystallization dish to achieve a slow evaporation rate (3-4 days). Finally, the vitrified film was removed and dried in a vacuum oven at 150°C for at least 12 hours to remove residual solvent prior to use.

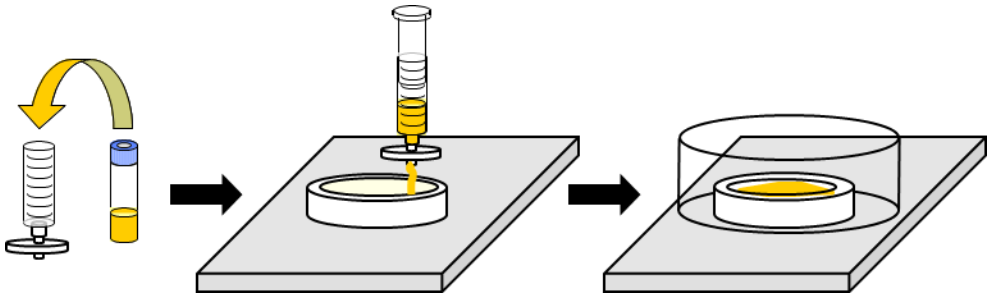

Figure 3.2: Schematic of solution casting process for polymeric dense films

3.3.2. Carbon Molecular Sieve Dense Film Membrane Formation

Carbon molecular sieve (CMS) dense films were formed by pyrolyzing polymeric films. Dried polymer films were cut into small circles using a 1" die cutter (McMaster Carr), placed on a channeled quartz plate (United Silica Products, Franklin, NJ), loaded into a quartz tune (National Scientific Company, GE Type 214 quartz tubing, Quakertown, PA) and placed in the pyrolysis set up shown in Figure 3.3. Details of the pyrolysis set up and procedure are given below.

3.3.2.1. Pyrolysis Set-up

A new pyrolysis set-up, shown in Figure 3.3, was built along with Liren Xu in the Koros Group under the Dow sponsored projects for C_2H_4/C_2H_6 separation using CMS membranes.

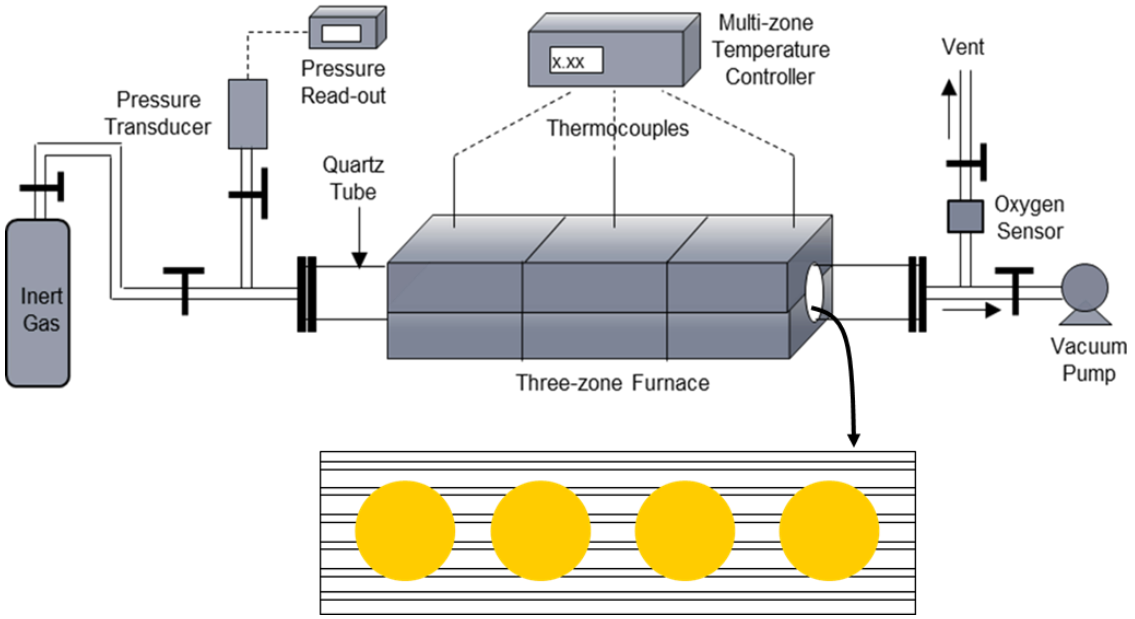

Figure 3.3: Pyrolysis set-up

The set-up was similar to the one reported previously [3, 4] with some important modifications. The current pyrolysis set-up consists of a three-zone furnace (Thermcraft, Inc., model XST-3-0-24-3C, Winston-Salem, NC) with three thermocouples connected independently to three channels of a multi-channel temperature controller (Omega Engineering, Inc., model CN1504TC, Stamford, CT), thus allowing accurate and uniform control of the temperature profile inside the quartz tube (55 mm I.D. x 4 ft length, National Scientific Company, GE Type 214 quartz tubing, Quakertown, PA). The quartz tube can be sealed on either side using an assembly of metal flanges with silicon O-rings (MTI Corporation, Richmond, CA). The set-up is equipped to perform pyrolysis under vacuum or purge gas environment. During vacuum pyrolysis, pressure inside the tube can be monitored using a 0-100 mtorr pressure transducer (MKS, model 628 Absolute Capacitance Manometer, Andover, MA) and liquid nitrogen trap assembly prevents damage of the vacuum pump (RV3, BOC Edwards). A mass flow controller

(MKS instruments, MA) allows accurate control of the purge gas flow rate during pyrolysis. Additionally, a digital flow meter can be used to monitor the gas flow rate before and after pyrolysis at the furnace vent. An oxygen analyzer (Cambridge Sensotec Ltd., Rapidox 2100 series, Cambridge, England), shown in Figure 3.4, is integrated into the set-up to monitor the concentration of oxygen present during pyrolysis.

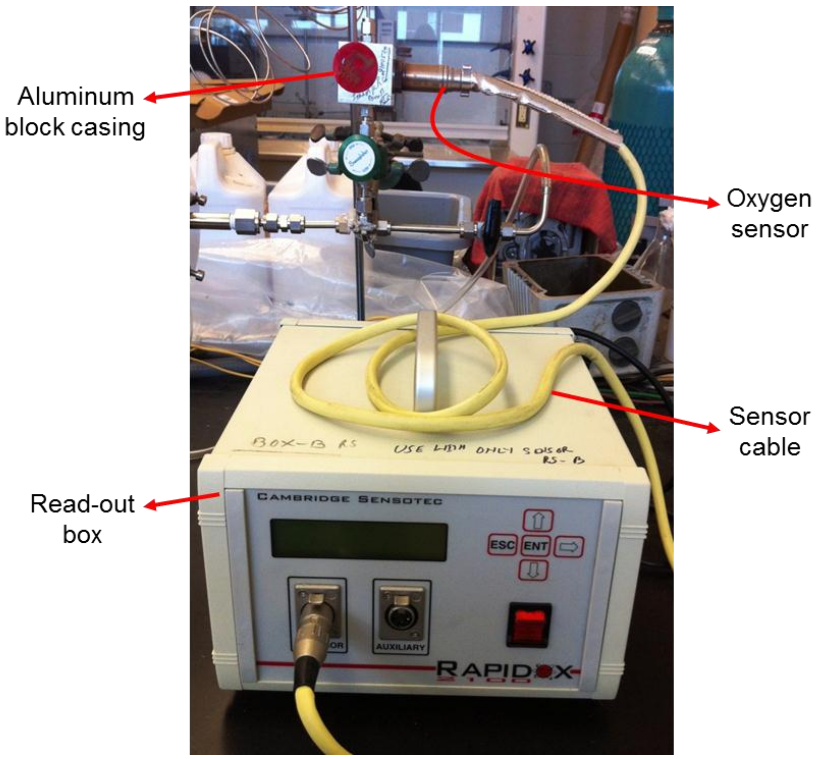

Figure 3.4: Oxygen analyzer

A custom made channeled quartz plate (United Silica Products, Franklin, NJ) shown in Figure 3.5, that allows diffusion of volatile by-products evolved during pyrolysis, was used as a support for dense film pyrolysis.

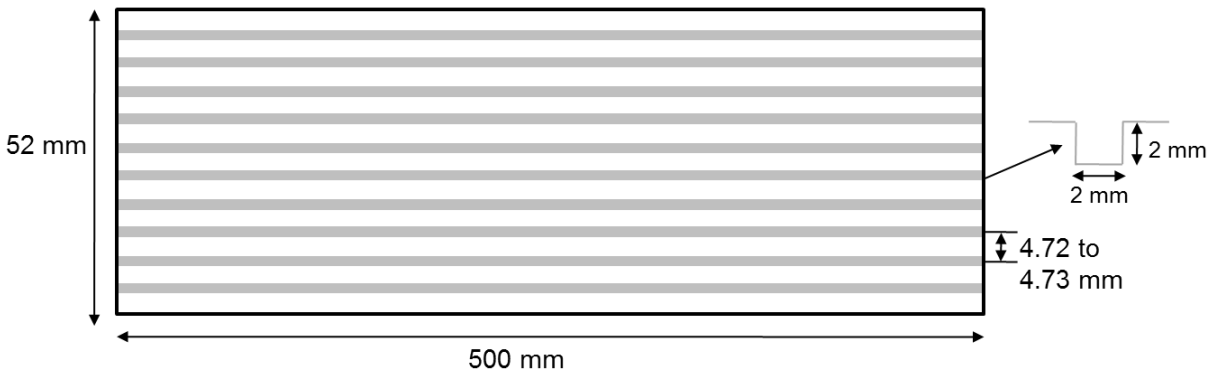

Figure 3.5: Custom made quartz plate for dense film pyrolysis

3.3.2.2. Pyrolysis Protocol

Dense film pyrolysis was carried out either under active vacuum (5-10 mtorr) or a continuous argon flow rate of 200 sccm. The following grades of argon were used for pyrolysis: Ultra High Purity (Airgas) or specialty gases containing 1.08, 10.1, 28.8 or 49.1 ppm oxygen in argon (Praxair). The final pyrolysis temperature (T_{max}) was varied between 500-800°C in all cases with a soak time of 2 hours at the final pyrolysis temperature unless otherwise specified. The heating protocols used are shown below:

Protocol 1 (Regular pyrolysis protocol)

1. 50°C→250°C at a ramp rate of 13.3°C/min
2. 250°C→(T_{max}-15)°C at a ramp rate of 3.85°C/min
3. (T_{max}-15)°C→T_{max}°C at a ramp rate of 0.25°C/min
4. Soak for 2 hours at T_{max}

During in the initial part of the study a slow pyrolysis protocol was used for temperatures over 550°C as shown below:

Protocol 2 (Slow pyrolysis protocol for T_{max}>550°C)

1. 50°C→250°C at a ramp rate of 13.3°C/min
2. 250°C→535°C at a ramp rate of 3.85°C/min
3. 535°C→550°C at a ramp rate of 0.25°C/min
4. 550°C→(T_{max}-15)°C at a ramp rate of 3.85°C/min
5. (T_{max}-15)°C→T_{max}°C at a ramp rate of 0.25°C/min
6. Soak for 2 hours at T_{max}

Figure 3.6 illustrates examples of the different pyrolysis protocols used in this study.

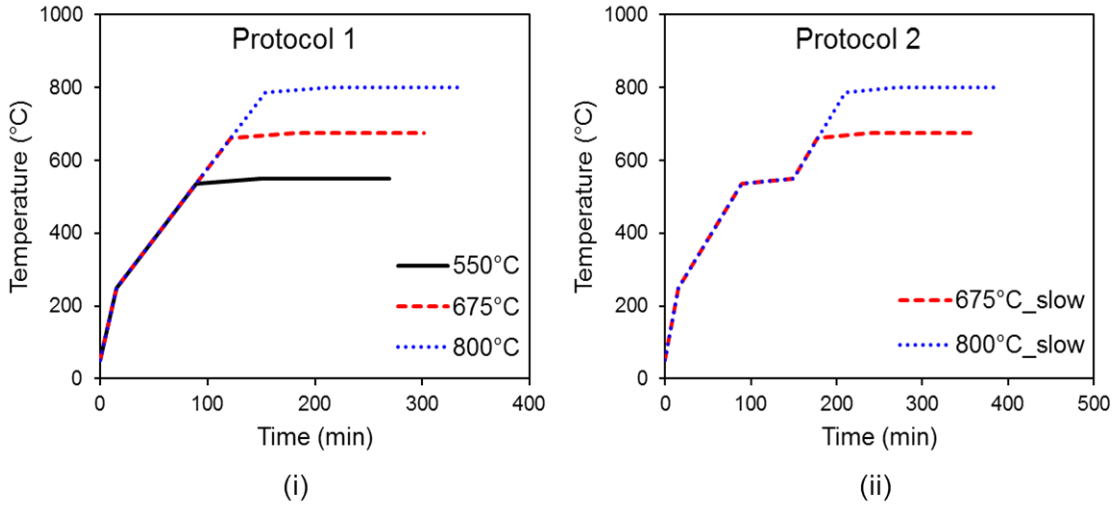

Figure 3.6: Examples of pyrolysis protocol used in this work (i) Protocol 1 illustrated for final pyrolysis temperatures of 550°C, 675°C and 800°C, (ii) Protocol 2 illustrated for final pyrolysis temperatures of 675°C and 800°C

For the regular protocol (Protocol 1), CMS dense films were named based on the starting polymer precursor and the final pyrolysis temperature. For example, P1-500°C-

CMS stands for CMS derived from Matrimid® (P1) at a final pyrolysis temperature of 500°C using Protocol 1. Similarly, P3-675°C-CMS stands for CMS derived from 6FDA:BPDA-DAM (P3) at a final pyrolysis temperature of 675°C using Protocol 1.

For the slow protocol (Protocol 2) for temperatures over 550°C, the CMS dense films were named following the above-mentioned convention but with the term "slow". For example, P1-675°C_slow-CMS stands for CMS derived from Matrimid® (P1) at a final pyrolysis temperature of 675°C using Protocol 2.

The pyrolysis atmosphere may also be indicated in the CMS nomenclature. For example, P1-500°C-CMS_UHP Ar stands for CMS derived from UHP Ar pyrolysis of Matrimid® (P1) at a final pyrolysis temperature of 500°C using Protocol 1.

After each heating cycle, the furnace was allowed to cool down naturally, while under vacuum or inert gas flow, to a temperature below 50°C before unloading the samples. All CMS samples were either tested directly after pyrolysis or stored under vacuum prior to testing in order to prevent changes in the CMS performance due to atmospheric exposure for prolonged periods of time.

After each pyrolysis run, both the quartz tube and the channeled quartz plate were thoroughly cleaned with acetone and baked in air at 800°C for 2 hours to clean out any residue and to prevent contamination in the subsequent run.

3.4. Characterization Techniques

3.4.1. Dense Film Permeation

Both polymeric and CMS dense films were characterized using permeation experiments. A permeation cell of the type shown in Figure 3.7(i) is used for dense film

permeation experiments. The cell is made of stainless steel and designed to sandwich a film between the upstream and downstream sides of a permeation system, using an o-ring assembly. The films were first masked by sandwiching between two concentric pieces of impermeable aluminum tape (Avery Dennison). Minimal pressure must be applied on the films during masking to prevent cracking of brittle CMS films. Using several layers of filter paper as a base for masking helps prevent cracking of CMS films during the masking process. The masked film along with 2-3 pieces of filter paper underneath are placed on the porous sintered meal support on the base of the cell and taped onto the permeation cell with a third piece of aluminum tape having I.D. slightly larger than the film and O.D. slightly smaller than the base of the permeation cell. Five minute epoxy (3M, DP-100) was then applied at the interface between the film and the tape to minimize any gas leak. The permeation cell is then assembled and loaded into a constant-volume permeation system. Figure 3.7(i) shows the schematic of a film masked into a permeation cell. Only a specific area of the film is available for permeation after the masking process, and this can be determined using image scanning and area analysis software (Image J). A digital image of a masked CMS film is shown in Figure 3.7(ii). Details of masking and preparation of permeation cell have also been described previously [5].

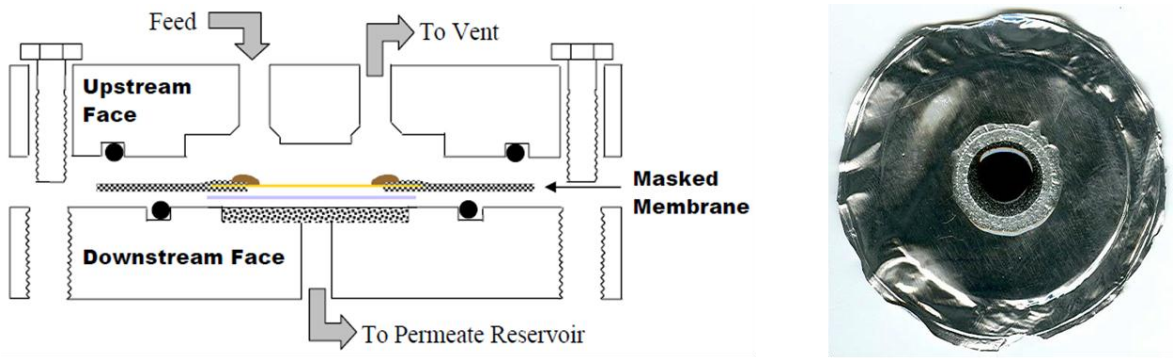

(i) (ii)

Figure 3.7: (i) Schematic showing the cross-section through a permeation cell with a masked film showing the membrane (yellow), filter paper (light blue), epoxy (brown), aluminum tape (checkered), o-rings (solid black circles), porous sintered metal support and bolts at either end [6], (ii) Digital image of a masked CMS film

The schematic of a constant-volume permeation system [7, 8] is shown in Figure 3.8 below.

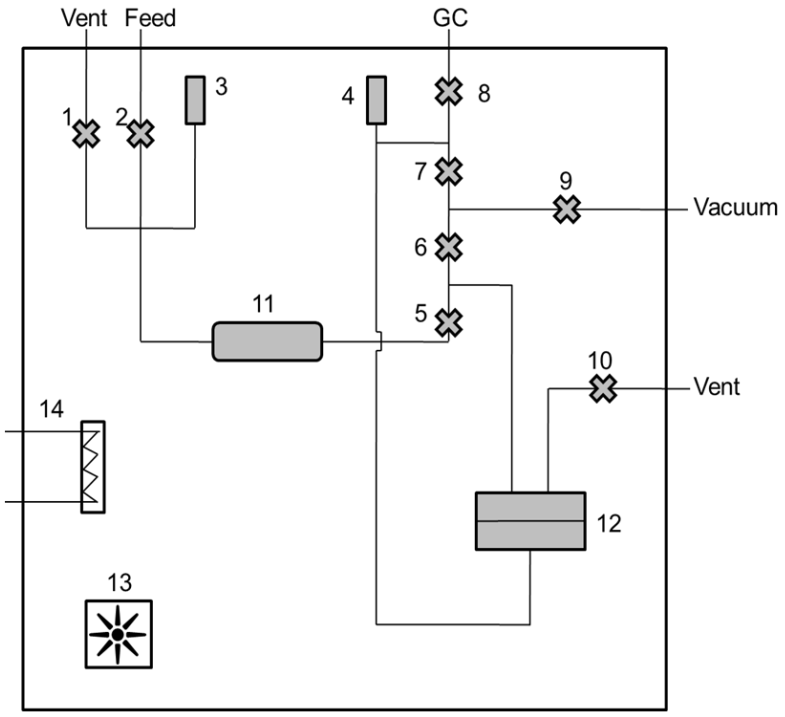

1. Vent valve 1
2. Feed valve
3. Upstream pressure transducer
4. Downstream pressure transducer
5. Upstream valve
6. Connector valve
7. Downstream valve
8. GC valve
9. Vacuum pump valve
10. Vent valve 2
11. Upstream volume
12. Permeation cell
13. Fan
14. Thermostat-controlled heater

Figure 3.8: Schematic of a constant volume permeation system

The entire system (upstream and downstream) was evacuated for over 24 hours and a leak rate was measured (<1% of the permeation rate of the slowest gas). After leak test and evacuation, the upstream was pressurized with feed gas, while the downstream was kept at vacuum. The system temperature was allowed to stabilize before the gas was allowed to contact the membrane. In case of CMS membranes, the upstream valve should be opened slowly and carefully to prevent the film from breaking due to sudden exposure to pressurized feed. Details of permeation experiment have been reported previously [7, 8]. The pressure rise in a constant downstream volume

was recorded over time using LabVIEW (National Instruments, Austin, TX) until steady state was achieved. The permeability was calculated as follows:

$$\mathrm{P} = \frac{(2.94 \times 10^4)(\mathrm{V})(\ell)(\mathrm{dp/dt})}{(\mathrm{T})(\mathrm{A})(\Delta \mathrm{p})} \tag{3.1}$$

where, P is the permeability in Barrer, $(\mathrm{dp/dt})$ is the steady state rate of pressure rise in torr/min, V is the downstream volume in cm^3, ℓ is the membrane thickness in mils, T is the absolute temperature in K, A is the membrane area in cm^2, and $\Delta \mathrm{p}$ is the pressure difference between the upstream and downstream in psia (equivalent to the upstream pressure for downstream under vacuum). Figure 3.9 shows a typical plot obtained from a permeation experiment.

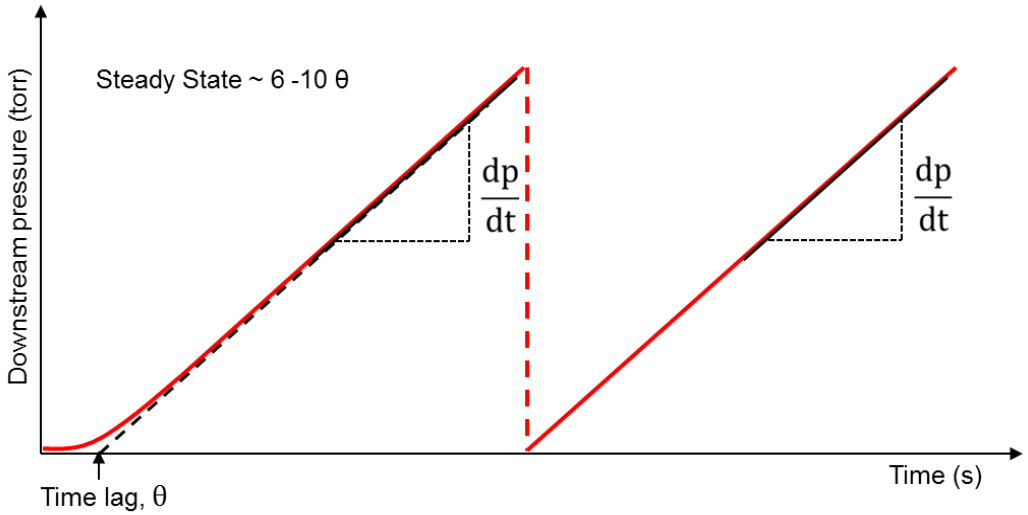

Figure 3.9: Cartoon representation of plot obtained from a permeation measurement

Steady state is said to be achieved at ~ 6-10 times the apparent time lag (θ) when (dp/dt) becomes constant. The permeation plot can also be used to estimate the apparent diffusivity (D) as follows:

$$D = \frac{\ell^2}{6\theta} \tag{3.2}$$

Before each subsequent permeation measurement the system was evacuated for at least 10 times the time lag of the previous gas tested to ensure a low enough leak rate.

Mixed gas permeation experiments were performed using a binary mixture containing 63.2 mol% C_2H_4 and 36.8 mol% C_2H_6. The feed stream flow over the membrane surface is controlled using a needle valve on the retentate side and the retentate flow is measured using a digital flow-meter. The percentage of feed that permeates through the membrane is referred to as the stage cut. In mixed gas experiments, a stage cut less than 1% was maintained to avoid concentration polarization [9]. Permeate collected in the downstream volume was sent to a gas chromatograph (GC) for analysis of the permeate composition. The GC used for analysis has a TCD detector with helium as the carrier gas. The GC was calibrated using standard calibration gases, acquired from Praxair, ranging from 95% to 5% C_2H_4.

3.4.2. Sorption

A pressure decay sorption apparatus [10, 11] shown in Figure 3.10 was used to measure equilibrium sorption properties of polymeric films and carbon molecular sieve samples.

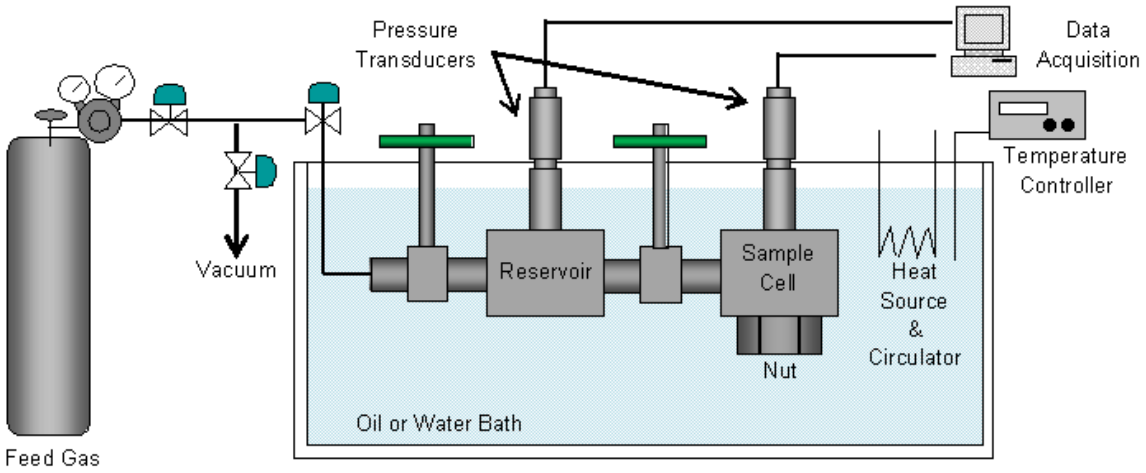

Figure 3.10: Schematic representation of a pressure decay sorption apparatus [4]

Polymeric films were used directly for sorption. In case of CMS materials, the fabricated flat sheet membrane was crushed into small pieces in between two pieces of weighing paper, loaded into a porous stainless steel filter element (0.5 micron, Swagelok) and wrapped using aluminum foil and a piece of stainless steel wire to ensure that the sample does not fall out or disperse. The samples were loaded into the sample cell chamber and the sorption cell was placed in an oil bath with a circulator and temperature controller to maintain uniform temperature. The entire system was evacuated for 24 hours prior to testing. The reservoir chamber was then charged with feed gas and the temperature was allowed to equilibrate for about 10-15 min. The valve between the reservoir and sample cell was then cracked to quickly introduce gas into the sample cell. The pressure in both the reservoir and sample chamber was monitored using pressure transducers and recorded over time using LabVIEW (National Instruments, Austin, TX) until the pressure became constant.

The volume of both the reservoir (res) and sample cell (sam) is known, so is the mass and density of the sample (mem). Additionally the initial (i) and final (f) pressures

in both the reservoir and sample cell are calculated from the acquired pressure vs. time data. The compressibility factors for the gases were calculated using the equations listed in Appendix A to account for non-ideal behavior. A mole balance was used to obtain the amount of gas taken up by the sample as follows:

$$n_{total} = n_{res}^{i} + n_{sam}^{i} + n_{mem}^{i} = n_{res}^{f} + n_{sam}^{f} + n_{mem}^{f} \quad (3.3)$$

where, n represents number of moles.

Gas uptake by the sample was plotted against pressure and the data was fitted to either the dual mode sorption model (for polymeric membranes) or Langmuir model (for CMS) to obtain sorption isotherms.

3.4.3. Thermo-Gravimetric Analysis (TGA)

TGA (Netzsch, STA 409 PC Luxx TGA/DSC) was performed to analyze the decomposition profile and mass loss due to pyrolysis. Prior to start, all samples were purged with argon (UHP, Air Gas) for at least 6 hours and measurements were carried out using 30 cc/min argon with the same heating protocols used for pyrolysis.

3.4.4. Fourier Transform Infrared Spectroscopy (FTIR)

FTIR was performed using a Bruker Tensor 27 FTIR spectrometer. Polymer film samples were analyzed in the transmission mode. For CMS samples, it was difficult to perform IR analysis in the transmission mode, hence IR was obtained using Harrick MVP2 micron ATR with 512 scans.

3.4.5. Differential Scanning Calorimetry (DSC)

The glass transition temperature (T_g) of polymers was analyzed using a differential scanning calorimeter (Q200, TA Instruments) in Dr. Bucknall's lab at Georgia Tech. The measurement was carried out using a standard heating-cooling-heating procedure at heating/cooling rates of 10°C/min in nitrogen atmosphere. The sample was heated beyond its expected glass transition temperature but below its decomposition temperature determined from TGA. The glass transition temperature was determined as the inflection point of the change in the heat flow during the second heating cycle.

3.4.6. Wide Angle X-Ray Diffraction (WAXD)

A Phillips Panalytical X-ray diffractometer in Prof. Nair's lab at Georgia Tech with a CuKα radiation of wavelength 1.54 Å was used for WAXD measurements. The measurement angle was varied from 4-60 degree. Bragg's law ($n\lambda=2d\sin\theta$) was used to determine the average d-spacing of the CMS materials.

3.4.7. Elemental Analysis

Elemental analysis was performed at Columbia Analytical Services. The elemental composition of CMS samples was determined by performing CHN analysis using combustion, O analysis using pyrolysis and F analysis using Bomb and Oxygen Flask Combustion.

3.4.8. Density and Porosity Measurements

Skeletal density and porosimetry measurements were performed at Micromeritics Analytical Services. Helium pycnometry was performed using a Micromeritics AccuPyc II 1340 Gas Displacement Density Analyzer to determine the skeletal density of CMS samples. Surface area and micropore volume were determined using CO_2 uptake measurements done using a Micromeritics ASAP 2020 Accelerated Surface Area and Porosimetry System. Density functional theory was used to analyze the CO_2 adsorption isotherms in order to characterize the micropore distribution of the CMS materials. The bulk density (ρ_b) of the samples were calculated using the skeletal density (ρ_s) and total pore volume (v_p) as

$$\frac{1}{\rho_b} = \frac{1}{\rho_s} + v_p \tag{3.4}$$

3.5. References

[1] Das M. Membranes for olefin/paraffin separations. Georgia Institute of Technology, Doctor of Philosophy, 2009.

[2] Chen CC. Thermally crosslinked polyimide hollow fiber membranes for natural gas purification. Georgia Institute of Technology, Doctor of Philosophy, 2011.

[3] Vu DQ. Formation and characterization of asymmetric carbon molecular sieve and mixed matrix membranes for natural gas purification. The University of Texas at Austin, Doctor of Philosophy, 2001.

[4] Kiyono M. Carbon molecular sieve membranes for natural gas separations. Georgia Institute of Technology, Doctor of Philosophy, 2010.

[5] Kiyono M, Williams PJ, Koros WJ. Effect of pyrolysis atmosphere on separation performance of carbon molecular sieve membranes. J Membrane Sci. 2010;359(1-2):2-10.

[6] Williams PJ. Analysis of factors influencing the performance of CMS membranes for gas separation. Georgia Institute of Technology, Doctor of Philosophy, 2006.

[7] Pye DG, Hoehn HH, Panar M. Measurement of gas permeability of polymers. I. Permeabilities in constant volume/variable pressure apparatus. J Appl Polym Sci. 1976;20(7):1921-31.

[8] Pye DG, Hoehn HH, Panar M. Measurement of gas permeability of polymers. II. Apparatus for determination of permeabilities of mixed gases and vapors. J Appl Polym Sci. 1976;20(2):287-301.

[9] Baker RW. Membrane technology and applications. New York: McGraw-Hill; 2000.

[10] Koros WJ, Paul DR. Design considerations for measurement of gas sorption in polymers by pressure decay. J Polym Sci Pol Phys. 1976;14(10):1903-7.

[11] Costello LM, Koros WJ. Temperature-dependence of gas sorption and transport properties in polymers - Measurement and applications. Ind Eng Chem Res. 1992;31(12):2708-14.

CHAPTER 4

PRELIMINARY ANALYSIS OF DIFFERENT POLYMERS AS PRECURSORS TO CARBON MOLECULAR SIEVE DENSE FILM MEMBRANES FOR ETHYLENE/ETHANE SEPARATION

4.1. Overview

The intrinsic polymer precursor properties can significantly affect the properties of the resulting CMS membrane; hence choosing the appropriate starting material for CMS fabrication and assessing its viability in ethylene/ethane (C_2H_4/C_2H_6) separation is a first crucial step. This is the main focus of Objective 1 of this thesis, covered in this Chapter. Section 4.2 summarizes the properties of the polymer precursors chosen for this study. Section 4.3 discusses the development of the polymeric C_2H_4/C_2H_6 upper bound line as a basis against which to compare the performance of CMS membranes. A review of the various approaches to overcome the polymeric C_2H_4/C_2H_6 upper bound by using advanced membrane types has been presented in Section 4.4. Finally, Sections 4.5 and 4.6 discuss preliminary analysis of the chosen precursors in forming CMS membranes for C_2H_4/C_2H_6 separation as well as the challenges in CMS dense film fabrication.

4.2. Polymer Precursors for Carbon Molecular Sieve Membrane Fabrication

Three polyimide materials were chosen as precursors to CMS dense films for C_2H_4/C_2H_6 separation:

(i) Matrimid®, a commercially available polyimide with attractive gas separation properties that can provide excellent economic scalability for industrial purposes.

(ii) 6FDA-DAM, a polyimide made from a fluorinated aromatic dianhydride (6FDA) with bulky CF_3 groups that hinder chain packing and a non-fluorinated high free volume diamine (DAM). 6FDA-DAM is an intrinsically high performing polymer for gas separation, and has a much higher fractional free volume (FFV) compared to Matrimid®. It may thus allow us to achieve high productivity CMS membranes whose selectivity may be tuned by optimizing the pyrolysis conditions.

(iii) 6FDA:BPDA-DAM, a copolyimide which allows the capability to tune the ratio of 6FDA and BPDA dianhydride monomers while maintaining the high free volume of the DAM diamine to tune the precursor over a range of intrinsic starting properties. In this work 6FDA:BPDA(1:1)-DAM has been chosen as the starting material since investigating different ratios may require a separate study by itself. The FFV of 6FDA:BPDA(1:1)-DAM is higher than Matrimid® but lower than 6FDA-DAM, allowing us to explore a range of permeability vs. selectivity combinations.

These polyimides have been well characterized in the literature, as well as in the Koros group in terms of their structure and intrinsic gas separation properties. Matrimid® and 6FDA:BPDA-DAM have also been fabricated into CMS membranes with attractive O_2/N_2 and CO_2/CH_4 properties. The three precursors were thus chosen based on their

history of use in the Koros group and, more importantly, because of the structural differences they offer in terms of chain packing that can affect the resulting CMS properties. The chemical structures of the polymers are shown in Figure 3.1. The fractional free volume (FFV), density and glass transition temperature (T_g) of the polymers are tabulated below in Table 4.1 [1-3].

Table 4.1: Polymer precursor properties [1-3]

Precursor	Density g/cm^3	FFV	Tg °C
Matrimid®	1.25	0.110	305
6FDA-DAM	1.33	0.190	395
6FDA:BPDA-DAM	1.32	0.145	425

Free-standing homogeneous dense films were prepared from each of the three polymers using a solution casting method described in Section 3.3.1. The intrinsic C_2H_4/C_2H_6 separation performance for each precursor was determined using pure gas permeation and sorption tests at 35°C. The precursor separation performance is shown in Table 4.2. The experimental sorption data fitted to dual mode sorption isotherm are shown in Figure 4.1.

Table 4.2: Pure gas C_2H_4/C_2H_6 transport properties of polymer precursor dense films (35°C, 50 psia)

Precursor	P_{C2H4} Barrer	P_{C2H4}/P_{C2H6}	$\mathbb{S}_{C2H4}$ $cm^3/(cm^3.cmHg)$	$\mathbb{S}_{C2H4}/\mathbb{S}_{C2H6}$
Matrimid®	0.45	4.5	0.06	1.31
6FDA-DAM	64	3.0	0.14	1.03
6FDA:BPDA-DAM	46	3.3	0.14	1.02

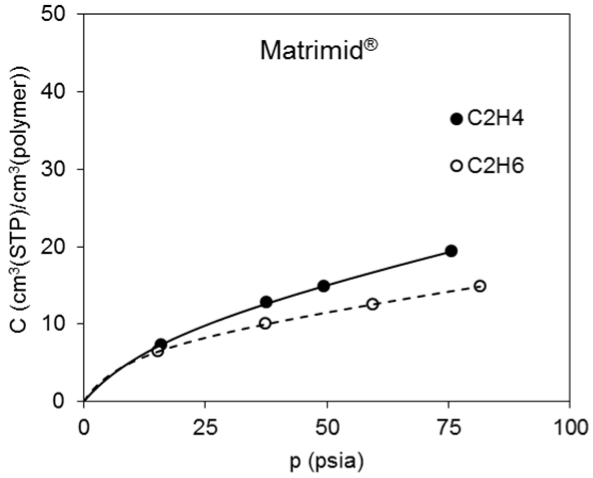

Matrimid®			
		C_2H_4	C_2H_6
C'_H	[cm^3/cm^3]	11.1	8.2
b	[1/psia]	0.054	0.104
k	[$cm^3/(cm^3.psia)$]	0.139	0.092

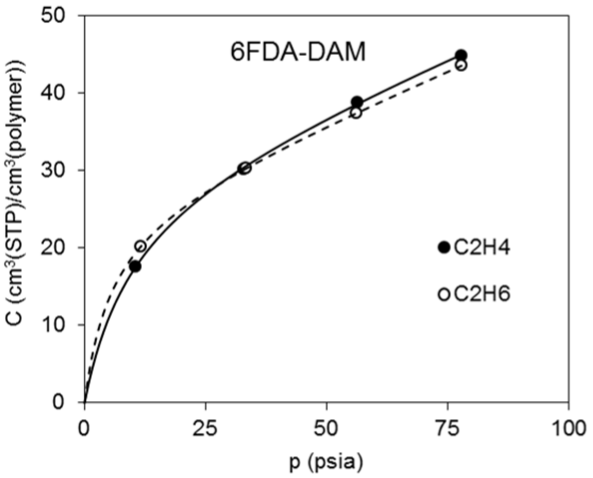

6FDA-DAM			
		C_2H_4	C_2H_6
C'_H	[cm^3/cm^3]	29.0	25.3
b	[1/psia]	0.101	0.184
k	[$cm^3/(cm^3.psia)$]	0.248	0.256

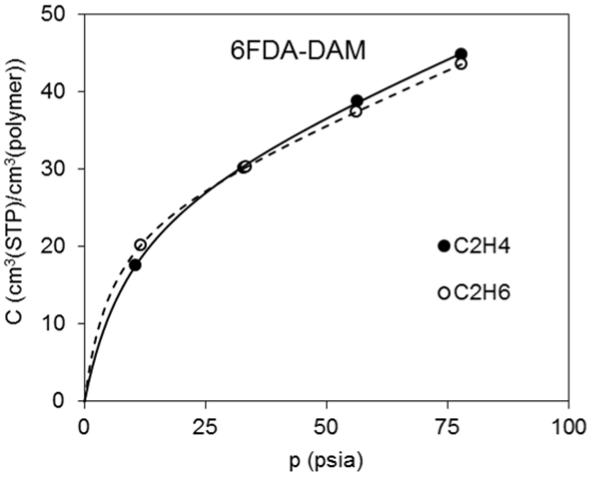

6FDA-DAM			
		C_2H_4	C_2H_6
C'_H	[cm^3/cm^3]	29.0	25.3
b	[1/psia]	0.101	0.184
k	[$cm^3/(cm^3.psia)$]	0.248	0.256

Figure 4.1: Pure gas C_2H_4 and C_2H_6 sorption isotherms for polymer precursors (35°C)

4.3. Basis For Assessing Separation Performance: The Polymeric Ethylene/Ethane Upper Bound

It is useful to establish a basis against which to compare performance of CMS membranes for C_2H_4/C_2H_6 separation. The upper bound trade-off curve [4, 5] for polymeric gas separation membranes is often used as a basis to gauge membrane performance. It is well known in the membrane literature that for gas separation using solution processable polymeric membranes, there is a trade-off between the permeability of the fast gas (A) vs. the selectivity of the gas pair ($\mathrm{A/B}$). This is referred to as the upper bound [4-6], and is typically represented by a log-log plot of α vs. P:

$$\alpha_{\mathrm{A/B}} = \frac{\beta_{\mathrm{A/B}}}{\mathrm{P_A}^{\lambda_{\mathrm{A/B}}}} \tag{4.1}$$

In 1991, Robeson [4] defined the upper bound for several gas pairs from the list of He, H_2, O_2, N_2, CO_2 and CH_4 based on a thorough analysis of literature data. He identified a linear relationship between the slope of the upper bound and the difference of the Lennard-Jones kinetic diameters of the given gas pair, thus indicating the dominance of a diffusion-based separation of these gas pairs for high performing polymers that define the upper bound. Continuous efforts to improve gas transport properties of hyper-rigid glassy polymers by tailoring their structure, and fluorinated polymers have successfully shifted the upper bound [5].

In 1999, Freeman [6] presented a fundamental analysis of the upper bound line for polymeric membrane materials, and presented a way to predict the slope ($\lambda_{\mathrm{A/B}}$) and front factor ($\beta_{\mathrm{A/B}}$) of the upper bound line as follows,

$$\lambda_{A/B} = \left(\frac{d_B}{d_A}\right)^2 - 1 \tag{4.2}$$

and

$$\beta_{A/B} = \frac{\mathbb{S}_A}{\mathbb{S}_B}\mathbb{S}_A{}^{\lambda_{A/B}}\exp\left\{-\lambda_{A/B}\left[b - f\left(\frac{1-a}{RT}\right)\right]\right\} \tag{4.3}$$

In Equation 4.2, d_A and d_B represent the kinetic diameters of the fast gas (A) and slow gas (B) respectively. As observed by Robeson [4, 5], Equation 4.2 directly suggests that the slope of the upper bound is a natural consequence of the size-sieving nature of stiff chain glassy polymers that generally define the upper bound. In Equation 4.3, $\mathbb{S}_A$ and $\mathbb{S}_B$ represent the solubility of the gases; the parameter f relates to interchain spacing and its value ranges from 0 for rubbery and low performance glassy polymers to ~14000 cal/mol for high performance rigid polyimides [6, 7]; a and b are linear free energy coefficients that correlate the diffusion front factor (D_{oA}) to the activation energy of diffusion (E_{DA}) as follows [8, 9],

$$\ln D_{oA} = a\frac{E_{DA}}{RT} - b \tag{4.4}$$

a and b are independent of gas type, with a being independent of polymer type as well and having a universal value of 0.64 [10]; b has a value of –ln(10^{-4} cm^2/s) for rubbery polymers and –ln(10^{-5} cm^2/s) for glassy polymers [11]. In the above equations, R represents the universal gas constant and T represents the absolute temperature.

The equations above allow predicting the slope (λ) of the upper bound with no adjustable parameters and the front factor (β) with only one adjustable parameter. As shown by Freeman [6], predictions of λ and β from the equations above furnished a good correlation with the slopes and front factors presented by Robeson [4, 5] for several gas pairs.

In 2003, Burns and Koros [12] presented the upper bound for C_3H_6/C_3H_8 separations. Here we present an experimental C_2H_4/C_2H_6 upper bound based on literature data, as well as extend the analysis by Freeman [6] to predict the C_2H_4/C_2H_6 upper bound for polymeric membrane materials in order to establish a basis against which to compare CMS performance.

4.3.1. Experimental Ethylene/Ethane Polymeric Upper Bound

Limited work has been done in the field of polymeric membrane-based C_2H_4/C_2H_6 separations and, as such, a comprehensive summary focusing solely on C_2H_4/C_2H_6 separation has not been presented or reviewed. We compiled all the literature data available for C_2H_4/C_2H_6 separation using polymeric membranes [13-18], as well as included measurements on polymers used in this work. This data is shown in Table 4.3. Table 4.4 lists the chemical names for abbreviations used for polymers in Table 4.3.

Table 4.3: C_2H_4/C_2H_6 separation performance for polymeric membranes

Precursor	T	p	P_{C2H4}	$\alpha_{C2H4/C2H6}$	Source
	°C	atm	Barrer		
6FDA-6FpDA	35	5.0	1.90	4.20	Chan (2002) [13]
6FDA-1,5-NDA	35	5.0	0.87	5.80	
6FDA-NDA	35	2.0	1.17	6.84	Chan (2003) [14]
6FDA-NDA/Durene (75:25)	35	2.0	4.46	5.62	
6FDA-NDA/Durene (50:50)	35	2.0	9.48	4.27	
6FDA-NDA/Durene (25:75)	35	2.0	36.70	3.60	
6FDA-Durene	35	2.0	76.70	2.89	
6FDA-TrMPD	50	2.0	58.00	2.90	Tanaka [15]
BPDA-TeMPD	50	2.0	5.80	4.30	
6FDA-mPD	35	3.8	0.30	3.30	Bickel [16]
6FDA-IPDA	35	3.8	1.40	3.80	
6FDA-6FpDA	35	3.8	2.10	4.40	
Matrimid®	35	3.4	0.45	4.50	This work
6FDA-DAM	35	3.4	64.00	3.00	
6FDA:BPDA-DAM	35	3.4	46.00	3.30	

Table 4.4: Chemical names for abbreviations in Table 4.3

Abbreviation	Chemical Name
6FDA	4,4'-(hexafluoroisopropylidene) diphthaic anhydride
6FpDA	4,4'-(hexafluoroisopropylidene) dianiline
NDA	1,5-naphthalene diamine
Durene	1,2,4,5-tetramethylbenzene
TrMPD (DAM)	2,4,6-trimethyl-1,3-phenylene diamine
BPDA	3,3',4,4'-biphenyltetracarboxylic dianhydride
TeMPD	2,3,5,6-tetramethyl-1,4-phenylenediamine
mPD	1,3-phenylene diamine
IPDA	4,4'-(isopropylidene) dianiline

Based on the data shown in Table 4.3 we plotted an experimental C_2H_4/C_2H_6 trade-off line, show in Figure 4.2.

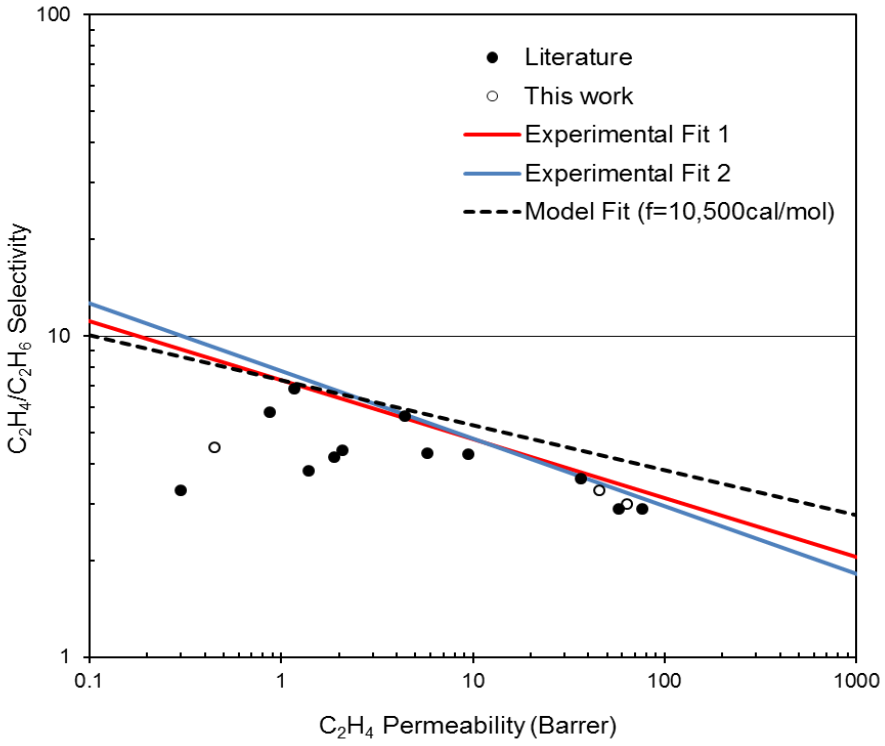

Figure 4.2: Plot showing C_2H_4/C_2H_6 data from Table 4.3 along with two fits for the experimental C_2H_4/C_2H_6 upper bound trade-off line, drawn to aid the eye, as well as the predicted C_2H_4/C_2H_6 upper bound line

All measurements reported are based on pure gas steady state permeation tests using dense films between 35-50°C and 2-5 atm feed pressures. As noted in the references [13-16], all permeation measurements were carried out with downstream under vacuum and low pressure feed stream conditions, such that plasticization effects in these materials due to C_2H_4 and C_2H_6 are essentially non-existent in the pressure range considered. Bickel & Koros [16] carried out pure gas C_2H_4 and C_2H_6 permeation

measurements at 35°C up to 17 atm feed pressure and reported no upswing in permeability with pressure, indicating that no plasticization effects occurred. Similarly Chan et al. [13, 14] reported no occurrence of plasticization for C_2H_4 and C_2H_6 feed pressures up to 16 atm. These reported data for the pressure dependence of C_2H_4 and C_2H_6 permeability provide adequate evidence to claim that plasticization effects are minimal in the feed pressure range of 2-5 atm considered for the upper bound analysis.

Measurements on 6FDA-6FpDA have been reported by both Bickel & Koros [16] and Chan et al. [13]; however, the measurements have been reported at two different pressures. Based on the so-called “dual mode sorption and transport” effects, it is understandable that the C_2H_4 permeability is lower at a higher feed pressure. Additionally measurements on 6FDA-NDA have been reported by Chan et al. [13, 14] at two different feed pressures, 2 atm and 5 atm and again the permeability, as expected is lower at the higher feed pressure. In order to keep the pressure range for the upper bound analysis as narrow as possible, we will consider the measurements for both 6FDA-6FpDA and 6FDA-NDA at the lower feed pressure, thus making the pressure range for the analysis as 2-3.8 atm.

Three of the data points are based on measurements made as part of this work on polyimides Matrimid®, 6FDA-DAM and 6FDA:BPDA-DAM, details of which have already been mentioned in the previous sections.

It should be noted that one of the polymers tested in this work, 6FDA-DAM, has the same chemical structure as 6FDA-TrMPD tested by Tanaka et al. [15], classified under a different chemical name. Although there is some difference in the results reported here and by Tanaka et al. [15], the values reported are fairly close and can be considered equivalent within experimental uncertainty related to polyimide synthesis procedures, membrane formation, testing and measurement.

Some of the literature data have not been considered for the upper bound development. In 1992 Ilinitch et al. [19] reported C_2H_4 and C_2H_6 permeability and C_2H_4/C_2H_6 selectivity for polyphenyleneoxide (PPO), two PPO-based copolymers and several rubbery polymers tested for a gas mixture containing 85vol% CH_4, 10vol% C_2H_4 and 5vol% C_2H_6. In a 1993 article the authors [20] published a corrigendum stating that due to a technical error, the permeabilities reported in 1992 were one order of magnitude higher than the actual values. These results have not been included in the upper bound analysis here since they are based on ternary gas mixtures, whereas all the data considered is based only on pure gas measurements. In addition, in 1993 Ilinich et al. [20] reported based on transient state permeation experiments for C_2H_4/C_2H_6 separation. These data have not been included in the upper bound analysis, which takes into account only steady state permeation measurements. Teplyakov & Meares [21] reported permeability data for several rubbery and glassy polymers. These measurements were reported at 25°C and have not been considered in the upper bound analysis. In any case, the results do not affect the position of the upper bound line since the reported performances are quite low. For example, for PVTMS, a glassy polymer, the C_2H_4 permeability is 12 Barrer with C_2H_4/C_2H_6 selectivity for only 1.6.

Two different fits, based on the highest performance points on the plot, have been shown for the experimental upper bound line, drawn to aid the eye. Fit 1 spans 6FDA-NDA, 6FDA-NDA/Durene (75:25) and 6FDA-NDA/Durene (25:75), while fit 2 spans 6FDA-NDA/Durene (75:25), 6FDA-NDA/Durene (25:75) and 6FDA/BPDA-DAM (50:50). It should be noted that the experimental C_2H_4/C_2H_6 upper bound is defined here based on only a few polymers. This is however not quite different from the upper bound for several other gas pairs (from He, H_2, O_2, N_2, CO_2 and CH_4) as defined by Robeson in 2008 [5], where only a few high performing polymer materials lie at the upper bound line.

4.3.2. Predicted Ethylene/Ethane Polymeric Upper Bound

The experimental upper bound shown in Figure 4.2 is based on high performing 6FDA-based polyimides which are the current, best available in-class polymeric materials for such gas separations, and can hence be considered a good estimate of the trade-off curve for C_2H_4/C_2H_6 separation. However, unlike the case of smaller gas pairs, since the sample space for consideration of the experimental C_2H_4/C_2H_6 upper bound is extremely limited, it is useful to consider modeling work in an effort to predict where the C_2H_4/C_2H_6 upper bound should lie.

As described earlier, a previous analysis by Freeman [6] provides a general quantitative description of the upper bound performance of polymeric membranes. Equations 4.2 and 4.3 presented above can be used to estimate the slope (λ) and front factor (β) of the upper bound.

The slope, λ can be predicted with no adjustable parameters, and depends only on the size of the molecules, suggesting that the slope of the upper bound is a natural consequence of the sieving nature of stiff chain 6FDA-based glassy polymers that generally define the upper bound. In order to apply the analysis to C_2H_4/C_2H_6 separations, the first step is to represent the sizes of C_2H_4 and C_2H_6. The molecular size for low molecular weight penetrants permeating through polymer membranes is often represented by either its kinetic diameter (based on the minimum equilibrium cross-sectional diameters) determined using molecular sieves or the collision diameter calculated from the Lennard-Jones potential. For light gases, Freeman [6] used the kinetic diameters of the molecules given by Breck [22] to obtain λ, and the values are in good agreement with the upper bound slope as published by Robeson [4]. For small molecules (except CO_2) the difference between the kinetic and Lennard-Jones diameters are negligibly small. However, for higher hydrocarbons, the difference between the two

starts becoming significant and the kinetic diameter may no longer provide a reasonable size for the molecules [17]. Burns & Koros [12] hence used the Lennard-Jones diameter instead of the kinetic diameter for C_3H_6 and C_3H_8. Table 4.5 reports the size of C_2H_4 and C_2H_6 from different sources.

Table 4.5: Size and Lennard Jones temperature of C_2H_4 and C_2H_6 from various sources

Source	σ (Å)			ε/k (K)	
	C_2H_4	C_2H_6	Remarks	C_2H_4	C_2H_6
van Krevelen [11]	4.16	4.44	LJ collision diameter	225	216
Reid & Sherwood [23]	4.163	4.443	LJ collision diameter	224.7	215.7
Hirschfelder [24]	4.232	4.418	Viscosity measurements	205	230
Hirschfelder [24]	4.1	4.5	Four center model	-	-
Bickel & Koros [16]	3.7	4.1	Dreiding force field	-	-
Breck [22]	3.9	-	Molecular sieve	-	-

As in the case of C_3H_6/C_3H_8, we used the Lennard-Jones collision diameter as the most appropriate currently available representation of the sizes of C_2H_4 and C_2H_6 in order to predict λ. It should be noted that while this is an acceptable representation of the sizes of C_2H_4 and C_2H_6 for transport through polymeric membranes and for the purpose of predicting the upper bound, it is by no means a good representation for molecular sieving materials like CMS. For CMS membranes, we define effective sizes for C_2H_4 and C_2H_6 later in this work based on their transport properties.

Thus, for C_2H_4/C_2H_6 transport in polymeric membranes, we take d_A = 4.16 Å and d_B = 4.44 Å (Table 4.5), and, from Equation 4.2, the predicted upper bound slope is

$$\lambda_{A/B} = \left(\frac{d_B}{d_A}\right)^2 - 1 = 0.14$$

The front factor β for the upper bound can be predicted with only one adjustable parameter f using Equation 4.3 In order to predict β from Equation 4.3 we need to define an average sorption coefficient for C_2H_4 and the average C_2H_4/C_2H_6 sorption selectivity, as well as the value of f.

Penetrant solubility in polymers is governed by the condensability of the gas and its interactions with the polymer matrix [6, 11, 17]. In the absence of any significant polymer-penetrant interactions, the penetrant solubility is typically dominated mainly by its chemical nature and scales with convenient measures of the penetrant condensability, such as its boiling point, critical temperature, Lennard-Jones temperature etc. [21, 25]. A general correlation between penetrant solubility in amorphous polymers and the penetrant Lennard-Jones temperature ($\frac{\varepsilon_A}{k}$) can be represented from classical thermodynamics as follows [11]:

$$\ln \mathbb{S}_A = M + N\left(\frac{\varepsilon_A}{k}\right) \tag{4.5}$$

van Krevelen [11] reported values for M and N at 25°C for both rubbery and glassy polymers. Thus, a simple linear relationship between the solubility of various gases at 25°C in glassy polymers and their Lennard-Jones temperatures is given as:

$$\log \mathbb{S}(298) = -7.4 + 0.010\left(\frac{\varepsilon}{k}\right) \pm 0.6 \tag{4.6}$$

Sorption coefficient of gases in polymers follows a van't-Hoff type relation with temperature [11, 26]:

$$\mathbb{S}(\mathrm{T}) = \mathbb{S}_{\mathrm{o}} \exp\left(-\frac{\mathrm{H}_{\mathbb{S}}}{\mathrm{RT}}\right) \tag{4.7}$$

where, $\mathrm{S_o}$ represents the front factor for sorption and $\mathrm{H_S}$ represents the heat of sorption.

van Krevelen also presented a simple linear relationship between the enthalpy of sorption for a gas in a glassy polymer and its Lennard-Jones temperature [11]:

$$10^{-3}\frac{\Delta \mathrm{H}_{\mathbb{S}}}{\mathrm{R}} = 0.5 - 0.010\left(\frac{\varepsilon}{\mathrm{k}}\right) \pm 1.2 \tag{4.8}$$

Equations 4.6, 4.7 and 4.8 thus allow us to obtain average solubility values for ethylene and ethane in glassy polymers at 35°C, the temperature considered for the upper bound analysis, as follows:

$$\log \mathbb{S}(\mathrm{T}) = \log \mathbb{S}(298) - 0.435\left(\frac{\Delta \mathrm{H}_{\mathbb{S}}}{\mathrm{R}}\right)\left(\frac{1}{\mathrm{T}} - \frac{1}{298}\right) \tag{4.9}$$

The average C_2H_4 solubility and C_2H_4/C_2H_6 solubility selectivity values at 35°C as obtained from the Equation 4.9 above are as follows:

$$\mathbb{S}_{\mathrm{C2H4}} = 0.008\left(\frac{\mathrm{cm^3(STP)}}{\mathrm{cm^3(polymer)cmHg}}\right)$$

$$\frac{\mathbb{S}_{\mathrm{C2H4}}}{\mathbb{S}_{\mathrm{C2H6}}} = 1.2$$

We also considered the experimental solubility data for C_2H_4 and C_2H_6 from literature [13-16]. Owing to the lack of tabulated data in some cases, some of the data points were read directly off the plots and may be approximate. Additionally we measured sorption isotherms for Matrimid®, 6FDA-DAM and 6FDA:BPDA-DAM, as reported in Section 4.2. The experimental solubility data is compiled in Table 4.6.

Table 4.6: Experimental C_2H_4 and C_2H_6 solubility data for polymers

Precursor	T	p	$\mathbb{S}_{C2H4}$	$\mathbb{S}_{C2H4}/\mathbb{S}_{C2H6}$	Source
	°C	atm	$cm^3/(cm^3.cmHg)$		
6FDA-1,5-NDA	35	5.0	0.085	1.10	[13]
6FDA-TrMPD	50	2.0	0.150	1.00	[15]
6FDA-6FpDA	35	3.8	0.125	1.12	[16]
Matrimid®	35	3.4	0.058	1.30	This work
6FDA-DAM	35	3.4	0.140	1.03	
6FDA:BPDA-DAM	35	3.4	0.138	1.02	
Average			0.116	1.10	

The C_2H_4 solubility obtained theoretically is lower than the experimental solubility average. The sample space for the average solubility is extremely limited and does not span the entire range of the upper bound. Additionally the data available are at different temperatures and pressures. While such effects are somewhat suppressed in the overall permeability due to the counteracting behavior of solubility and diffusivity, the effect on solubility alone may be significant. The experimental solubility value may still give a reasonable estimate of the C_2H_4/C_2H_6 upper bound; however, owing to insufficient

experimental data we consider the theoretical averages for prediction of the upper bound.

The only adjustable parameter in predicting β is f, a parameter relating the activation energy for diffusion to the square of the penetrant diameter as follows [27]:

$$E_{DA} = cd_A^2 - f \tag{4.10}$$

where c and f depend on the polymer. The value of f ranges from zero for rubbery polymers and low performance glassy polymers to 14,000 cal/mol for the polyimide prepared by Haraya et al. [7] . Freeman [6] used a value of f =12,600 cal/mol based on a best fit of the model predictions to Robeson's upper bound [4] for several light gas pairs. Here we vary f from 10,000-14,000 cal/mol in order to predict the theoretical C_2H_4/C_2H_6 upper bound and compare it with the experimental upper bound.

Figure 4.2 shows the predicted upper bound for a value of f =10,500 cal/mol against the experimental upper bound. All of the experimental data points lie below the predicted upper bound line. The values of λ and β obtained from the theoretical prediction as well as those obtained for the experimental upper bound are summarized in Table 4.7.

Table 4.7: Slope and front factor values for C_2H_4/C_2H_6 upper bound

	$\lambda_{C2H4/C2H6}$	$\beta_{C2H4/C2H6}$ (Barrer)$^{\lambda}$
Theoretical Prediction	7.3	0.14
Experimental Fit 1	7.3	0.18
Experimental Fit 2	7.8	0.21

Clearly, a value for f =10,500 cal/mol furnishes a very good agreement between the predicted C_2H_4/C_2H_6 upper bound and experimental fit 1.

4.4. Advanced Membranes for Ethylene/Ethane Separation

The upper bound trade-off indicates that for polymeric membranes, C_2H_4/C_2H_6 selectivity over 10 may only be achieved for extremely low C_2H_4 permeability <0.5 Barrer. On the other hand, for C_2H_4 permeability over 10 Barrer, selectivity cannot exceed 6. The theory essentially implies that there are two ways to overcome the polymeric upper bound: (i) by increasing the solubility selectivity of the membrane material towards C_2H_4, and (ii) by increasing the sieving capability of the membranes to enhance the C_2H_4/C_2H_6 diffusion selectivity. The following sections discuss these two approaches and advanced membranes that are capable of overcoming the polymeric C_2H_4/C_2H_6 upper bound.

4.4.1. Facilitated Transport Membranes

The average C_2H_4/C_2H_6 solubility selectivity for polymeric membranes is close to ~1.2. In theory, increasing the solubility selectivity of C_2H_4 over C_2H_6 in the membrane material can lead to enhanced overall selectivity surpassing the upper bound. This could be achieved by functionalizing the membrane materials with groups or ions that preferentially interact with C_2H_4 over C_2H_6, thus increasing C_2H_4 uptake. Facilitated transport membranes have attracted research interest because of their potential to achieve this favorable sorption selectivity. They can perform separations more efficiently than simple, passive, polymeric membranes. In a facilitated transport process, passive

diffusion across a concentration gradient is supplemented by the presence of a carrier agent that selectively and reversibly binds with a desired compound targeted for separation, enhancing its movement across a barrier. Metal salts, such as those of silver, copper etc. present as the carrier agent in the membrane, form electron donor/acceptor complexes with olefins (in this case C_2H_4) through interactions of the olefin π-orbitals with the metal ion, thus enhancing their movement across the membrane. While the exact mechanism for transport of olefins across the membrane by complexation is complex, it has been suggested that facilitated transport occurs by either mobile diffusion of the Ag^+-solute complex through the membrane or by movement of the olefin across fixed silver sites by a hopping mechanism [28-30].

In principle, facilitated transport membranes are capable of achieving exceptional selectivity for C_2H_4 over C_2H_6, capable of transcending the upper bound. Such membranes have been investigated by several researchers [28-33]. However, several articles focus on an initial performance and do not consider membrane stability, which can be a serious concern in facilitated transport membranes. Although the starting performance for facilitated transport membrane for C_2H_4/C_2H_6 separation is far beyond the polymeric upper bound, the membranes typically degrade rapidly with large performance losses, thus making them questionable for practical application [28, 29]. A comprehensive review on olefin/paraffin separation using facilitated membranes has been presented by Azhin et al. [34] and more recently by Faiz & Li [29]. These articles describe in detail the different forms of facilitated transport membranes, their separation performance as well as their advantages and disadvantages. Here, we briefly summarize the performance of different types of facilitated transport membranes and focus on the challenges in practically using these membranes for C_2H_4/C_2H_6 separations.

Facilitated transport membranes can be fabricated in two main forms: (i) liquid membranes and (ii) solid membrane electrolytes [29, 33]. Table 4.8 shows examples of

C_2H_4/C_2H_6 separation performance for different types of liquid and electrolyte membranes.

Table 4.8: C_2H_4/C_2H_6 separation performance for different types of facilitated transport membranes [29, 34]

Class	Membrane type	Carrier	P_{C2H4} Barrer	P_{C2H4}/P_{C2H6}	Source
SLM	PEO	$AgNO_3$	1200	290	[35]
	Cellulose filter	$AgNO_3$	-	1000	[35]
ILM	Nafion	$AgBF_4$	400-700	30-400	[36]
	PS	$AgNO_3$	1800	200	[37]
FLM	PDMS/PPSQ	$AgNO_3$	28000	55	[38]
	PP	$AgNO_3$	1000	500	[39]
HFMC	SPEEK	$AgNO_3$	10000	2700	[40]
	SPEEK/SPEEK	$AgNO_3$	180	3800	[40]
Solid Electrolyte	PEO	$AgBF_4$	11.1	120	[33]
	CA	$AgBF_4$	-	10-280	[41]
	PVMK	$AgBF_4$	-	40-250	[42]

PEO- poly(ethylene oxide); PS- polysulfone; PP- polypropylene; CA- cellulose acetate; PVMK- poly(vinyl methyl ketone); PDMS/PPSQ- polydimethylsiloxane/polyphenylsilsesquioxane; SPEEK- sulfonated poly(ether ether ketone)

Liquid membranes can either be fabricated as immobilized liquid membranes (ILMs) or as flowing liquid membranes (FLMs). ILMs are the simplest form of facilitated transport membranes made by impregnating a microporous membrane with a solution carrier [29]. The carrier is held within the pores of the membrane by either capillary forces (supported liquid membranes) or by electrostatic interactions with the membrane

ion exchange sites (ion exchange membranes). Although ILMs have shown very high starting selectivities for C_2H_4/C_2H_6 separation, in some cases >1000, their mechanical and long term physical stability is poor because of rapid solvent and carrier loss during high pressure operations, thus resulting in a decrease in C_2H_4 flux and C_2H_4/C_2H_6 selectivity. Although it has been proposed to saturate the feed and sweep streams with water vapor to overcome this issue, it is highly impractical to do so because of the large costs incurred in the addition and subsequent removal of water vapor from the streams.

Flowing liquid membranes (FLM) [29], that make use of a continuously circulated aqueous carrier stream, have also been investigated in several forms in order to address some of the physical stability problems in ILMs owing to solvent and carrier loss. Each of these configurations however has their own drawbacks which makes them impractical for commercial applications. For example, although FLMs show promising stability, the permeation rates through these membranes can be very low due to small membrane surface areas and inefficient gas-liquid contact. Hollow fiber membrane contactor (HFMC) type flowing liquid membranes allow continuous gas-liquid contact with large surface area; however they still suffer from several shortcomings such as membrane wetting and limited membrane thermal and chemical stability, which destroy the long term application of the separation process.

Membrane electrolytes are a more recent class of facilitated transport membranes which do not use liquids as facilitation carriers; instead olefin transport occurs in the solid state [28, 29, 33]. They are composed of metal salts dissolved in the polymer matrix, where both anions and cations are sufficiently mobile without the need of a solvent to promote ionic motion and conductivity. The main advantage of polymer electrolyte membranes over liquid facilitated transport membranes is their physical stability and the fact that they can be operated with dry feeds. Unlike ILMs, these membranes have the advantage of sustaining higher pressure difference across the

membrane without physical loss of the complexing agent. However, one of the major shortcomings of membrane electrolytes is the issue of long term chemical stability, with decline in membrane performance occurring due to reduction of silver ions to silver nanoparticles and other silver compounds. Silver ions can be reduced in the presence of light. In addition, impurities present in the feed stream such as H_2, H_2S, and C_2H_2 etc. can poison the carrier ions, thus degrading the membranes. Once the membrane is degraded, regeneration is impractical [28, 29]. Further jeopardizing the performance of membrane electrolytes is a recently reported phenomenon called olefin-conditioning [28]. Electrolyte membranes are not stable even in the presence of ideal C_2H_4/C_2H_6 mixtures, and it has been shown that over time the presence of an olefin (C_2H_4), which can complex with silver ions, irreversibly alters and degrades the membrane. Hence, the very species targeted for separation become the cause for membrane instability. Over time, a decrease in the C_2H_4 permeance is the primary cause for selectivity decline. To date, an effective strategy to mitigate the effect of "olefin conditioning" has not been identified [28].

Facilitated transport membranes therefore still present a large challenge in improving the stability of the olefin complexing agent to develop membranes with lifetimes satisfactory for commercial application. Significant fundamental research and perhaps even the development of a breakthrough, intrinsically stable carrier may be required for making facilitated transport membranes practical for industrial implementation.

4.4.2. Molecular Sieve Membranes

A second approach to overcome the polymeric upper bound is to increase the sieving capability of membranes which will in turn increase the C_2H_4/C_2H_6 diffusion selectivity. Over time, increasing polymer chain rigidity while simultaneously increasing

inter-chain spacing, for example by introducing packing-inhibiting bulky groups and intrinsically rigid linkages, has pushed the upper bound for several gas pairs [5]. Nevertheless, polymers cannot achieve a true molecular sieving effect owing to flexible chains, and pushing the sieving capability of solution processable polymers by tailoring their structure may have reached its limits.

Materials such as zeolites, metal organic frameworks (MOFs) including zeolitic imidazolate frameworks (ZIFs), carbon molecular sieves (CMS) etc. on the other hand consist of rigid pore structures with arrays of channels of molecular dimensions which can offer the possibility of size and shape selective separations, and are thus capable of surpassing the polymeric upper bound [43].

4.4.2.1. Crystalline Molecular Sieve Membranes

Most studies relating to C_2H_4/C_2H_6 separation using crystalline molecular sieves have focused on cyclic batch adsorption/desorption type processes, but in principle, a steady state membrane process can be a more attractive alternative [44]. Enriching C_2H_4 from C_2H_4/C_2H_6 mixtures is truly one of the most challenging separations as evidenced by the incapability of small pore eight-ring zeolitic molecular sieves, such as zeolite NaA, CHA, AlPOs, SAPOs, and DD3R to discriminate C_2H_4 and C_2H_6 molecules on the basis of size selectivity [45-47]. These zeolitic molecular sieves, which are considered to be the most size-selective crystalline molecular sieves, have been shown to be highly promising for C_3H_6/C_3H_8 with diffusion selectivity in the range of 10^3-10^5; however, can hardly separate C_2H_4 and C_2H_6 by a factor of more than 3 based on the differences in diffusion rates.

Adsorption of C_2H_4, in some cases, is drastically favorable over C_2H_6 in alumina-rich cationic zeolites (e.g. zeolite A and X) and metal-organic frameworks (e.g.

Fe_2(dobdc)) due to strong interactions between the C_2H_4 C-C double-bonds and adsorbents surfaces, which leads to an solubility selectivity in the range of 10 to 20 [46, 48, 49]. Unfortunately, these promising selectivities are only achievable at very low surface densities and diminish quickly as the feed pressure reaches atmosphere and saturation limits are approached. Therefore, for pure zeolite or MOF membranes with feed pressures higher than several atmospheres, the C_2H_4/C_2H_6 permselectivity are expected to be less than 5 in almost all cases, which is far from being commercially attractive.

Zeolitic imidazolate framework-8 (ZIF-8) belongs to the sub-family of MOFs with zeolite or zeolite-like topologies and has recently been extensively studied due to its interesting molecular sieving properties, promising for gas separations [50-55]. While ZIF-8 has been shown to be highly kinetically selective for C_3H_6/C_3H_8 and n-C_4H_{10} over iso-C_4H_{10} [52], both computational and experimental studies have suggested that the C_2H_4/C_2H_6 selectivity in ZIF-8 is quite limited [56-60]. Pan & Lai [56] investigated ZIF-8 membranes for separation of hydrocarbon mixtures and their membranes show a pure component C_2H_4/C_2H_6 selectivity close to 2. ZIF-8 membranes fabricated by Caro & coworkers [60, 61] showed an ideal C_2H_4/C_2H_6 selectivity of 4.2 for pure component feeds, and for an equimolar mixture of C_2H_4/C_2H_6 a selectivity of 2.8 and 2.4 respectively for 1 and 6 bar feed pressure were reported. This moderate C_2H_4 selectivity over C_2H_6 was explained by the interplay of a preferential C_2H_6 adsorption selectivity competing with preferential C_2H_4 diffusion selectivity.

Thus, zeolite or MOF/ZIF membranes have thus far not been shown to deliver attractive C_2H_4/C_2H_6 selectivity. Figure 4.3 shows a plot of the C_2H_4/C_2H_6 separation performance of crystalline molecular sieves against the polymeric upper bound. Another limitation of using these pure zeolite or MOF/ZIF membranes is the expensive fabrication

cost and their brittle nature, as well as difficulty in fabricating a sufficiently coherent and robust membrane on a large scale.

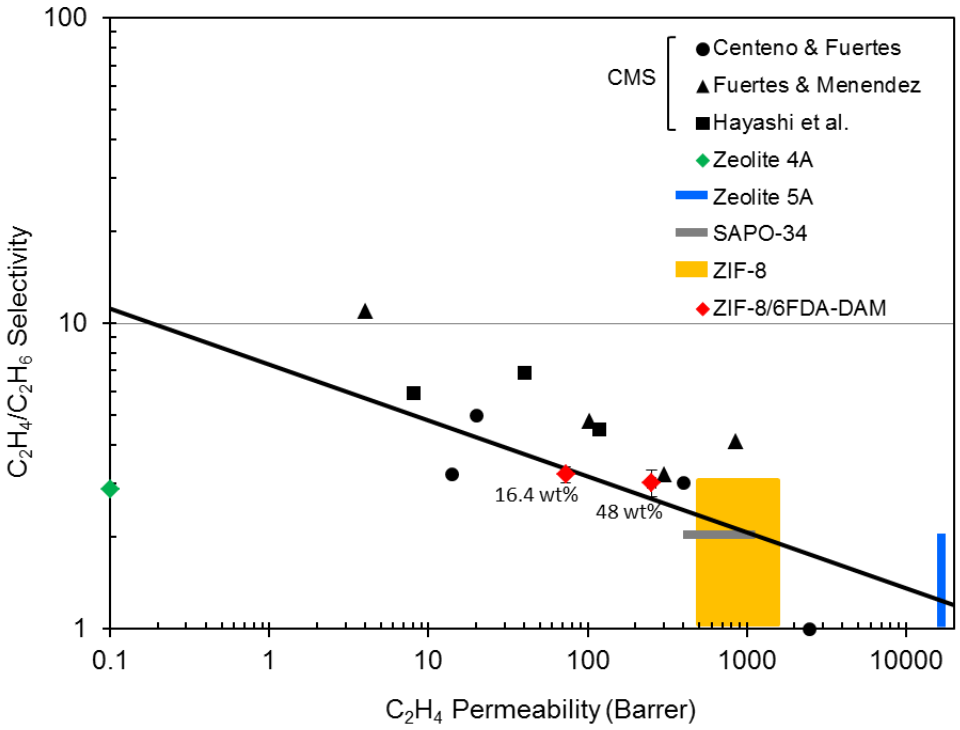

Figure 4.3: Plot showing C_2H_4/C_2H_6 separation performance of crystalline molecular sieves [46, 52, 62-64], mixed matrix membranes [51, 52] and carbon molecular sieve membranes [65-67] with respect to the polymeric C_2H_4/C_2H_6 upper bound line

4.4.2.2. Mixed Matrix Membranes

Mixed matrix membranes, which are formed by dispersing molecular sieve particles/platelets in polymer matrices, are promising approaches for gas/vapor separations that combine the ease of processing polymers with the superior separation performance of molecular sieves [68]. Figure 4.3 shows C_2H_4/C_2H_6 separation performance of mixed matrix membranes fabricated with polyimide 6FDA-DAM and ZIF-

8, suggesting that attractive C_2H_4/C_2H_6 selectivity cannot be achieved with this platform. Maxwell model calculations showed that the C_2H_4/C_2H_6 permselectivity in ZIF-8 is fairly poor [52], which is generally consistent with permeation results of pure ZIF-8 membranes noted previously. Similarly unfavorable selectivities were also seen from mixed matrix membranes prepared with ZIF-8 and poly (1,4-phenylene ether-ether-sulfone) [69]. Apparently, attractive C_2H_4/C_2H_6 selectivity thus cannot be obtained using the mixed matrix approach unless a highly selective molecular sieving material can be identified. Additionally, mixed matrix membrane fabrication poses challenges relating to adhesion at the polymer-sieve interface, which may make it hard to fabricate a sufficiently coherent and defect-free membrane.

4.4.2.3.Carbon Molecular Sieve Membranes

CMS membranes have shown the potential to outperform the polymeric upper bound for gas pairs such as O_2/N_2, CO_2/CH_4 and even C_3H_6/C_3H_8 [43, 70-72]. As described in Chapter 2, the structure of CMS membranes is visualized to be made up of disorder sp^2-hybridized condensed hexagonal graphite-like sheets with pores formed from packing imperfections. They are amorphous materials with so-called 'slit-like' pores [73], and the ideal pore structure of such materials can be described as a combination of larger micropores (~ 6-20 Å) connected by smaller ultramicropores (< 6 Å), resulting in a bimodal pore size distribution. The ultramicropores in CMS membranes can discriminate between molecules of different size and shape allowing molecular sieving separation of penetrant molecules, and can be imagined to be analogous to the limiting dimension of a zeolite cage window [18, 74-76]. However, zeolites are crystalline materials consisting of a 3-D framework of $[SiO4]^{-4}$ and $[AlO4]^{-5}$ tetrahedra linked to form ordered structures of rings and cages with uniform, well-defined dimensions [73, 77]. CMS membranes, on the

other hand, are amorphous materials with a distribution of pore sizes that may be tuned by varying parameters such as the starting polymer precursor, pyrolysis conditions etc. [3, 18]. Figure 4.4 shows a schematic representation of the structures and pore size distribution in zeolite 4A and CMS materials.

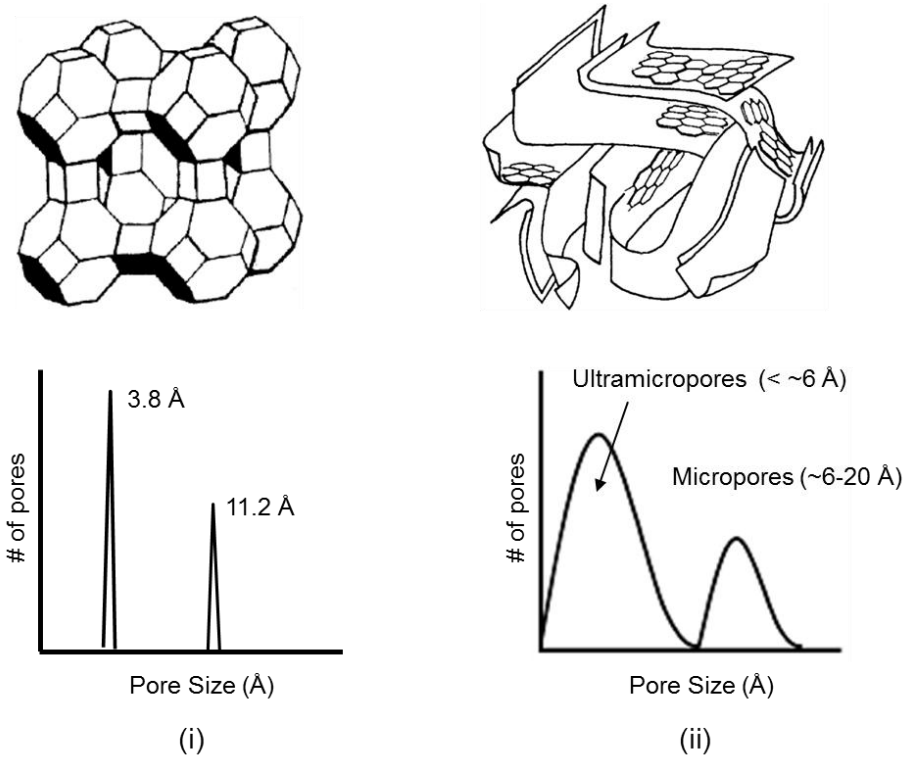

Figure 4.4: Schematic of the structure and pore size distribution of (i) Zeolite 4A [77] and (ii) CMS membrane [73, 78]

An important feature distinguishing CMS from zeolites is that while zeolites and zeolite-like materials have a pore opening with a 2-D size restriction, the pore structure of CMS membranes is "slit-like" [73] with a pore opening having a 1-D size restriction. This allows CMS membranes a unique advantage in separating C_2H_4 from C_2H_6. C_2H_4 has a somewhat planar molecular configuration while C_2H_6 is bulkier in shape. The rigid

"sit-like" CMS pores can very effectively discriminate between the subtle shape and configurational differences of C_2H_4 and C_2H_6, thus enabling easy passage of the "slimmer" C_2H_4 while hindering several degrees of rotational freedom of the bulkier C_2H_6. The zeolite pore opening cannot take advantage of the planar configuration of C_2H_4. From this perspective, CMS membranes should be somewhat theoretically ideal for C_2H_4/C_2H_6 separations. Figure 4.5 illustrates this concept. Chapter 6 discusses in detail aspects of the configurational advantage allowed by CMS membranes for separation of C_2H_4 over C_2H_6.

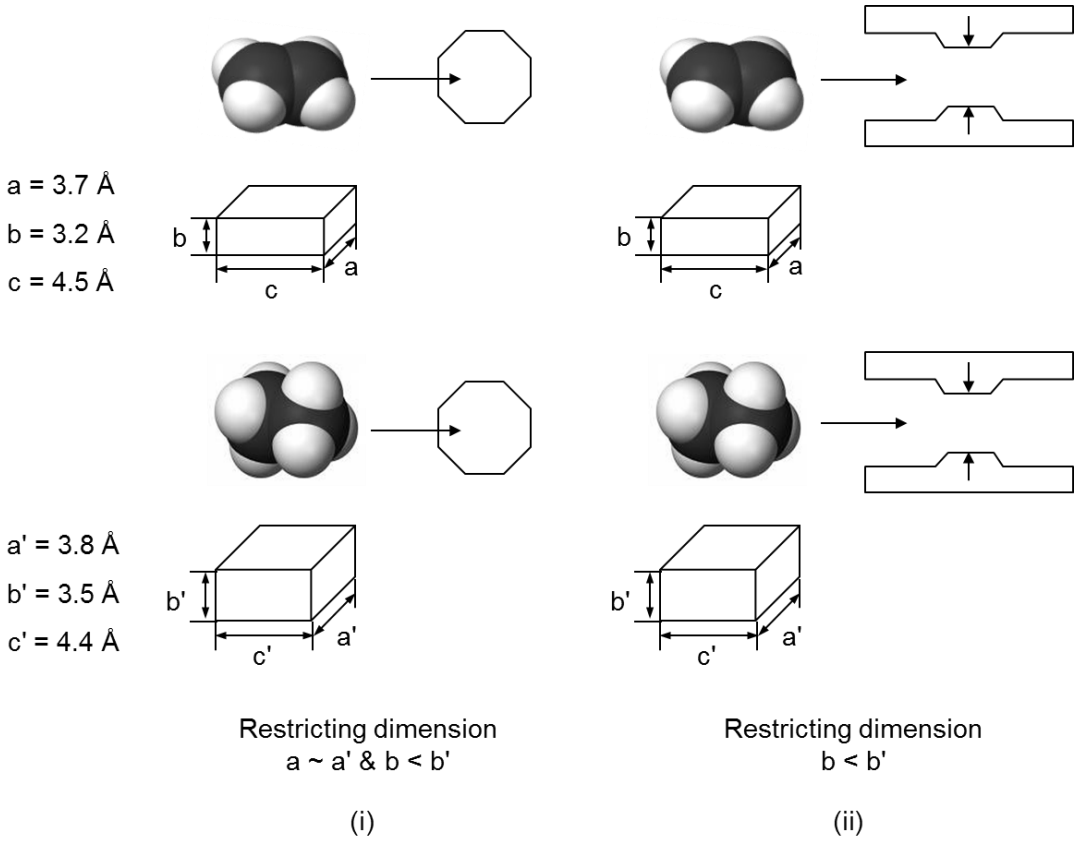

Figure 4.5: Illustration of the concept of the restricting dimensions for C_2H_4 and C_2H_6 in transport through (i) zeolites and (ii) CMS membranes. The dimensions of C_2H_4 and C_2H_6 were obtained using space filling CPK models. In a zeolite pore opening, the restricting dimensions for C_2H_4 and C_2H_6 transport are both a~a' and b<b', such that the limiting dimension (a and a') has 0.1 Å difference. For CMS membranes, the limiting dimension for C_2H_4 and C_2H_6 in the "slit-like" pore opening is b<b', which has a 0.3 Å difference allowing greater diffusive advantage

C_2H_4/C_2H_6 separation using carbon molecular sieve (CMS) membranes has been studied by few researchers [66, 67, 79-82]. Fuertes & Menendez [66] prepared carbon membranes by carbonization (vacuum, 700°C) of a thin phenolic resin film deposited on the inner surface of an alumina tube support. They studied the effect of pre-oxidation and post-oxidation in air on the separation characteristics of their membranes. In some cases, their carbon membranes were modified by chemical vapor deposition (CVD) before or after air-oxidation. Their membranes show C_2H_4/C_2H_6 selectivity in the range of 1-11 depending on the treatment conditions. Similarly, Centeno & Fuertes [79] also fabricated CMS membranes by carbonizing a thin phenolic resin film deposited on the inner face of a ceramic tube. They studied the effect of varying different pyrolysis conditions such as the pyrolysis temperature, ramp rate, soak time and the pyrolysis atmosphere on their membranes. The C_2H_4/C_2H_6 selectivity they reported ranges from 0.97 (reverse selective) to ~5. Hayashi et al. [67] prepared CMS membranes by carbonizing a BPDA-pp'ODA polyimide film formed on the outer surface of a porous alumina support in an inert argon stream at 700°C. Their membranes show C_2H_4/C_2H_6 selectivity between 4.4-6.9 depending on the number of coatings and the testing temperature. Okamoto et al. [80] prepared carbonized hollow fiber membranes by pre-oxidation and subsequent pyrolysis of a BPDA-based asymmetric hollow fiber precursor at temperatures of 500-700°C under nitrogen. Their membranes were studied primarily for C_3H_6/C_3H_8 and 1,3-butadiene/n-butane separation and showed a low C_2H_4/C_2H_6 selectivity of 3.1 with 600°C pyrolysis. The C_2H_4/C_2H_6 selectivity reported by Suda & Haraya [81] for CMS dense films fabricated via pyrolysis of polyimide Kapton at 1000°C under vacuum and further calcination at 400°C is ~5. The CMS C_2H_4/C_2H_6 separation performance from literature is shown against the polymeric upper bound in Figure 4.3. Clearly CMS membranes show that ability to outperform the polymeric upper bound.

4.5. Preliminary Investigation of Carbon Molecular Sieve Dense Film Membranes for Ethylene/Ethane Separation

As discussed in the previous section, few researchers have investigated C_2H_4/C_2H_6 separation using CMS membranes, and generally the membranes were not specifically developed for C_2H_4/C_2H_6 separation. Additionally, the drawback for the carbon membranes reviewed above is that in most cases the CMS membrane fabrication either involved multiple processing steps which adds to complication and cost, or were formed on supports which could not only be expensive but may also involve issues such as not being able to coherently fabricate a thin, defect free CMS membrane. One of the main goals of this study is to establish a basis for guiding research aimed at providing a convenient, potentially scalable hollow fiber membrane formation technology for C_2H_4/C_2H_6. Hence the focus is on developing free standing homogeneous dense films for fundamental analysis, with a method for optimizing performance based on tuning the pyrolysis parameters, without any additional steps. It is thus useful to carry out a preliminary investigation of the chosen precursors, Matrimid®, 6FDA-DAM and 6FDA:BPDA-DAM, in developing CMS dense films for C_2H_4/C_2H_6 separation.

For this preliminary investigation, the pyrolysis conditions were chosen based on literature [3, 73, 83]. CMS dense films were fabricated from all three precursors at final pyrolysis temperatures of 550°C and 800°C under vacuum pyrolysis conditions. Protocol 1 was used for pyrolysis at 550°C and Protocol 2 was used for 800°C pyrolysis. A description of the pyrolysis protocols can be found in Section 3.3.2. The resultant CMS films were tested for pure gas C_2H_4 and C_2H_6 permeation at 35°C using 50 psia feed pressure. Table 4.8 summarizes the C_2H_4/C_2H_6 separation performance for the

fabricated CMS membranes. Recall that P1, P2 and P3 stand for the precursors Matrimid®, 6FDA-DAM and 6FDA:BPDA-DAM respectively. The CMS membranes are designated based on the starting precursor, final pyrolysis temperature, pyrolysis protocol and the pyrolysis atmosphere (refer to Section 3.3.2 for nomenclature). The results for both the precursor (Table 4.2) and CMS dense films from vacuum pyrolysis (Table 4.9) are plotted against the upper bound as shown in Figure 4.6.

Table 4.9: Pure gas C_2H_4/C_2H_6 transport properties of CMS dense films fabricated from vacuum pyrolysis for preliminary analysis (35°C, 50 psia)

Precursor	CMS	P_{C2H4} Barrer	P_{C2H4}/P_{C2H6}
Matrimid®	P1-550°C-CMS_Vacuum	14.8	6.6
	P1-800°C_slow-CMS_Vacuum	~ 0.2	~ 12
6FDA-DAM	P2-550°C-CMS_Vacuum	1.5	1.1
	P1-800°C_slow-CMS_Vacuum	3	6.8
6FDA:BPDA-DAM	P3-550°C-CMS_Vacuum	15.1	4.7
	P1-800°C_slow-CMS_Vacuum	2.1	6.9

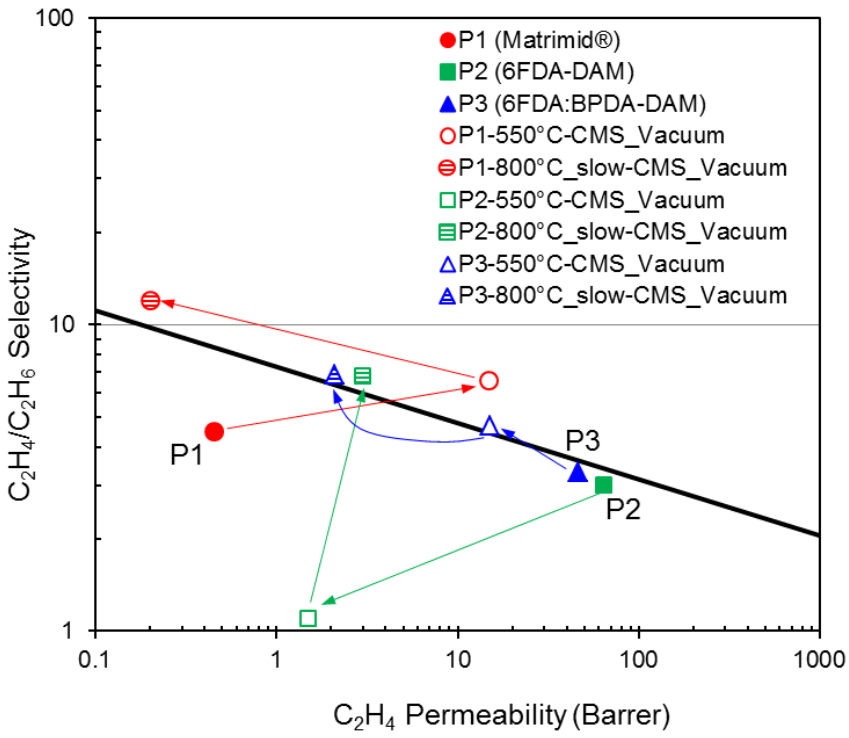

Figure 4.6: Pure gas C_2H_4/C_2H_6 transport performance of precursor and CMS dense films from vacuum pyrolysis shown again the upper bound line (35°C, 50 psia)

Clearly, Matrimid® (P1) CMS dense films from both 550°C and 800°C vacuum pyrolysis surpass the upper bound line. There is however a significant trade-off between the C_2H_4 permeability and C_2H_4/C_2H_6 selectivity with the pyrolysis temperature. The C_2H_4 permeability for P1-550°C-CMS_Vacuum represents a >3000% (i.e. over 30 times) increase from the precursor permeability, while the selectivity increase is ~47%. For the same pyrolysis conditions, Steel [73] reported a CO_2/CH_4 selectivity of 65, which represents ~100% increase from the precursor selectivity reported in their study. The C_2H_4/C_2H_6 selectivity at 550°C obtained in our study is however not significantly higher compared to the starting polymer, nor is it much higher than that reported by previous researchers [66, 67, 80]. P1-800°C_slow-CMS_Vacuum on the other hand can give C_2H_4/C_2H_6 selectivity as high as 12, a ~167% increase from the precursor material, and

is the highest C_2H_4/C_2H_6 selectivity reported so far. However, the corresponding C_2H_4 permeability is extremely low and drops to < 0.2 Barrer, which may not be practical for commercial applications. Again, in the case of CO_2/CH_4 separation, the CO_2 permeability for Matrimid® pyrolyzed at 800°C under vacuum still remained quite high (66 Barrer) along with an exceptionally high CO_2/CH_4 selectivity of 209 [73], Thus, while the preliminary analysis demonstrates the C_2H_4/C_2H_6 separation potential for CMS derived from Matrimid®, the pyrolysis conditions that were chosen directly from Steel's study [73] are clearly not optimum for C_2H_4/C_2H_6 separation. Such optimization is a key focus for Objective 2 of this study and will be discussed in detail in Chapter 5.

For CMS membranes derived from vacuum pyrolysis of the 6FDA-based polymer precursors, the results obtained were quite unexpected. For 6FDA-DAM pyrolyzed at 550°C, the performance drops below that of the precursor and lies well below the polymeric upper bound. For 800°C vacuum pyrolysis the 6FDA-DAM based CMS can just surpass the upper bound; however, both the permeability and selectivity are not quite promising. Similarly, for CMS derived from 6FDA:BPDA-DAM, the performance lies right at the upper bound line for both 550°C and 800°C vacuum pyrolysis. These results were rather surprising since, given the higher intrinsic permeability of the starting polymer, the permeabilities of 6FDA-based CMS were expected to be much higher. This unusual behavior could be an outcome of the combined effects of the polymer precursor, the pyrolysis conditions as well as the gas pair in consideration, which can be extremely complicated. Deconvoluting these effects and developing fundamental understanding of the effects of different parameters on C_2H_4/C_2H_6 separation performance is thus critical, and will be discussed in detail in Chapter 5.

4.6. Challenges in Carbon Molecular Sieve Dense Film Formation

Production of "testable" (suitable for permeation measurements) CMS dense films can be challenging. Since CMS films are brittle compared to polymer films, it is important to get CMS films that can be handled and masked appropriately for permeation measurements (See Section 3.4.1 for details). Several factors have been identified as being responsible in the formation of testable CMS dense films. Before discussing these factors, it is useful to describe the various different types of films that can result from precursor film pyrolysis. For convenience, the resultant CMS films can be categorized into four types: (i) flat films (testable), (ii) slightly curled (bent) films (testable) (iii) over-curled films (not testable) and (iv) crinkled (wavy) films (not testable), shown in Figure 4.7.

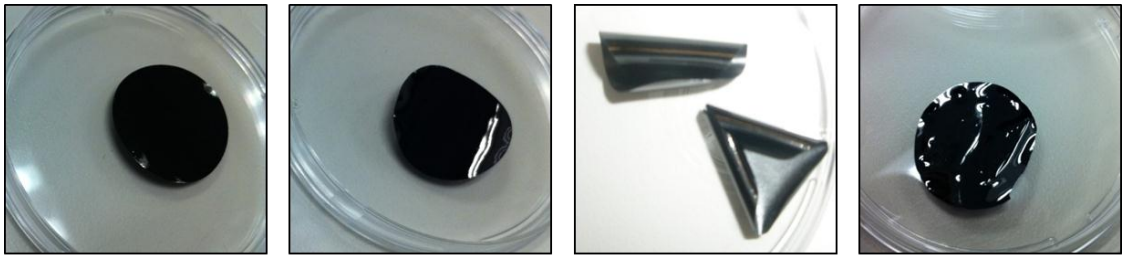

(i) (ii) (iii) (iv)

Figure 4.7: Different types of CMS films formed as a result of pyrolysis (i) flat film, (ii) slightly curled film, (iii) over-curled film, (iv) crinkled film.

Flat films can easily be masked for permeation. Slightly curled films generally resulted from pyrolysis under inert gas (argon) atmosphere. Such films are sufficiently flexible to be masked for permeation with a >95% success rate. Over-curled films and

crinkled films are impossible to mask and invariably break. The detailed cause in terms of pyrolysis conditions for these different types of films is not yet well understood, but with experience the first two types (i & ii) can be created and tested relatively easily. Several factors have been identified as being responsible for causing curling and crinkling of CMS films.

A primary reason for production of crinkled or over-curled films is believed to be stress present on the precursor films prior to pyrolysis, which can result due to several factors. The casting technique for precursor films is extremely important. A Teflon disc is preferred as the casting substrate for solution casting of precursor films, as opposed to so-called “ring casting” on a glass surface using a metal ring. Casting on a Teflon disc minimized inherent stress on the resulting precursor film by preventing adhesion of the final vitrified polymer films to the surface of the substrate. In addition, it is important to maintain a very slow evaporation rate during the casting process to minimize resultant stress on the precursor films due to vitrification. Precursor films cast on Teflon resulted in >90% success rate in formation of testable CMS dense films while ring-casting on a glass surface resulted in crinkled or over-curled films in most cases. It was also found that using thicker precursor dense films resulted in less curling of films due to pyrolysis. Lastly, cutting of precursor films into small circles for pyrolysis can also result in stresses. In order to avoid this, films were cut using a sharp die-cutter by hitting uniformly with one single blow of a hammer. This results in distribution of the stress on the unwanted area around the desired circle. On some occasions, scissors were used to detach the circular film at points that were not cut using the die-cutter.

The nature of the support used for pyrolysis is also important. Pyrolysis over a wire mesh support results in CMS films bearing impressions of the wire mesh with stress points at which they tend to crack easily. A solid quartz support results in over-curled films presumably because of hindered transfer of the pyrolysis by-products. A ribbed or

channeled quartz plate, on the other hand, may allow for free diffusion of the pyrolysis by-products thus resulting in testable CMS film formation. This study thus uses a custom made channeled quartz plate (Figure 3.5) for the production of CMS dense films for C_2H_4/C_2H_6 separation. It has also been found that use of the same quartz support and quartz tube over an extended period of time eventually tends to create crinkled CMS films. After repeated burn out in air, the ribbed quartz plate and quartz tube eventually show signs of erosion with a somewhat roughened surface, and this presumably causes the odd crinkling effect.

The starting precursor plays an important role in the type of CMS film resulting from pyrolysis. For example, Matrimid® requires greater care in handling compared to 6FDA-DAM and 6FDA:BPDA-DAM in order to obtain testable CMS films. Experiments were conducted to remove residual stresses on Matrimid® precursor films prior to pyrolysis by soaking the polymer films just below as well as at the glass transition temperature (305°C) of Matrimid® for 2 hours. This however did not significantly affect the resultant CMS dense films. We believe that differences in the chemical structure and nature of the precursors largely affect the morphology of the CMS membranes. For example, Matrimid® pyrolysis results in evolution of tan colored by-products that stain the quartz tube as well as large amounts of carbon deposits that leave the quartz plate "black" at the end of pyrolysis. The 6FDA-based polymers however when pyrolyzed do not result in colored by-products and seem to have a self-cleaning effect on both the quartz tube and plate, perhaps due to trace HF evolution during pyrolysis. In addition, the glass transition temperature and storage modulus of the polymers are also important in maintaining morphology of CMS membranes, especially in the hollow fiber configuration. Some of these details will be discussed in Chapter 5.

4.7. Summary

Three polymer precursors Matrimid®, 6FDA-DAM and 6FDA:BPDA-DAM were chosen as precursors to CMS membranes for C_2H_4/C_2H_6 separation. The intrinsic properties of the polymers were evaluated as well as the polymeric C_2H_4/C_2H_6 upper bound line was established as a basis against which to compare CMS performance. Further, preliminary fabrication of CMS membranes from all three precursors was considered using pyrolysis conditions chosen from literature. While this preliminary investigation demonstrated the viability of the precursors in forming CMS membranes capable of C_2H_4/C_2H_6 separation, it clearly illustrates that the "one size fits all" strategy cannot be applied to CMS fabrication. Detailed investigation and fundamental understanding of the effects of various pyrolysis parameters on the CMS morphology and the resulting C_2H_4/C_2H_6 separation performance is critical. Individual optimization of CMS derived from different precursor materials must be considered. This forms the basis for Objective 2 of this thesis which is discussed in Chapter 5.

4.8. References

[1] Guiver MD, Robertson GP, Dai Y, Bilodeau F, Kang YS, Lee KJ, et al. Structural characterization and gas-transport properties of brominated matrimid polyimide. J Polym Sci Pol Chem. 2002;40(23):4193-204.

[2] Kim JH, Koros WJ, Paul DR. Physical aging of thin 6FDA-based polyimide membranes containing carboxyl acid groups. Part I. Transport properties. Polymer. 2006;47(9):3094-103.

[3] Williams PJ. Analysis of factors influencing the performance of CMS membranes for gas separation. Georgia Institute of Technology, Doctor of Philosophy, 2006.

[4] Robeson LM. Correlation of separation factor versus permeability for polymeric membranes. J Membrane Sci. 1991;62(2):165-85.

[5] Robeson LM. The upper bound revisited. J Membrane Sci. 2008;320(1-2):390-400.

[6] Freeman BD. Basis of permeability/selectivity tradeoff relations in polymeric gas separation membranes. Macromolecules. 1999;32(2):375-80.

[7] Haraya K, Obata K, Itoh N, Shndo Y, Hakuta T, Yoshitome H. Gas permeation and separation by an asymmetric polyimide hollow fiber membrane. J Membrane Sci. 1989;41:23-35.

[8] Barrer RM. Activated diffusion in membranes. T Faraday Soc. 1939;35(1):0644-55.

[9] van Amerongen GJ. The permeability of different rubbers to gases and Its relation to diffusivity and solubility. J Appl Phys. 1946;17(11):972-85.

[10] Barrer RM, Skirrow G. Transport and equilibrium phenomena in gas elastomer systems .1. Kinetic phenomena. J Polym Sci. 1948;3(4):549-63.

[11] van Krevelen DW. Properties of polymers. 3 ed: Elsevier Science; 1997.

[12] Burns RL, Koros WJ. Defining the challenges for C3H6/C3H8 separation using polymeric membranes. J Membrane Sci. 2003;211(2):299-309.

[13] Chan SS, Wang R, Chung TS, Liu Y. C-2 and C-3 hydrocarbon separations in poly(1,5-naphthalene-2,2 '-bis(3,4-phthalic) hexafluoropropane) diimide (6FDA-1,5-NDA) dense membranes. J Membrane Sci. 2002;210(1):55-64.

[14] Chan SS, Chung T-S, Liu Y, Wang R. Gas and hydrocarbon (C2 and C3) transport properties of co-polyimides synthesized from 6FDA and 1,5-NDA (naphthalene)/Durene diamines. J Membr Sci. 2003;218(1-2):235-45.

[15] Tanaka K, Taguchi A, Hao J, Kita H, Okamoto K. Permeation and separation properties of polyimide membranes to olefins and paraffins. J Membr Sci. 1996;121(2):197-207.

[16] Staudt-Bickel C, Koros WJ. Olefin/paraffin gas separations with 6FDA-based polyimide membranes. J Membrane Sci. 2000;170(2):205-14.

[17] Semenova SI. Polymer membranes for hydrocarbon separation and removal. J Membrane Sci. 2004;231(1-2):189-207.

[18] Rungta M, Xu L, Koros WJ. Carbon molecular sieve dense film membranes derived from Matrimid (R) for ethylene/ethane separation. Carbon. 2012;50(4):1488-502.

[19] Ilinitch OM, Semin GL, Chertova MV, Zamaraev KI. Novel polymeric membranes for separation of hydrocarbons. J Membrane Sci. 1992;66(1):1-8.

[20] Ilinich OM, Zamaraev KI. Separation of ethylene and ethane over polyphenyleneoxides membranes: transient increase of selectivity. J Membrane Sci. 1993;82(1-2):149-55.

[21] Teplyakov V, Meares P. Correlation aspects of the selective gas permeabilities of polymeric materials and membranes. Gas Separation & Purification. 1990;4(2):66-74.

[22] Breck DW. Zeolite molecular sieves. New York: John Wiley & Sons; 1974.

[23] Reid C, Sherwood TK. The properties of gases and liquids: their estimation and correlation. New York: Mcgraw-hill; 1976.

[24] Hirschfelder, Oakland K. Molecular theory of gases and liquids. New York: Wiley Interscience; 1964.

[25] Petropolous JH. Mechanisms and theories for sorption and diffusion of gases in polymers. In: Paul DR, Yampol'skii YP, eds. Polymeric gas separation membranes. Boca Raton: CRC Press 1994.

[26] Koros WJ, Paul DR, Huvard GS. Energetics of gas sorption in glassy-polymers. Polymer. 1979;20(8):956-60.

[27] Brandt WW. Model calculation of the temperature dependence of small molecule diffusion in high polymers. J Phys Chem-Us. 1959;63(7):1080-4.

[28] Merkel T, Blanc R, Zeid J, Suwarlim A, Firat B, Wijmans S, et al. Separation of olefin/paraffin mixtures with carrier facilitated membranes: U.S. Department of Energy; 2007.

[29] Faiz R, Li K. Olefin/paraffin separation using membrane based facilitated transport/chemical absorption techniques. Chem Eng Sci. 2012;73:261-84.

[30] Eldridge RB. Olefin paraffin separation technology - A review. Ind Eng Chem Res. 1993;32(10):2208-12.

[31] Ho WS, Dalrymple DC. Facilitated transport of olefins in Ag+-containing polymer membranes. J Membrane Sci. 1994;91(1-2):13-25.

[32] Ho WSW, Doyle G, Savage DW, Pruett RL. Olefin separations via complexation with cuprous diketonate. Ind Eng Chem Res. 1988;27(2):334-7.

[33] Pinnau I, Toy LG. Solid polymer electrolyte composite membranes for olefin/paraffin separation. J Membrane Sci. 2001;184(1):39-48.

[34] Azhin M, Kaghazchi T, Rahmani M. A review on olefin/paraffin separation using reversible chemical complexation technology. J Ind Eng Chem. 2008;14(5):622-38.

[35] Teramoto M, Matsuyama H, Yamashiro T, Katayama Y. Separation of ethylene from ethane by supported liquid membranes containing silver-nitrate as a carrier. J Chem Eng Jpn. 1986;19(5):419-24.

[36] Eriksen OI, Aksnes E, Dahl IM. Facilitated transport of ethene through Nafion membranes .1. Water Swollen Membranes. J Membrane Sci. 1993;85(1):89-97.

[37] Tsou DT, Blachman MW, Davis JC. Silver-facilitated olefin/paraffin separation in a liquid membrane contactor system. Ind Eng Chem Res. 1994;33(12):3209-16.

[38] Bessarabov DG, Sanderson RD, Jacobs EP, Beckman IN. High-efficiency separation of an ethylene ethane mixture by a large-scale liquid-membrane contactor containing flat-sheet nonporous polymeric gas-separation membranes and a selective flowing-liquid absorbent. Ind Eng Chem Res. 1995;34(5):1769-78.

[39] Teramoto M, Matsuyama H, Yamashiro T, Okamoto S. Separation of ethylene from ethane by a flowing liquid membrane using silver-nitrate as a carrier. J Membrane Sci. 1989;45(1-2):115-36.

[40] Nymeijer K, Visser T, Assen R, Wessling M. Super selective membranes in gas-liquid membrane contactors for olefin/paraffin separation. J Membrane Sci. 2004;232(1-2):107-14.

[41] Ryu JH, Lee H, Kim YJ, Kang YS, Kim HS. Facilitated olefin transport by reversible olefin coordination to silver ions in a dry cellulose acetate membrane. Chem-Eur J. 2001;7(7):1525-9.

[42] Kim HS, Ryu JH, Kim H, Ahn BS, Kang YS. Reversible olefin complexation by silver ions in dry poly(vinyl methyl ketone) membrane and its application to olefin/paraffin separations. Chem Commun. 2000(14):1261-2.

[43] Singh A, Koros WJ. Significance of entropic selectivity for advanced gas separation membranes. Ind Eng Chem Res. 1996;35(4):1231-4.

[44] Ruthven DM. Molecular sieve separations. Chem-Ing-Tech. 2011;83(1-2):44-52.

[45] Agarwal K, John M, Pai S, Newalkar BL, Bhargava R, Choudary NV. SAPO-34 assisted C3 separation: Modeling and simulation. Micropor Mesopor Mat. 2010;132(3):311-8.

[46] Ruthven DM, Reyes SC. Adsorptive separation of light olefins from paraffins. Microporous Mesoporous Mat. 2007;104(1-3):59-66.

[47] Karger J, Ruthven DM. Diffusion in zeolites and other microporous solids.: John Wiley & Sons, Inc.; 1991.

[48] Bloch ED, Queen WL, Krishna R, Zadrozny JM, Brown CM, Long JR. Hydrocarbon separations in a metal-organic framework with open iron(II) coordination sites. Science. 2012;335(Copyright (C) 2012 American Chemical Society (ACS). All Rights Reserved.):1606-10.

[49] Yang RT. Adsorbents: Fundamentals and applications: John Wiley & Sons, Inc.; 2003.

[50] Li K, Olson DH, Seidel J, Emge TJ, Gong H, Zeng H, et al. Zeolitic imidazolate frameworks for kinetic separation of propane and propene. J Am Chem Soc. 2009;131(30):10368-9.

[51] Zhang C, Dai Y, Johnson JR, Karvan O, Koros WJ. High performance ZIF-8/6FDA-DAM mixed matrix membrane for propylene/propane separations. J Membr Sci. 2012;389:34-42.

[52] Zhang C, Lively RP, Zhang K, Johnson JR, Karvan O, Koros WJ. Unexpected molecular sieving properties of zeolitic imidazolate framework-8. The Journal of Physical Chemistry Letters. 2012:2130-4.

[53] Bae T-H, Lee JS, Qiu W, Koros WJ, Jones CW, Nair S. A high-performance gas-separation membrane containing submicrometer-sized metal-organic framework crystals. Angew Chem, Int Ed. 2010;49(Copyright (C) 2012 American Chemical Society (ACS). All Rights Reserved.):9863-6, S/1-S/6.

[54] Dai Y, Johnson JR, Karvan O, Sholl DS, Koros WJ. Ultem®/ZIF-8 mixed matrix hollow fiber membranes for CO2/N2 separations. J Membr Sci. 2012;401–402(0):76-82.

[55] Ordonez MJC, Balkus KJ, Jr., Ferraris JP, Musselman IH. Molecular sieving realized with ZIF-8/Matrimid mixed-matrix membranes. J Membr Sci. 2010;361(Copyright (C) 2012 American Chemical Society (ACS). All Rights Reserved.):28-37.

[56] Pan Y, Lai Z. Sharp separation of C2/C3 hydrocarbon mixtures by zeolitic imidazolate framework-8 (ZIF-8) membranes synthesized in aqueous solutions. Chem Commun. 2011;47(37):10275.

[57] Gücüyener C, van den Bergh J, Gascon J, Kapteijn F. Ethane/ethene separation turned on its head: Selective ethane adsorption on the metal−organic framework ZIF-7 through a gate-opening mechanism. J Am Chem Soc. 2010;132(50):17704-6.

[58] Chmelik C, Freude D, Bux H, Haase J. Ethene/ethane mixture diffusion in the MOF sieve ZIF-8 studied by MAS PFG NMR diffusometry. Microporous Mesoporous Mater. 2011;147(Copyright (C) 2012 American Chemical Society (ACS). All Rights Reserved.):135-41.

[59] Bux H, Chmelik C, van Baten JM, Krishna R, Caro J. Novel MOF-membrane for molecular sieving predicted by IR-diffusion studies and molecular modeling. Adv Mater. 2010;22(42):4741-3.

[60] Bux H, Chmelik C, Krishna R, Caro J. Ethene/ethane separation by the MOF membrane ZIF-8: Molecular correlation of permeation, adsorption, diffusion. J Membr Sci. 2011;369(1-2):284-9.

[61] Chmelik C, Bux H, Voss H, Caro J. Adsorption and diffusion - Basis for molecular understanding of permeation through molecular sieve membranes. Chem-Ing-Tech. 2011;83(1-2):104-12.

[62] Olson DH, Camblor MA, Villaescusa LA, Kuehl GH. Light hydrocarbon sorption properties of pure silica Si-CHA and ITQ-3 and high silica ZSM-58. Micropor Mesopor Mat. 2004;67(1):27-33.

[63] Dai W, Scheibe M, Li L, Guan N, Hunger M. Effect of the methanol-to-olefin conversion on the PFG NMR self-diffusivities of ethane and ethene in large-crystalline SAPO-34. Journal of Physical Chemistry C. 2011;116(3):2469–76.

[64] Romero-Perez A, Aguilar-Armenta G. Adsorption kinetics and equilibria of carbon dioxide, ethylene, and ethane on 4A(CECA) zeolite. J Chem Eng Data. 2010;55(9):3625-30.

[65] Centeno TA, Fuertes AB. Supported carbon molecular sieve membranes based on a phenolic resin. J Membrane Sci. 1999;160(2):201-11.

[66] Fuertes AB, Menendez I. Separation of hydrocarbon gas mixtures using phenolic resin-based carbon membranes. Sep Purif Technol. 2002;28(1):29-41.

[67] Hayashi J, Mizuta H, Yamamoto M, Kusakabe K, Morooka S, Suh SH. Separation of ethane/ethylene and propane/propylene systems with a carbonized BPDA-pp'ODA polyimide membrane. Ind Eng Chem Res. 1996;35(11):4176-81.

[68] Moore TT, Mahajan R, Vu DQ, Koros WJ. Hybrid membrane materials comprising organic polymers with rigid dispersed phases. AIChE J. 2004;50(Copyright (C) 2012 American Chemical Society (ACS). All Rights Reserved.):311-21.

[69] Díaz K, López-González M, del Castillo LF, Riande E. Effect of zeolitic imidazolate frameworks on the gas transport performance of ZIF8-poly(1,4-

phenylene ether-ether-sulfone) hybrid membranes. Journal of Membrane Science. 2011;383(1–2):206-13.

[70] Steel KM, Koros WJ. An investigation of the effects of pyrolysis parameters on gas separation properties of carbon materials. Carbon. 2005;43(9):1843-56.

[71] Kiyono M, Williams PJ, Koros WJ. Effect of pyrolysis atmosphere on separation performance of carbon molecular sieve membranes. J Membrane Sci. 2010;359(1-2):2-10.

[72] Singh-Ghosal A, Koros WJ. Air separation properties of flat sheet homogeneous pyrolytic carbon membranes. J Membrane Sci. 2000;174(2):177-88.

[73] Steel KM. Carbon membranes for challenging gas separations. The University of Texas at Austin, Doctor of Philosophy, 2000.

[74] Marsh H. Introduction to carbon science: Butterworths; 1989.

[75] Jenkins GM, Kawamura K. Polymeric carbons - Carbon fiber, glass and char. London: Cambridge University Press 1976.

[76] Pierson. Handbook of carbon, graphite, diamond, and fullerenes NY: Noyes Publication 1993.

[77] Vu DQ. Formation and characterization of asymmetric carbon molecular sieve and mixed matrix membranes for natural gas purification. The University of Texas at Austin, Doctor of Philosophy, 2001.

[78] Stoeckli HF. Microporous carbons and their characterization: The present state of the art. Carbon. 1990;28(1):1-6.

[79] Centeno TA, Vilas JL, Fuertes AB. Effects of phenolic resin pyrolysis conditions on carbon membrane performance for gas separation. J Membrane Sci. 2004;228(1):45-54.

[80] Okamoto K, Kawamura S, Yoshino M, Kita H, Hirayama Y, Tanihara N, et al. Olefin/paraffin separation through carbonized membranes derived from an asymmetric polyimide hollow fiber membrane. Ind Eng Chem Res. 1999;38(11):4424-32.

[81] Suda H, Haraya K. Alkene/alkane permselectivities of a carbon molecular sieve membrane. Chem Commun. 1997(1):93-4.

[82] Barsema JN, van der Vegt NFA, Koops GH, Wessling M. Carbon molecular sieve membranes prepared from porous fiber precursor. J Membrane Sci. 2002;205(1-2):239-46.

[83] Jones CW, Koros WJ. Carbon molecular-sieve gas separation membranes .1. Preparation and characterization based on polyimide precursors. Carbon. 1994;32(8):1419-25.

CHAPTER 5

ANALYSIS OF THE EFFECTS OF PYROLYSIS PARAMETERS ON THE ETHYLENE/ETHANE SEPARATION PERFORMANCE OF CARBON MOLECULAR SIEVE DENSE FILM MEMBRANES

5.1. Overview

The pore structure and separation performance of carbon molecular sieve (CMS) membranes can be tailored by controlling several parameters in the CMS fabrication process. In this study, the effects of pyrolysis parameters such as the heating protocol and pyrolysis atmosphere have been investigated. Individual optimization of the ethylene/ethane (C_2H_4/C_2H_6) separation performance for CMS derived from each precursor has been addressed. Sections 5.2, 5.4 and 5.5 discuss the effects of various pyrolysis parameters on the performance of CMS derived from Matrimid®, 6FDA-DAM and 6FDA:BPDA-DAM respectively. The discovery of the presence of a physical aging effect in CMS membranes is reported in Section 5.3. Section 5.2.5 presents a discussion of different characterization techniques used to study the nature and the pore structure of CMS membranes. A method based on different sized gas molecules as probes of the CMS pore structure was developed to characterize the critical molecular-sieving CMS ultramicropores. This, in conjunction with separation performance data, provides insights into the structure-performance relationships of the engineered CMS materials. Finally, Section 5.6 analyzes the effect of the starting polymer precursor on CMS structure and performance by comparing CMS derived from Matrimid® and 6FDA:BPDA-DAM using identical pyrolysis conditions. All measurements reported in this Chapter were carried out at 35°C.

5.2. Carbon Molecular Sieve Membranes Derived from Matrimid®

Matrimid® is a commercially available polyimide with attractive gas separation properties. It has been extensively investigated for gas separation in the polymeric membrane form in the Koros Group. Additionally it has also been investigated for fabrication of CMS for separation of O_2/N_2 and CO_2/CH_4. Preliminary investigation of Matrimid® using these past studies as a basis revealed attractive C_2H_4/C_2H_6 separation performance surpassing the polymeric upper bound line. However the CMS fabrication conditions for O_2/N_2 and CO_2/CH_4 separation were not found to be optimum for C_2H_4/C_2H_6 separation, as discussed in Chapter 4. This section investigates the effects of pyrolysis temperature, ramp rate and pyrolysis atmosphere on C_2H_4/C_2H_6 separation performance to identify a set of fabrication parameters that yield optimum performance.

5.2.1. Effect of Pyrolysis Temperature for Vacuum Pyrolysis

Matrimid® dense films were pyrolyzed under vacuum (5-10 mtorr) for a range of pyrolysis temperatures between 500-800°C, specifically at 500°C, 525°C and 550°C using Protocol 1, and 650°C, 675°C, 700°C and 800°C using the slow Protocol 2. A description of the two protocols can be found in Section 3.3.2. The CMS dense films obtained were tested for pure gas C_2H_4 and C_2H_6 permeability at 35°C using 50 psia feed pressure. The C_2H_4 permeability and the C_2H_4/C_2H_6 selectivity are shown in Figure 5.1. For all pyrolysis temperatures, the CMS membranes derived from Matrimid® can surpass the polymeric C_2H_4/C_2H_6 upper bound line.

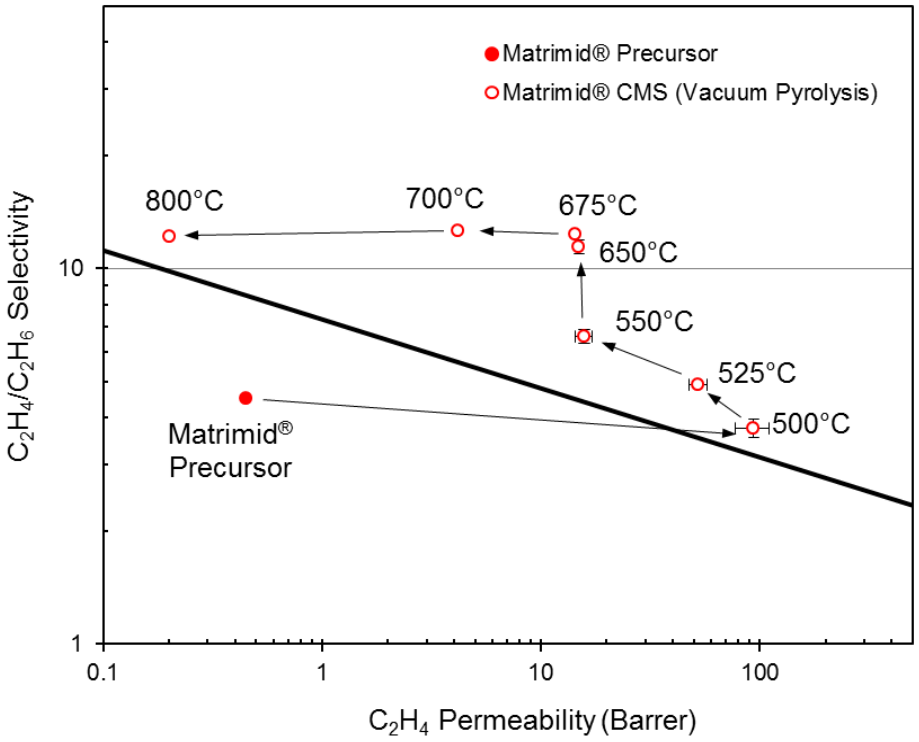

Figure 5.1: Plot showing pure gas C_2H_4/C_2H_6 separation performance (35°C, 50 psia) of CMS dense films derived from vacuum pyrolysis of Matrimid® at different pyrolysis temperature. Error bars represent standard deviations from multiple measurements

Figure 5.2 shows the C_2H_4 permeability and the C_2H_4/C_2H_6 selectivity plotted as a function of the final pyrolysis temperature. As the pyrolysis temperature increases the permeability drops drastically up to 550°C with a corresponding increase in the selectivity. From 550°C up to 675°C, the selectivity continues to increase significantly, and becomes almost two-fold, with a very small loss in the permeability. Beyond 675°C, the permeability again plummets, but there is no significant increase in the selectivity. The optimum trade-off between the C_2H_4 permeability and the C_2H_4/C_2H_6 selectivity thus apparently lies in the pyrolysis temperature range of 650-675°C.

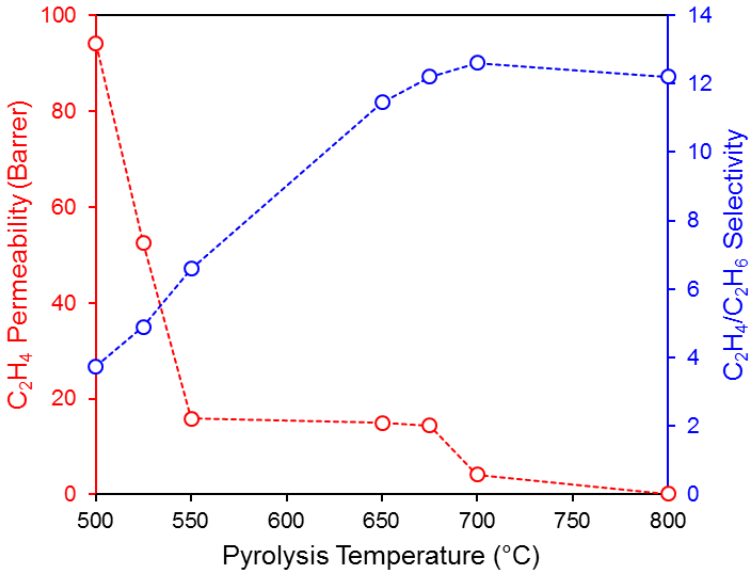

Figure 5.2: Effect of final pyrolysis temperature on C_2H_4 permeability and C_2H_4/C_2H_6 selectivity of CMS dense films derived from vacuum pyrolysis of Matrimid®

The apparent time lag information from pure gas permeation measurements was used to estimate the diffusion coefficients as described in Section 3.4.1. These were further used to calculate the average sorption coefficients. As seen from Figure 5.3(i), the C_2H_4 diffusion coefficient follows a trend similar to its permeability, decreasing with increase in the pyrolysis temperature. The sorption coefficient, as seen from Figure 5.3(ii) does not seem to follow any particular trend and direct sorption experiments may be useful for further analysis. Nevertheless, the sorption coefficients for all pyrolysis temperatures are on the same order of magnitude and quite similar, such that the impact on permeability is small compared to the effect of diffusion. The diffusion selectivity increases with pyrolysis temperature from 3-9 (Figure 5.3(i)) and remains fairly constant thereafter, following a trend similar to the overall selectivity. The sorption selectivity (plotted on the same scale as diffusion selectivity) remains in the range of 1.1-1.3 (Figure 5.3(ii)) and, relative to the diffusion selectivity, changes little with the pyrolysis temperature despite overall selectivity changes. Diffusion effects thus show a dominant

effect on the overall transport behavior of the CMS membranes, and the changes resulting from sorption are small. Since the ultramicropore windows in the CMS pore structure limit diffusion of different gases based on size and shape, these molecular sieving ultramicropores are presumably the critical features dominant in controlling the transport behavior of CMS membranes.

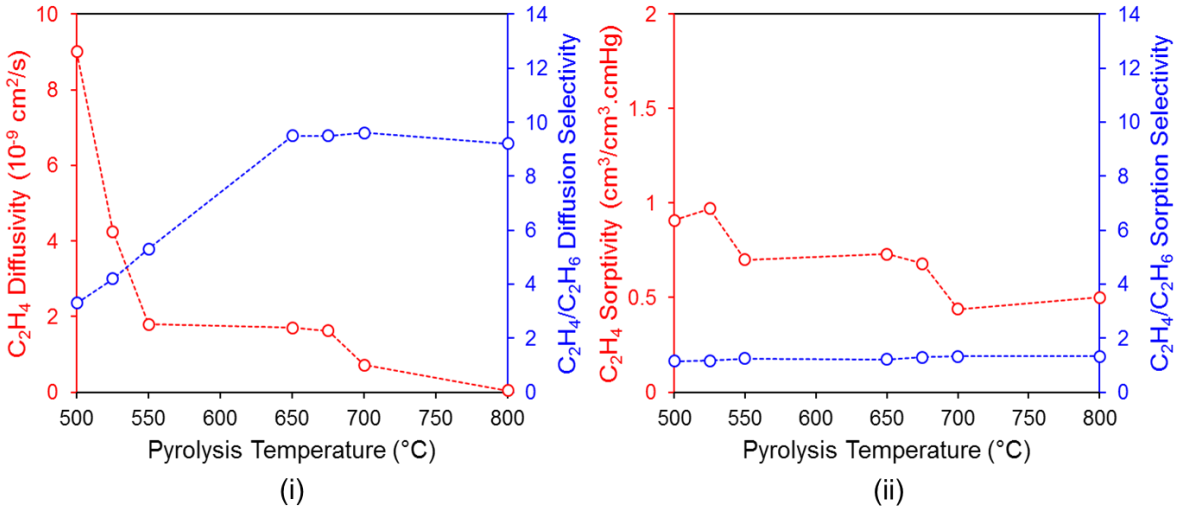

Figure 5.3: (i) C_2H_4 diffusivity and C_2H_4/C_2H_6 diffusion selectivity of CMS dense films derived from vacuum pyrolysis of Matrimid® shown as a function of the final pyrolysis temperature. Diffusion coefficients were calculated using apparent permeation time lag information. (ii) C_2H_4 sorption coefficient and C_2H_4/C_2H_6 sorption selectivity of CMS dense films derived from vacuum pyrolysis of Matrimid® shown as a function of the final pyrolysis temperature. Sorption coefficients were obtained from permeability and diffusivity calculated from permeation time lag

The effects of pyrolysis temperature on C_2H_4/C_2H_6 transport can be explained qualitatively by considering the changes in the cartoon CMS structures and hypothetical ultramicropore size distributions [1, 2]. Figure 5.4(i) shows the expected effect of increasing pyrolysis temperature on the intrinsic CMS structure. As depicted, pyrolysis at a lower pyrolysis temperature yields an "open" CMS framework which collapses at

higher pyrolysis temperatures. Figure 5.4(ii) shows a hypothetical representation of the CMS pore size distribution change with pyrolysis temperature. In Figure 5.4(ii), penetrant molecules are represented according to size along the abscissa, thereby providing an effective semi-quantitative molecular scale ruler. A given penetrant has free diffusive access to all inter-connected pores to the right of the line drawn at its characteristic size. Further, the ratio of the areas under the curve to the right of the respective line for each penetrant represents the selectivity. With an increase in pyrolysis temperature the entire CMS framework condenses, and the critical molecular sieving ultramicropore distribution is believed to shift to a smaller average pore size. This shift results in a decrease in the diffusivity, and hence overall permeability, for both C_2H_4 and C_2H_6. This decrease in permeability is however accompanied by an increase in the selectivity since, in going to a higher pyrolysis temperature (as represented by a shift from T_1 to T_2 in Figure 5.4) a relatively larger number of pores still remain accessible to the somewhat planar C_2H_4 molecule but not to the bulkier C_2H_6 molecule. There is however a limit to such increase in selectivity with pyrolysis temperature (represented from a shit from T_2 to T_3 in Figure 5.4), as for the 800°C pyrolysis, when most of the pores may become blocked to both C_2H_4 and C_2H_6, resulting in a drastic loss in permeability with no significant improvement in the selectivity.

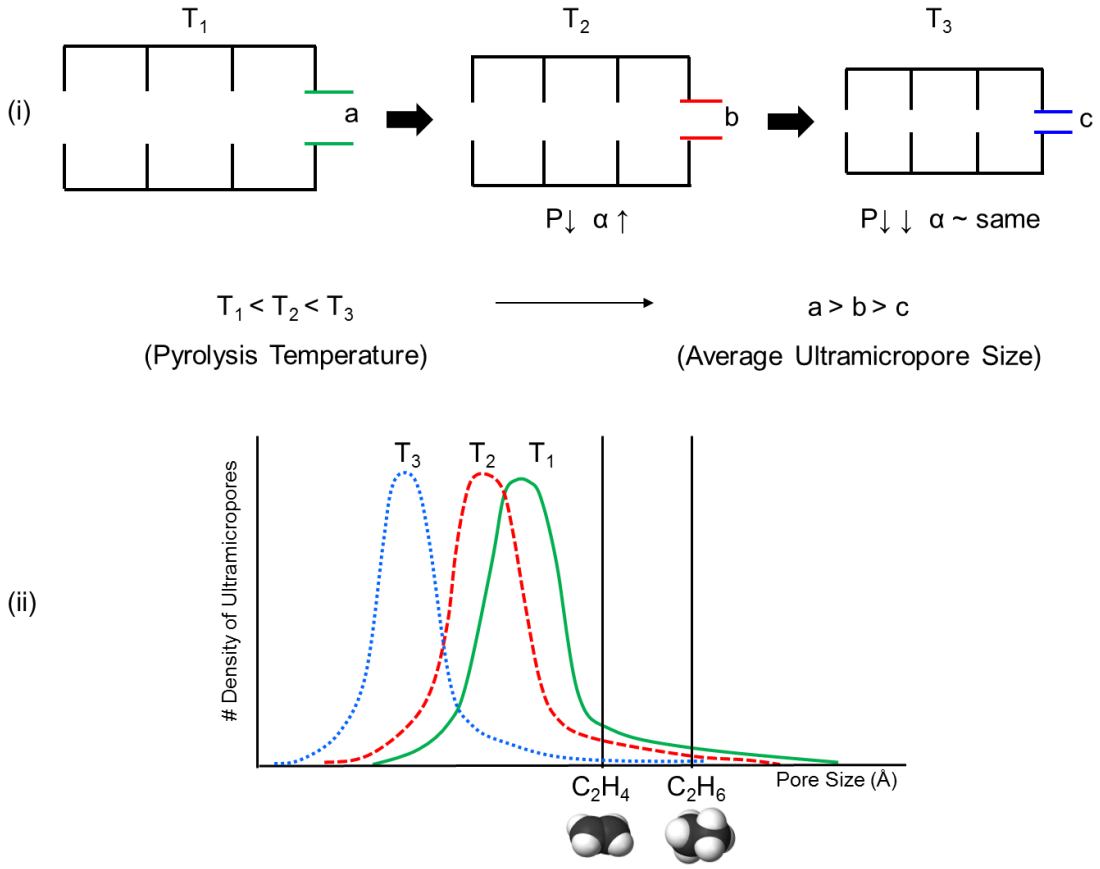

Figure 5.4: Effect of final pyrolysis temperature on (i) CMS cartoon structures, (ii) hypothetical ultramicropore distribution

5.2.2. Further Optimization of Ethylene/Ethane Separation Performance

CMS dense films in the previous section were derived from vacuum pyrolysis using a slow pyrolysis protocol, Protocol 2 for pyrolysis temperatures over 550°C. The effect of modifying the pyrolysis protocol at higher pyrolysis temperatures was studied by carrying out vacuum pyrolysis at 675°C using Protocol 1 instead of the slow Protocol 2. A definition of the two protocols can be found in Section 3.3.2. The effect of modifying the heating protocol is not significant. However, the CMS dense film resulting from vacuum pyrolysis of Matrimid® at 675°C (P1-675°C-CMS_Vacuum) shows a small increase in the C_2H_4 permeability over Protocol 2 (P1-675°C_slow-CMS_Vacuum)

without significant selectivity loss, yielding a C_2H_4 permeability ~17 Barrer and C_2H_4/C_2H_6 selectivity ~12. This eliminates the need for use of the slow Protocol 2 at higher pyrolysis temperatures. Thus, only Protocol 1 was used for CMS fabrication in all further studies.

Table 5.1: Pure gas C_2H_4/C_2H_6 separation performance (35°C, 50 psia) of P1-675°C-CMS_Vacuum (Protocol 1) and P1-675°C_slow-CMS_Vacuum (Protocol 2)

CMS	P_{C2H4} Barrer	P_{C2H4}/P_{C2H6}
P1-675°C-CMS_Vacuum	16.7	11.7
P1-675°C_slow-CMS_Vacuum	14.4	12.2

As seen from the TGA curves shown in Figure 5.5, P1-675°C-CMS_Vacuum shows a slightly larger mass loss compared to the P1-675°C_slow-CMS_Vacuum. These results compare well with mass loss data collected during the actual pyrolysis process. For P1-675°C-CMS_Vacuum, rapid mass loss starts around 450°C, the decomposition temperature for Matrimid®, and continues until 660°C due to the evolution of pyrolysis by-products. After 660°C, densification of the carbon matrix takes place with a very small mass loss. For the P1-675°C_slow-CMS_Vacuum instead, rapid mass loss takes place from ~450°C to ~535°C. The mass loss then slows down approaching 550°C, owing to a decrease in the ramp rate. This results in a shoulder in the P1-675°C_slow-CMS_Vacuum mass loss curve (Figure 5.5), before densification of the carbon matrix starts to occur. Thus the P1-675°C_slow-CMS_Vacuum shows a smaller overall mass loss with greater shrinkage of the CMS pores. Evolution of pyrolysis by-

products results in defects which are believed to form the CMS pore structure, and sintering of the defects leads to ultramicropore tuning. It appears reasonable, therefore, that P1-675°C-CMS_Vacuum shows slightly higher permeability compared to the P1-675°C_slow-CMS_Vacuum.

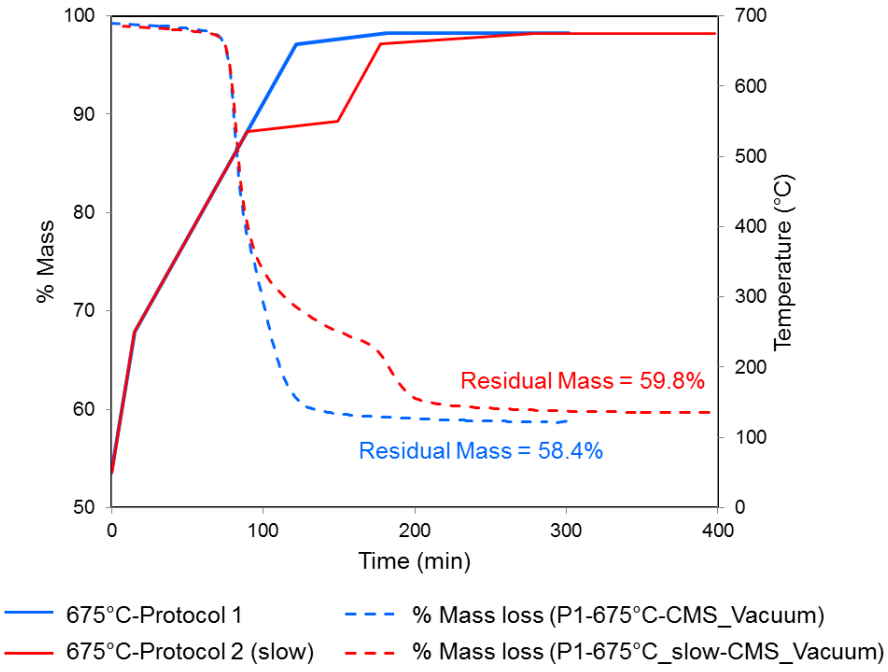

Figure 5.5: TGA mass loss curves for P1-675°C-CMS_Vacuum and P1-675°C_slow-CMS_Vacuum

5.2.3. Vacuum vs. Inert Pyrolysis

CMS dense films were prepared by pyrolyzing Matrimid® in the presence of argon (UHP grade, Airgas) purge at 500°C, 550°C, 675°C and 800°C using Protocol 1. Details related to inert pyrolysis can be found in Section 3.3.2. As shown in Figure 5.6, in general, inert pyrolysis yields CMS with slightly higher permeability and a slightly lower

selectivity. Nevertheless, CMS membranes from inert pyrolysis of Matrimid® show performance comparable to vacuum pyrolysis.

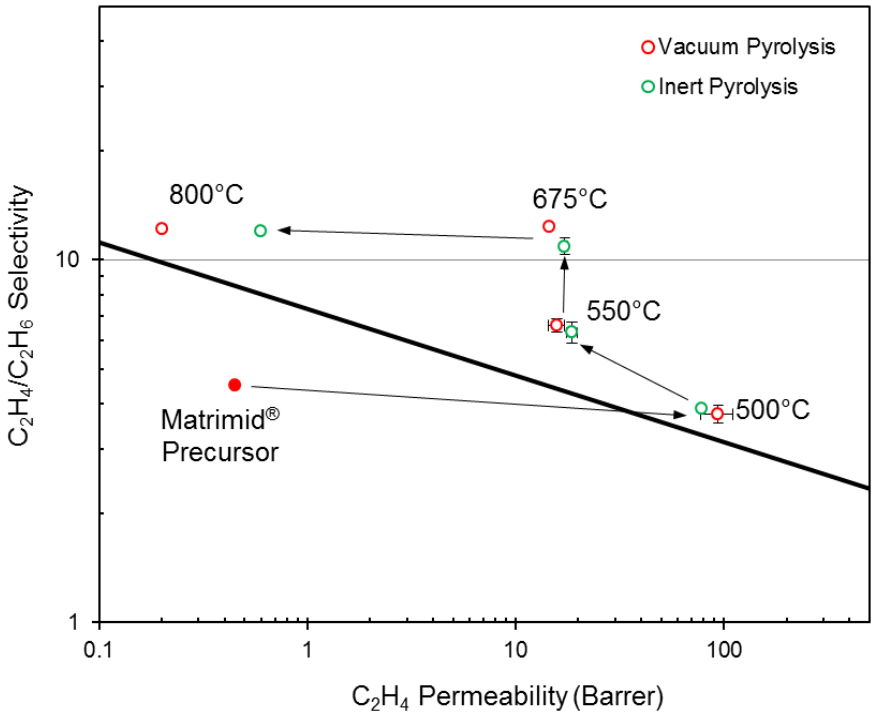

Figure 5.6: Plot showing pure gas C_2H_4/C_2H_6 separation performance (35°C, 50 psia) of CMS dense films derived from vacuum pyrolysis and UHP Ar pyrolysis of Matrimid® at different pyrolysis temperatures. Error bars represent standard deviations from multiple measurements

Figure 5.7 shows the diffusion and sorption trends calculated from direct sorption measurements for CMS resulting from inert pyrolysis at different temperatures. It should be noted that the diffusion coefficients for inert pyrolysis are higher than for the vacuum pyrolysis case at all pyrolysis temperatures. The trends of the C_2H_4 diffusivities and sorption coefficients and C_2H_4/C_2H_6 diffusion and sorption selectivity as a function of the pyrolysis temperature are similar to the vacuum pyrolysis case, with diffusion dominating the overall trends.

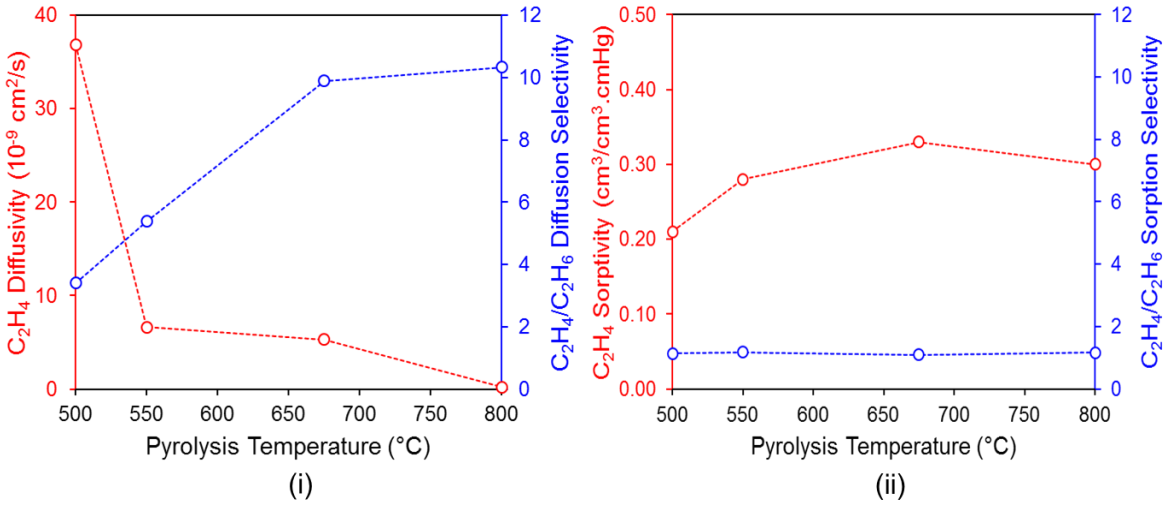

Figure 5.7: (i) C_2H_4 diffusivity and C_2H_4/C_2H_6 diffusion selectivity of CMS dense films derived from UHP Ar pyrolysis of Matrimid® shown as a function of the final pyrolysis temperature. Diffusion coefficients were back-calculated from permeation and sorption. (ii) C_2H_4 sorption coefficient and C_2H_4/C_2H_6 sorption selectivity of CMS dense films derived from UHP Ar pyrolysis of Matrimid® shown as a function of the final pyrolysis temperature. Sorption coefficients were obtained from direct sorption measurements

While vacuum pyrolysis is useful to carry out benchmark studies for fundamental understanding, only inert pyrolysis will be used for further analysis since it is more feasible from a scale-up perspective. Additionally, inert pyrolysis conditions are easier to control by careful monitoring of the oxygen content during pyrolysis using the oxygen sensor, and may thus yield more reproducible results.

5.2.4. Pure Gas vs. Mixed Gas Performance

Mixed gas permeation tests using a binary mixture of 63.2 mol% C_2H_4 and 36.8 mol% C_2H_6 were carried out on CMS dense films derived from inert argon pyrolysis of Matrimid® dense films. The results of both pure gas and mixed gas tests are summarized in Figure 5.8 below. In all cases, the CMS performance for mixed gas is somewhat lower than the pure gas, especially in terms of the C_2H_4 permeability. This results due to the

complicated competition effects between C_2H_4 and C_2H_6 when they are both present simultaneously. The permeabilities of both the gases are decreased due to these competition effects which result in hindered diffusion through the membrane. The effect on C_2H_4/C_2H_6 selectivity is not as significant and this may be due to the similar nature of C_2H_4 and C_2H_6. Nevertheless, mixed gas performances are more realistic representations of membrane performance. A detailed discussion of the binary gas transport performance of CMS and mixed gas modeling is presented in Chapter 6.

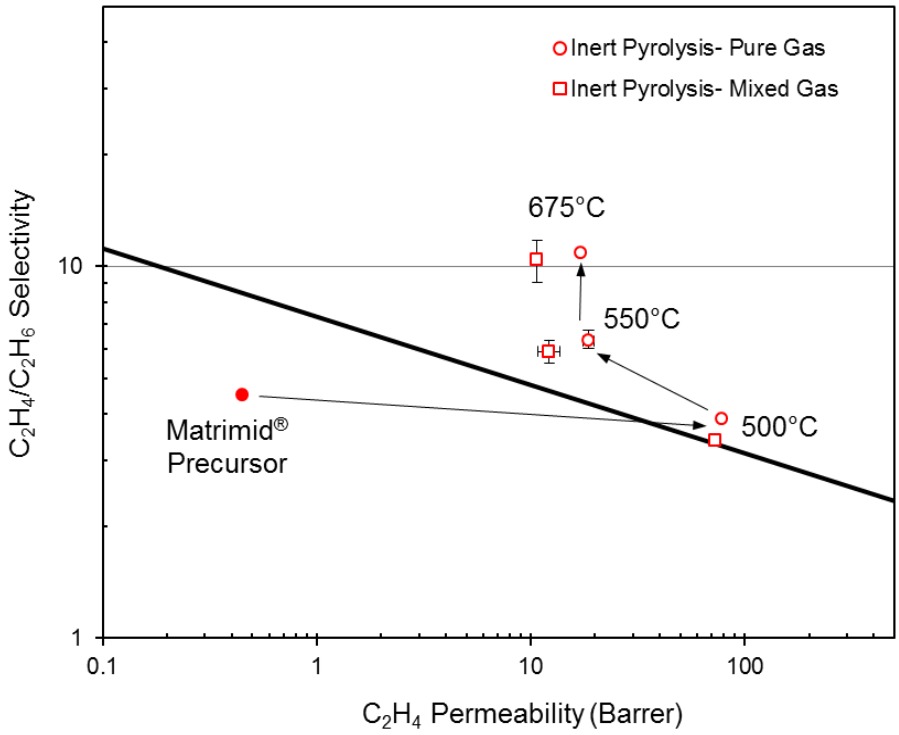

Figure 5.8: Plot showing pure gas and mixed gas C_2H_4/C_2H_6 separation performance (35°C, 50 psia) of CMS dense films derived from UHP Ar pyrolysis of Matrimid® at different pyrolysis temperatures. Error bars represent standard deviations from multiple measurements

5.2.5. Characterization of Carbon Molecular Sieve Membranes Derived from Matrimid®

The C_2H_4/C_2H_6 separation performance for CMS pyrolyzed from Matrimid® using different pyrolysis conditions was reported above. Several characterization techniques were considered to gain insight into the nature and the pore morphology of the engineered CMS materials, in order to understand the observed transport trends in relation to the CMS structure.

5.2.5.1. TGA-FTIR and Elemental Analysis

The decomposition profile for Matrimid® was studied using TGA-FTIR. The polymeric samples were heated under argon purge and the evolved gases were sent to the FTIR chamber to analyze the composition of the evolved by-products. As seen from the TGA plots, pyrolysis of Matrimid® to form CMS results in ~40% mass loss, with the mass loss being slightly higher at a higher pyrolysis temperature. Pyrolysis of Matrimid® produces mainly CO_2 (2110 cm^{-1}), CO (2190 cm^{-1}) and CH_4 (3017 cm^{-1}). The TGA and TGA-FTIR plots are shown in Figures 5.9 and 5.10 respectively.

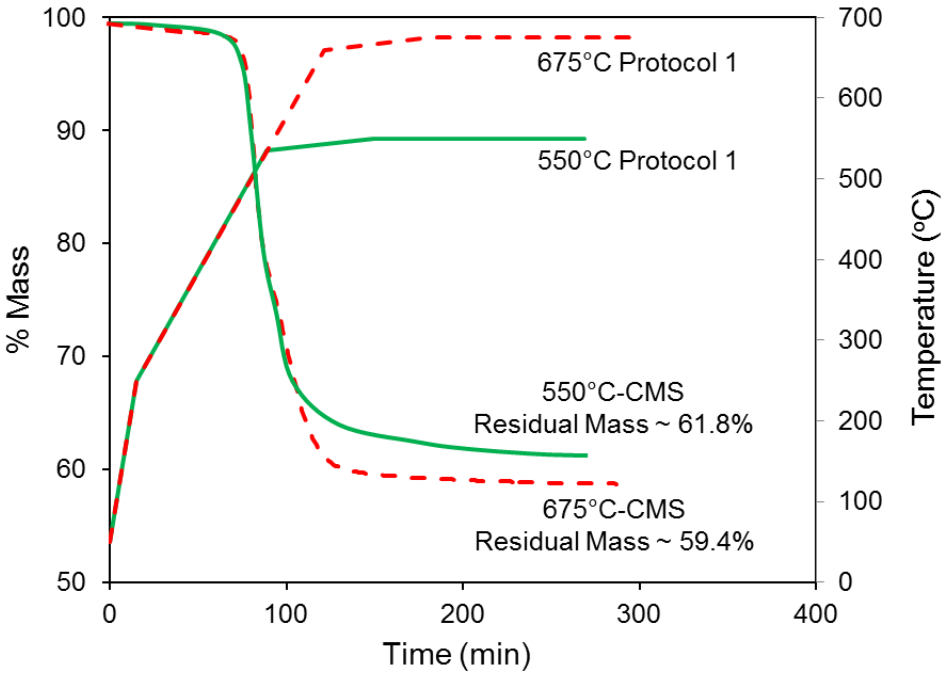

Figure 5.9: Mass loss curves for pyrolysis at 550°C and 675°C using Protocol 1. The primary y-axis shows % mass and secondary y-axis represents temperature in °C

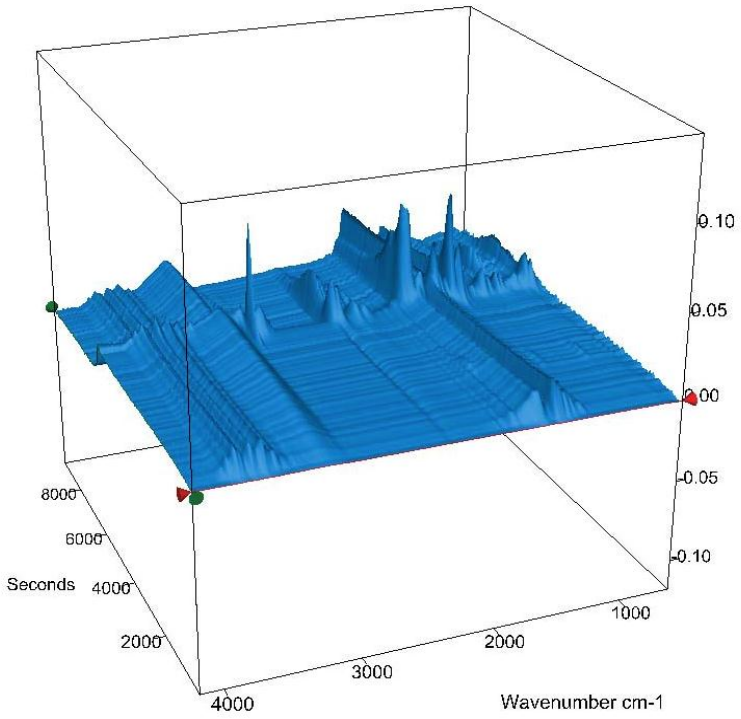

Figure 5.10: TGA-FTIR plot showing by-products evolved during Matrimid® pyrolysis [3]

Pyrolysis of a polymer to form CMS involves several stages. Below ~425-450°C, very small weight loss takes place due to removal of water and residual solvent, and possibly due to further imidization or crosslinking of the polymer. Above ~400°C the films turn black in color and linear conjugated C-C systems start to form [4, 5]. Rapid mass loss starts around ~450°C, the decomposition temperature of Matrimid®. The carbonization process is complex, and several reactions may take place at the same time such as cleavage, condensation, isomerization, dehydrogenation etc. [6-8]. The decomposition mechanism is not fully understood. The early stages of carbonization involve cleavage of bonds within the macromolecular system to give free radicals. Rapid mass loss is associated with the evolution of by-products in the form of small molecules such as CO_2, CO, CH_4, as reported from TGA-FTIR studies. Such eliminations generate microporosity within the rigid macromolecular system and, at the same time free radicals generated at surfaces combine with each other or extract hydrogen from the system. The carbonization process is thus a simultaneous process of elimination of small molecules and the subsequent re-arrangements of carbon atoms to form more stable six-membered rings of disordered carbon lamellae [4, 9]. Around 550°C, depending on the system, all of the aliphatic carbon is converted to aromatic C-H, resulting in the final CMS residue with over 85% carbon [9]. Further heating at a given pyrolysis temperature may not result in significant mass loss and pore sintering effects may cause in microstructural rearrangements, resulting in pore shrinkage (see Figure 5.9). Going to a higher pyrolysis temperature may result in some further mass loss (as seen from the TGA plot shown in Figure 5.9). At the same time, it is speculated that the extent of pore sintering microstructural changes resulting from the rearrangement of carbon lamellae may be greater at a higher temperature, resulting in ultramicropore tuning.

Table 5.2 shows the elemental compositions for the precursor Matrimid® (theoretical) and CMS produced from pyrolysis of Matrimid® at 675°C in UHP argon

purge (experimental). Clearly, the carbon content increases due to pyrolysis and the CMS shows over 90% carbon. Most of the hydrogen and oxygen is removed due to pyrolysis, but not nitrogen.

Table 5.2: Elemental composition of Matrimid® precursor and CMS derived from UHP Ar pyrolysis of Matrimid® at 675°C using Protocol 1

	Carbon	Hydrogen	Nitrogen	Oxygen
	wt %	wt %	wt %	wt %
Precursor	76.09	4.35	5.07	14.49
CMS	90.50	1.32	3.27	1.89

5.2.5.2. Raman Spectroscopy

The vibrational characteristics of carbonaceous materials exhibited in Raman spectra allow distinct resonances from ordered and disordered regions of the material. Raman spectroscopy may be used to characterize disorder in sp^2 hybridized carbon materials [9-11]. Ordered graphitic layers show resonance between 1580 cm^{-1} and 1600 cm^{-1}, designated as the G band. This band narrows and moves closer to 1580 cm^{-1} (the resonance for graphite) with an increase in order and graphitization. A second resonance peak may occur, centered around 1350-1380 cm^{-1}, and is assigned as the D (defect) band. This D band disappears with increasing order and graphitization. The D band is not present in single crystals of graphite. The intensity of the D band and the ratio between the intensities of the disorder-induced D band and the graphite G band may be used to quantify disorder in the material. The Raman spectrum for Matrimid® CMS is shown in Figure 5.11. Clearly a broad G band appears closer to 1600 cm^{-1} for

the CMS materials. Additionally, the spectrum shows a broad, high intensity peak corresponding to the D band. Raman spectroscopy thus confirms that CMS membranes are highly disordered amorphous materials formed of sp^2 hybridized graphene-like sheets.

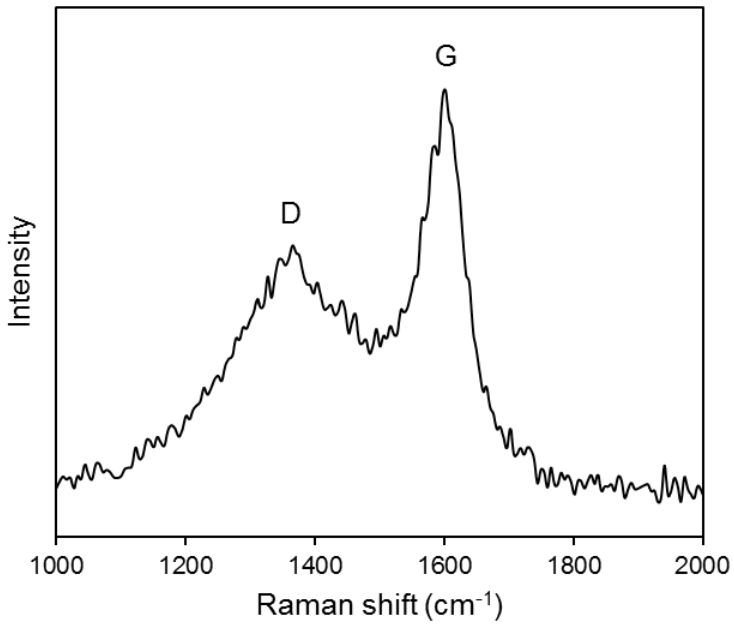

Figure 5.11: Raman spectrum for CMS derived from UHP Ar pyrolysis of Matrimid® at 550°C using Protocol 1 (Data courtesy: Liren Xu)

5.2.5.3. Wide Angle X-ray Diffraction (WAXD)

X-ray analysis can provide a measure of the amount of order present in carbon materials and the size of the crystallites that make up the ordered structure [6, 9]. The interlayer spacing (d-spacing) can be determined from x-ray diffraction using Bragg's law as $n\lambda=2d\sin\theta$, where λ is the x-ray wavelength (λ = 1.54 Å for CuKα radiation) and θ is the Bragg angle. The x-ray diffraction (XRD) pattern of graphite is shown in Figure

5.12(i). It shows a sharp, well defined peak at 3.35 Å resulting from the (002) plane reflection. As mentioned previously, most polymers when pyrolyzed form char and do not graphitize to any extent, regardless of the temperature and duration of heat treatment. They form highly disordered and amorphous materials with no long range order. The XRD patterns of CMS materials are shown in Figure 5.12(ii). Both the 550°C and 675°C CMS show a broad peak at a d-spacing of ~3.8 Å. This indicates that CMS membranes are highly disordered and amorphous materials with little to no crystalline order. The peak becomes narrower and more well-defined at a higher pyrolysis temperature indicating increasing order with an increase in pyrolysis temperature. For carbon materials derived from polymers, some reduction in d-spacing may be observed with an increase in temperature resulting from an increase in ordering of the carbon lamellae; however, this d-spacing does not shrink below 3.44 nm for most polymer-based turbostratic carbons. A peak also appears at a d-spacing of ~2.1 Å. This corresponds to the (100) plane of graphite. A spread in this peak usually reflects the turbostratic nature of the material. This peak was more pronounced for the 675°C material, indicating an increase in ordering with an increase in pyrolysis temperature. Thus XRD patterns provide evidence that the CMS membranes studied in this work are amorphous, highly disordered, turbostratic materials with graphene-like sp^2 hybridized sheets. A small increase in ordering at higher pyrolysis temperatures may be the reason why CMS derived at a higher pyrolysis temperature result in lower permeabilities and higher selectivities. However, because of the amorphous nature of CMS, x-ray diffraction studies do not offer any insights that may allow detailed interpretation of the gas transport properties of the engineered CMS membranes.

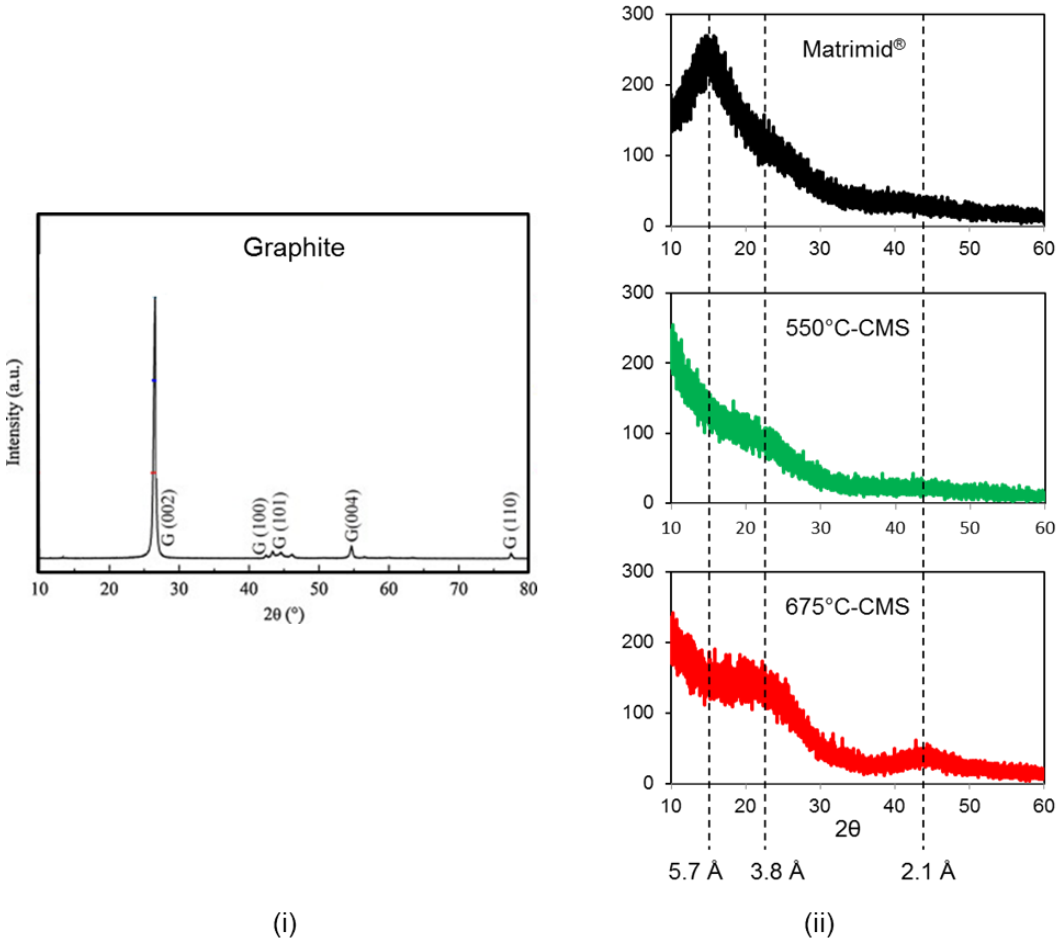

Figure 5.12: XRD pattern for (i) graphite [12], (ii) Matrimid® precursor and CMS derived from inert argon pyrolysis of Matrimid® at 550°C and 675°C using Protocol 1

5.2.5.4. Positron Annihilation Lifetime Spectroscopy (PALS)

PALS, based on measurements of positron lifetimes in annihilation γ-ray spectra, is useful in characterizing porosity in solids. Fu et al. [13] used PALS to study the porosity of CMS materials. Usually, the ortho-positronium annihilation lifetime (T_3) is used to analyze pore structures. For carbon materials, however, most ortho-positronium annihilations occur on the surface, which is inadequate to resolve a third distinct component (T_3) in the spectra. In such situations, one could consider estimating

characteristics of micropores from the free-positron annihilation lifetime (T_2); however, a quantitative empirical equation that relates micropore size to T_2 is not yet available. The authors used the free-positron annihilation lifetime distribution as a qualitative measure of CMS pore characteristics. Values for T_2 were assumed proportional to the pore size. Their results are shown in Figure 5.13. When the pyrolysis temperature was increased, the T_2 distribution curve shifted to smaller lifetimes, became narrower, and showed an increase in intensity, suggesting a shift to a smaller average pore size with an increase in the pyrolysis temperature. This may explain why gas permeability decreases with an increase in the pyrolysis temperature. Additionally, vacuum pyrolysis yields CMS with a smaller average pore size compared to nitrogen (inert) pyrolysis, as indicated by the shift of the T_2 distribution curves to smaller lifetimes. Correspondingly, CMS prepared from vacuum pyrolysis show a slightly lower permeability compared to inert pyrolysis. PALS is useful in understanding the general trend of gas permeability as a function of the pyrolysis temperature and pyrolysis atmosphere; however, like XRD, it does not provide any insights that may explain the specific transport behavior of the fabricated CMS, nor does it serve as a quantitative tool to interpreting CMS pore sizes.

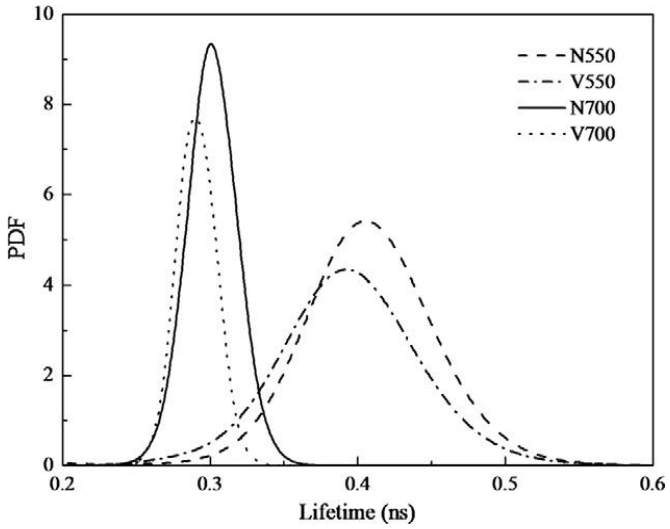

Figure 5.13: Free positron lifetime distributions from PALS spectra for CMS derived from Matrimid® [13]. The abbreviations on the chart are as follows: N550- Pyrolysis at 550°C in nitrogen, V550- Pyrolysis at 550°C in vacuum, N700- Pyrolysis at 700°C in nitrogen, V700- Pyrolysis at 700°C in vacuum

5.2.5.5. Microscopy

Previous researchers have used high resolution transmission electron microscopy (HRTEM) and atomic force microscopy (AFM) to study the morphology of CMS materials [13, 14]. HRTEM images, shown in Figure 5.14(i), however do not show any distinct morphology, and is thus not very useful in characterizing the porosity of CMS membranes. AFM imaging of the CMS topography also failed to reveal any features at the angstrom level, as seen from Figure 5.14(ii). Microscopy is thus not a very powerful tool to characterize the CMS morphology and pores.

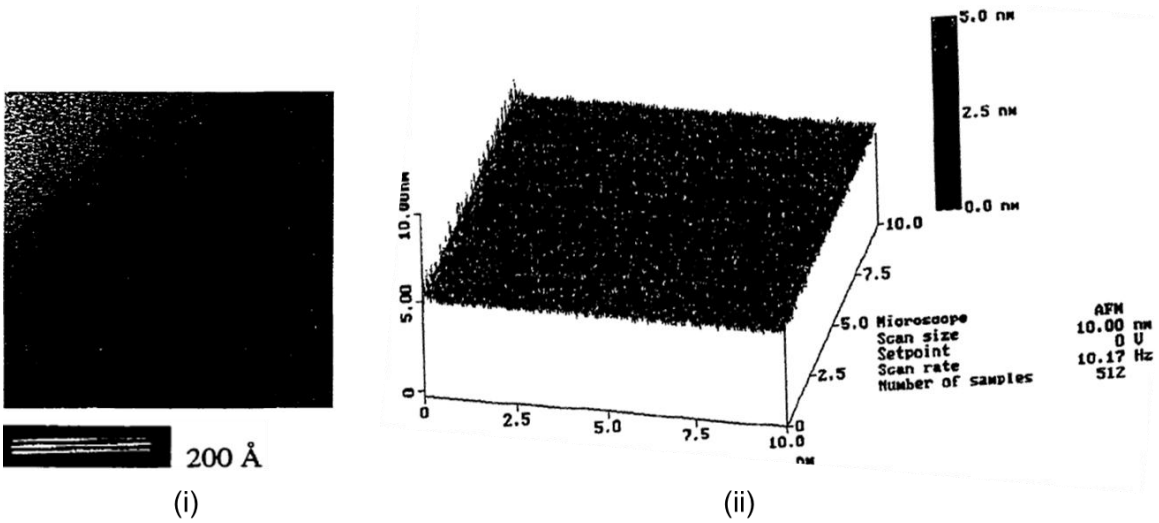

(i) (ii)

Figure 5.14: (i) HRTEM image of CMS at a magnification of 40,000X [14]; (ii) AFM line plot of CMS [14]

5.2.5.6. Density and Pore Size Distribution from CO_2 Sorption

CMS skeletal density measurements using helium pycnometry and pore volume measurements based on CO_2 uptake measurements were done at Micromeritics. This was used to further calculate the bulk density of CMS samples using Equation 3.4. The results are shown in Table 5.3 for CMS derived from UHP Ar pyrolysis of Matrimid® at 500°C, 550°C and 675°C. From the CO_2 uptake data, pore size distribution analysis was also provided by Micromeritics using density functional theory analysis (Figure 5.15)

Table 5.3: Density and pore volume of CMS derived from UHP Ar pyrolysis of Matrimid® at 500°C, 550°C and 675°C.

	Total Pore Volume		Pore Volume <4.2 Å		Skeletal Density	Bulk Density	Total S.A.
	cm^3/g	cm^3/cm^3	cm^3/g	cm^3/cm^3	g/cm^3	g/cm^3	m^2/g
P1-500°C-CMS	0.0560	0.0779	0.0008	0.0010	1.39	1.29	191.2
P1-550°C-CMS	0.1041	0.1509	0.0018	0.0026	1.45	1.26	478.1
P1-675°C-CMS	0.1136	0.1818	0.0081	0.0130	1.60	1.35	466.8

As seen from Table 5.3, the skeletal density of the CMS samples increased with the final pyrolysis temperature, meaning that there is more carbon per unit volume. This suggests that a more "closed" CMS structure results at higher pyrolysis temperatures. The total pore volume per unit volume of the CMS samples, however, increased with pyrolysis temperature (Table 5.3). The 500°C-CMS shows a very low pore volume compared to 550°C-CMS and 675°C-CMS. During pyrolysis, the polymer starts decomposing at ~450°C and the evolution of by-products results in the formation of large pores in the sample. At 500°C, the sample porosity may still be developing and the evolution of by-products is not complete. As a result, one may expect that a small number of large pores are present in the CMS derived at 500°C. The total pore volume is still small since by-product evolution and transition from polymer to CMS may not be complete at this stage. The restricting ultramicropore windows may not be completely developed and the CMS may have a very "open" structure with greater fraction of larger pores (see Figure 5.15 which shows pore size distributions obtained from CO_2 uptake measurements using density functional theory analysis done at Micromeritics). This explains the very high permeability of the 500°C-CMS although its C_2H_4/C_2H_6 selectivity is exceptionally low, even below that of the polymer precursor. As the pyrolysis

temperature increases (550°C and 675°C), further mass loss takes place due to continued by-product evolution and microstructural rearrangements, resulting in an increase in the material porosity (total pore volume in Table 5.3 increases at higher pyrolysis temperatures). At the same time pore sintering effects at higher temperatures may result in fragmenting of larger pores into smaller ones and also cause further shrinkage of the pores. As a result, the CMS material may become more porous, albeit denser and tighter in packing at higher pyrolysis temperatures. This is supported by the higher pore volume for < 4.2 Å pore widths at the higher pyrolysis temperatures, as well as an increase in the total surface area of the CMS samples at higher pyrolysis temperature (Table 5.3). In fact in going from 550°C to 675°C, although the total pore volume does not change significantly, there is a significant increase in the number density of smaller pores (Table 5.3). This may be why the 675°C-CMS C_2H_4 permeability is essentially equivalent to the 550°C-CMS, although its C_2H_4/C_2H_6 selectivity is almost two-fold higher. The permeability-selectivity trends however cannot be conclusively determined based on pore size distributions obtained from these measurements, since it cannot give any information about pores smaller than ~ 4 Å. However, since the critical molecular sieving ultramicropores are expected to be smaller than this size, it is critical to be able to characterize pores smaller than ~ 4 Å to understand the diffusion behavior.

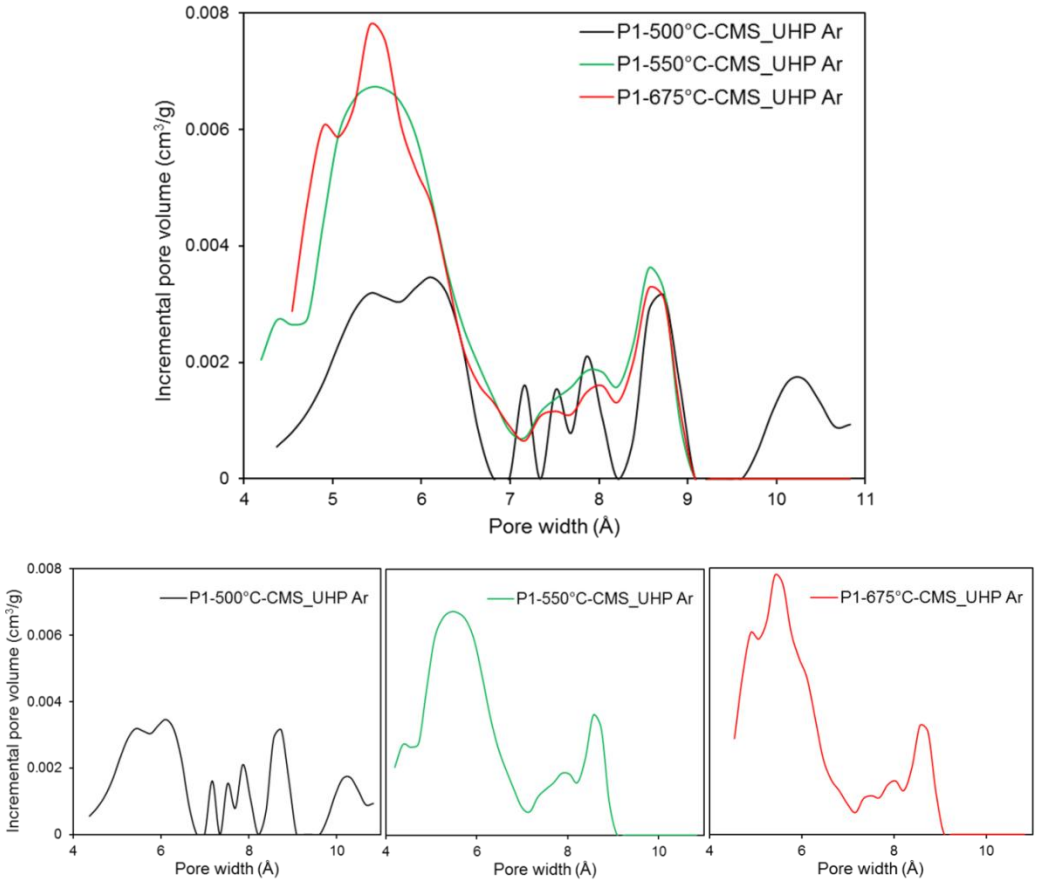

Figure 5.15: Pore size distributions obtained from CO_2 uptake measurements using density functional theory analysis for CMS obtained from UHP Ar pyrolysis of Matrimid at 500°C (black), 550°C (green) and 675°C (red). Sorption measurements and pore size analyses were done at Micromeritics

5.2.5.7. Gas Probe Molecular Ruler

It is clear from the above characterizations that, owing to the amorphous nature of CMS materials and the presence of very small angstrom level pores, it is hard to characterize them using traditional characterization techniques based on spectroscopy or microscopy. Sorption measurements can give an idea about the micropore distribution; however such measurements fail to conclusively characterize the critical smaller pore sizes. As shown in Sections 5.2.1 and 5.2.3, gas diffusion dominates the overall permeability and selectivity trends of the CMS membranes, whereas the effects

due to sorption are relatively less critical. It is thus important to be able to characterize the diffusion limiting critical ultramicropores of the CMS membranes in order to understand their gas transport properties in relation to the CMS structure. A gas probe method [15] was used in this study to infer the CMS pore distributions based on the transport properties of different gases as molecular size probes of the CMS pores. This was further used to establish semi-quantitative, diffusion-based, critical ultramicropore distributions that can facilitate understanding of transport in CMS membranes in relation to their structure.

Direct permeation and sorption measurements were carried out, and this was used to obtain the average transport diffusivities of different gases. The sizes and critical temperatures [15-17] of the different gases are shown in Table 5.4. The sizes of C_2H_4 and C_2H_6 have been defined based on their dominant transport behavior in the CMS slit-like pores, using space filling CPK models and calibrated "slits". This will be discussed further with respect to the transport properties of the molecules in the CMS membranes.

Table 5.4: Size (σ) and critical temperature (T_c) of different gas molecules tested. Parameters for common gases (H_2, CO_2, O_2, N_2 and CH_4) were adopted from [16], that of noble gases (He, Ne, Ar, Kr, Xe) were adopted from [17], and that of SF_6 was adopted from [15]. The size of C_2H_4 and C_2H_6 were determined using space-filling CPK models and calibrated "slits"

Gas	He	Ne	H_2	CO_2	O_2	Ar	N_2	Kr	C_2H_4	CH_4	C_2H_6	Xe	SF_6
σ (Å)	2.6	2.8	2.89	3.3	3.46	3.5	3.64	3.7	3.75	3.8	3.85	4.1	5.5
T_c (K)	5.3	44.5	33.2	304	155	151	126	209	283	191	306	290	319

Three cases were analyzed: CMS derived from UHP Ar pyrolysis of Matrimid® at 500°C, 550°C and 675°C using Protocol 1 (i.e. P1-500°C-CMS_UHP Ar, P1-550°C-CMS_UHP Ar and P1-675°C-CMS_UHP Ar). The permeabilities, average sorption coefficients and average transport diffusivities of the different penetrant gases for the three CMS membranes are shown in Figures 5.16, 5.17 and 5.18 respectively. Additionally, the thermodynamically corrected diffusivities are shown in Figure 5.19. The different gas transport properties were calculated using the data and equations reported in Appendix B.

As seen from Figure 5.16, the 500°C-CMS shows the highest permeability for all gas molecules, followed by the 550°C-CMS, and the 675°C-CMS shows the lowest permeabilities. This follows from the discussion above that pyrolysis at higher temperatures causes the CMS framework to condense and shifts the pore distribution to a smaller average size (Figure 5.4), thus resulting in a decrease in the permeability of all gases with the pyrolysis temperature.

It is interesting to note in Figure 5.16 that the trend of gas permeabilities does not follow the order of the gas molecule size, i.e. it does not necessarily decrease with an increase in the penetrant size. Gas transport through membranes can be complicated and may depend not just on the penetrant size but also on its shape and condensability (critical temperature), as well as its interactions with the CMS material and slit-like pore structure. For example, C_2H_4 is much more sorptive compared to CH_4 and Kr. In addition, as discussed in Section 4.4.2, planar molecules such as C_2H_4 can have significant configuration-related advantages over round or bulkier molecules such as Kr, CH_4 and C_2H_6 in transport through the CMS "slit-like" pores [14]. These are known as "entropic selective factors" [18]. Detailed discussion relating to entropic effects is presented in Chapter 6. Sorption and entropic advantages thus result in a higher C_2H_4 permeability compared to that of similar sized penetrants such as Kr and CH_4 (see

Figure 5.16). On the other hand, the permeability of highly condensable but larger gases, for example CO_2, may be higher than the permeability of smaller penetrants like He and Ne. Similarly, the permeability of C_2H_4 is higher than N_2 (see Figure 5.16) In order to understand these unusual permeability trends, the gas permeabilities were factored into the sorption and diffusion coefficients to deconvolute the effects of penetrant condensability from penetrant size and shape.

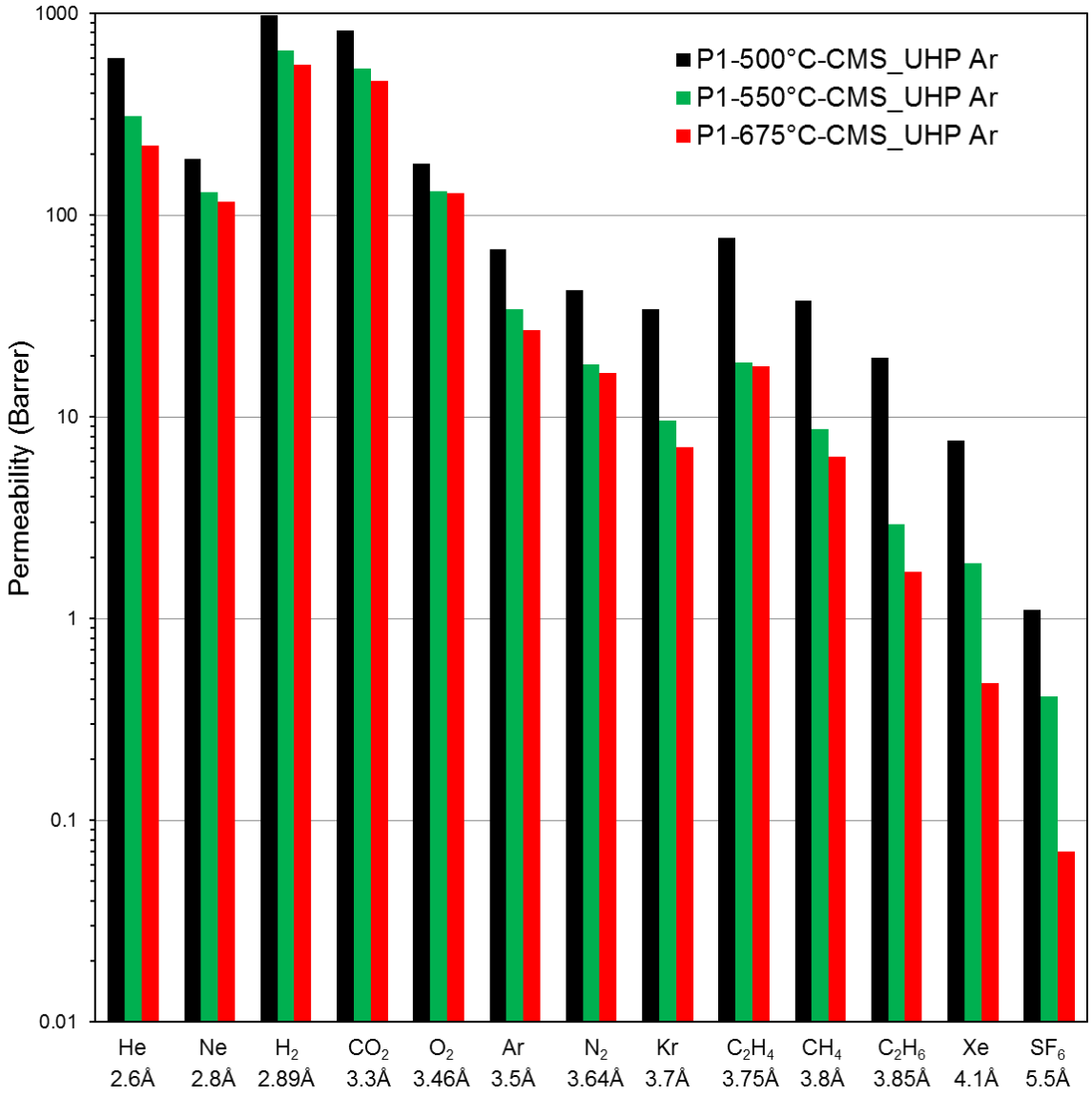

Figure 5.16: Permeabilities of different penetrants for CMS derived from UHP Ar pyrolysis of Matrimid® at 500°C (black), 550°C (green) and 675°C (red). Permeability measurements were made at 35°C using 50 psia feed pressure

Figure 5.17 shows a plot of the average sorption coefficients of different gases in the CMS obtained via UHP Ar pyrolysis of Matrimid® at 500°C, 550°C and 675°C (i.e. P1-500°C-CMS_UHP Ar, P1-550°C-CMS_UHP Ar and P1-675°C-CMS_UHP Ar). In general, the gas solubility follows the order of the critical temperatures, shown in Table 5.4. This explains the "out-of-place" permeabilities of gases like H_2 and CO_2 compared to

He, and C_2H_4 compared to N_2. Although He is a small molecule that can sample most of the CMS pores, its sorption coefficient is small because of its low critical temperature. As a result its overall permeability is less than that of H_2 and CO_2, despite its smaller size. SF_6 on the other hand has a high critical temperature which makes it highly condensable; however, because of its large size and bulky shape, it is excluded from most of the CMS pores, resulting in low sorption uptake. As seen from Figure 5.17, there is a general increase in the sorption coefficients of most gases with an increase in the pyrolysis temperature. This trend is opposite that of the overall permeability, and may be a result of an increase in the pore volume per unit volume of the CMS and increased material density for CMS derived from higher temperature pyrolysis (Refer to Table 5.3 and prior discussion in Section 5.2.5.6 for details).

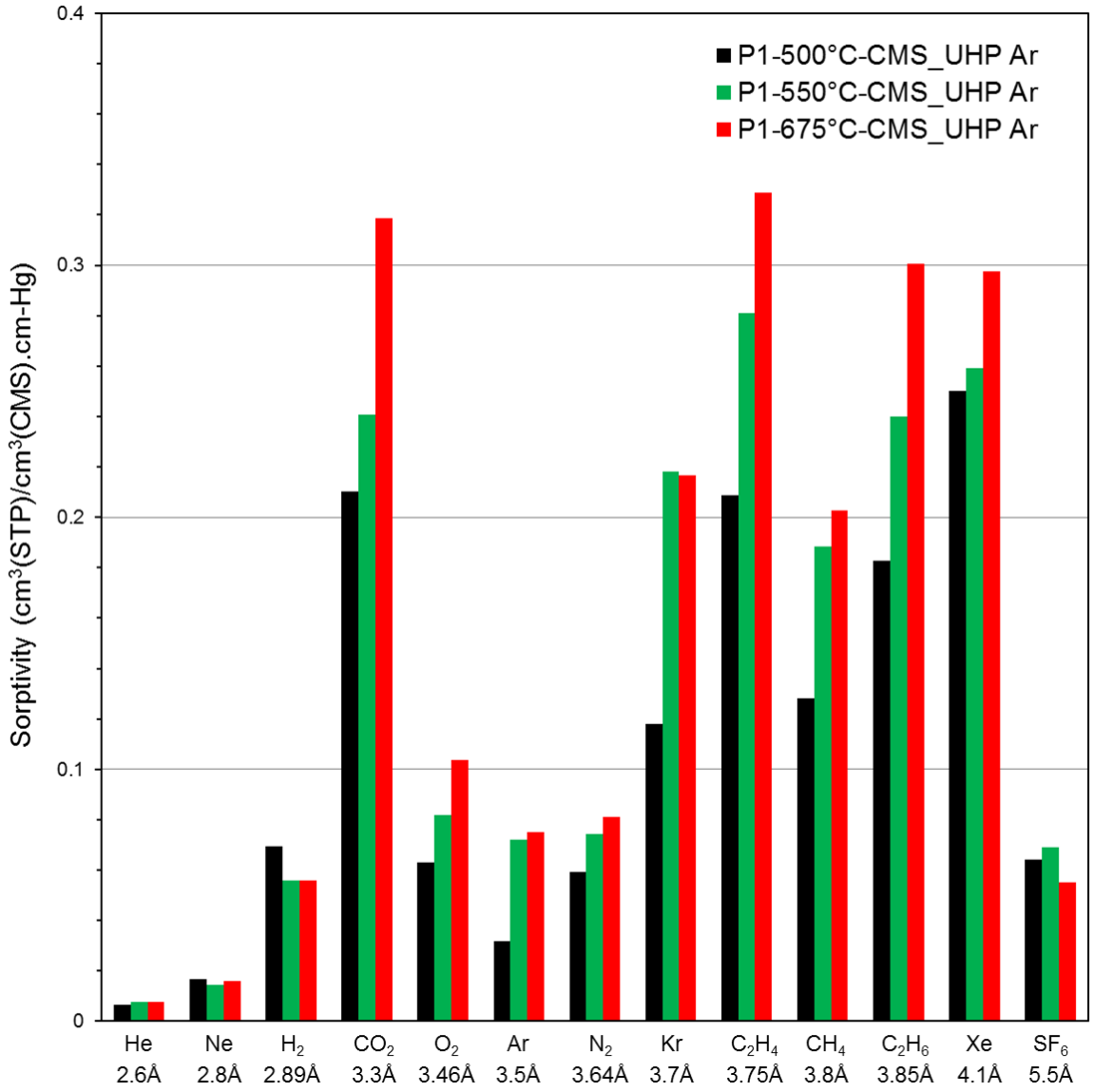

Figure 5.17: Average sorption coefficients obtained from direct equilibrium sorption measurements at of different penetrants for CMS derived from UHP Ar pyrolysis of Matrimid® at 500°C (black), 550°C (green) and 675°C (red). The sorption coefficients reported are for 50 psia equilibrium pressure at 35°C

Figure 5.18 shows the average transport diffusivities of different gases obtained using their permeabilities and sorption coefficients. Clearly, the diffusion coefficients decrease as a function of the final pyrolysis temperature, following a similar overall trend as the permeabilities as a function of pyrolysis temperature. The diffusion coefficients for

all gases is much larger for the 500°C-CMS compared to the 550°C-CMS and the 675°C-CMS, thus suggesting a more "open" CMS structure resulting from 500°C pyrolysis. As seen from Figure 5.18, with an increase in the penetrant size there is a general decrease in the penetrant diffusivity, unlike the trend observed for permeability with penetrant size. For example, factoring out the much higher sorption uptake for CO_2 compared to He leaves the He diffusivity higher than CO_2. Similarly, factoring out the much higher sorption uptake for C_2H_4 compared the N_2 leaves a N_2 diffusivity higher than C_2H_4, as expected based on their size. The diffusion coefficients for similar sized gas molecules C_2H_4, CH_4 and Kr, although on the same order of magnitude, reflect the shape advantage that the "planar" C_2H_4 can have over "round" molecules like CH_4 and Kr. The average transport diffusivities shown in Figure 5.17 are, however, still dependent on the penetrant concentration in the membrane. In order to get further insight into the transport properties of similar sized gas molecules, it is useful to look at the concentration independent corrected diffusivities of the penetrants.

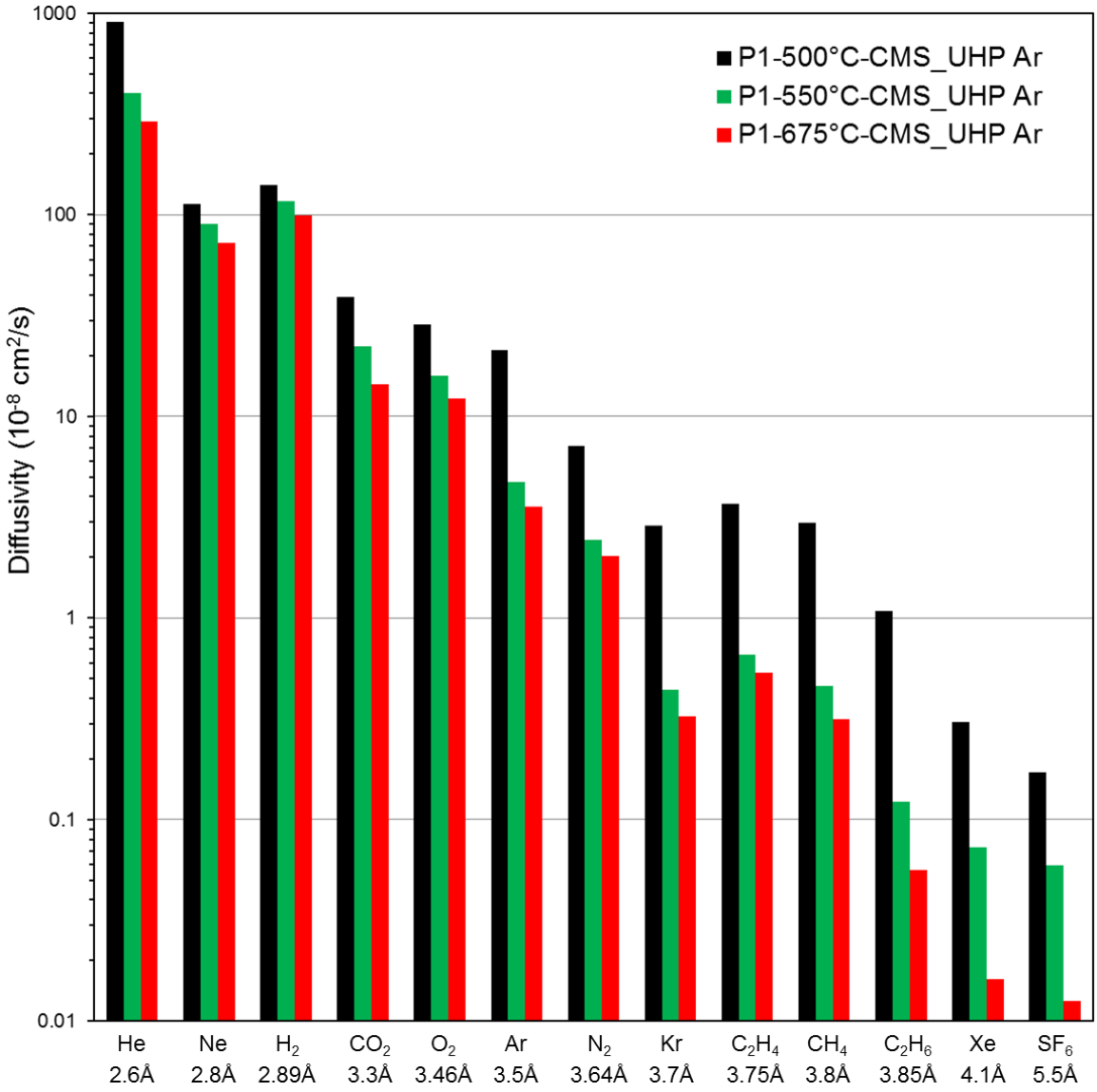

Figure 5.18: Average transport diffusivities of different penetrants for CMS derived from UHP Ar pyrolysis of Matrimid® at 500°C (black), 550°C (green) and 675°C (red). Diffusion coefficients were back-calculated from permeabilities and sorption coefficients at 35°C, 50 psia

As mentioned above, gas transport can be a complicated function of several parameters such as the gas size, shape, critical temperature and interaction with the membrane material. Deconvoluting the effects of sorption and diffusion is useful in understanding some of the transport trends as a function of the penetrant size and

shape. The average transport diffusivity reported in Figure 5.18 however has a built in concentration factor which depends on adsorbate loading, as described in Equations 2.21 and 2.22. This effect can be significant for strongly condensable gases, which does not allow an "apples to apples" comparison of different gases based exclusively on the size and shape. The effects due to the concentration dependence of the transport diffusivity can be especially important in considering the transport of penetrants having similar size but significantly variable critical temperatures, for example, C_2H_4, CH_4 and Kr (see Table 5.4). Thus, in order to study the molecular sieving behavior of CMS slit-shaped pores, it will be more meaningful to consider the thermodynamically corrected, concentration independent diffusivities of the gases (see Appendix B for calculation of corrected diffusivities). The results are shown in Figure 5.19 for CMS derived from UHP Ar pyrolysis of Matrimid® at 500°C, 550°C and 675°C. Clearly, the corrected diffusivities (Figure 5.19) are lower than the transport diffusivities (Figure 5.18), especially for highly condensable gases like CO_2, C_2H_4, C_2H_6, Xe etc. that can show strong concentration dependence. It is interesting to note the corrected diffusivities of C_2H_4, CH_4 and Kr in Figure 5.19. While the corrected diffusivities for C_2H_4, CH_4 and Kr are on the same order of magnitude, it is interesting to note that in case of the 500°C-CMS, the corrected diffusivity of C_2H_4 is slightly lower than CH_4 and Kr. C_2H_4, thus, does not show any particular diffusive advantage in the 500°C-CMS based on its shape when compared to similar sized molecules CH_4 and Kr. This shape advantage is however present for the 675°C-CMS as reflected by the slightly higher corrected diffusivity of C_2H_4 compared to CH_4 and Kr (Figure 5.19). Pyrolysis at 500°C yields a very open CMS framework such that the critical pore dimensions may be too large to differentiate between similar sized penetrants based on their shape. With an increase in the pyrolysis temperature, the CMS framework condenses such that the pores become more restricted and can distinguish between subtle configurational changes resulting from shape differences of

similar sized gas molecules. Thus the corrected diffusivities are more meaningful in understanding the molecular sieving behavior of the engineered CMS membranes in the region of interest based exclusively on the penetrant size and shape. Detailed discussions centered on the effects of shape and size on penetrant diffusivity are presented in Chapter 6.

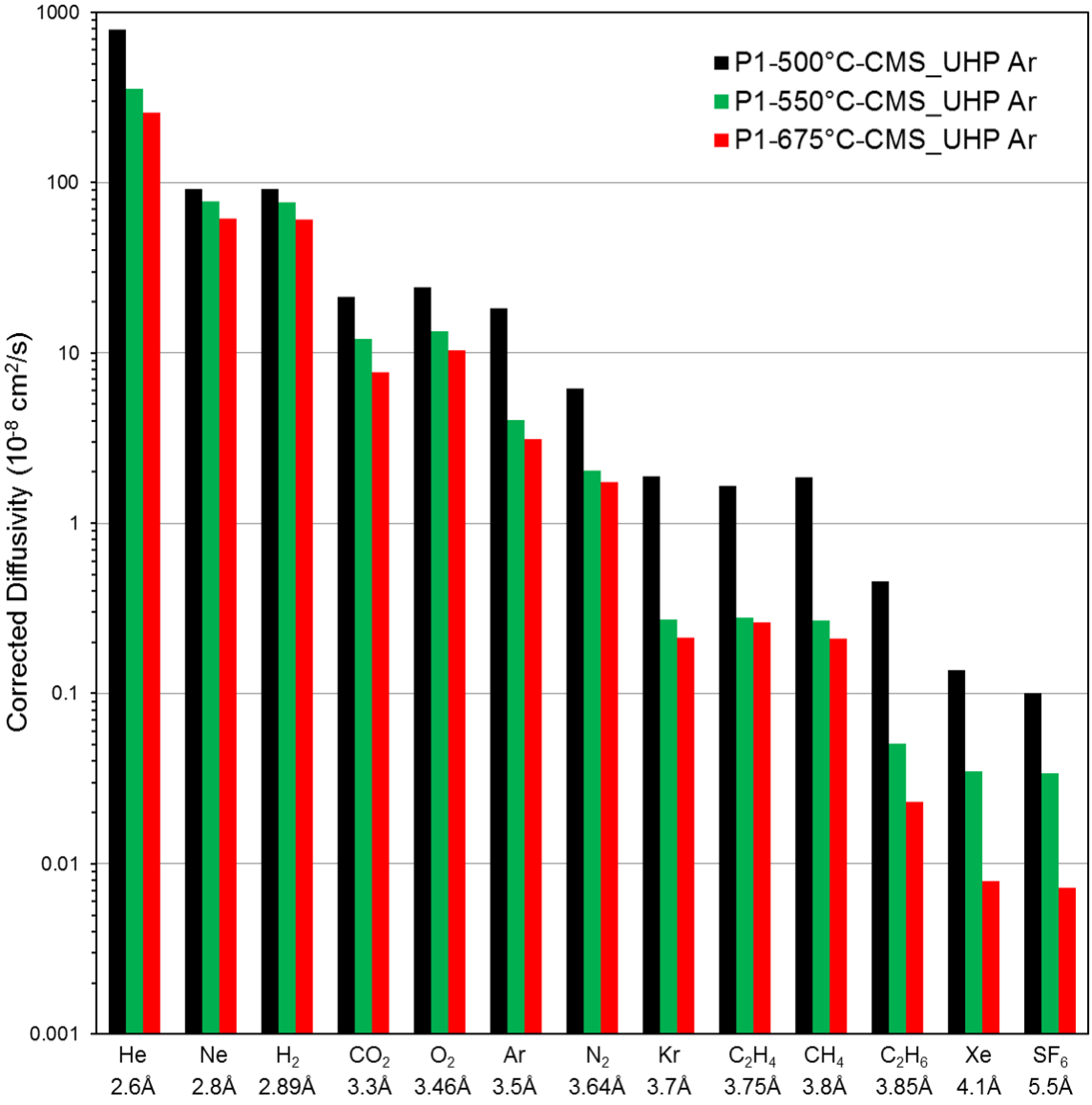

Figure 5.19: Corrected diffusivities of different penetrants at 35°C for CMS derived from UHP Ar pyrolysis of Matrimid® at 500°C (black), 550°C (green) and 675°C (red)

Another critical outcome of the diffusivity trends (Figure 5.19) for different gas molecules is as follows: The diffusion coefficient of He is exceptionally large compared to that of all the other gas molecules, especially for the 500°C-CMS. The diffusion coefficients show a significant drop for molecules over ~ 3.5 Å and reduce to negligible values for molecules over 4 Å in size. This suggests that a large majority of the CMS ultramicropores may lie in the 2.6-3.5 Å range (and possibly < 2.6 Å for the higher pyrolysis temperatures), and the interconnected diffusion-limiting pores may tail off at the larger size end. While the 500°C-CMS may still show significant diffusivities for larger penetrants, the 550°C-CMS and 675°C-CMS by comparison show drastically low diffusivities for penetrants bigger than ~ 4 Å size. This suggests that a majority of the larger diffusion-limiting pores that are present in the 500°C-CMS are eliminated at higher pyrolysis temperatures. The diffusivity trends of the different sized penetrants, shown in Figure 5.19, thus agree with changes in the CMS cartoon structures and hypothetical ultramicropore distributions with pyrolysis temperature, as depicted in Figure 5.4. These features are further discussed below based on the constructed semi-quantitative ultramicropore size distributions for CMS derived from UHP Ar pyrolysis of Matrimid® at 500°C, 550°C and 675°C (i.e. P1-500°C-CMS_UHP Ar, P1-550°C-CMS_UHP Ar and P1-675°C-CMS_UHP Ar) shown in Figure 5.21.

5.2.5.8. Diffusion Size Pore Distribution (DSPD)

The corrected gas diffusivities were used to obtain semi-quantitative critical, interconnected diffusion-limiting ultramicropore distributions, termed as diffusion size pore distribution (DSPD), for CMS derived from UHP Ar pyrolysis of Matrimid® at 500°C, 550°C and 675°C. Gas penetrants were chosen spanning the entire size range, namely He, Ne, CO_2, Ar, N_2, CH_4, Xe and SF_6. The sizes of the gases are reported in Table 5.4.

The effects due to sorption and diffusion are assumed to be decoupled, with diffusion governing the overall CMS transport. In the context of the DSPD, any reference to diffusivity will by default imply corrected diffusivity. Corrected diffusivities can be calculated using the data and equations shown in Appendix B. Semi-quantitative DSPD were constructed as illustrated by the hypothetical distribution shown in Figure 5.20(i) below. Gas penetrants were placed by size along the x-axis spanning the CMS diffusion-size pores, ranging from 2.6 Å (the smallest penetrant tested- He) to 5.5 Å (the largest penetrant tested- SF_6). A gas penetrant may have diffusive access to all interconnected pores larger than its size. As such, the area under the DSPD curve to the right of the marked penetrant size represents the diffusive pores accessible to the gas molecule, and scales with its corrected diffusivity. For example the hashed blue area under the curve in Figure 5.20(i) represents the number density of diffusion-size pores accessible to He and scales with the He diffusivity. The area of the curve between any two gas molecules then scales with the difference of the corrected diffusivities of the two penetrants. For example the pink area under the curve in Figure 5.20(i) scales with the difference of the diffusivities of He and Ne. Given the negligible diffusivity of SF_6 in all cases, it is assumed to be completely excluded from the diffusive pores such that the curve was terminated at 5.5 Å. The idea in Figure 5.20(i) was inspired by preliminary studies of the CMS critical diffusive pore distributions by Kiyono et al. [15] (see Appendix C for details).

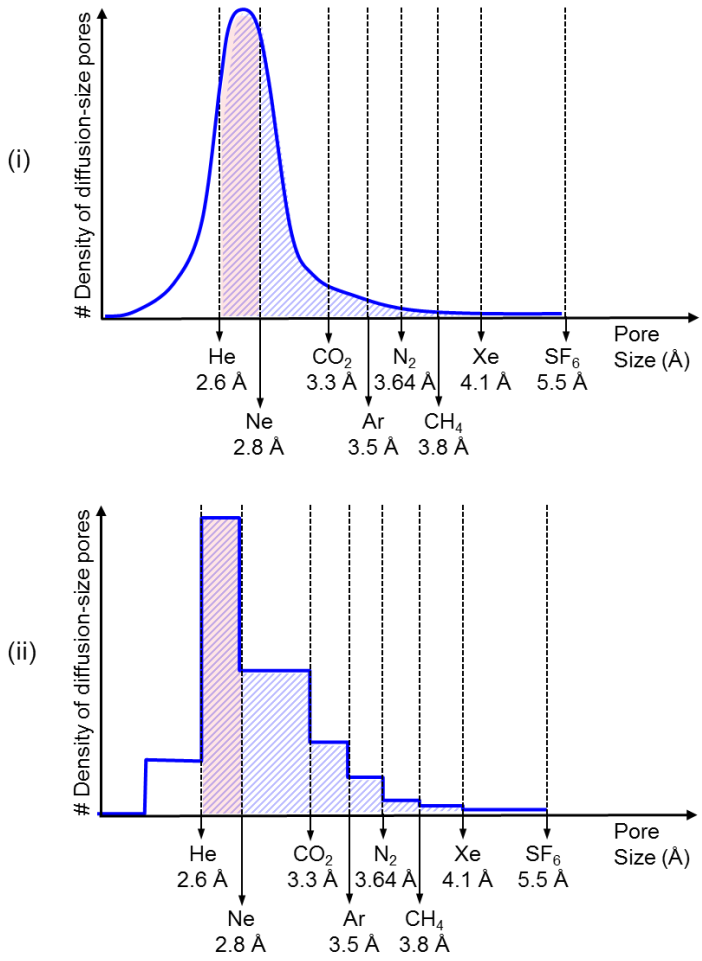

Figure 5.20: Hypothetical representation of a semi-quantitative diffusion size pore distribution (DSPD) based on the corrected diffusivities of different sized penetrants: (i) Smooth distribution curve, (ii) Step distribution curve

DSPDs were constructed as described above. The shape of the curve in Figure 5.20(i) was fit by a trial and error method, which can be extremely tedious. In addition, it may also leave some room for ambiguity in the actual shape of the curve (Appendix C). Thus, instead of representing the distribution as a smooth curve, the distribution was represented in step form, as shown in Figure 5.20(ii) since it corresponds to discrete measurements. As such, the cumulative area under the curve to the right of any penetrant size scales with its corrected diffusion coefficient. For example the hashed

blue area under the step distribution curve in Figure 5.20(ii) represents the number density of diffusive pores accessible to He and scales with the He diffusivity. The area of the rectangle between any two gas molecules then scales with the difference of the corrected diffusivities of the two penetrants. For example the pink rectangular area in Figure 5.20(i) scales with the difference of the diffusivities of He and Ne. Further, the ratio of the areas to the right of two given penetrants may represent the diffusion selectivity for the gas pair. The constructed DSPDs for CMS derived from inert argon pyrolysis of Matrimid® at 500°C, 550°C and 675°C are shown in Figure 5.21. The method of semi-quantitative DSPD construction has been described in detail in Appendix C using P1-675°C-CMS_UHP Ar as an example.

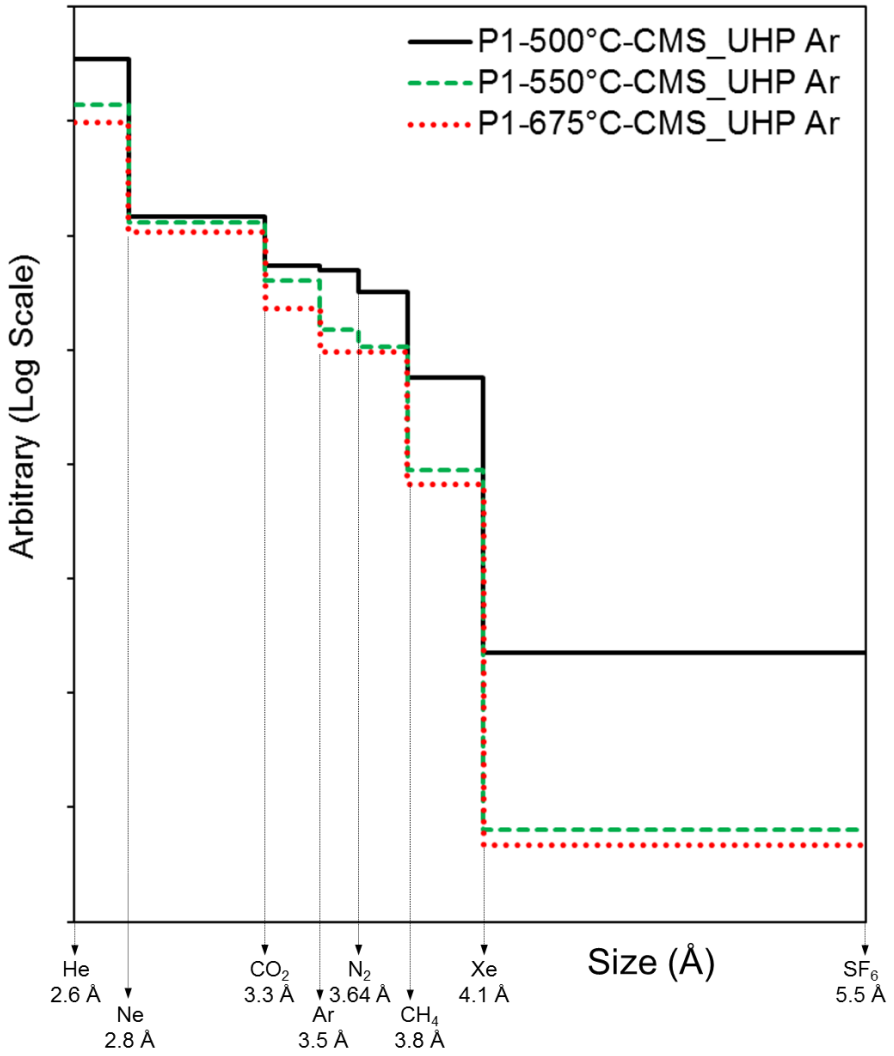

Figure 5.21: Semi-quantitative diffusion size pore distributions (DSPDs) for CMS derived from UHP Ar pyrolysis of Matrimid® at 500°C (black), 550°C (green), and 675°C (red)

As seen from the DSPDs in Figure 5.21, the 500°C-CMS has a large number density of pores in the 2.6-2.8 Å range, which quickly falls off at larger sizes, reflecting the huge difference between the diffusivity of helium and that of the larger gases. The 550°C-CMS and 675°C-CMS show a similar trend, however, by comparison, the number density of pores between 2.6-2.8 Å is much smaller at these higher pyrolysis temperatures. It is possible that for the higher temperature CMS, a significant number of

diffusive pores may be smaller than 2.6 Å; however, this cannot be confirmed by the current gas probe technique. In all cases, the distribution shows a long tail as that the number density of larger pores gets increasingly smaller with size; thus larger penetrants can sample a very small fraction of the total diffusion size pores. The 500°C-CMS distribution however still shows a significant number density of diffusive pores of larger size, that are lost at the higher pyrolysis temperatures. This is represented by the relatively smaller area under the curve in this region for the 550°C-CMS and 675°C-CMS compared to the 500°C-CMS. A close comparison of the DSPDs for the 550°C-CMS and the 675°C-CMS reveals that the ratio of the areas of the two curves in the 3.6-3.8 Å range is much smaller compared to the ratio of the areas of the two curves between 3.8-4.1 Å (Figure 5.21). Since C_2H_4 (3.75 Å) lies in the 3.6-3.8 Å region, the C_2H_4 diffusivities for the 550°C-CMS and the 675°C-CMS are thus quite similar. On the other hand, for C_2H_6 (3.85 Å) which lies in the 3.8-4.1 Å range, the diffusivity is higher for the 550°C-CMS compared to the 675°C-CMS. Thus, the C_2H_4/C_2H_6 diffusion selectivity for the 550°C-CMS is lower than for the 675°C-CMS. The experimental C_2H_4/C_2H_6 corrected diffusion selectivity for the 550°C-CMS and 675°C-CMS are ~5.6 and ~10.4 respectively. Thus analysis of the areas under the DSPD curves helps explain why the optimum pyrolysis temperature for Matrimid® lies at ~675°C for C_2H_4/C_2H_6 separation (see Figure 5.6). The semi-quantitative diffusion size pore distributions shown in Figure 5.21 are thus useful in explaining the transport properties and molecular sieving behavior of CMS derived from Matrimid® at different pyrolysis temperatures in relation to the pore structure.

5.2.6. Translating Carbon Molecular Sieve Dense Film Properties to Hollow Fibers

The translation of CMS dense film properties into the CMS hollow fiber form, which is preferred for practical use, was pursued by Liren Xu in the Koros Group. Defect-free Matrimid® precursor fibers were used for pyrolysis. Details of the spinning conditions have been reported previously by Xu et al. [19]. The pyrolysis conditions were maintained the same as those specified in Section 5.2.1 for dense films. Pure gas C_2H_4 and C_2H_6 permeation tests were used to evaluate the separation properties of CMS hollow fibers at 35°C. Details of hollow fiber permeation measurements can be found elsewhere [19]. Figure 5.22 shows the C_2H_4 permeance and the C_2H_4/C_2H_6 selectivity for the CMS fibers as a function of the final pyrolysis temperature. A comparison of Figures 5.2 and 5.22 shows that the dense film permeability and the hollow fiber permeance follow a similar trend with the pyrolysis temperature, as does the C_2H_4/C_2H_6 selectivity. Additionally, very good agreement was obtained between the dense film and the hollow fiber selectivity at all pyrolysis temperatures.

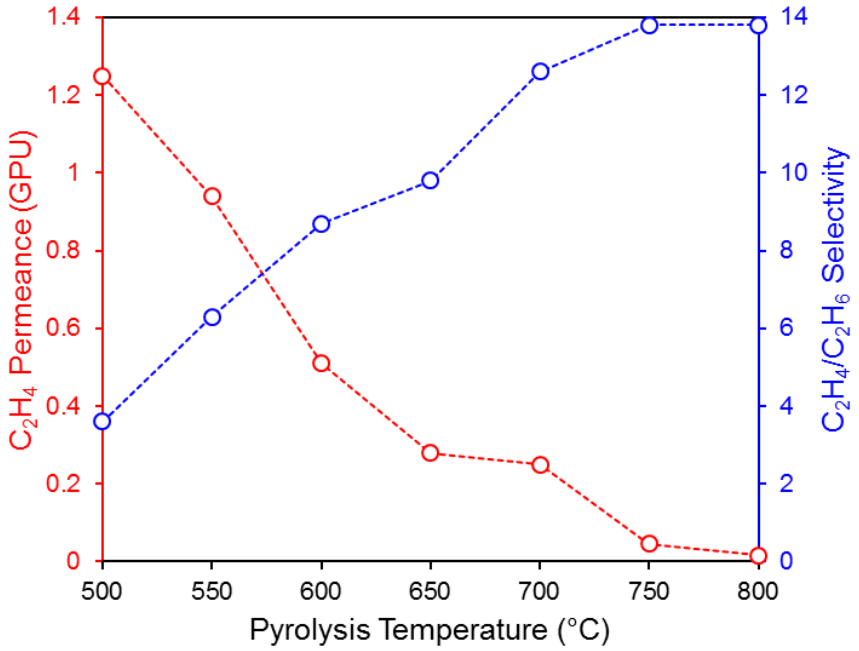

Figure 5.22: Effect of final pyrolysis temperature on C_2H_4 permeance and C_2H_4/C_2H_6 selectivity of CMS hollow fibers derived from vacuum pyrolysis of Matrimid® [19]

As in the case of dense films, the pyrolysis temperature range of ~ 650-675°C/700°C was found to be optimum for C_2H_4/C_2H_6 separation using CMS hollow fibers, and a high selectivity of ~10-12 was obtained. However, while the dense film configuration yields an attractive permeability higher than that of the starting precursor, the permeance in the hollow fiber configuration drops drastically. The reason for this loss in flux in the CMS hollow fiber form is as follows: Due to intensive heat treatment during pyrolysis the porous substructure of the fiber collapses in going from the precursor to the CMS fiber. The fundamental cause for this collapse is the increased polymer chain flexibility and loss in the storage modulus close to the glass-rubber transition temperature of the polymer [19]. This results in an increased effective separation layer thickness in the CMS hollow fiber. As a result, the flux of the Matrimid® derived CMS hollow fibers derived decreases drastically.

While several approaches including precursor modification are being pursued in the Koros Group to avoid this undesired permeance loss resulting from substructure collapse in Matrimid®, a fundamental alternative is to use a different starting material. 6FDA-DAM and 6FDA:BPDA-DAM are much more rigid polyimides compared to Matrimid® with higher glass-rubber transition temperatures (Table 4.1) that are closer to the decomposition temperature of the polymer. Additionally, 6FDA-DAM and 6FDA:BPDA-DAM have a higher fractional free volume compared to Matrimid® (Table 4.1), due to the presence of bulky -CF_3 groups, which is expected to yield a more open CMS structures with higher permeability. Pyrolysis of 6FDA:BPDA-DAM has also been shown to yield bulky fluorine-based by-products like CHF_3 and trace HF besides CO, CO_2 and CH_4 evolved during Matrimid® pyrolysis [3, 20]. This presumably leads to a more open pore structure for CMS derived from 6FDA:BPDA-DAM resulting in higher permeability in comparison to Matrimid®. This should be true for 6FDA-DAM pyrolysis as well. SEM images of CMS hollow fibers [19, 21] derived from Matrimid®, 6FDA-DAM and 6FDA:BPDA-DAM (Figure 5.23) show that the 6FDA-polymers have lower substructure collapse compared to Matrimid®. A detailed account of this can be found in Liren Xu's thesis in the Koros Group. 6FDA:BPDA-DAM is in fact the most preferred precursor in terms of morphology and retaining asymmetry in the CMS hollow fiber form.

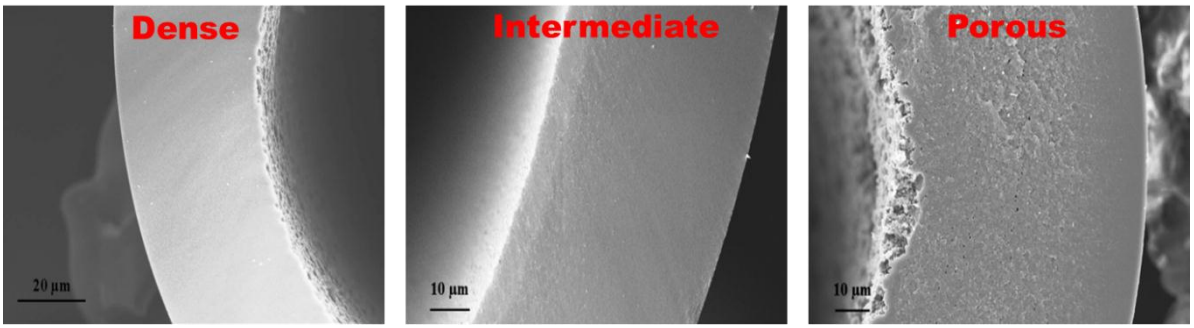

Figure 5.23: SEM images of CMS hollow fibers derived from (i) Matrimid®, (ii) 6FDA-DAM and (iii) 6FDA:BPDA-DAM [19, 21]

Thus, in terms of the hollow fiber macro-morphology and the expected "open" CMS microstructure of the 6FDA-based CMS compared to Matrimid® CMS, 6FDA-based precursors could be more promising in achieving higher C_2H_4 flux which is critical to practical membrane applications. A detailed analysis of CMS dense films derived from both 6FDA-DAM and 6FDA:BPDA-DAM is presented in Sections 5.4 and 5.5 respectively.

5.3. Physical Aging in Carbon Molecular Sieve Membranes

Before discussing performance optimization of CMS derived from 6FDA-based precursors, it is important to discuss the time-dependent transport behavior of CMS membranes, resulting from a physical aging phenomenon, encountered in this work. This was especially significant in CMS membranes derived from 6FDA-DAM and 6FDA:BPDA-DAM. As seen above, CMS dense films derived from Matrimid® showed very consistent results for multiple measurements made on films derived using the same

pyrolysis conditions. Additionally, good agreement between C_2H_4/C_2H_6 selectivity in the dense film and the hollow fiber forms was reported (see Figures 5.2 and 5.22). Unlike CMS membranes derived from Matrimid®, the permeation results for CMS derived from 6FDA-based precursors showed significant scatter in data for multiple films fabricated using the same pyrolysis conditions. The dense film and the hollow fiber configuration were also not found to agree too well. The complicated asymmetric morphology of the CMS hollow fibers and the differences in polymer chain alignment from shear elongation effects during fiber spinning vs. slow vitrification in dense films may result in differences from the dense films form. It was however necessary to extensively probe the causes for inconsistencies in CMS performance within the dense film form for multiple tests. Careful control and monitoring of the CMS behavior and performance revealed during a later stage in this study that the CMS transport properties can show history and time dependence. This was found both in the CMS dense film configuration in the current study, and in the CMS hollow fiber form by Liren Xu in the Koros Group. The discovery introduces another controlling variable for CMS performance. The phenomenon was termed "physical aging" in CMS membranes and is discussed in detail below.

5.3.1. Physical Aging in Glassy Polymers

As described in Section 2.3, the detailed mechanism involved in gas transport in polymers can be different at temperatures below and above the glass-rubber transition temperature (T_g) of the polymer, i.e. depending on whether the polymer is in a rubbery state (above T_g) or a glassy state (below T_g) [22]. The differences essentially arise from the characteristic scales of the micromotions that can occur at a segmental level in rubbery and glassy polymers. In glasses well below the T_g, the intramolecular backbone motions occurring over time scales of seconds or microseconds are much less extensive

than in rubbers. The severely hindered segmental motions and longer relaxation times result in "trapped packing defects" in the polymer matrix below the T_g, referred to as "excess free volume" or "unrelaxed volume" (see Figure 2.6). As such, glassy polymers are not in a state of true thermodynamic equilibrium, and, over time, tend to approach equilibrium packing by eliminating the excess free volume. This is referred to as "physical aging", which results in time-dependent transport in glassy polymers, with a decrease in the gas permeability and an increase in selectivity over time [22, 23]. Figure 5.24 shows a cartoon representation of physical aging in glassy polymers.

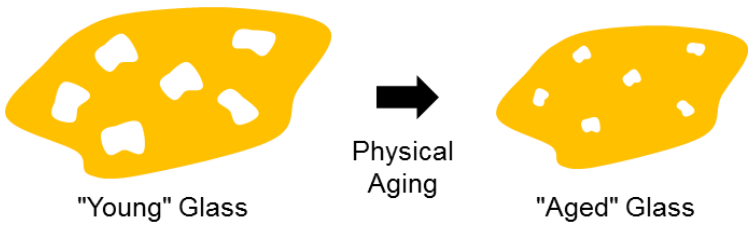

Figure 5.24: Cartoon representation of physical aging in glassy polymers showing the trapped excess free volume eliminated over time due to aging

As described in Section 2.3.2, gas sorption in glassy polymers is well described by a dual mode sorption model. The gas sorbed in a glassy polymer consists of two distinct molecular populations: (i) molecules sorbed in the dense polymer matrix by an ordinary dissolution process described by Henry's law isotherm, similar to that above T_g (as in the case of rubbery polymers), and (ii) molecules sorbed in a limited number of holes or microvoids in the polymer matrix corresponding to the unrelaxed excess free volume in glassy polymers, described by a Langmuir isotherm [22, 23]. A reduction in the number of microvoid Langmuir sorption sites as a consequence of physical aging

results in decreased sorption in glassy polymers, as illustrated in Figure 5.25, thus affecting overall transport behavior.

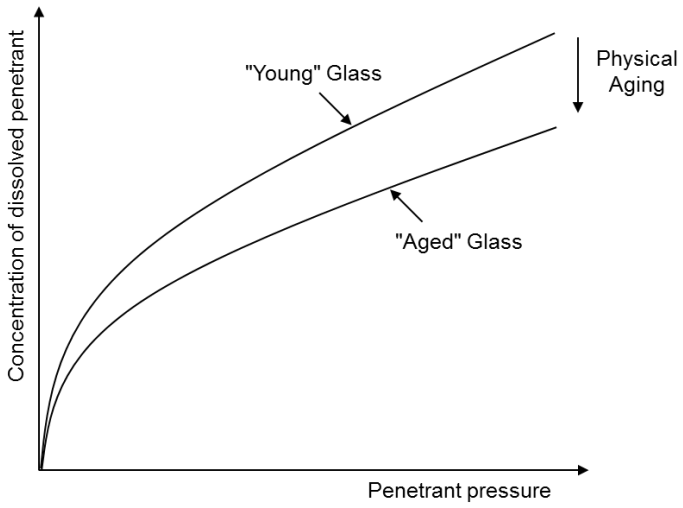

Figure 5.25: Effect of physical aging on sorption behavior of glassy polymers

Pinnau and coworkers [24, 25] were the first to show dramatic time-dependent gas transport properties in asymmetric films. Pfromm & Koros [26] later showed similar time-dependent behavior in free standing films of polysulfone and polyimide 6FDA-IPDA. Their work showed strong dependence of physical aging on film thickness, demonstrating evidence of accelerated aging in thin films and a less dramatic time dependence in thicker films. Physical aging behavior is also dependent on the polymer itself. Recently, Cui et al. [27] studied the aging behavior of two glassy 6FDA-based polyimides: 6FDA-DAM and 6FDA-mPDA. Their results showed that owing to its high fractional free volume (FFV), 6FDA-DAM thin films have very high O_2 permeability at an early stage, followed by an order of magnitude decrease in permeability relative to the initial value over a 1000 hour period. 6FDA-mPDA thin films were shown to have

moderate aging rates comparable to thin films made from polyimides such as Matrimid® with much lower FFV. The time-dependent behavior of polymers also depends on its previous history such as thermal treatment, exposure to highly condensable penetrants etc. For example, Huang & Paul [28] studied the effect of temperature of physical aging of thin glassy films based on polysulfone and poly(2,6-dimethyl-1,4-phenylene oxide). For both polymers, their results showed that aging rate increases with aging temperature for a given film thickness. In fact, thermal annealing is often used to accelerate aging in glassy polymers and to quickly bring its performance to a stable value. The study of physical aging in glassy polymers is important not just from an academic perspective but also from a practical stand point due to the presence of a thin separation layer in asymmetric hollow fibers.

5.3.2. Discovery of Physical Aging in Carbon Molecular Sieve Membranes

Aging and stability issues reported in the literature for CMS membranes are generally related to changes in the CMS performance resulting from exposure to different environments, for example, air, moisture, organic contaminants etc. Several researchers have reported the adsorption of water to significantly affect CMS membrane performance. Jones and Koros [29] reported pronounced permeability loss with increasing water activity. According to Gawrys et al. [30], at low relative humidity, only active polar centers may be involved and the adsorption is weak such that the negative effects on CMS separation may be undone. As the relative humidity increases, the loss of separation performance may be significant. Hydrogen bonding between neighboring water molecules may lead to formation of clusters of adsorbed water molecules which may block the CMS pore structure. Figure 5.26 shows a cartoon representation of the hypothetical effect of moisture on the CMS pore structure.

Figure 5.26: Cartoon representation of CMS aging in presence of moisture

Kiyono [3] investigated the effect on CMS performance due to prolonged exposure to moisture at 80% relative humidity (RH), and reported an increasing loss in performance over time. Sorption analysis of the pristine and exposed CMS membranes showed a decrease in the Langmuir saturation capacity in CMS films exposed to moisture, thus suggesting that water molecules may form clusters in the CMS micropore sites. Further, regeneration studies done by heating the humidity exposed CMS films under vacuum at 105°C resulted only in partial recovery of performance as reported by Kiyono [3]. These results are summarized in Figure 5.27. Similar observations have also been documented by Menendez & Fuertes [31] and Lagorsse et al. [32].

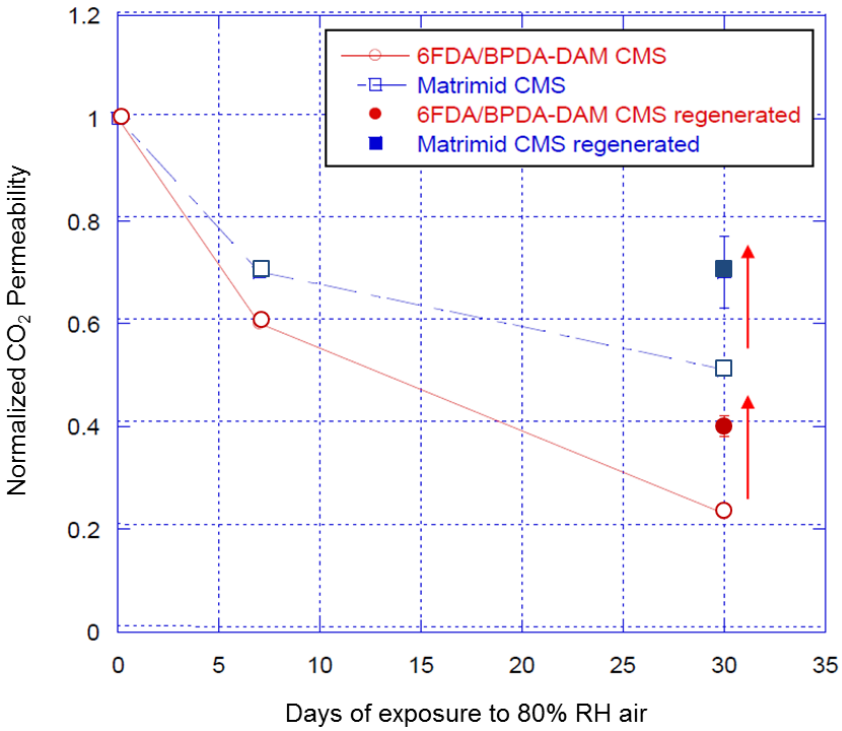

Figure 5.27: Plot showing effect of humidity on CO_2 permeability of CMS membranes and performance recovery from regeneration at 105°C under vacuum [3]

In order to counteract CMS performance loss in presence of moisture, several researchers have investigated the effect of coating the membrane with a highly permeable and hydrophobic film which does not prohibitively reduce the flux of the membrane. The resulting carbon composite membrane shows greater resistance to humidity while retaining good performance [3, 33, 34].

Both Menendez & Fuertes [31] and Lagorsse et al. [32] also investigated the effect of CMS storage in nitrogen and in oxygen and/or dry air on CMS performance. While no performance loss was observed under nitrogen storage conditions, prolonged exposure to oxygen and dry air was found to result in CMS aging resulting from a slow irreversible chemisorption of oxygen at the CMS pore constrictions (similar to the oxygen doping phenomenon at higher temperatures, as described in Section 2.4.3). Further,

CMS storage in pure propylene was not shown to cause any damage to the CMS performance [31, 32].

Jones & Koros [35] investigated the effect of CMS exposure to organic contaminants such as hexane, toluene, phenol, and pump oil etc. and reported significant permeance loss. Because of their organophilic nature, CMS membranes are apparently highly susceptible to adverse effects from exposure to organics contaminants which may adsorb into the membrane and block the CMS pores. They also reported a promising regeneration technique based on the use of pure propylene at unit or near unit activity as a cleaning agent to reverse the adverse effects due to organic exposure [35].

The studies reported above all suggest that CMS performance can be adversely affected in the presence of oxygen, moisture, heavy organic etc. CMS performance may however be preserved by storage in environments that eliminate the presence of such interacting molecules, for example by storage in inert, dry conditions, under vacuum or in the presence of hydrocarbon feeds such as pure propylene. The existence of a "physical aging" effect similar to glassy polymers, which occurs by the natural tendency of the system to move towards thermodynamic equilibrium, has not been reported previously in CMS membranes. Such behavior may not typically be expected to occur in CMS membranes owing to their rigid nature vs. the flexible nature of polymer chains. It was however discovered in the current study that CMS membranes derived from glassy polymers may exhibit a behavior similar to the parent material and show time-dependent performance resulting from physical aging.

The first evidence of physical aging was observed in CMS membranes derived from 6FDA-DAM. As mentioned before, early studies of 6FDA-based CMS membranes showed considerable scatter in performance for multiple films fabricated using the same pyrolysis conditions. An example of pure gas C_2H_4 and C_2H_6 permeation measurements

made on several CMS dense films fabricated from UHP Ar pyrolysis of 6FDA-DAM at 675°C using Protocol 1 (P2-675°C-CMS_UHP Ar) is shown in Figure 5.28.

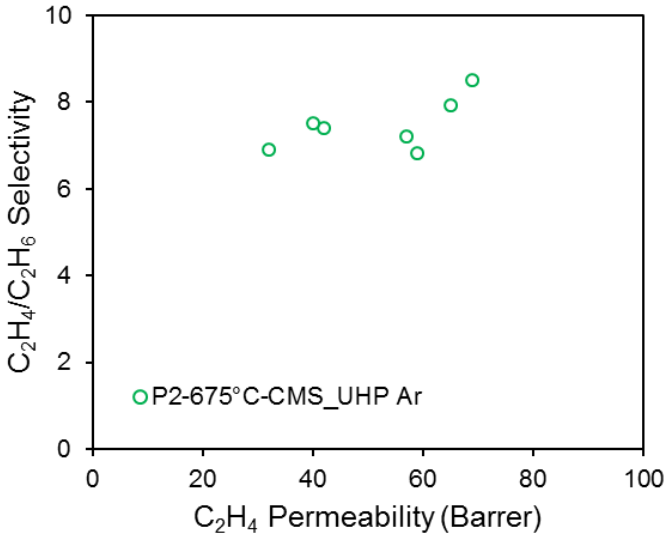

Figure 5.28: Pure gas C_2H_4/C_2H_6 separation performance of multiple CMS dense films derived from inert pyrolysis of 6FDA-DAM at 675°C (35°C, 50psia)

Considerable scatter in the data led us to carefully monitor and control not just the CMS fabrication conditions but also the testing procedures for CMS dense films. Multiple permeation measurements on the same film over prolonged testing periods (~ 4 weeks) revealed that despite inconsistency in the initial separation performance CMS films derived using the same pyrolysis conditions eventually converged to the same performance. This is illustrated for two 6FDA-DAM CMS films (P2-675°C-CMS_UHP Ar) in Figure 5.29 below. The main difference between the two films was the initial testing time after pyrolysis: while Film 1 was masked for permeation measurement immediately after pyrolysis, Film 2 was stored under vacuum for ~ 2 days prior to masking.

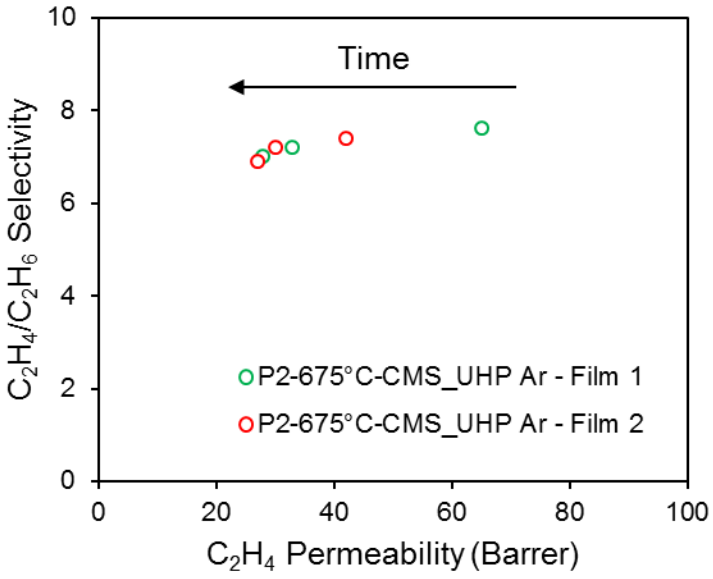

Figure 5.29: Multiple measurements over a ~ 4 week testing period illustrate that pure gas C_2H_4/C_2H_6 separation performance for two P2-675°C-CMS_UHP Ar films eventually converges to a similar value despite initial inconsistency

These preliminary tests demonstrated that (i) C_2H_4/C_2H_6 separation performance for CMS dense films derived from 6FDA-DAM changes over time showing a decrease in C_2H_4 permeability, (ii) CMS performance reaches a stable value over time and the C_2H_4/C_2H_6 separation performance for multiple films derived using the same pyrolysis conditions eventually converge to a consistent value. It should be noted that the CMS dense films were either continuously exposed to pure C_2H_4 or C_2H_6 feeds during permeation measurements or under active vacuum in between runs, thus eliminating the possibility of aging resulting from exposure to air (oxygen) or moisture. The possibility of membrane exposure to pump oil vapor should also not be likely since an aluminum foreline trap was used; however this possibility was further verified as will be discussed shortly. The time-dependent behavior observed thus essentially suggested the possibility of a physical aging effect in CMS membranes derived from 6FDA-DAM.

A similar behavior was observed by Liren Xu in the Koros Group for C_2H_4/C_2H_6 separation performance of CMS hollow fibers derived from 6FDA-DAM. Figure 5.30 shows the time dependent performance of CMS hollow fibers fabricated from UHP Ar pyrolysis of 6FDA-DAM precursor hollow fiber at 675°C using Protocol 1. During use, the fiber module was either under active C_2H_4 or C_2H_6 permeation test or under vacuum between runs. For the remaining period, when not in use the module was capped and stored in atmospheric air.

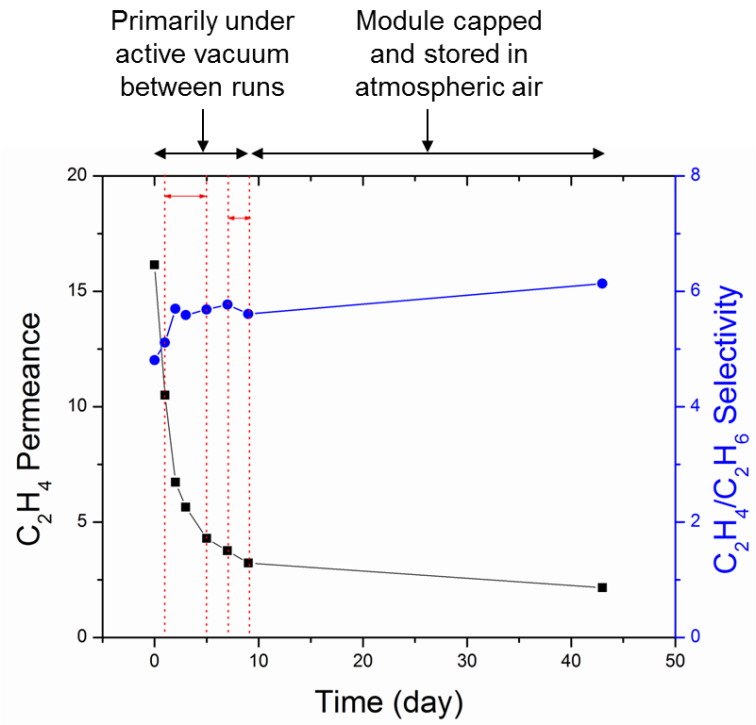

Figure 5.30: Aging of CMS hollow fiber derived from UHP Ar pyrolysis of 6FDA-DAM at 675°C using Protocol 1 (Data courtesy: Liren Xu)

As seen from Figure 5.30, the C_2H_4 permeance decreased with time, while the C_2H_4/C_2H_6 selectivity increased initially and then remained fairly constant. A drastic loss

in permeance was observed over the first few days following CMS fabrication, and it quickly approached a stable value. In atmospheric storage conditions, permeance loss might have been related to slow aging attributed to oxygen chemisorption at the CMS constrictions. This may explain the slight increase in selectivity as shown by the last measurement point in Figure 5.30. However, aging effects due to air (oxygen) or moisture would be eliminated during the initial testing period (up to day 10) when the fiber module was either under active feed or under active vacuum. Again the possibility of vacuum pump oil vapor should not be present but was nevertheless verified. As mentioned earlier, Jones & Koros reported that the performance of CMS membranes exposed to organic contaminants could essentially be recovered to that of the pristine CMS membranes by using pure propylene at or near unit activity as a cleaning agent. The current CMS hollow fiber membranes from Liren Xu's work however did not show performance recovery following propylene cleaning, thus suggesting that the performance loss may not be due to exposure to vacuum pump oil. Further tests by Liren Xu in the Koros Group on CMS hollow fibers derived from 6FDA-DAM showed that membranes stored in inert argon (UHP Grade, Airgas) also showed loss in permeance over time. Storage in inert argon eliminates the possibilities of performance loss as a result of aging due to exposure to air or oxygen, moisture and organic contaminants. These findings thus confirmed the presence of a physical aging effect in CMS membranes derived from 6FDA-DAM.

In order to further probe this time dependent behavior in 6FDA-DAM-based CMS membrane, pure gas C_2H_4 and C_2H_6 sorption measurements were carried out on CMS dense films derived from UHP Ar pyrolysis of 6FDA-DAM at 675°C (P2-675°C-CMS_UHP Ar). As seen from the sorption isotherms in Figure 5.31, the Langmuir saturation capacity (C'_H) for both C_2H_4 and C_2H_6 decreases over time. In fact, for both test 1 and test 2, the experimental sorption data shows a poor fit (R^2 ~ 0.92) to the

Langmuir isotherm model whereas the experimental data for test 3 follows Langmuir behavior (R^2 ~ 0.98). The C'_H and b values are summarized in Table 5.5.

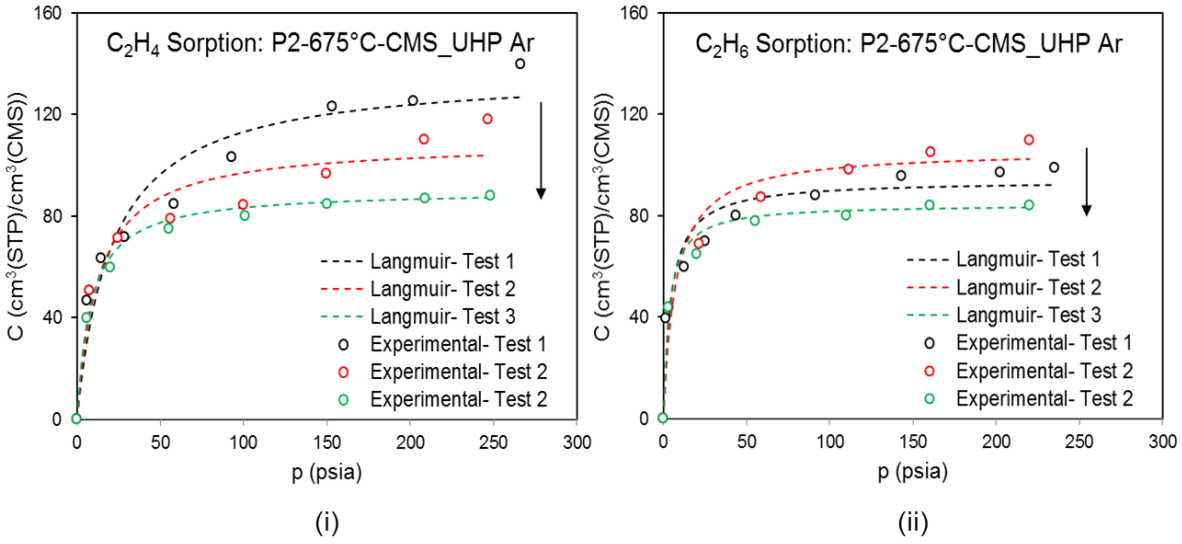

Figure 5.31: Time dependent behavior of pure gas C_2H_4 and C_2H_6 sorption isotherms for P2-675°C-CMS_UHP Ar

Table 5.5: Time dependent behavior of Langmuir isotherm parameters for sorption isotherms of C_2H_4 and C_2H_6 sorption isotherms for P2-675°C-CMS_UHP Ar as shown in in Figure 5.34

		C_2H_4		
		Test 1	Test 2	Test 2
C'_H	[cm^3/cm^3]	136.8	109.2	93.1
b	[1/psia]	0.048	0.080	0.145
		C_2H_6		
		Test 1	Test 2	Test 2
C'_H	[cm^3/cm^3]	105.8	93.9	84.6
b	[1/psia]	0.136	0.221	0.239

A decrease in C'_H over time suggests a behavior somewhat analogous to the physical aging phenomenon in glassy polymers. As described in Section 5.3.1, over time the glassy polymer matrix relaxes eliminating trapped excess free volume. This reduces the number of Langmuir sorption sites resulting in a decrease in C'_H for the "aged" glass compared to "young" glass, as illustrated in Figure 5.25. It is hypothesized that CMS membranes derived from highly rigid glassy polymers may exhibit a physical aging behavior somewhat analogous to that seen in the parent material. CMS membranes are believed to be formed of randomly oriented and disordered graphene-like sheets with pores formed from packing imperfections (see Section 2.2). These graphene-like sheets may be present in a thermodynamically unstable state when the CMS membrane is just fabricated via pyrolysis of the glassy polymer precursor. Over time, they may rearrange to a more stable state with denser packing, analogous to glassy polymers relaxing over time by elimination of excess trapped free volume. This results in a decrease in permeability (or permeance) over time. Figure 5.32 shows a cartoon illustration of this hypothetical concept. Of course, the time scale of relaxation in CMS may be much smaller than for glassy polymers. The sorption behavior in CMS as reported above (Figure 5.31) supports this hypothesis. As seen from sorption test 1 and 2, the experimental C_2H_4 and C_2H_6 sorption data show a poor fit to Langmuir isotherm, but actually fit the dual mode sorption model better, suggesting the presence of a "glassy" dual environment behavior in CMS during the early stages following pyrolysis. The aged CMS membranes show a good fit of experimental sorption data to the Langmuir model (test 3), as expected for molecular sieving materials.

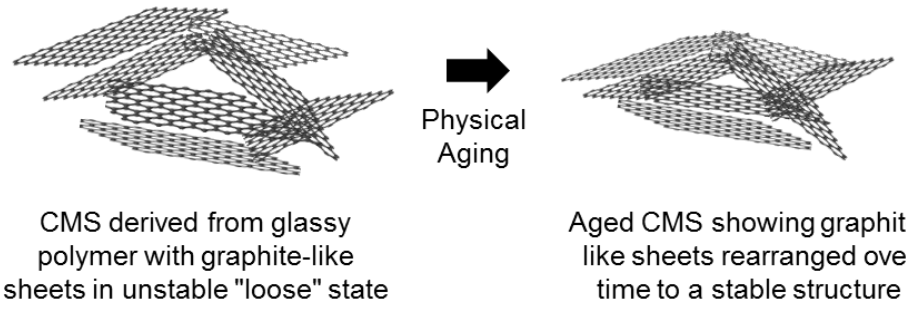

Figure 5.32: Cartoon representation of physical aging in CMS membranes derived from glassy polymer precursors

5.3.3. Comparison of Physical Aging in Carbon Molecular Sieve Membranes Derived from Different Polymer Precursors

The effect of physical aging over time is much easier to monitor in CMS hollow fibers compared to CMS dense films. This is related to differences in the separation layer thickness in the two membrane configurations as well as testing procedures. The dense film thickness for the CMS films is typically in the range of 60-70 µm while for the CMS hollow fibers discussed earlier it is less than ~10 µm. Details of dense film permeation measurement are described in Section 3.4.1. In case of dense film testing, the film is initially maintained under active vacuum for over 24 hours in order to degas the film and the adhesive aluminum tape used for masking, in order to achieve a low enough leak rate. This initial vacuum may have already resulted in significant physical aging of the dense film prior to the first measurement. Additionally, for pure gas measurements, the order of testing is C_2H_4 followed by C_2H_6. The dense film must be degassed for a time period equal to at least ten times the time lag of C_2H_4 prior to testing C_2H_6 to ensure that the leak rate is low enough. This means that the dense film would have aged further during the vacuum time between C_2H_4 and C_2H_6. This could result in

the overestimation of the permselectivity when the membrane is still in an unstable state. It may thus be more appropriate to use mixed gas measurements to monitor physical aging. In the case of hollow fiber permeation, the membrane requires degassing under vacuum for only a few hours before the first measurement, since the separation layer thickness is much smaller in this case. The same is true for degassing between runs. Additionally, the flux in the hollow fiber configuration is much higher than in the dense film configuration owing to its extremely high surface area to volume ratio, and this, coupled with the thin separation layer, implies that apparent steady state can be sensed much faster in fibers than in films. As a result, a series of rapid permeation measurements can be made on hollow fibers in a short period, which is not possible in dense films. Details of fiber permeation experiments have been reported by Xu et al. [19]. In order to monitor the physical aging behavior in CMS dense films, the testing protocol was modified from the one described in Section 3.4.1. Mixed gas measurements were used to monitor the trend of permeability and selectivity over time. Additionally, the dense film was not initially degassed for over 24 hours under vacuum after the masking process. Instead freshly fabricated and masked films were degassed for only 3-4 hours under vacuum and then exposed directly to C_2H_4/C_2H_6 mixed gas for the first measurement. The measurement was allowed to run for days till steady state was achieved. After this initial test, the films were maintained under active vacuum until test 2, however other gases were also tested between subsequent C_2H_4/C_2H_6 mixed gas tests. Nevertheless, the membrane was either under active test conditions in presence of feed gas or under active vacuum in between tests.

Controlled studies following the testing protocol described above were carried out to investigate the effect of physical aging in CMS derived from all three precursors: Matrimid®, 6FDA-DAM and 6FDA:BPDA-DAM. Fresh CMS samples were prepared from all three precursors by pyrolysis in UHP Ar purge at 675°C using Protocol 1. A series of

mixed gas tests were conducted over time on the resulting CMS samples, designated as P1-675°C-CMS_UHP Ar, P2-675°C-CMS_UHP Ar and P3-675°C-CMS_UHP Ar. The results are summarized in Figures 5.33, 5.34 and 5.35 respectively.

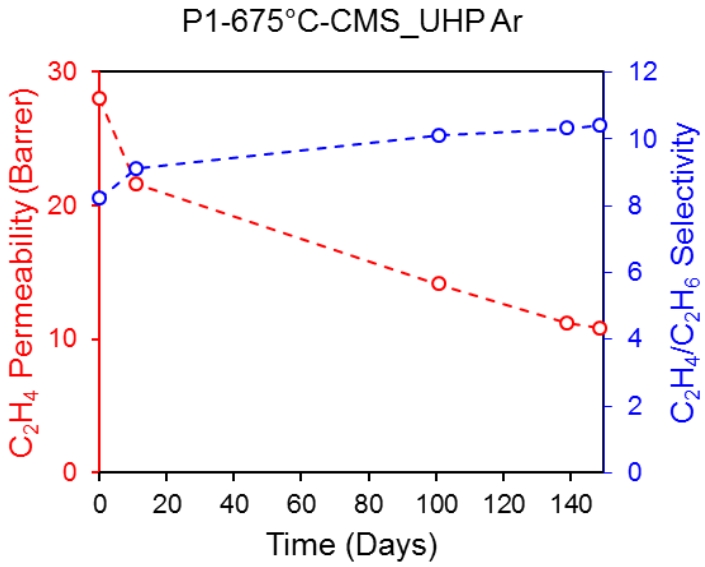

Figure 5.33: Effect of physical aging on C_2H_4 permeability and C_2H_4/C_2H_6 selectivity of CMS dense film derived from UHP Ar pyrolysis of Matrimid® at 675°C

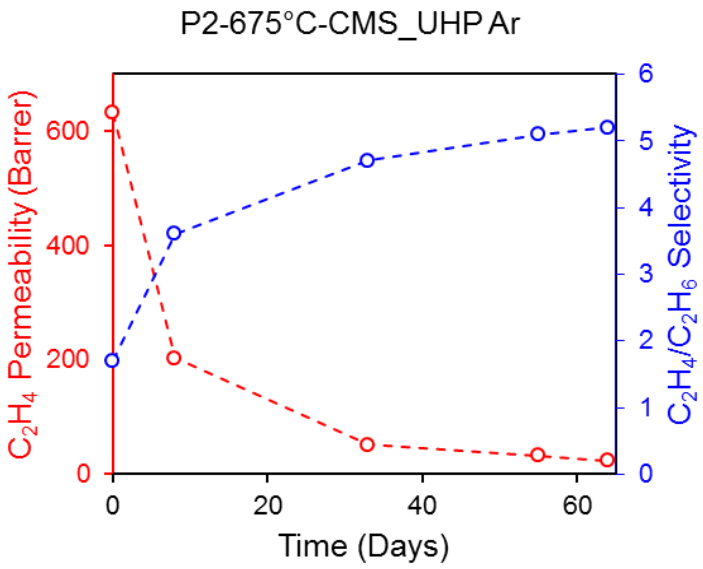

Figure 5.34: Effect of physical aging on C_2H_4 permeability and C_2H_4/C_2H_6 selectivity of CMS dense film derived from UHP Ar pyrolysis of 6FDA-DAM at 675°C

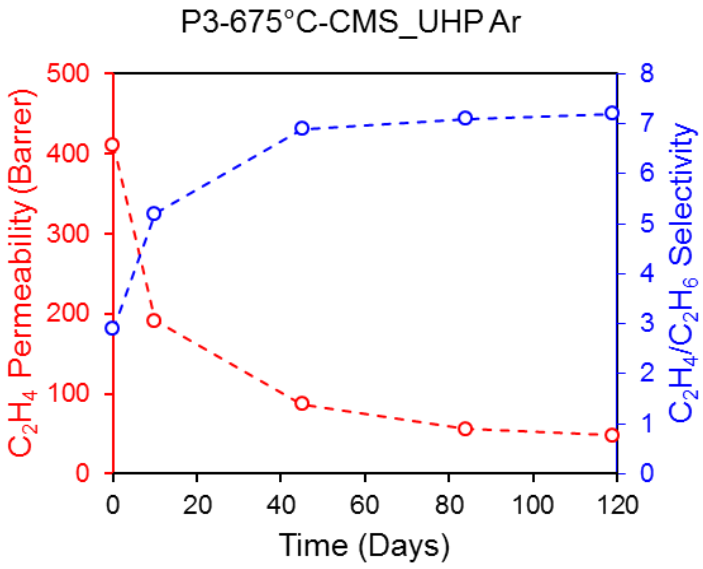

Figure 5.35: Effect of physical aging on C_2H_4 permeability and C_2H_4/C_2H_6 selectivity of CMS dense film derived from UHP Ar pyrolysis of 6FDA:BPDA-DAM at 675°C

Figure 5.36(i) shows the normalized C_2H_4 permeability (P_t/P_0, where P_0 is the permeability on day 0 and P_t is the permeability at time t in days) over time and Figure

5.36(ii) shows the normalized C_2H_4/C_2H_6 selectivity (α_t/α_0, where α_0 is the selectivity on day 0 and α_t is the selectivity at time t in days) over time of the three CMS dense films: P1-675°C-CMS (Matrimid®), P2-675°C-CMS (6FDA-DAM) and P3-675°C-CMS (6FDA:BPDA-DAM), overlaid on the same plot for easy comparison.

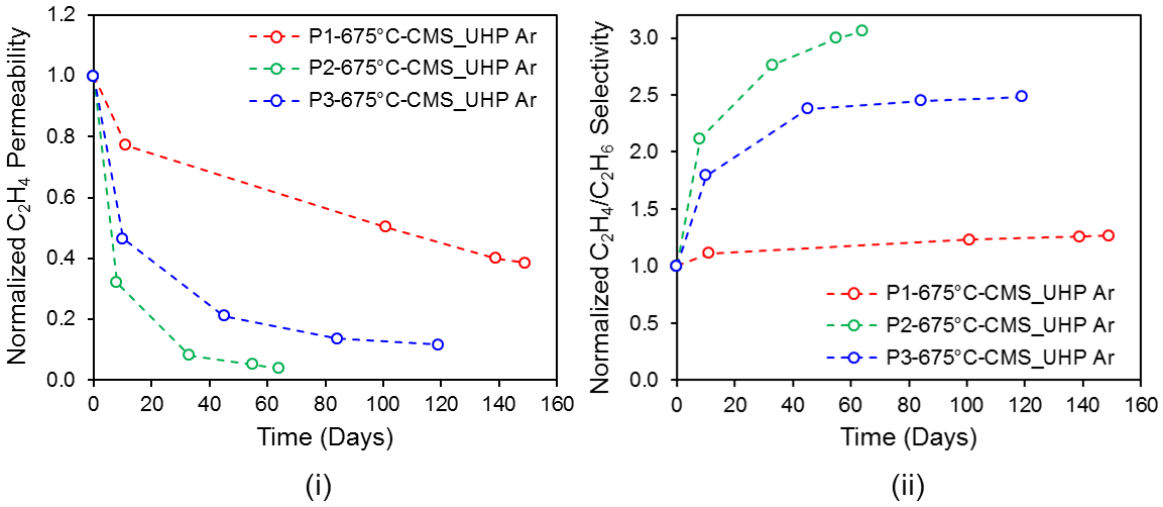

Figure 5.36: Physical aging effects in CMS dense films derived from Matrimid® (red), 6FDA-DAM (green) and 6FDA:BPDA-DAM (blue): (i) Normalized C_2H_4 permeability (P_t/P_0, where P_0 is the permeability on day 0 and P_t is the permeability at time t in days) as a function of time and (ii) Normalized C_2H_4/C_2H_6 selectivity (α_t/α_0, where α_0 is the selectivity on day 0 and α_t is the selectivity at time t in days) as a function of time

Clearly, physical aging in CMS shows strong dependence on the parent polymer material, as seen from Figure 5.36. Owing to the high fractional free volume (FFV) of 6FDA-DAM, the initial C_2H_4 permeability of CMS derived from 6FDA-DAM was found to be the highest (Figure 5.34), followed by 6FDA:BPDA-DAM CMS (Figure 5.35) and then Matrimid® CMS (Figure 5.33). However, physical aging is also the most significant in CMS derived from 6FDA-DAM, followed by 6FDA:BPDA-DAM CMS and not so significant in Matrimid® CMS (Figure 5.36). Additionally, CMS derived from 6FDA-DAM

age the fastest, followed by 6FDA:BPDA-DAM whereas the rate of physical aging in Matrimid® is comparatively slower (Figure 5.36). In fact, a comparison of CMS derived from 6FDA-DAM and 6FDA:BPDA-DAM shows that although the starting permeability for the 6FDA-DAM CMS is much higher than that for the 6FDA:BPDA-DAM CMS, it quickly ages to a much lower final value. These physical aging trends are quite evident from Figure 5.36. The results suggest that the physical aging behavior in CMS derived from glassy polymers may be analogous to physical aging in glassy polymers, since polymers with a higher FFV tend to age much more rapidly.

The initial permeability values in Figures 5.33, 5.34 and 5.35 should be treated with caution. The CMS is in a highly unstable state right after fabrication and aging may occur so rapidly that it can be tricky to catch the initial value, and significant deviations may result from several measurements. Additionally, while the film was maintained under active vacuum between measurements 1 and 2, they were also exposed to several other gases subsequently in between the mixed gas measurements. The aging trends reported may thus be expected to be slower than if the film had been maintained solely under active vacuum between each test. Since the physical aging phenomenon was discovered at a much later stage during this study, time constraints did not allow for such controlled measurements, but may be useful for detailed future analysis.

Similar trends reported for CMS dense films were also observed by Liren Xu in the Koros Group in CMS hollow fibers derived from the three polymers: Matrimid®, 6FDA-DAM and 6FDA:BPDA-DAM. The CMS hollow fibers were derived from UHP Ar pyrolysis at 550°C using Protocol 1. The normalized permeance and selectivity hollow fiber trends for both vacuum and atmospheric air storage are shown in Figure 5.37(i) and Figure 5.37(ii) respectively. Aging effects for vacuum storage solely represent physical aging. Aging effects for atmospheric storage could be the combined effects of physical aging and aging resulting from exposure to oxygen and trace moisture. In all cases,

aging is greater and faster under vacuum storage compared to atmospheric storage, thereby suggesting that oxygen and trace moisture may not be major factors. Similar to CMS dense films, 6FDA-DAM CMS hollow fiber shows fastest and largest physical aging, followed by 6FDA:BPDA-DAM CMS hollow fiber. Matrimid® CMS hollow fiber shows relatively small performance change over time.

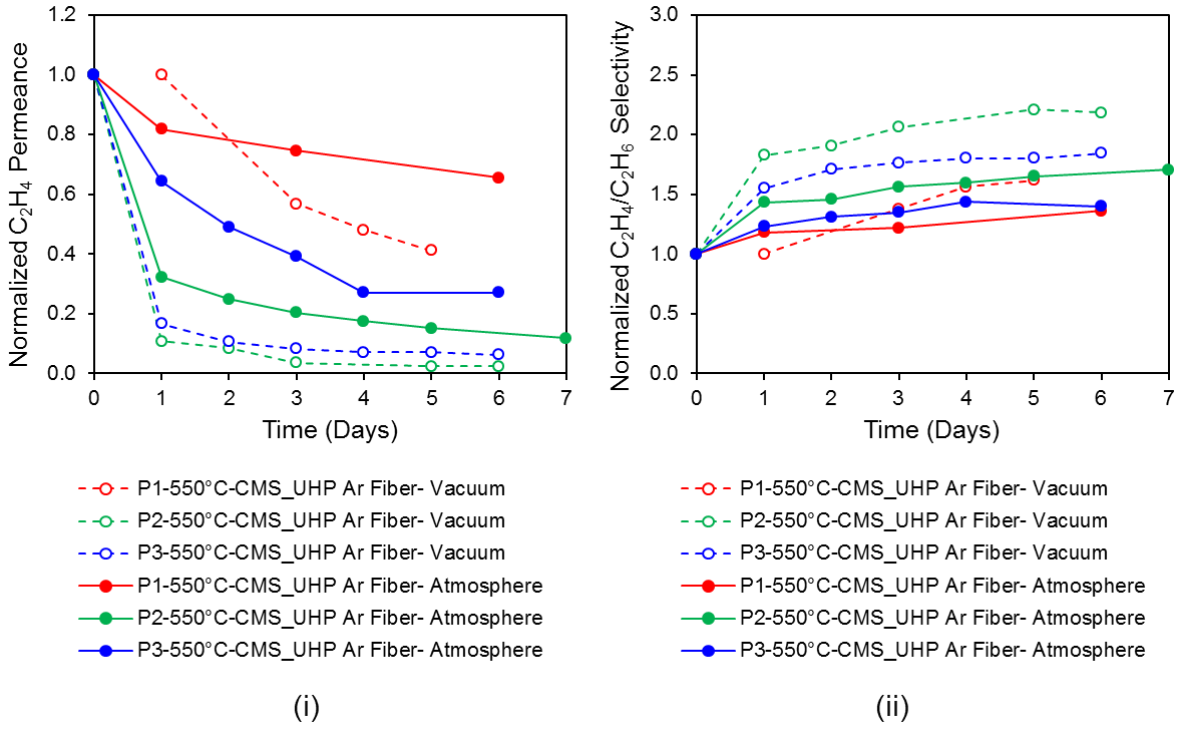

Figure 5.37: Normalized aging behavior of (i) C_2H_4 permeance and (ii) C_2H_4/C_2H_6 selectivity of CMS hollow fibers derived from Matrimid® (red), 6FDA-DAM (green), and 6FDA:BPDA-DAM (blue) (Data courtesy: Liren Xu)

Another important point to note is that CMS hollow fibers reach a stable value in several days as compared to months in CMS dense films. This is probably because of the thin separation layer in fibers compared to dense films, which is again analogous to the physical aging behavior of glassy polymers. Note, however, that a fundamental

difference exists between simple glassy polymers and "glassy" CMS, since the latter cannot be "rejuvenated" by heating, as can be done for glassy polymers by heating above the glass-rubber transition temperature [28].

5.3.4. Implications of Physical Aging in Carbon Molecular Sieve Membranes

Physical aging of CMS membranes adds another important controlling parameter to CMS performance besides CMS fabrication parameters such as the polymer precursor, pyrolysis conditions, pre-treatment and post-treatment conditions. This entails careful control of the CMS testing procedures. It was found that the kinetics of physical aging is dependent on the history and storage conditions of the CMS. Aging was found to be greater and more rapid for vacuum storage conditions compared to atmospheric storage. Freshly fabricated CMS membranes could be stored under vacuum for a certain period of time in order to stabilize the membrane prior to testing. By contrast, the CMS performance can be quite stable (but different from vacuum stabilized "aged" samples) when under active test since the gas has a dilating effect of the CMS structure. This may present opportunities to trap the CMS at an attractive metastable state by running it continuously in the presence of feed gas for practical applications. It is also important to consider that although analysis of physical aging in CMS is important for fundamental understanding, it may not be a "show-stopper" for practical CMS application where the membrane module would be in active use after an initial stabilization period.

Physical aging kinetics in vacuum storage also led us to understand another important fact. It may be recalled from Section 4.5 that while Matrimid® pyrolysis under vacuum conditions resulted in attractive C_2H_4/C_2H_6 separation performance, that of 6FDA-DAM and 6FDA:BPDA-DAM yielded drastically low permeabilities. CMS derived from Matrimid® may be quite stable even after they are just fabricated, indicated by its

relatively small physical aging effect. By comparison, the disordered graphene-like sheets in CMS derived from 6FDA-DAM and 6FDA:BPDA-DAM are in a highly unstable state and rapidly collapse to a stable state under vacuum. The phenomenon of structure collapse in such highly unstable CMS membranes derived from 6FDA-DAM and 6FDA:BPDA-DAM may be exaggerated when the CMS structure is being formed in the presence of vacuum at high temperature during pyrolysis. Thus vacuum pyrolysis of 6FDA-DAM and 6FDA:BPDA-DAM may lead to a condensation of the CMS microstructure even as the disordered graphitic structure is being formed. This may explain the unexpected loss in permeability for CMS resulting from vacuum pyrolysis of 6FDA-DAM and 6FDA:BPDA-DAM (refer to Figure 4.6).

Similar to physical aging in polymers, physical aging in CMS membranes shows dependence on the separation layer thickness. As shown, CMS hollow fibers with a thin separation layer age much more rapidly and come to a stable state compared to dense films. The physical aging effect could also be temperature dependent, as is the case in polymers. This was not investigated but may be an area for future work.

Physical aging seems to impact the permeabilities of other penetrants such as O_2, N_2, CO_2, CH_4 etc. as well, as seen from some preliminary measurements. However, the extent of the effect of physical aging in CMS on different penetrants was not analyzed in detail. It is anticipated that physical aging would have a smaller impact on penetrants of smaller size. It is likely that physical aging may result in a loss of the larger pores such that the effect of the tail end of the CMS pore size distribution may me be more significant. This is illustrated in Figure 5.38. Thus larger gases like C_2H_4 and C_2H_6 that lie at the tail end of the distribution may be expected to show a greater performance loss as a result of physical aging. This hypothesis must however be verified by detailed analysis of the effects of physical aging in CMS membranes on the performance of different penetrants, and may be an interesting avenue to pursue for future studies.

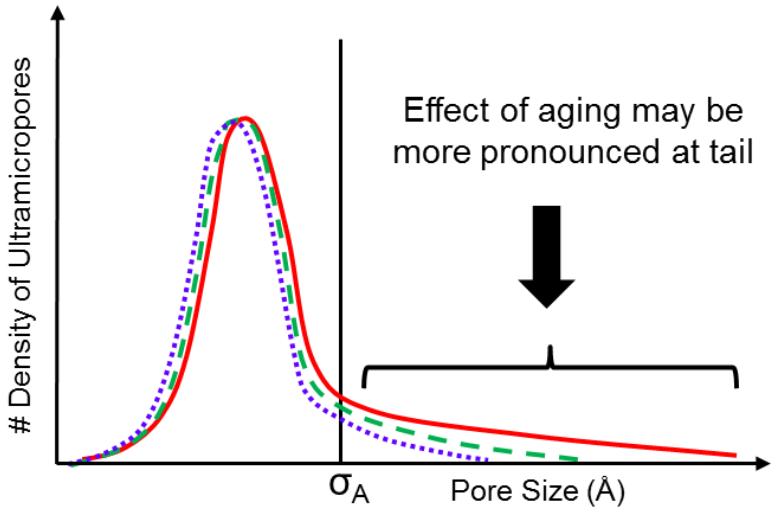

Figure 5.38: Likely effect of physical aging on the pore size distribution of CMS

Finally, physical aging is precursor dependent. It was shown that CMS membranes derived from 6FDA-DAM show the greatest aging effect, followed by 6FDA:BPDA-DAM and finally Matrimid®. Thus from the point of aging Matrimid® may be the most preferred precursor while 6FDA-DAM is the least preferred. However, it was shown earlier that CMS hollow fibers derived from Matrimid® show substructure collapse resulting in a very thick separation layer, which drastically reduces permeance. Thus it may not be feasible for practical use. 6FDA:BPDA-DAM shows the least collapse and shows a porous substructure with a thin separation layer. 6FDA-DAM shows intermediate collapse. Thus 6FDA:BPDA-DAM is the most preferred precursor from a fiber morphology perspective. Considering the effects of both fiber morphology and physical aging on CMS performance, 6FDA:BPDA-DAM may be the most preferred current precursor in this study for CMS fabrication for C_2H_4/C_2H_6 separations.

Table 5.6: Preferred precursor in this study for CMS fabrication for C_2H_4/C_2H_6 separation based on the effects of substructure collapse and physical aging

Precursor	Substructure Collapse	Physical Aging
Matrimid®	Most	Least
6FDA-DAM	Intermediate	Most
6FDA:BPDA-DAM	Least	Intermediate

5.4. Carbon Molecular Sieve Membranes Derived from 6FDA-DAM

As described in the previous section, early studies on CMS dense films derived from 6FDA-DAM showed significant deviation in data from film to film for the same pyrolysis conditions. The reason for this was found to be the time and history dependence of the CMS membranes resulting from physical aging. As a result of this physical aging phenomenon, the permeability of the 6FDA-DAM CMS was shown to fall to very low values, even below that of 6FDA:BPDA-DAM, although the starting polymer has a very high fractional free volume. 6FDA-DAM CMS selectivity however still remains lower than both 6FDA:BPDA-DAM CMS and Matrimid® CMS. As such, 6FDA-DAM is not a preferred precursor for C_2H_4/C_2H_6 separation. Thus, after the discovery of the excessive physical aging effect, only limited studies were done on the investigation of effects of pyrolysis parameters on 6FDA-DAM for fundamental understanding. Only purge pyrolysis conditions were used in this study since 6FDA-DAM based CMS did not show attractive performance from preliminary analysis under vacuum, as reported in Section 4.5. CMS samples were obtained from pyrolysis using Protocol 1, described in

Section 3.3.2. Measurements were made on aged CMS samples at 35°C using 50 psia feed pressure. The results from the study are summarized below.

5.4.1. Effect of Pyrolysis Temperature

As shown in the case of Matrimid®, the pyrolysis temperature is an effective tool in tuning CMS properties, and locating the optimum pyrolysis temperature is useful in achieving a balance between the permeability and selectivity. An increase in the pyrolysis temperature generally results in a decrease in permeability and an increase in selectivity. The optimum pyrolysis temperature for Matrimid® was found to be in the range of 650-675°C. The effect of pyrolysis temperature was thus analyzed on 6FDA-DAM pyrolysis as the first critical tuning parameter. The results are shown in Figure 5.39. Unlike Matrimid®, for the 6FDA-DAM CMS the selectivity remained low, even at higher pyrolysis temperatures. For example, recall that Matrimid® CMS from 675°C UHP Ar pyrolysis showed C_2H_4 permeability of ~11 Barrer with C_2H_4/C_2H_6 selectivity of ~10.5 (mixed gas). By comparison, the 6FDA-DAM 675°C CMS shows a permeability of ~24 Barrer with a selectivity of only ~ 5.3.

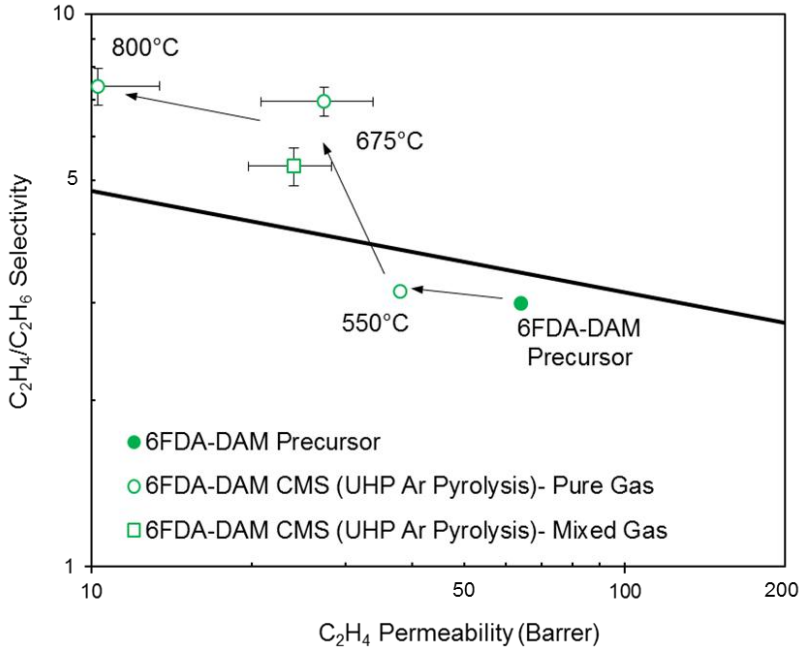

Figure 5.39: Plot showing C_2H_4/C_2H_6 separation performance (35°C, 50 psia) of CMS dense films derived from UHP Ar pyrolysis of 6FDA-DAM at different pyrolysis temperature. Error bars represent standard deviations from multiple measurements

5.4.2. Effect of Oxygen Doping

An oxygen doping method was used to achieve further optimization of the 6FDA-DAM CMS. As described in Section 2.4.3, detailed studies by Williams [20] and Kiyono et al. [3] showed that even trace amounts of oxygen can significantly affect CMS performance. This process was termed as oxygen doping and was used to tune the CO_2/CH_4 separation properties of CMS membranes by carefully controlling the amount of oxygen present in the pyrolysis purge gas. When oxygen is present in trace amounts in the inert pyrolysis gas, it can selectively chemisorb at the ultramicropore sites (Figure 2.16). Ultramicropores are essentially conceptualized to be present as defects in the carbon and can be ~17 times more reactive compared to the basal plane [9, 36]. O_2-doping thus affects the critical diffusion-limiting ultramicropore distribution, but not the

micropores, and allows tuning of the separation performance. The concept of oxygen-doping is described in detail in Section 2.4.3. The method must be used cautiously since it is highly dependent on the intrinsic structure of the "undoped" carbon and the gas pair in consideration. In this study, oxygen doping was not used in the case of Matrimid® since the C_2H_4 permeability of the un-doped CMS at optimum selectivity was not exceptionally high, indicating a "tight" intrinsic starting structure. This may lead to clogging of the pore windows as a result of oxygen doping, which would adversely affect performance. CMS derived from 6FDA-DAM on the other hand have an open intrinsic structure relative to Matrimid® CMS resulting in higher permeability. In this case, oxygen doping may be used advantageously to enhance the selectively. The amount of oxygen present during doping is also critical since "over-doping" may again result in pore clogging. These concepts are illustrated in Figure 5.40.

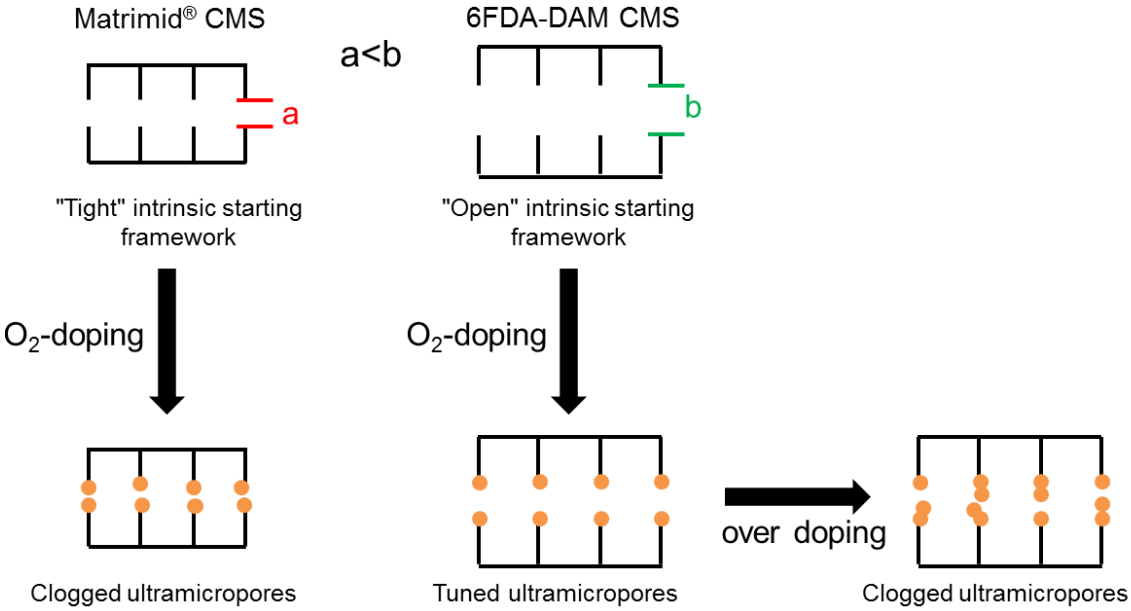

Figure 5.40: Cartoon representations of the effect of oxygen doping on pore structure of CMS derived from Matrimid- and 6FDA-DAM

Oxygen doping studies were carried out on 6FDA-DAM pyrolyzed at 675°C using Protocol 1 in presence of argon containing 30 and 50 pm O_2. The results are shown below in Figure 5.41. The data reported is from mixed gas measurements at 35°C. Clearly, oxygen doping at 30 ppm shows an enhancement in the C_2H_4/C_2H_6 selectivity compared to the UHP Ar pyrolysis. In going from 30 to 50 ppm however, no selectivity improvement is noticed but the C_2H_4 permeability drops further. This may be a result of "over-doping". It should be noted that while oxygen doping does show a selectivity improvement for the 6FDA-DAM CMS, the separation factors are still not attractive especially when considering the corresponding permeability loss. Many of these effects are however likely to be a result of the undesired performance loss due to excessive physical aging in the 6FDA-DAM CMS. Clearly, 6FDA-DAM may not be an ideal precursor of choice for CMS membranes for C_2H_4/C_2H_6 separation. Parallel studies on hollow fibers done by Liren Xu in the Koros Group show similar trends, pointing to the same conclusion.

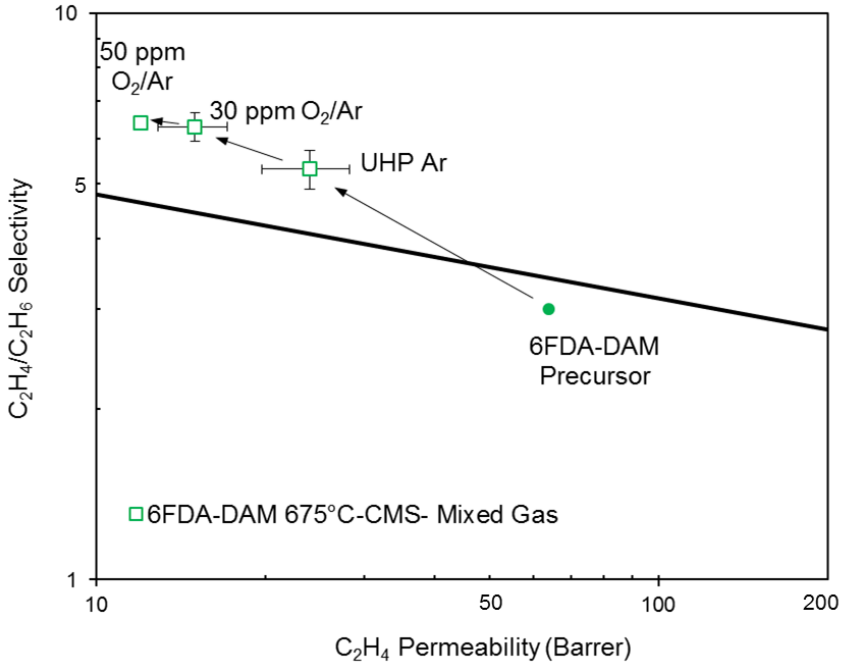

Figure 5.41: Plot showing effect of O_2-doping on C_2H_4/C_2H_6 separation performance (35°C, 50 psia, binary gas) of CMS dense films derived from pyrolysis of 6FDA-DAM at 675°C. Error bars represent standard deviations from multiple measurements

5.4.3. Effect of Polymer Molecular Weight

During an earlier stage of the study, it was found that CMS derived from different batches of 6FDA-DAM having different molecular weights showed variable performance for the same pyrolysis conditions. A considerable amount of time was spent in trying to probe the reasons for these differences; however no conclusive evidence was found. In retrospect, the differences in the performances may have been an artifact of the significant physical aging effect in CMS derived from 6FDA-DAM. Analyses of the effects of molecular weight were not pursued in further detail. It is not expected that the polymer molecular weight should result in significant variability in CMS performance. It may, however, be a good idea to verify this in the future since it can be important for CMS scale-up.

5.5. Carbon Molecular Sieve Membranes Derived from 6FDA:BPDA-DAM

As pointed out previously, at this point 6FDA:BPDA-DAM is the preferred precursor from the point of fiber morphology, which is important to achieve fluxes reasonable for practical use. Optimization of the pyrolysis conditions for C_2H_4/C_2H_6 separation using CMS membranes derived from 6FDA:BPDA-DAM are considered in this section. Only purge pyrolysis conditions were used since 6FDA:BPDA-DAM based CMS showed attractive performance from preliminary analysis under vacuum, as reported in Section 4.5. Measurements were made on aged CMS samples at 35°C using 50 psia feed pressure. The results from the study are summarized below.

5.5.1. Effect of Pyrolysis Temperature

The C_2H_4/C_2H_6 separation performance of CMS derived from UHP Ar pyrolysis of 6FDA:BPDA-DAM dense films at different final pyrolysis temperatures using Protocol 1 is shown in Figure 5.42. As seen for both Matrimid® and 6FDA-DAM, an increase in the final pyrolysis temperature resulted in an increase in the C_2H_4/C_2H_6 selectivity and a decrease in permeability of the 6FDA:BPDA-DAM CMS. It is important to point out that although the general trend may be similar, the effect of final pyrolysis temperature on CMS properties is precursor dependent. In the case of Matrimid®, changing the final pyrolysis temperature between 550°C to 675°C did not result in any significant C_2H_4 permeability loss, but the C_2H_4/C_2H_6 selectivity was enhanced two fold. A further increase in the pyrolysis temperature resulted in a precipitous drop in permeability with no selectivity improvement (see Figure 5.6). In the case of 6FDA-DAM, while the C_2H_4 permeability decreased with final pyrolysis temperature, unattractive C_2H_4/C_2H_6 selectivities resulted even at higher pyrolysis temperatures (see Figure 5.40). For the

6FDA:BPDA-DAM CMS, the C_2H_4 permeability vs. C_2H_4/C_2H_6 selectivity trends as a function of the final pyrolysis temperature are more balanced, showing a continuous permeability decrease and selectivity increase with pyrolysis temperature (Figure 5.42).

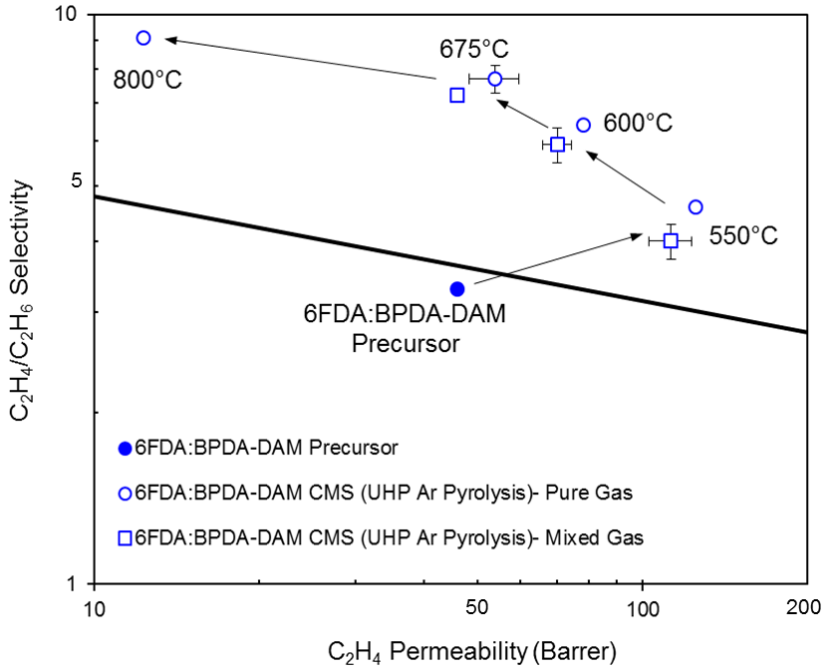

Figure 5.42: Plot showing C_2H_4/C_2H_6 separation performance (35°C, 50 psia) of CMS dense films derived from UHP Ar pyrolysis of 6FDA:BPDA-DAM at different pyrolysis temperature. Error bars represent standard deviations from multiple measurements

5.5.2. Effect of Oxygen Doping and Post-Oxygen Doping

While CMS derived from 6FDA:BPDA-DAM pyrolysis at 675°C under UHP argon shows good performance in terms of a permeability-selectivity balance, there is further room for performance optimization using oxygen doping, not just at 675°C but also at 600°C and 550°C since the permeabilities were quite high. By comparison, Matrimid®

would not allow such opportunities for optimization based on oxygen doping because of lower permeabilities resulting from its "tighter" structure.

Oxygen doping using 30 and 50 ppm oxygen in argon purge gas during pyrolysis was carried out at 550°C, 600°C and 675°C. Additionally, a post oxygen doping method using 30 and 50 ppm oxygen in argon was also used as another tuning parameter for CMS performance. The difference between oxygen doping and post oxygen doping is as follows: For oxygen doping, pyrolysis is carried out for the entire pyrolysis cycle in the presence of inert purge gas containing trace concentrations of oxygen. By comparison, for post oxygen doping, the CMS structure is first derived by pyrolysis at the final pyrolysis temperature in the presence of UHP argon. Thereafter, the fabricated CMS is quickly heated back up to a temperature higher than the final pyrolysis temperature in the presence of inert gas containing trace oxygen. This second step is called post pyrolysis as it occurs after the actual CMS formation via pyrolysis. Since oxygen doping occurs during this post pyrolysis step as opposed to during pyrolysis, the process is termed as "post-oxygen doping". Protocol 1 described in Section 3.3.2 was used for pyrolysis in all cases. The heating protocol listed below was used for post-oxygen doping CMS derived from UHP argon pyrolysis.

Post-oxygen doping protocol:

5. 50°C→ T_{post} at a ramp rate of 10°C/min
6. Soak for 15 min at T_{post}

where, T_{post} is the temperature to which the CMS is heated in post pyrolysis, and post-pyrolysis temperature (T_{post}) > pyrolysis temperature.

The post oxygen doping concept, termed as dual temperature secondary oxygen doping (DTSOD), was initially used by Dr. Rachana Singh in the Koros Group to optimize the performance of CMS membranes for O_2/N_2 separation. Figure 5.43 shows a

comparison of the effects of final pyrolysis temperature, oxygen doping and post oxygen doping on the CMS cartoon structures.

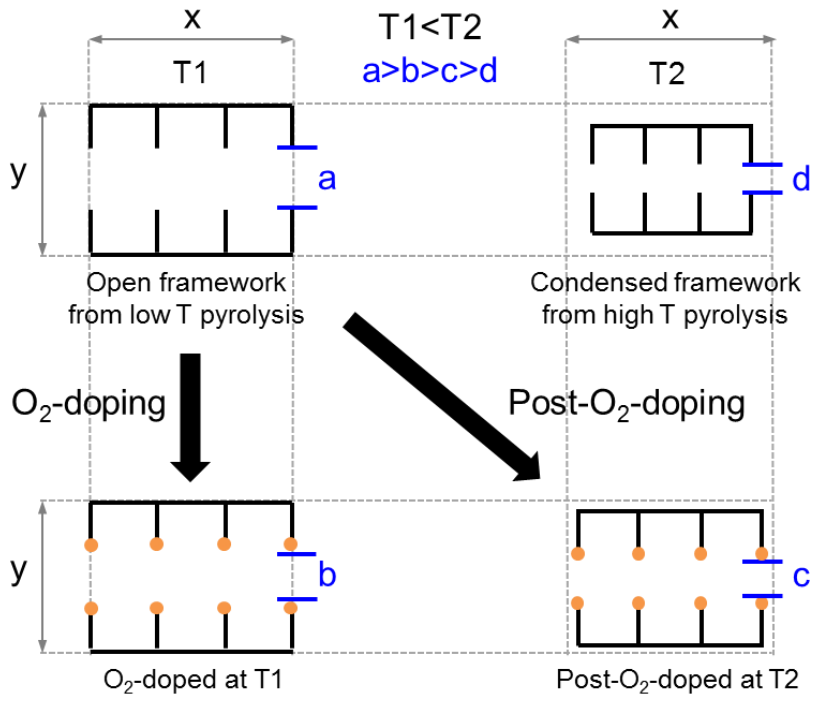

Figure 5.43: Schematic representation of the effects of final pyrolysis temperature, oxygen doping and post oxygen doping on CMS cartoon structures

As seen from Figure 5.43, pyrolysis at a lower pyrolysis temperature T1 results in an open intrinsic CMS framework. For oxygen doping during pyrolysis at T1, the intrinsic open framework may not condense but the ultramicropores are tuned by selective chemisorption of oxygen at the ultramicropore (smaller pore window) sites. During pyrolysis at a higher pyrolysis temperature T2, the CMS framework is extensively condensed compared to CMS derived from T1 pyrolysis. When oxygen doping is carried out during pyrolysis at T2, ultramicropore tuning occurs on this condensed CMS framework. By difference, for post oxygen doping, the CMS is first derived at T1 thus

resulting in an open intrinsic starting framework. Next as the CMS is quickly heated up to a higher temperature T2 in the presence of oxygen during post-pyrolysis oxygen doping, there may be very little condensation of the CMS framework along with ultramicropore tuning resulting from oxygen chemisorption, as opposed to exaggerated condensation from slow heating during pyrolysis at T2. Thus, post oxygen doping allows another tool for tuning CMS performance. It can essentially take advantage of the combined effects of oxygen doping and higher temperature, however the resulting effects of both may be milder compared to oxygen doping or pyrolysis at higher temperature.

The following cases were studied: (i) Oxygen doping: pyrolysis at 550°C and 600°C in 30 and 50 ppm O_2/Ar, pyrolysis at 675°C in 30 ppm O_2/Ar; (ii) Post oxygen doping: pyrolysis at 550°C in UHP Ar followed by post pyrolysis at 600°C in 30 and 50 ppm O_2/Ar, pyrolysis at 600°C in UHP Ar followed by post pyrolysis at 650°C in 30 ppm O_2/Ar. The results of oxygen doping and post oxygen doping are shown in Figure 5.44. Performances reported are for 50 psia binary gas feed at 35°C for aged CMS samples.

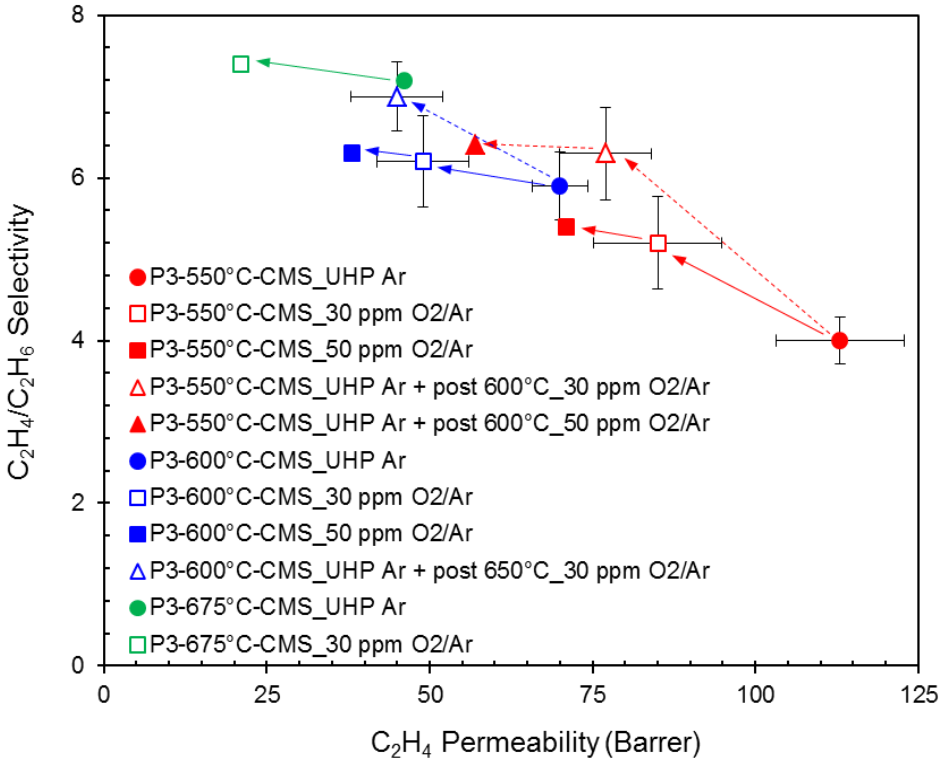

Figure 5.44: Effects of oxygen doping and post-oxygen doping on the C_2H_4/C_2H_6 separation performance (35°C, 50 psia, binary gas) of CMS derived from 6FDA:BPDA-DAM. Error bars represent standard deviations from multiple measurements

At all pyrolysis temperatures, oxygen doping at 30 ppm resulted in C_2H_4/C_2H_6 selectivity increase along with C_2H_4 permeability loss. In going from 30 ppm to 50 ppm, the selectivity enhancement is not significant but further permeability loss occurs. This may be a result of "over-doping" (Figure 5.40). Oxygen doping depends on the final pyrolysis temperature. The effects of oxygen doping on selectivity are much more significant at a lower pyrolysis temperature. With increase in the final pyrolysis temperature, the selectivity enhancement becomes less obvious while the permeability continues to decrease. This is related to the fact that the "closed" CMS framework at a higher pyrolysis temperature allows less room for ultramicropore tailoring via oxygen doping.

Post oxygen doping shows an improvement in C_2H_4/C_2H_6 selectivity over the undoped or oxygen doped CMS for both pyrolysis temperatures, as seen from Figure 5.44. For CMS derived from 550°C UHP Ar pyrolysis, post treatment at 600°C using 30 ppm O_2/Ar shows improved selectivity over both P3-550°C-CMS_30 ppm O_2/Ar and P3_550°C-CMS_50 ppm O_2/Ar. In fact, when compared to 600°C UHP Ar CMS (P3_600°C-CMS_UHP Ar), the post oxygen doped CMS shows a higher permeability, yet comparable selectivity. In increasing the oxygen amount from 30 to 50 ppm during post oxygen doping, the permeability decreases drastically with no increase in selectivity, which is likely the outcome of "over-doping" (Figure 5.43). For CMS derived from 600°C UHP Ar pyrolysis, post treatment at 650°C using 30 ppm O_2/Ar still shows performance improvement over the P3-600°C-CMS_30 ppm O_2/Ar and P3-600°C_50 ppm O_2/Ar CMS. Although the standard deviations for multiple measurements must be considered, the C_2H_4/C_2H_6 performance trends from oxygen doping and post oxygen doping can be noticed from the above studies. These tools can be used for effective performance optimization depending on the end goal. It should be noted that while oxygen doping can have significant improvements on separations involving smaller molecules with a larger size difference, such as CO_2/CH_4 (3.3 Å for CO_2 vs. 3.8 Å for CH_4) as reported by Kiyono et al. [37], the effects are subtle on C_2H_4/C_2H_6 separation because of their similar sizes (3.75 Å for C_2H_4 vs. 3.85 Å for C_2H_6) although the trends point in the right direction.

Equilibrium sorption measurements were carried out in order to further understand the effects of oxygen doping and post oxygen doping on the CMS structure. Three cases were analyzed: CMS derived from pyrolysis of 6FDA:BPDA-DAM at 600°C using UHP Ar (P3-600°C-CMS_UHP Ar), CMS derived from pyrolysis of 6FDA:BPDA-DAM at 600°C using 30 ppm O_2/Ar (P3-600°C-CMS_30 ppm O_2/Ar), and CMS derived from pyrolysis of 6FDA:BPDA-DAM at 600°C using UHP Ar and post-oxygen doped at

650°C using 30 ppm O_2/Ar (P3-600°C-CMS_UHP Ar + post 650°C_30 ppm O_2/Ar). The sorption isotherms are shown in Figure 5.45. Clearly, both oxygen doping and post oxygen doing do not have a significant impact on the sorption behavior of the different CMS. This further suggests that oxygen doping takes place at the ultramicropore sites and does not have a significant impact on the micropore structure (refer to Figure 5.43). In case of post oxygen doping as well, a rapid heating rate to a higher temperature during post pyrolysis does not significantly impact the sorption behavior, suggesting that the CMS framework is not significantly collapsed during post oxygen doping while the ultramicropores are further tuned as a result of oxygen doping (refer to Figure 5.43).

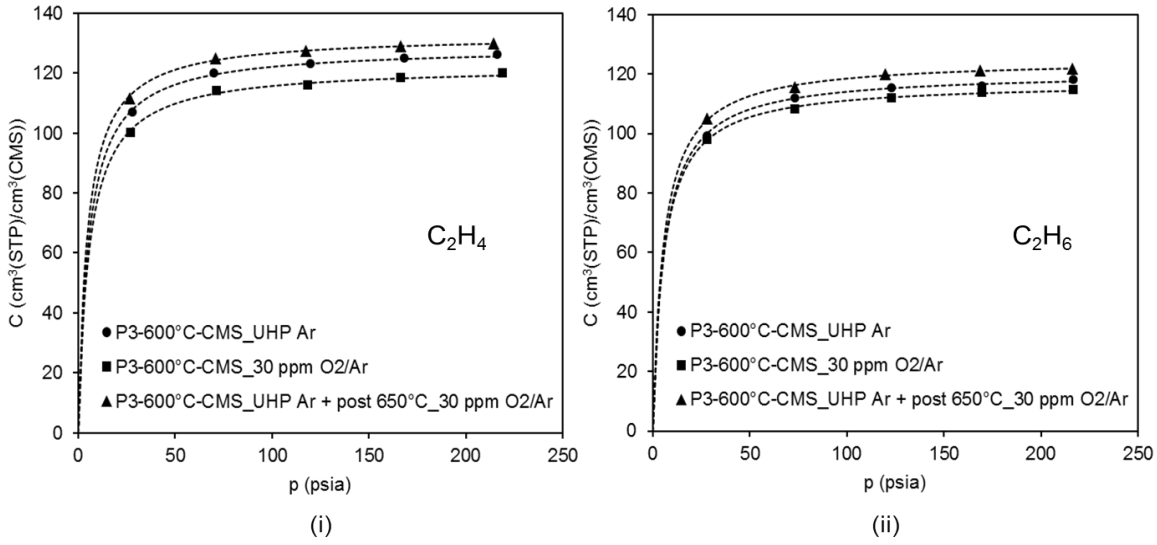

Figure 5.45: Effect of oxygen doping and post oxygen doping on the sorption isotherms of (i) C_2H_4 and (ii) C_2H_6 for CMS derived from 6FDA:BPDA-DAM

5.6. Comparison of Carbon Molecular Sieve Membranes Derived from Matrimid® and 6FDA:BPDA-DAM

The previous sections considered detailed analyses of the effects of various pyrolysis parameters on CMS derived from different polymer precursors to achieve individual optimization of their C_2H_4/C_2H_6 separation performance. In this section, the pyrolysis conditions were kept constant in order to compare differences in CMS performance and structure resulting from different starting polymer precursors. CMS samples derived from UHP Ar pyrolysis of Matrimid® and 6FDA:BPDA-DAM at 675°C using Protocol 1 (P1-675°C-CMS_UHP Ar and P3-675°C-CMS_UHP Ar) were used for comparison. Throughout Section 5.6, "red" designates CMS derived from Matrimid® and "blue" designates CMS derived from 6FDA:BPDA-DAM. All measurements reported were done at 35°C on aged CMS samples using pure gas feeds. 6FDA-DAM was not considered for comparison because of its anomalous separation behavior resulting from excessive physical aging.

5.6.1. Ethylene/Ethane Separation Performance

Figures 5.46, 5.47 and 5.48 show a comparison of the C_2H_4/C_2H_6 separation performance for CMS derived from Matrimid® and 6FDA:BPDA-DAM. As seen from Figures 5.46 and 5.47, 6FDA:BPDA-DAM CMS shows a higher C_2H_4 permeability, diffusivity and sorption coefficient compared to Matrimid® CMS. This indicates a more open overall CMS framework (larger micropores and ultramicropores) for the 6FDA:BPDA-DAM CMS compared to the Matrimid® CMS, as depicted in Figure 5.49. The C_2H_4/C_2H_6 permselectivity and diffusion-based selectivity of the Matrimid® CMS are higher than the 6FDA:BPDA-DAM CMS, while the sorption-based selectivities are

similar, as seen from Figure 5.48. This suggests that the Matrimid® CMS has more selective molecular sieving ultramicropores compared to the 6FDA:BPDA-DAM CMS for the C_2H_4/C_2H_6 pair.

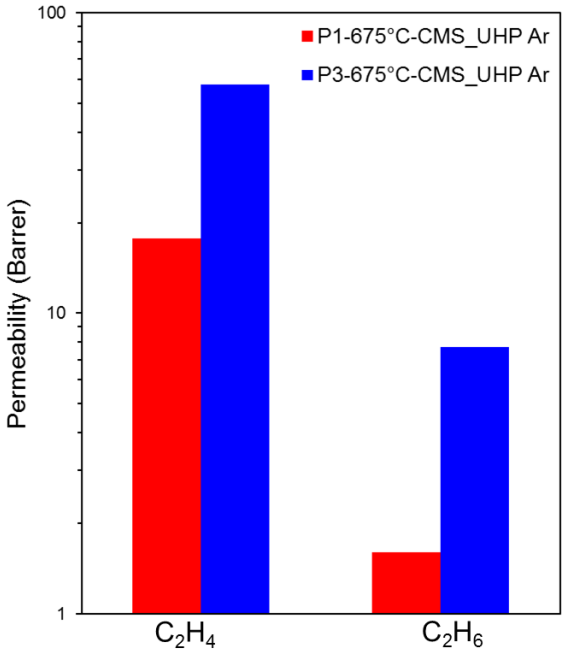

Figure 5.46: C_2H_4 and C_2H_6 permeabilities of CMS derived from Matrimid® (red) and 6FDA:BPDA-DAM (blue). Permeability measurements at 35°C, 50 psia feed pressure

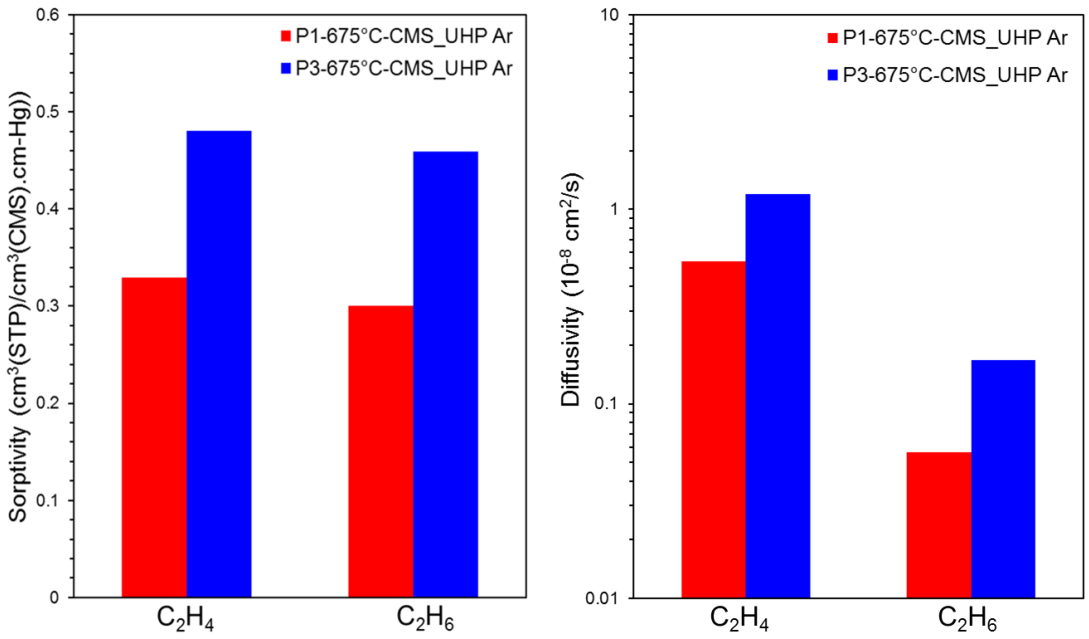

Figure 5.47: (i) Average C_2H_4 and C_2H_6 sorption coefficients obtained from direct equilibrium sorption measurements on CMS derived from Matrimid® (red) and 6FDA:BPDA-DAM (blue). The sorption coefficients reported are for 50 psia equilibrium pressure at 35°C. (ii) Average C_2H_4 and C_2H_6 transport diffusivities for CMS derived from Matrimid® (red) and 6FDA:BPDA-DAM (blue). Diffusion coefficients were back-calculated from permeabilities and sorption coefficients at 35°C, 50 psia

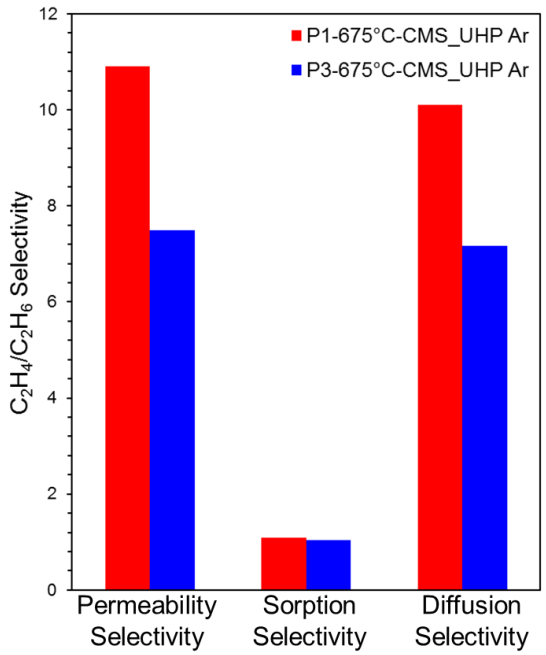

Figure 5.48: C_2H_4/C_2H_6 selectivities based on permeability, sorption and diffusion for CMS derived from Matrimid® (red) and 6FDA:BPDA-DAM (blue)

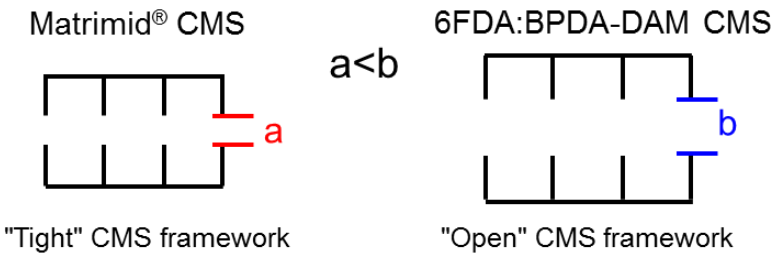

Figure 5.49: Cartoon representation of the structure of CMS membranes derived from Matrimid® and 6FDA:BPDA-DAM

5.6.2. TGA-FTIR Analysis

6FDA:BPDA-DAM has a higher fractional free volume (FFV) compared to Matrimid® because of the presence of bulky -CF_3 groups in the polymer backbone that hinder polymer chain packing (refer to Tables 3.1 and 4.1 for the chemical structure and FFV information). Hence, the intrinsic permeability of 6FDA:BPDA-DAM polymer is higher than that of Matrimid® polymeric membrane, while its selectivity is lower. Additionally, as seen from TGA-FTIR analysis represented in Figure 5.50, pyrolysis of 6FDA:BPDA-DAM results in the evolution of bulky fluorine based components such as CHF_3 (1150-1178 cm^{-1}) and trace HF (4250-4500 cm^{-1}), besides CO_2 (2110 cm^{-1}), CO (2190 cm^{-1}) and CH_4 (3017 cm^{-1}) that are evolved during Matrimid® pyrolysis. This leads to a more open CMS structure for the 6FDA:BPDA-DAM CMS compared to that of the Matrimid® CMS, as depicted in Figure 5.49.

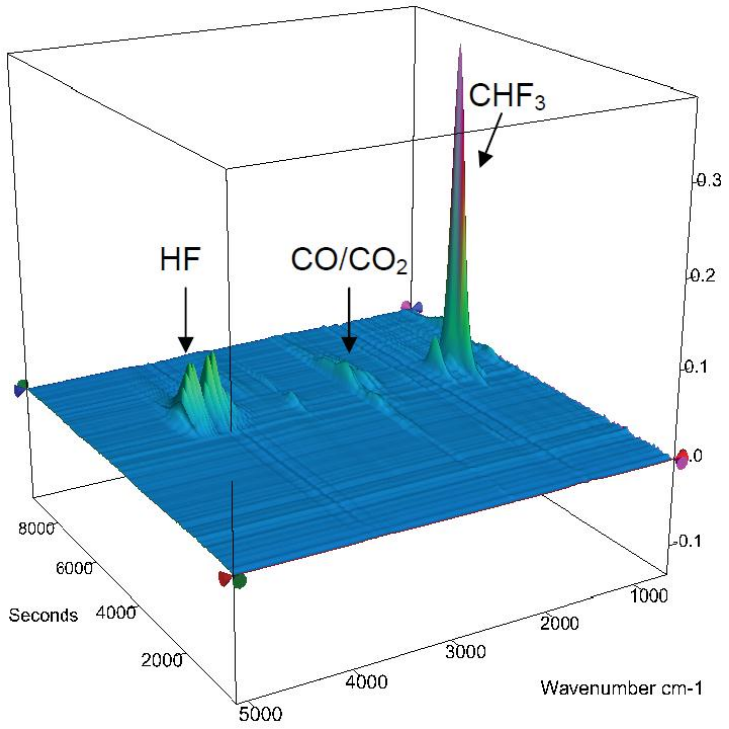

Figure 5.50: TGA-FTIR plot showing by-products evolved during 6FDA:BPDA-DAM pyrolysis [3]. Compare with TGA-FTIR plot showing by-products evolved during Matrimid® pyrolysis (Figure 5.10)

5.6.3. Sorption Isotherms & Pore Size Distribution from CO_2 Sorption

Gas sorption measurements for a range of gases shown in Table 5.4 were carried out on CMS derived from UHP Ar pyrolysis of Matrimid® and 6FDA:BPDA-DAM at 675°C. As described earlier, gas molecules sit in the larger micropore sites of the CMS pore structure in the sorbed state and make diffusive jumps from one sorption site to the next. Penetrant diffusion is limited by the critical ultramicropore windows (refer to Figure 2.12). Sorption uptake measurements can thus give an idea about the CMS micropore structures for Matrimid® vs. 6FDA:BPDA-DAM. The sorption isotherms of the different gases are shown in Figure 5.51 for both the Matrimid® CMS and the 6FDA:BPDA-DAM CMS. If the limiting pore window were small enough to effectively

exclude the larger penetrant in a gas pair, true molecular sieving would occur, and in this case, no uptake of the sieved component would be shown on the sorption isotherm. For CMS membranes, however, a distribution of pore sizes exists. As such, not all pores would be inaccessible to the larger gas molecule and CMS membranes may still exhibit sorption uptake of the larger molecule.

Gas sorption depends on the penetrant condensability (critical temperature) and its interactions with the CMS membrane medium and pore structure. As seen from the sorption isotherms in Figure 5.51, there is a general increase in sorption uptakes in the order of increasing penetrant critical temperature. Although helium can sample most of the pores, its sorption uptake is very small owing to its low critical temperature. On the other hand, although SF_6 has a very high critical temperature and is highly condensable by nature, it shows low sorption uptake since it is excluded from most of the critical CMS pores because of its large size.

For all gases measured, the 6FDA:BPDA-DAM CMS shows a higher saturation capacity compared to the Matrimid® CMS, as seen from Figure 5.51. This indicates that 6FDA:BPDA-DAM CMS has larger micropore volume compared to Matrimid®. A similar trend was also reported by Kiyono et al. for CMS derived from Matrimid® and 6FDA:BPDA-DAM pyrolysis at 550°C [15]. It is interesting to note from Figure 5.51, that for gas molecules over ~ 3.7 Å size (refer to Table 5.4 for penetrant sizes), the 6FDA:BPDA-DAM CMS shows especially higher sorption uptakes compared to the Matrimid® CMS. A larger majority of the Matrimid® CMS critical pores may exclude these bigger penetrants thus resulting in much lower uptakes compared to the 6FDA:BPDA-DAM. This suggests that the overall pore structure for the Matrimid® CMS is "tighter" than the 6FDA:BPDA-DAM CMS. For even bigger penetrants like SF_6, both Matrimid® and 6FDA:BPDA-DAM based CMS show very low uptakes, suggesting that a negligible fraction of the critical CMS pores are larger than 5.5 Å.

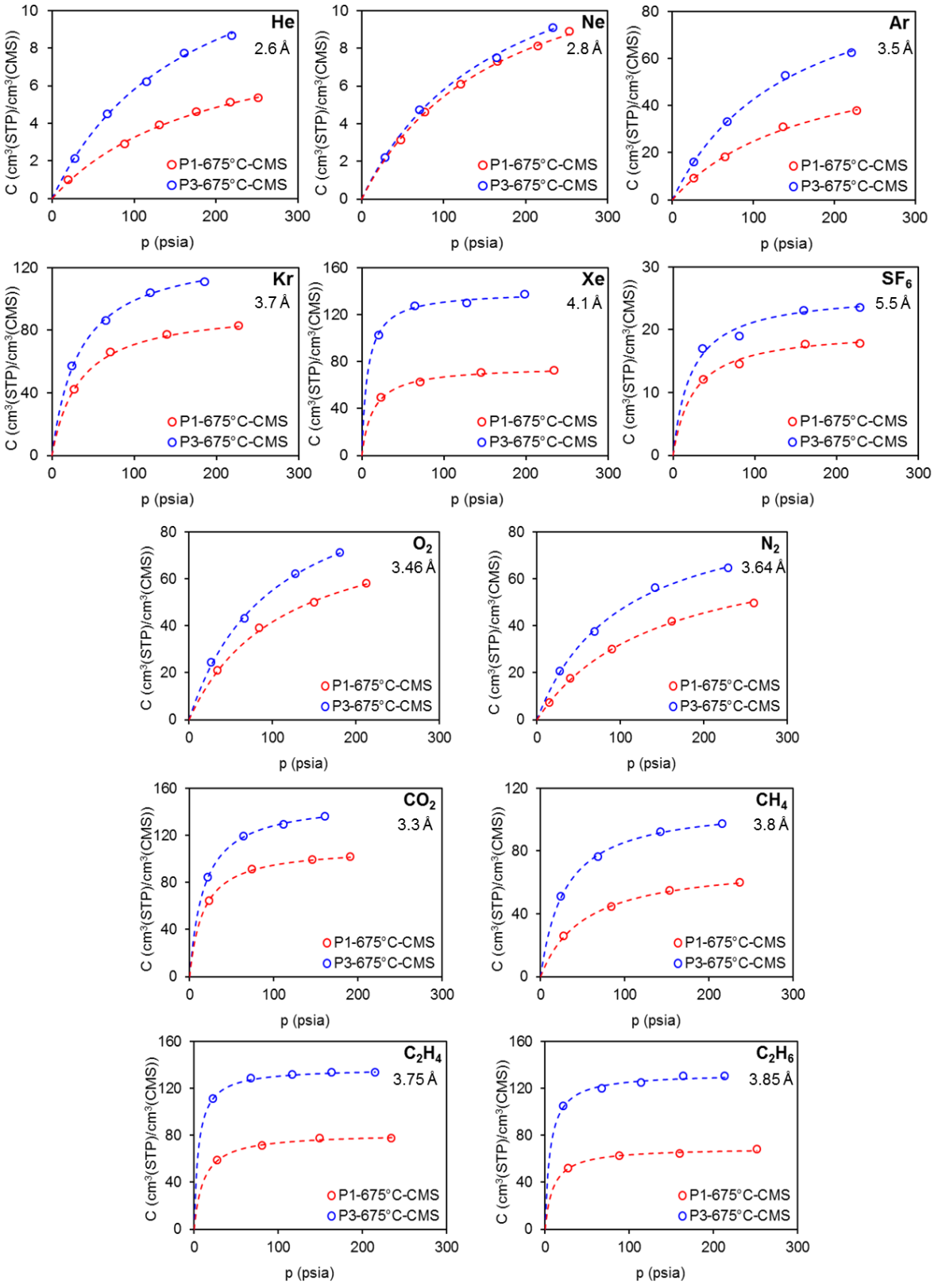

Figure 5.51: Sorption isotherms of different gases for CMS derived from UHP Ar pyrolysis of Matrimid® (red) 6FDA:BPDA-DAM (blue) at 675°C

Pore size distribution analyses obtained from CO_2 uptake measurements using density functional theory (Micromeritics) further support the above findings. This is shown in Figure 5.52. Clearly, the 6FDA:BPDA-DAM CMS has a much larger overall pore volume compared to Matrimid® CMS.

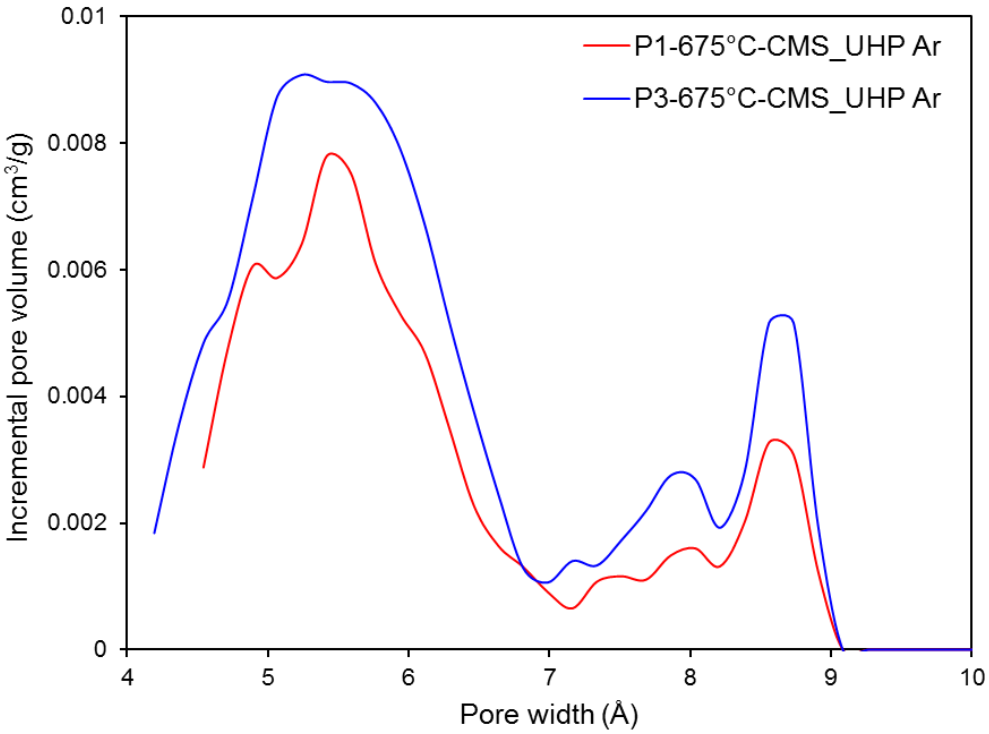

Figure 5.52: Pore size distribution obtained from CO_2 uptake measurements for CMS derived from UHP Ar pyrolysis of Matrimid® (red) and 6FDA:BPDA-DAM (blue) at 675°C. CMS samples were sent to Micromeritics for this analysis

5.6.4. Gas Probe Molecular Ruler

As described in Section 5.2.5, a gas probing method was used to infer the CMS structure based on the transport properties of different gases as molecular size probes of the CMS pores. This was further used to establish semi-quantitative diffusion-based

critical ultramicropore distributions that can facilitate understanding of transport in CMS membranes in relation to their structure.

Direct permeation and sorption measurements were carried out and this was used to obtain the average transport diffusivities of different gases. The sizes and critical temperatures of the different gases are shown in Table 5.4. Measurements were made at 35°C on CMS derived from UHP Ar pyrolysis of Matrimid® and 6FDA:BPDA-DAM at 675°C. The permeability, average sorption coefficients and average transport diffusivities of the different penetrant gases for the two CMS membranes: P1-675°C-CMS_UHP Ar and P3-675°C-CMS_UHP Ar are shown in Figures 5.53, 5.54 and 5.55 respectively. The thermodynamically corrected diffusivities are shown in Figure 5.56. The different transport properties were obtained using the data and equations shown in Appendix B.

As seen from Figure 5.53, for all gases, the 6FDA:BPDA-DAM CMS shows much higher permeabilities compared to Matrimid®. This follows from the discussion above that 6FDA:BPDA-DAM pyrolysis results in a more open intrinsic CMS structure compared to Matrimid® (see Figure 5.49). The gas permeabilities do not necessarily follow any particular order with the penetrant size, as seen in Figure 5.53. As explained previously, gas transport through membranes depend on a combination of several factors such as the penetrant size and shape, its condensability (critical temperature), as well as its interactions with the CMS material and slit-like pore structure. The gas permeabilities were factored into the sorption and diffusion coefficients to deconvolute the effects of penetrant condensability from penetrant size and shape.

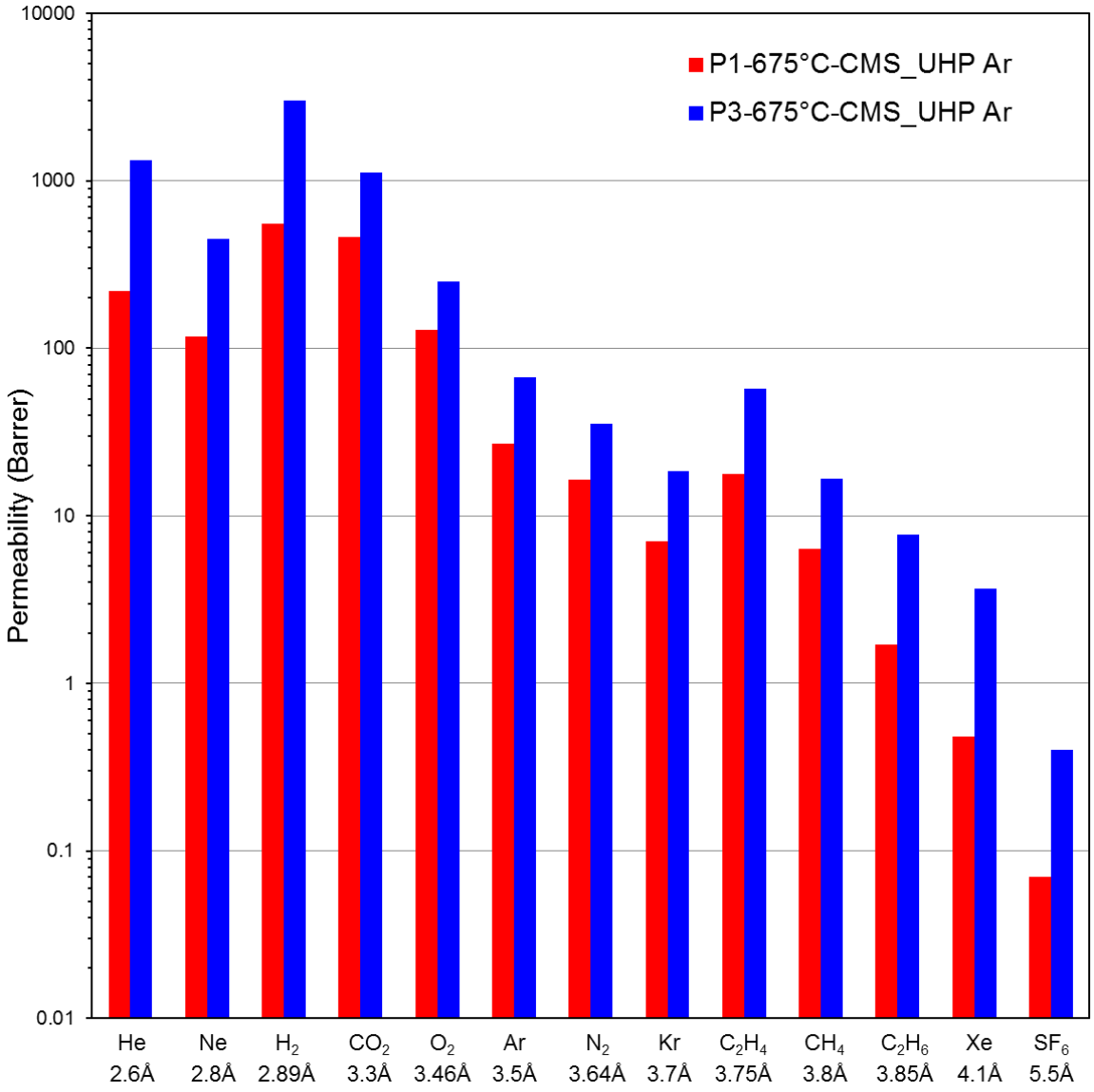

Figure 5.53: Permeabilities of different penetrants for CMS derived from UHP Ar pyrolysis of Matrimid® (red) and 6FDA:BPDA-DAM (blue) 675°C. Permeability measurements were made at 35°C using 50 psia feed pressure

Figure 5.54 shows a plot of the average sorption coefficients of different gases in the Matrimid® and 6FDA:BPDA-DAM CMS membranes. The gas sorption trends in relation to the CMS structure for the two cases have already been explained in detail previously 5.6.3. 6FDA:BPDA-DAM CMS show much higher sorption coefficients resulting from higher saturation capacities compared to the Matrimid® CMS. This

suggests that the 6FDA:BPDA-DAM CMS has a much larger micropore volume compared to Matrimid®. The high sorption coefficients for gases like H_2, CO_2, C_2H_4 etc. explain their higher permeabilities compared to smaller neighboring penetrants. In general, the gas solubility follows the order of the critical temperatures (Table 5.4).

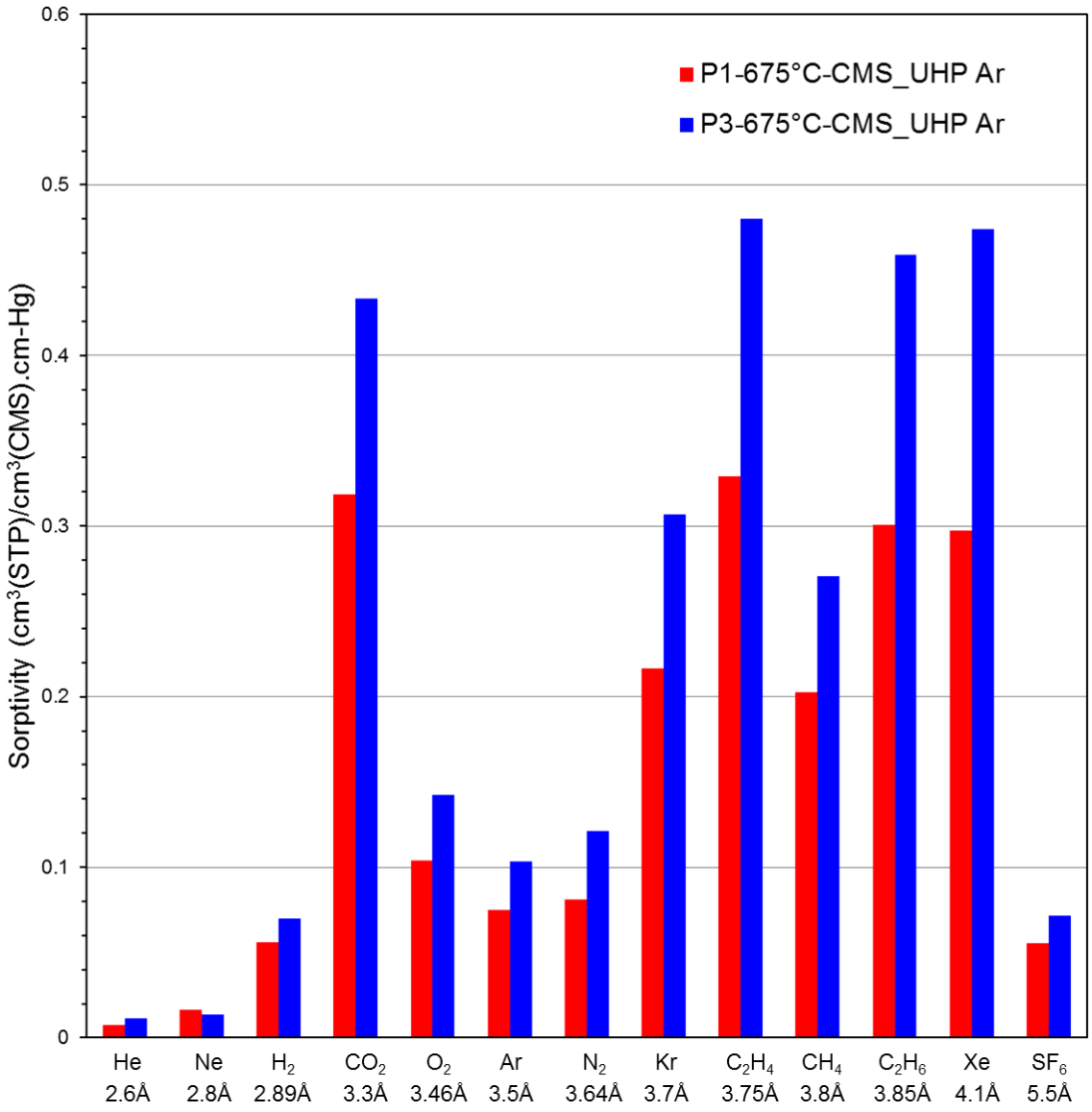

Figure 5.54: Average sorption coefficients obtained from direct equilibrium sorption measurements of different penetrants for CMS derived from UHP Ar pyrolysis of Matrimid® (red) and 6FDA:BPDA-DAM (blue) 675°C. The sorption coefficients reported are for 50 psia equilibrium pressure at 35°C

Figures 5.55 and 5.56 show the average transport diffusivities and the thermodynamically corrected diffusivities (see Appendix B) of the different gases for the Matrimid® and the 6FDA:BPDA-DAM CMS. The corrected diffusivities are more meaningful in understanding the molecular sieving nature of the critical CMS pores since it is independent of the penetrant concentration and depends exclusively on its shape and size. Clearly, the corrected diffusion coefficients show a general decrease with penetrant size in both cases. The gas diffusivities for all penetrants are much larger for the 6FDA:BPDA-DAM CMS compared to the Matrimid® CMS. Since the ultramicropore windows are the diffusion limiting pores in CMS materials, this suggests that the average ultramicropore size of the 6FDA:BPDA-DAM CMS is larger than the Matrimid® CMS. For both the Matrimid® and the 6FDA:BPDA-DAM CMS, the diffusion coefficients drop precipitously with an increase in the penetrant size and become almost negligible for penetrants over 4 Å. This suggests that the critical ultramicropore distributions tail off at the larger size end. This has been discussed in further detail in Section 5.6.5.

As seen from Figure 5.56, while the corrected diffusivities for C_2H_4, Kr and CH_4 are on the same order of magnitude, the corrected diffusivity of C_2H_4 is consistently slightly higher than that of CH_4 and Kr in both the Matrimid® CMS and the 6FDA:BPDA-DAM CMS. This shows that the "slit-shaped" CMS pore structure [14] can effectively discriminate between the shape and subtle configurational changes of similar sized gas molecules. C_2H_4 being a somewhat "planar" molecule has a diffusive advantage in the CMS compared to the bulkier and round CH_4 and Kr, despite their similar sizes. Detailed discussions centered on the effects of shape and size on penetrant diffusivity are presented in Chapter 6.

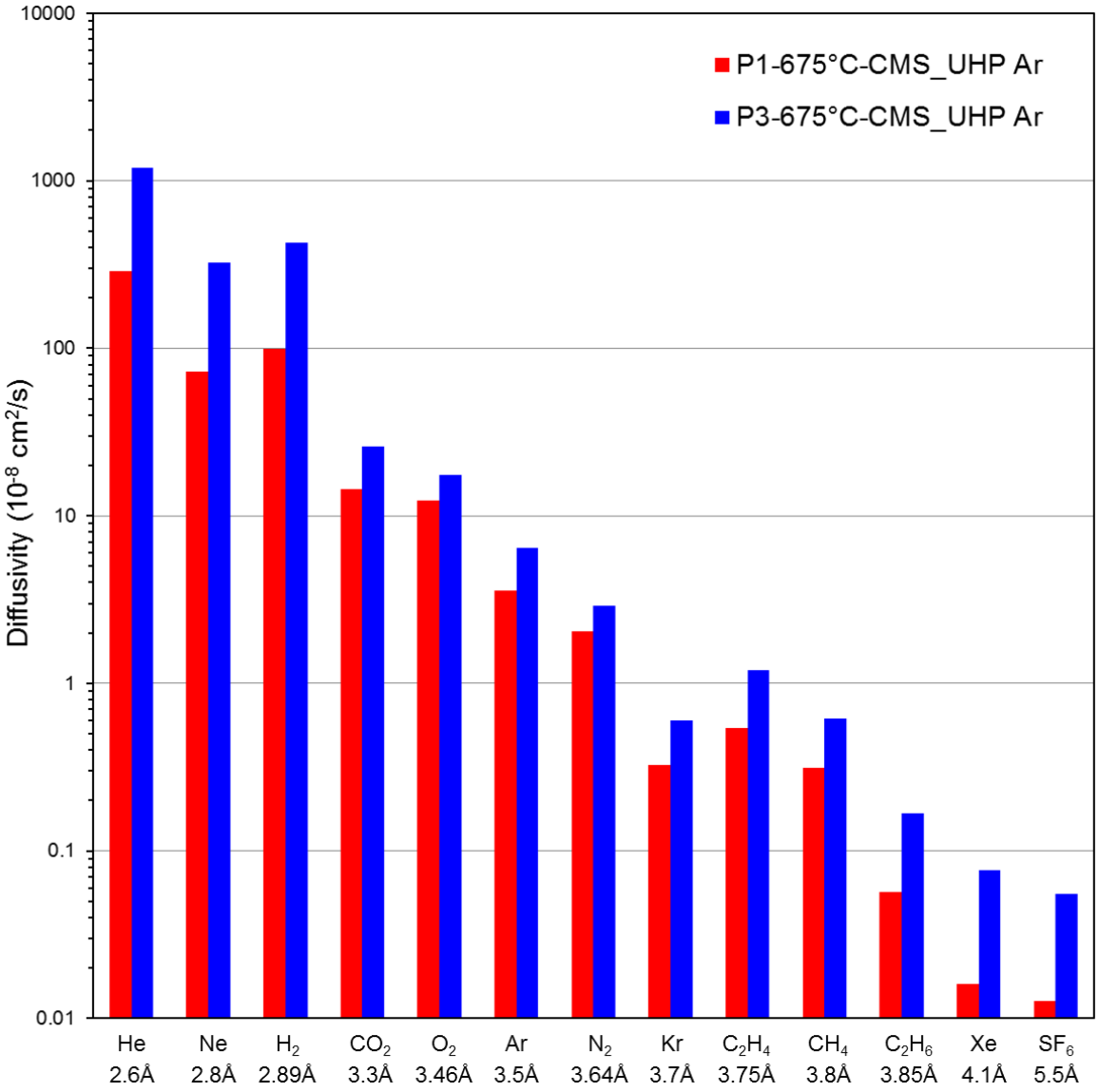

Figure 5.55: Average transport diffusivities of different penetrants for CMS derived from UHP Ar pyrolysis of Matrimid® (red) and 6FDA:BPDA-DAM (blue) 675°C. Diffusion coefficients were back-calculated from permeabilities and sorption coefficients at 35°C and 50 psia feed pressure

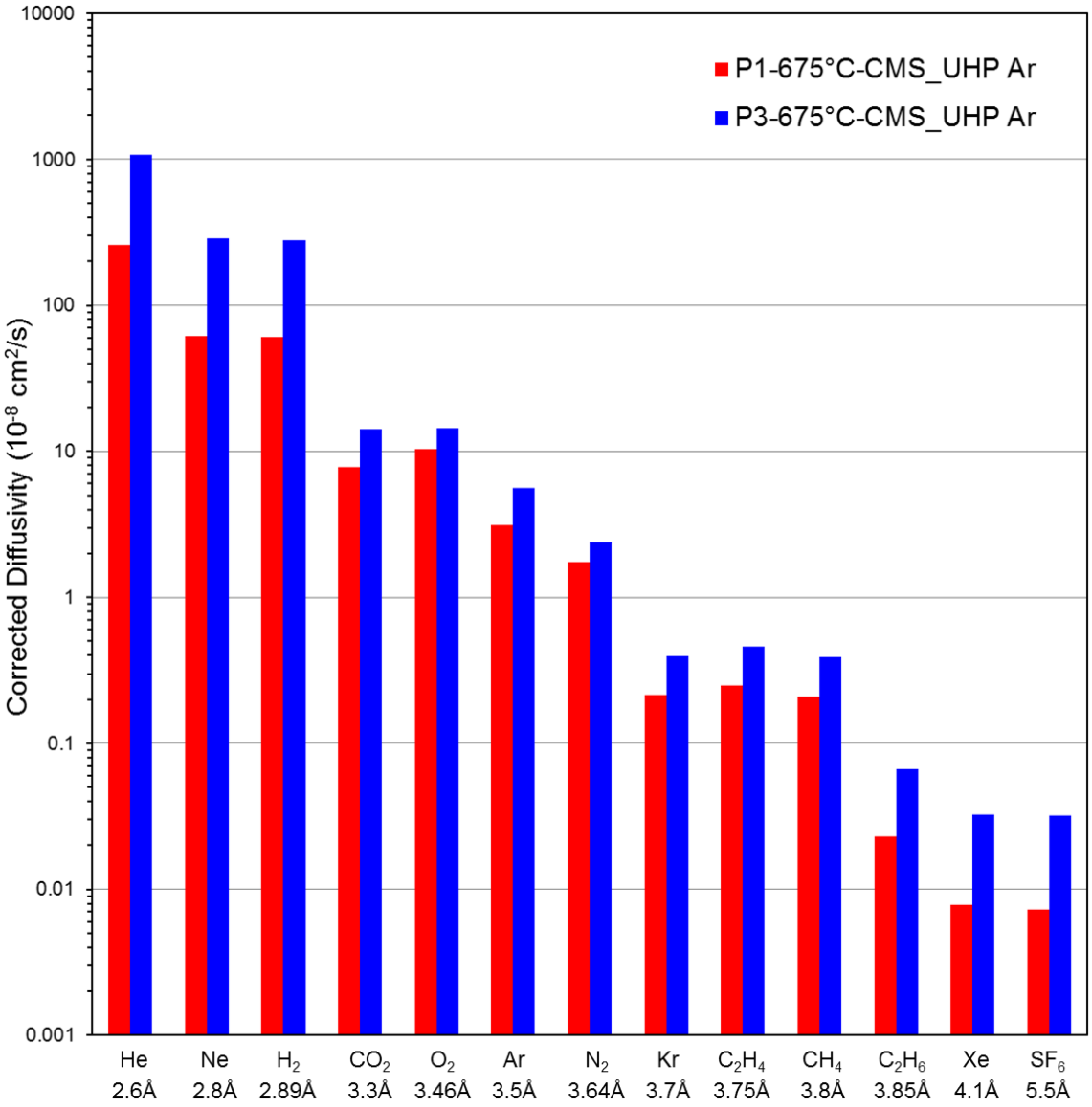

Figure 5.56: Corrected diffusivities of different penetrants at 35°C for CMS derived from UHP Ar pyrolysis of Matrimid® (red) and 6FDA:BPDA-DAM (blue) at 675°C

5.6.5. Diffusion Size Pore Distribution (DSPD)

The corrected diffusivities were used to obtain semi-quantitative diffusion size pore distributions (DSPDs) for the Matrimid® and the 6FDA:BPDA-DAM CMS obtained from UHP Ar pyrolysis at 675°C. The method for DSPD construction is described in Section 5.2.5 and Appendix C. Any reference to diffusivity in this section by default

implies corrected diffusivity unless otherwise specified. The constructed DSPDs are shown in Figure 5.57.

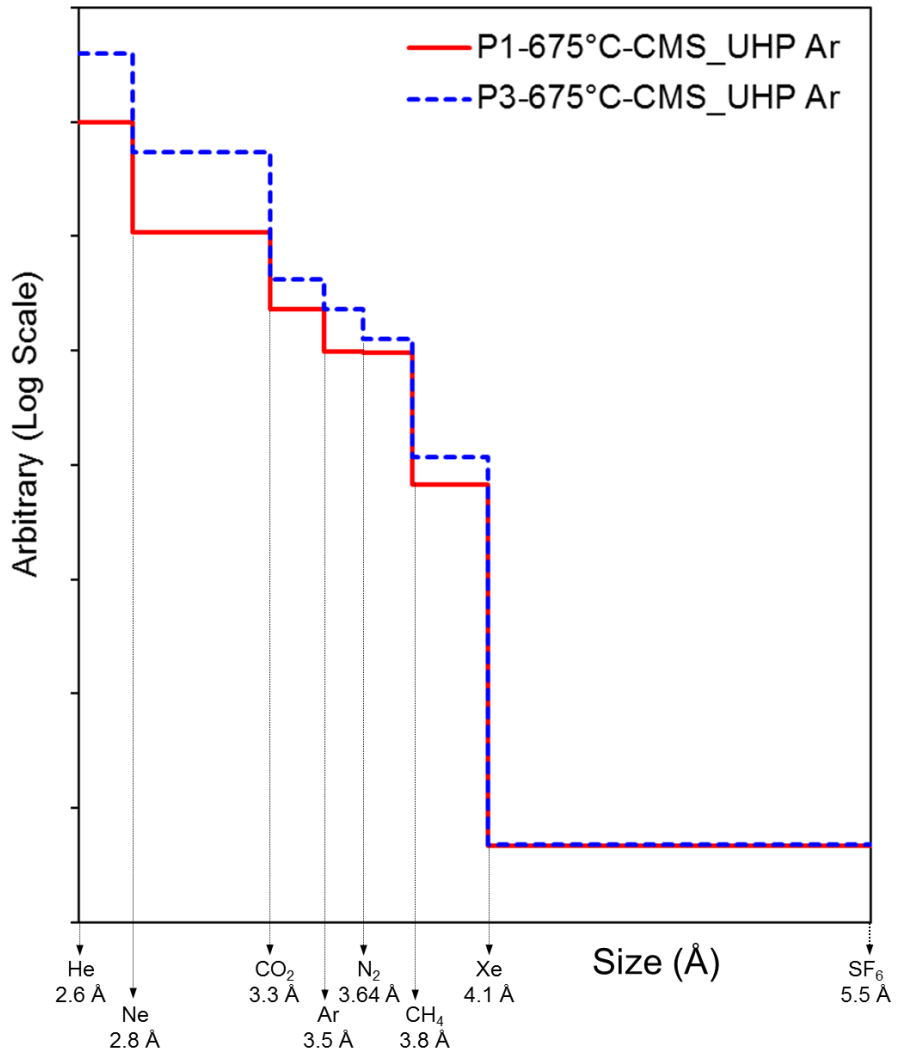

Figure 5.57: Semi-quantitative diffusion size pore distributions (DSPDs) for CMS derived from UHP Ar pyrolysis of Matrimid® (red) and 6FDA:BPDA-DAM (blue) at 675°C

As seen from Figure 5.57, the total area under the curve for 6FDA:BPDA-DAM CMS is greater than for the Matrimid® CMS. This suggests that 6FDA:BPDA-DAM CMS

clearly has a much larger number density of critical interconnected diffusion accessible pores compared to the Matrimid® CMS. The ratio of the areas under the DSPD curves for 6FDA:BPDA-DAM CMS vs. Matrimid® CMS (i.e. the ratio of helium diffusivities) is approximately 4.2. A larger fraction of the critical diffusive pores lie in the 2.6-3.3 Å range for the 6FDA:BPDA-DAM CMS and in the 2.6-2.8 Å range (and possibly < 2.6 Å) for the Matrimid® CMS. The distribution starts to tail off over 3.3 Å in both cases with an increasingly smaller number density of diffusion size pores being accessible to larger penetrants.

The semi-quantitative DSPDs presented here are useful in establishing structure-performance relationships for the engineered CMS materials. They can serve as a useful tool in understanding performance behavior CMS membranes for a given separation. For example consider CO_2/CH_4 separation and C_2H_4/C_2H_6 separation using the CMS membranes derived from Matrimid® and 6FDA:BPDA-DAM. The CO_2 diffusivity of the 6FDA:BPDA-DAM CMS is approximately ~1.8 times that of the Matrimid® CMS. The diffusion selectivities for CO_2/CH_4 is ~37 for the Matrimid® CMS and ~36 for the 6FDA:BPDA-DAM CMS. Analysis of the DSPDs (Figure 5.57) reveals that the 6FDA:BPDA-DAM CMS has a significantly larger number density of pores accessible to CO_2 (area under the curve to the right of CO_2) compared to the Matrimid® CMS. This results in a much higher CO_2 diffusivity in the 6FDA:BPDA-DAM CMS compared to the Matrimid® CMS. By comparison, the ratio of the number densities of pores accessible to CH_4 (area under the curves to the right of CH_4) is relatively smaller between CMS derived from the two precursors. Thus, the ratio of the CH_4 diffusivities of the 6FDA:BPDA-DAM and Matrimid® CMS is smaller compared to the ratio of their CO_2 diffusivities. This explains why the CO_2/CH_4 selectivity for the 6FDA:BPDA-DAM CMS is similar to the Matrimid® CMS (i.e. the 6FDA:BPDA-DAM CMS does not represent a permeability-selectivity trade-off despite the higher fractional free volume of the starting

polymer). The CO_2 sorption uptakes for the 6FDA:BPDA-DAM CMS is also much higher than the Matrimid® CMS. Thus the overall CO_2 permeability for the 6FDA:BPDA-DAM CMS is much higher than the Matrimid® CMS (~2.4 times higher for 50 psia feed pressure). The CO_2/CH_4 sorption selectivities of the 6FDA:BPDA-DAM and Matrimid® CMS, on the other hand, are similar. This coupled with the similar diffusivity selectivity yields similar overall CO_2/CH_4 permselectivity for the 6FDA:BPDA-DAM CMS compared to Matrimid® CMS. Thus 6FDA:BPDA-DAM CMS is ideal for CO_2/CH_4 separation and there is no permeability-selectivity trade-off resulting from the use of a more open precursor material for CMS fabrication.

Now consider C_2H_4/C_2H_6 separation. Both C_2H_4 and C_2H_6 lie at the tail end of the DSPD shown in Figure 5.57. Given the similar sizes of C_2H_4 (3.75 Å) and C_2H_6 (3.85 Å) this region does not allow significant leverage for the smaller molecule over the larger. The C_2H_4 diffusivity for the 6FDA:BPDA-DAM CMS is ~2.1 times that of the Matrimid® CMS, however its diffusion selectivity lower. Analysis of the areas under the two curves in the 3.6-3.8 Å region and 3.8-4.1 Å region (Figure 5.57) shows that both the C_2H_4 and C_2H_6 diffusivity for the 6FDA:BPDA-DAM CMS is higher compared to Matrimid® CMS, resulting in a selectivity trade-off. Thus based on the nature of the DSPD, there is a trade-off between the C_2H_4 diffusivity and C_2H_4/C_2H_6 diffusion selectivity resulting from the use of a more "open" precursor material for CMS fabrication. The C_2H_4 sorption coefficient is higher for the 6FDA:BPDA-DAM CMS compared to the Matrimid® CMS. This coupled with a higher diffusivity results in a higher C_2H_4 permeability for the 6FDA:BPDA-DAM CMS compared to the Matrimid® CMS. The sorption selectivity for the two membranes is similar. Thus following the trend of the diffusivity selectivity, the overall C_2H_4/C_2H_6 permselectivity for the 6FDA:BPDA-DAM CMS is lower than the Matrimid® CMS. Thus, unlike the CO_2/CH_4 case, use of a more open starting precursor

polymer 6FDA:BPDA-DAM for CMS fabrication results in a C_2H_4/C_2H_6 selectivity trade-off with the C_2H_4 permeability.

Thus the DSPDs are useful not just in understanding the differences in the pore structures of CMS derived from different precursors, but also the effects on the performance of different gas pairs. It is important to note that the cases explained are exclusive to CMS fabricated from UHP Ar pyrolysis of Matrimid® and 6FDA:BPDA-DAM at 675°C using Protocol 1 and will be different depending on the starting material and CMS fabrication conditions.

5.7. Coupled Effects of Precursor and Pyrolysis Temperature on Carbon Molecular Sieve Membranes

All prior discussion considered one of the following: (i) The effects of pyrolysis parameters, specifically the final pyrolysis temperature on the properties of CMS derived from the same precursor; (ii) The effects of the polymer precursor on the properties of CMS derived using identical pyrolysis conditions. It is also interesting to consider the combined effects of polymer precursor and pyrolysis temperature on CMS membrane structure and performance based on the diffusion size pore distributions (DSPDs). Figure 5.58 shows a comparison of the distributions for Matrimid® (P1) pyrolyzed at two temperatures 500°C and 675°C and 6FDA:BPDA-DAM (P3) pyrolyzed at 675°C. The samples are designated as P1-500°C-CMS_UHP Ar (black), P1-675°C-CMS_UHP Ar (red) and P3-675°C-CMS_UHP Ar (blue).

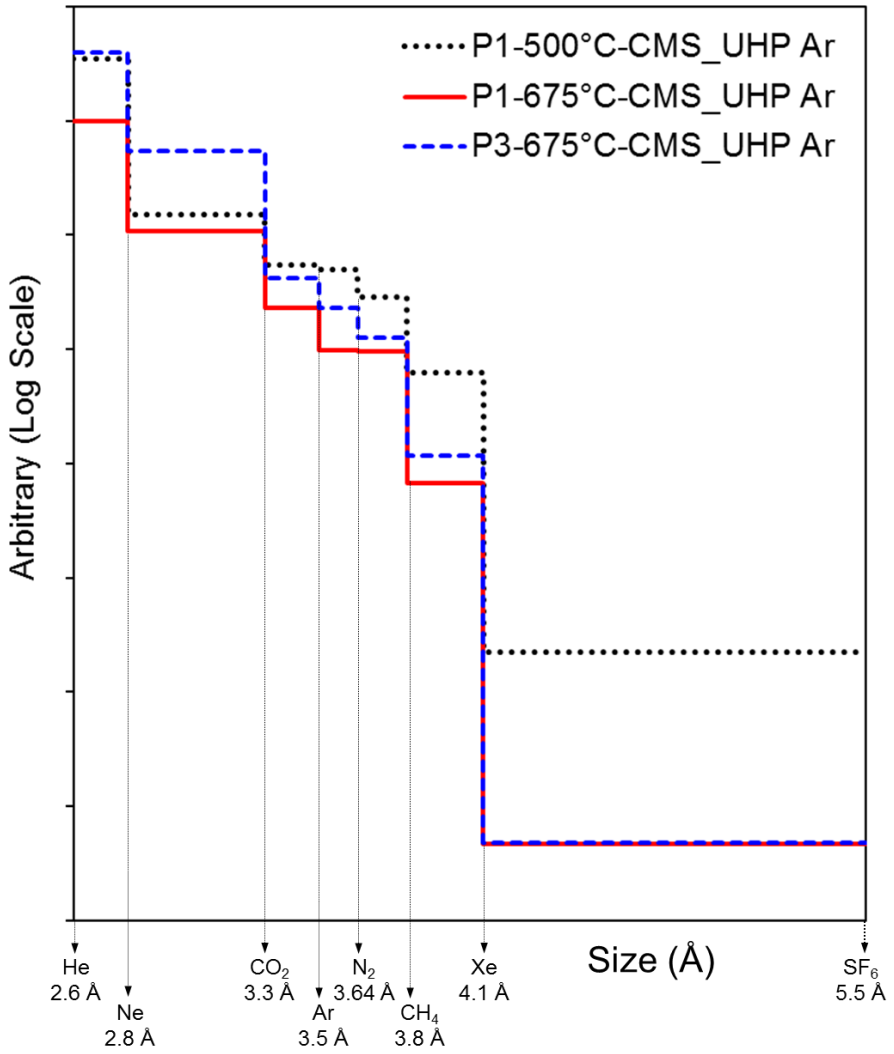

Figure 5.58: Semi-quantitative diffusion size pore distributions (DSPDs) for CMS derived from UHP Ar pyrolysis of Matrimid® at 500°C (black) and 675°C (red) and 6FDA:BPDA-DAM at 675°C (blue)

As seen from Figure 5.58, CMS derived from the pyrolysis of Matrimid® at a lower pyrolysis temperature of 500°C consistently yields a much higher number density of pores (area under the curve) in all pore size ranges compared to CMS derived from Matrimid® at a higher pyrolysis temperature of 675°C (Compare the distributions for P1-500°C-CMS and P1-675°C-CMS where the precursor is held constant). Similarly, CMS derived from pyrolysis of 6FDA:BPDA-DAM at 675°C also consistently yields a much

higher number density of pores (area under the curve) in all pore size ranges compared to CMS derived from Matrimid® at the 675°C (Compare the distributions for P3-675°C-CMS and P1-675°C-CMS where the pyrolysis temperature is held constant).

The coupled effects of the polymer precursor and pyrolysis temperature on the CMS pore size distribution may however be more complex. Consider CMS obtained from pyrolysis of Matrimid® at 500°C (P1-500°C-CMS) vs. CMS derived from pyrolysis of 6FDA:BPDA-DAM at 675°C (P3-675°C-CMS). In this case both the polymer precursor and the pyrolysis temperature have been varied. A comparison of the two distributions (Figure 5.58) shows a larger number density of pores in the 2.6-3.3 Å range for the P3-675°C-CMS compared to P1-500°C-CMS. However, the number density of pores beyond 3.3 Å is larger for P1-500°C-CMS compared to P3-675°C-CMS. This suggests that although 6FDA:BPDA-DAM is more open starting material compared to Matrimid®, high temperature pyrolysis has an effect of eliminating the larger tail end pores possibly resulting in a sharper and narrower DSPD.

Further consider the areas under the curve to the right of 3.3 Å and 3.8 Å for the three cases in Figure 5.58, i.e. for CO_2/CH_4 separation. CMS obtained from pyrolysis of Matrimid® at a lower pyrolysis temperature of 500°C shows a higher CO_2 permeability by comparison to CMS derived from Matrimid® pyrolysis at 675°C, resulting from the larger number density of pores (area under the curve to the right of 3.3 Å) for the Matrimid® 500°C CMS. At the same time, the CH_4 diffusivity (area under the curve to the right of 3.8 Å) is also significantly higher than the Matrimid® 675°C-CMS. This represents a lower CO_2/CH_4 selectivity for the Matrimid® 500°C-CMS. Thus, going to a lower pyrolysis temperature using the same precursor, Matrimid®, results in a permeability-selectivity trade-off for CO_2/CH_4 separation. By comparison, changing the precursor from Matrimid® to 6FDA:BPDA-DAM rather than changing the pyrolysis temperature does not result in this undesired trade-off between permeability and selectivity. The reason for this was

explained in detail with respect the DSPD curves for the Matrimid® 675°C-CMS and the 6FDA:BPDA-DAM 675°C-CMS in Section 5.6.5. Table 5.7 show the CO_2/CH_4 separation performance for the three CMS membranes: P1-500°C-CMS_UHP Ar, P1-675°C-CMS_UHP Ar and P3-675°C-CMS_UHP Ar.

Table 5.7: CO_2/CH_4 separation performance of different CMS membranes

Precursor	Pyrolysis Temperature	CMS Designation	P_{CO2} (Barrer)	P_{CO2}/P_{CH4}
Matrimid®	500°C	P1-500°C-CMS_UHP Ar	825	21.8
Matrimid®	675°C	P1-675°C-CMS_UHP Ar	460	71.4
6FDA:BPDA-DAM	675°C	P3-675°C-CMS_UHP Ar	1125	68.3

Thus, the DSPDs can be useful not just in explaining the transport properties of CMS membranes with respect to their structure, but also in engineering CMS for a target application by considering the effects of precursor vs. pyrolysis processing conditions.

5.8. Summary

The pore structure and separation performance of CMS membranes can be tailored by controlling several pyrolysis parameters in the CMS fabrication process such as the heating protocol, pyrolysis atmosphere etc. The effects of these parameters on CMS structure and performance depend on the starting polymer material as well as the target gas separation. Detailed analyses of the effects of these parameters on C_2H_4/C_2H_6 separation performance of CMS derived from three precursors: Matrimid®, 6FDA-DAM and 6FDA:BPDA-DAM were reported. The evolution in C_2H_4/C_2H_6 separation performance with the pyrolysis parameters was considered with respect to the CMS schematic pore structures and hypothetical critical pore distributions. It was shown that the overall permeability and selectivity trends of CMS membranes are primarily dominated by their diffusion behavior. These insights were used to achieve optimum CMS fabrication conditions for C_2H_4/C_2H_6 separation using each precursor.

A discussion of different techniques such as TGA-FTIR and elemental analysis, Raman spectroscopy, WAXD, PALS, TEM and AFM, density and micropore volume measurements, gas transport etc. to characterize the nature and the pore structure of CMS membranes was also presented. Traditional characterization techniques based on spectroscopy and microscopy, as well as micropore distribution analyses were found inconclusive in interpreting CMS performance in relation to its pore morphology. A novel method based on measuring the transport properties of different sized gases as molecular scale probes of the CMS pores was developed to infer pore structure and critical pore size distributions. This, in conjunction with separation performance data, provided critical insights into the structure-performance relationships of the engineered CMS materials.

The discovery of the presence of a physical aging effect in CMS membranes derived from certain glassy polymers was reported. This results in a time-dependent behavior of CMS separation performance. Analogous to physical aging in glassy polymers, CMS membrane physical aging exhibits dependence on factors such as the starting precursor material, separation layer thickness, history etc. This finding adds another controlling factor to CMS performance besides the CMS fabrication parameters. The effect of physical aging was most significant in CMS derived from 6FDA-DAM and makes it an unattractive precursor for C_2H_4/C_2H_6 separation. Physical aging had the least effect on Matrimid® CMS and 6FDA:BPDA-DAM CMS was intermediate.

While the current study focuses on CMS dense films owing to their simple geometry that allow fundamental analysis, considerations related to translation to the practically useful CMS hollow fiber form were also presented based on Liren Xu's work in the Koros Group. Considering the combined effects of "substructure collapse" on the CMS fiber macro-morphology and "physical aging" on the CMS microstructure, 6FDA:BPDA-DAM was found to be the most preferred precursor for CMS fabrication for C_2H_4/C_2H_6 separation in this study.

5.9. References

[1] Steel KM, Koros WJ. Investigation of porosity of carbon materials and related effects on gas separation properties. Carbon. 2003;41(2):253-66.

[2] Steel KM, Koros WJ. An investigation of the effects of pyrolysis parameters on gas separation properties of carbon materials. Carbon. 2005;43(9):1843-56.

[3] Kiyono M. Carbon molecular sieve membranes for natural gas separations. Georgia Institute of Technology, Doctor of Philosophy, 2010.

[4] Jenkins GM, Kawamura K. Polymeric carbons - Carbon fiber, glass and char. London: Cambridge University Press 1976.

[5] Barsema JN, Klijnstra SD, Balster JH, van der Vegt NFA, Koops GH, Wessling M. Intermediate polymer to carbon gas separation membranes based on Matrimid PI. J Membrane Sci. 2004;238(1-2):93-102.

[6] Pierson. Handbook of carbon, graphite, diamond, and fullerenes NY: Noyes Publication 1993.

[7] Hatori H, Yamada Y, Shiraishi M, Yoshihara M, Kimura T. The mechanism of polyimide pyrolysis in the early stage. Carbon. 1996;34(2):201-8.

[8] Ehlers GFL, Fisch KR, Powell WR. Thermal degradation of polymers with phenylene units in the chain. IV. Aromatic polyamides and polyimides. J Polymer Sci Part A: Polymer Chemistry. 1970;8(12):3511-27.

[9] Marsh H. Introduction to carbon science: Butterworths; 1989.

[10] Tuinstra F, Koenig JL. Raman spectrum of graphite. J Chem Phys. 1970;53(3):1126-&.

[11] Dresselhaus MS, Jorio A, Souza AG, Saito R. Defect characterization in graphene and carbon nanotubes using Raman spectroscopy. Philos T R Soc A. 2010;368(1932):5355-77.

[12] Lai J, Guo HJ, Wang ZX, Li XH, Zhang XP, Wu FX, et al. Preparation and characterization of flake graphite/silicon/carbon spherical composite as anode materials for lithium-ion batteries. J Alloy Compd. 2012;530:30-5.

[13] Fu YJ, Liao KS, Hu CC, Lee KR, Lai JY. Development and characterization of micropores in carbon molecular sieve membrane for gas separation. Micropor Mesopor Mat. 2011;143(1):78-86.

[14] Steel KM. Carbon membranes for challenging gas separations. The University of Texas at Austin, Doctor of Philosophy, 2000.

[15] Kiyono M, Williams PJ, Koros WJ. Effect of polymer precursors on carbon molecular sieve structure and separation performance properties. Carbon. 2010;48(15):4432-41.

[16] Breck DW. Zeolite molecular sieves. New York: Wiley & Sons; 1974.

[17] Reid C, Sherwood TK. The properties of gases and liquids: their estimation and correlation. New York: Mcgraw-hill; 1976.

[18] Singh A, Koros WJ. Significance of entropic selectivity for advanced gas separation membranes. Ind Eng Chem Res. 1996;35(4):1231-4.

[19] Xu L, Rungta M, Koros WJ. Matrimid (R) derived carbon molecular sieve hollow fiber membranes for ethylene/ethane separation. J Membrane Sci. 2011;380(1-2):138-47.

[20] Williams PJ, Koros WJ. Gas separation by carbon membranes. In: Li NN, Fane AG, Winston Ho WS, Matsura T. Advanced membrane technology and applications. New Jersey: John Wiley & Sons Inc. 2008.

[21] Xu L, Rungta M, Brayden MK, Martinez MV, Stears BA, Barbay GA, et al. Olefins-selective asymmetric carbon molecular sieve hollow fiber membranes for hybrid membrane-distillation processes for olefin/paraffin separations. J Membrane Sci. 2012 (in press).

[22] Koros WJ. Barrier polymers and structures. Washington DC: American Chemical Society 1990.

[23] Koros WJ. Transport properties. In: Mark HM. Encyclopedia of polymer science and technology. 3ed: Wiley-Interscience 2004.

[24] Pinnau I, Hellums MW, Koros WJ. Gas-transport through homogeneous and asymmetric polyestercarbonate membranes. Polymer. 1991;32(14):2612-7.

[25] Pfromm PH, Pinnau I, Koros WJ. Gas-transport through integral-asymmetric membranes - A comparison to isotropic film transport-properties. J Appl Polym Sci. 1993;48(12):2161-71.

[26] Pfromm PH, Koros WJ. Accelerated physical aging of thin glassy polymer-films - Evidence from gas-transport measurements. Polymer. 1995;36(12):2379-87.

[27] Cui LL, Qiu WL, Paul DR, Koros WJ. Physical aging of 6FDA-based polyimide membranes monitored by gas permeability. Polymer. 2011;52(15):3374-80.

[28] Huang Y, Paul DR. Effect of temperature on physical aging of thin glassy polymer films. Macromolecules. 2005;38(24):10148-54.

[29] Jones CW, Koros WJ. Characterization of ultramicroporous carbon membranes with humidified feeds. Ind Eng Chem Res. 1995;34(1):158-63.

[30] Gawrys M, Fastyn P, Gawlowski J, Gierczak T, Niedzielski J. Prevention of water vapour adsorption by carbon molecular sieves in sampling humid gases. J Chromatogr A. 2001;933(1-2):107-16.

[31] Menendez I, Fuertes AB. Aging of carbon membranes under different environments. Carbon. 2001;39(5):733-40.

[32] Lagorsse S, Magalhaes FD, Mendes A. Aging study of carbon molecular sieve membranes. J Membrane Sci. 2008;310(1-2):494-502.

[33] Jones CW, Koros WJ. Carbon composite membranes - A solution to adverse humidity effects. Ind Eng Chem Res. 1995;34(1):164-7.

[34] Kusakabe K, Yamamoto M, Morooka S. Gas permeation and micropore structure of carbon molecular sieving membranes modified by oxidation. J Membrane Sci. 1998;149(1):59-67.

[35] Jones CW, Koros WJ. Carbon molecular-sieve gas separation membranes .2. Regeneration following organic exposure. Carbon. 1994;32(8):1427-32.

[36] Grisdale RO. The properties of carbon contacts. J Appl Phys. 1953;24(10):1288-96.

[37] Kiyono M, Williams PJ, Koros WJ. Effect of pyrolysis atmosphere on separation performance of carbon molecular sieve membranes. J Membrane Sci. 2010;359(1-2):2-10.

CHAPTER 6

ANALYSIS OF THE EFFECTS OF TESTING CONDITIONS ON THE ETHYLENE/ETHANE SEPARATION PERFORMANCE OF CARBON MOLECULAR SIEVE DENSE FILM MEMBRANES

6.1. Overview

Characterizing the effects of testing conditions, i.e. the testing temperature, pressure and feed composition on CMS performance is important not just from a practical stand point, but also for a fundamental understanding of the nature of CMS membrane separation. Section 6.2 discusses the effects of testing temperature on CMS transport evaluated between 25-50°C. Transport and thermodynamics fundamentals have been applied to clarify why CMS membranes outperform polymeric membrane performance, as well as to compare between CMS formed from different precursors and processing conditions. The pressure dependence of ethylene and ethane transport in the CMS is presented in Section 6.3. Effects of the feed pressure on ethylene/ethane (C_2H_4/C_2H_6) separation for downstream vacuum conditions have been described based on experimental results. Additionally, preliminary modeling predictions of the effect of feed to permeate pressure ratio of CMS performance have also been considered. Section 6.4 assesses the effects on C_2H_4/C_2H_6 separation for a binary mixture of the two and compares the results against pure gas performance, to get a more realistic measure of the CMS performance resulting from competition and bulk flow effects. In addition to experimental analysis, modeling work to predict multicomponent transport in CMS membranes has also been considered.

6.2. Effects of Testing Temperature on Carbon Molecular Sieve Membrane Performance

Consideration of the membrane performance as a function of the operating temperature is important for practical application, since membranes are rarely operated at ambient temperatures. Moreover, temperature dependence helps understand the fundamental transport behavior of membranes towards different penetrants. A comparison of the temperature dependence of polymeric vs. CMS membranes, as well as CMS membranes derived from different precursors and processing conditions can also elucidate the fundamental nature of polymeric and CMS membrane gas separation. Any reference to "temperature" in this Section 6.2 will by default imply "operating/testing temperature" unless otherwise specified, while the CMS fabrication temperature is addressed as "pyrolysis temperature". The effects of operating temperature on the C_2H_4/C_2H_6 separation performance of CMS membranes were analyzed in this work. All performances reported in Section 6.2 are at 50 psia pure gas feed pressure.

6.2.1. Temperature dependence of Ethylene/Ethane Separation

Pure gas permeation and sorption measurements between 25-50°C on dense film membranes were used to evaluate the temperature dependence of C_2H_4/C_2H_6 separation. Limitations on the epoxy and pressure transducers used for permeation experiments restricted the highest temperature measured to 50°C. Temperature-dependence measurements were made on a Matrimid® precursor dense film (P1), CMS dense films derived from UHP Ar pyrolysis of Matrimid® at 500°C, 550°C and 675°C, and a CMS dense film derived from UHP Ar pyrolysis of 6FDA:BPDA-DAM at 675°C. The permeation and sorption coefficients obtained were further used to calculate the average

transport diffusivities. In addition the thermodynamically corrected diffusivities were also estimated using Equation 2.23. The different transport properties were calculated using the data and equations in Appendix B. The results are plotted as a function of temperature in Figures 6.1-6.5, and summarized in Table 6.1.

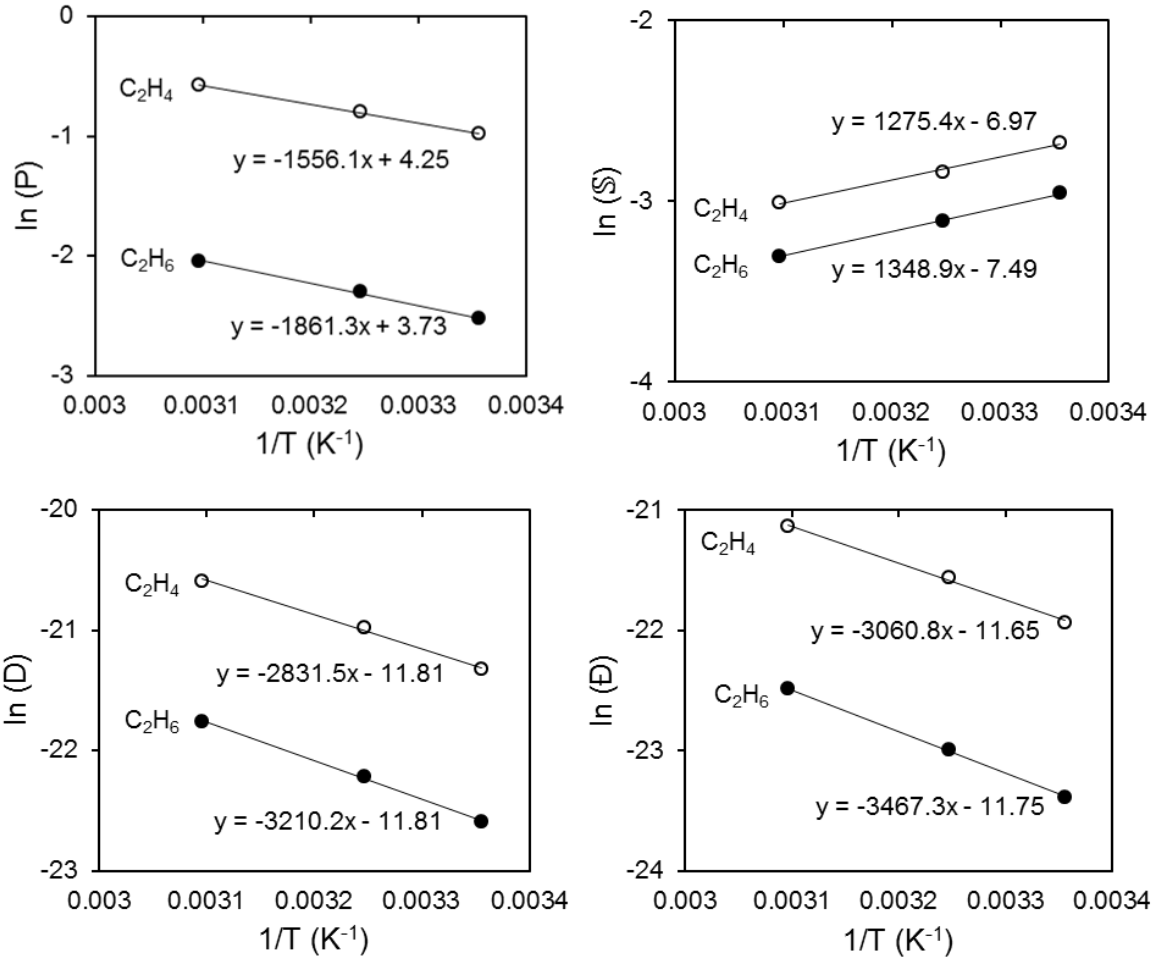

Figure 6.1: Temperature dependence of C_2H_4 and C_2H_6 transport in Matrimid® precursor dense film (P1): Arrhenius-type plots of Permeability (P), diffusivity (D) and corrected diffusivity (Đ), and van't-Hoff type plot of sorption coefficient (𝕊)

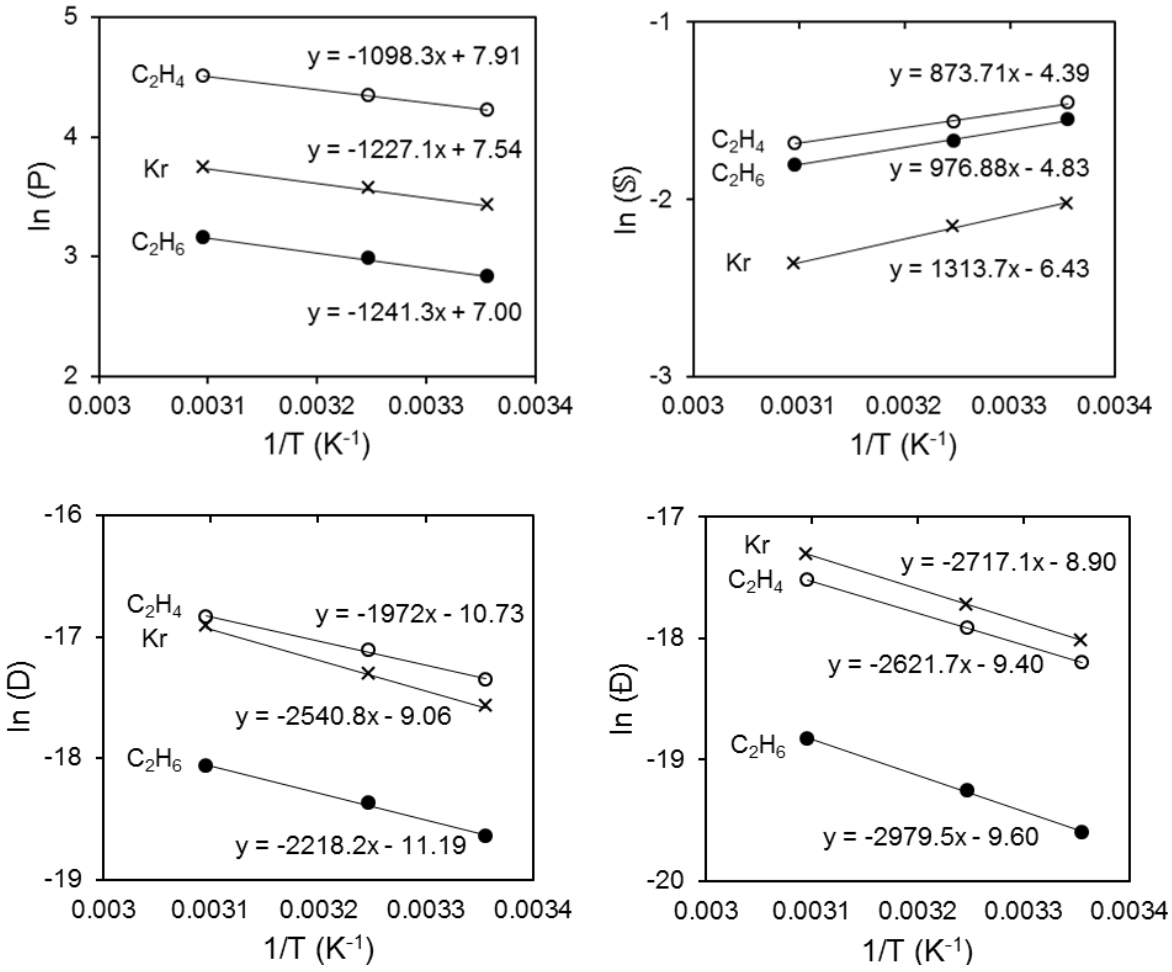

Figure 6.2: Temperature dependence of C_2H_4, C_2H_6 and Kr transport in CMS dense film derived from UHP Ar pyrolysis of Matrimid® at 500°C (P1-500°-CMS): Arrhenius-type plots of permeability (P), diffusivity (D) and corrected diffusivity (Đ), and van't-Hoff type plot of sorption coefficient (𝕊)

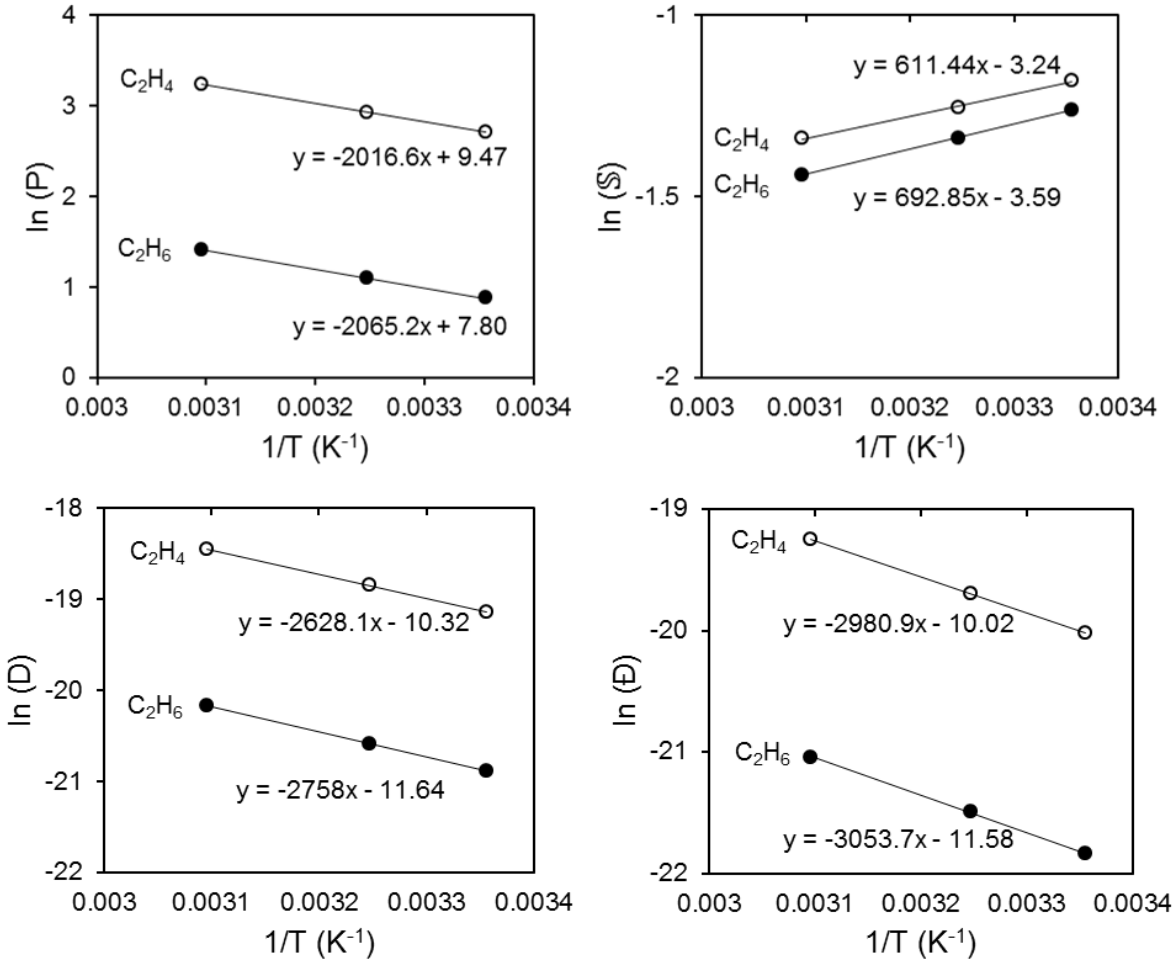

Figure 6.3: Temperature dependence of C_2H_4 and C_2H_6 transport in CMS dense film derived from UHP Ar pyrolysis of Matrimid® at 550°C (P1-550°-CMS): Arrhenius-type plots of permeability (P), diffusivity (D) and corrected diffusivity (Đ), and van't-Hoff type plot of sorption coefficient (𝕊)

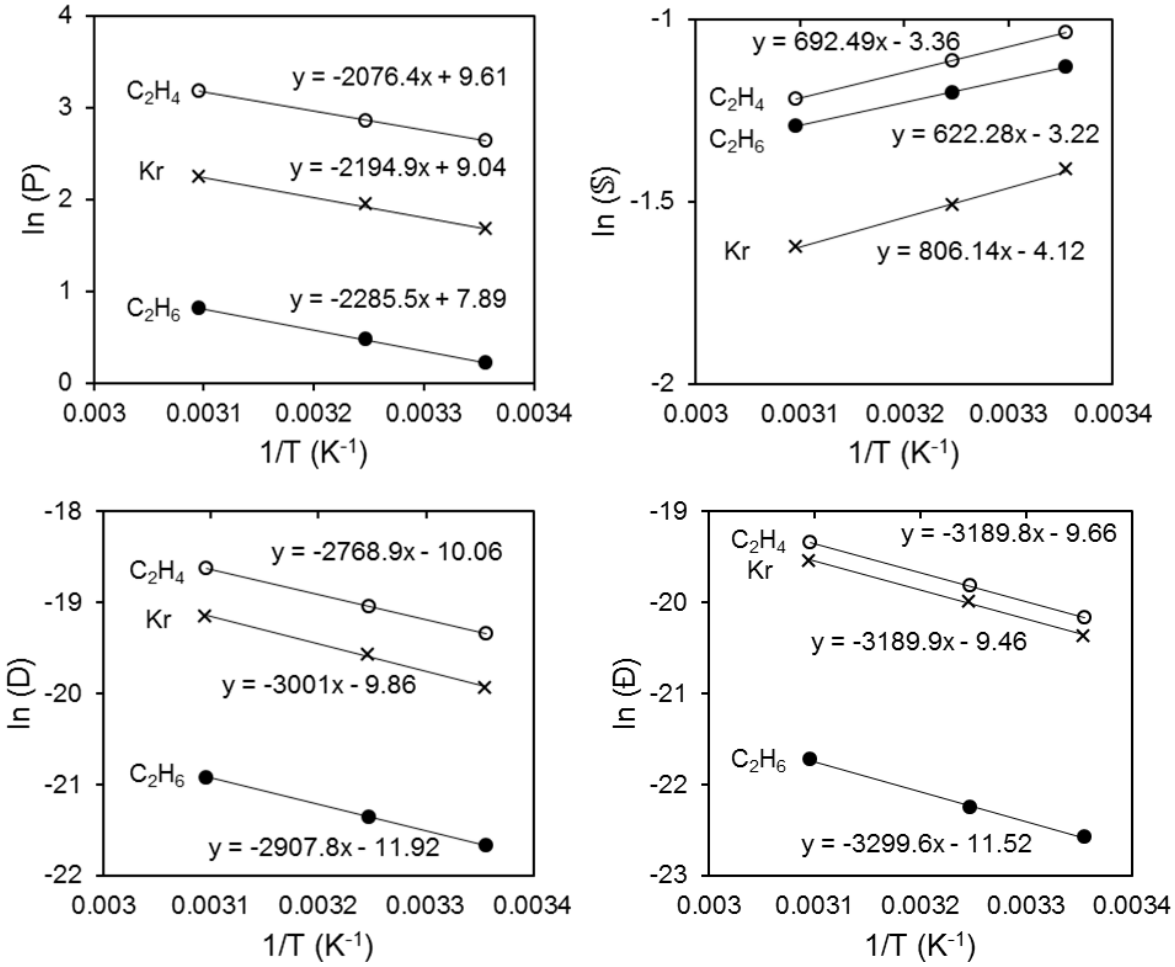

Figure 6.4: Temperature dependence of C_2H_4, C_2H_6 and Kr transport in CMS dense film derived from UHP Ar pyrolysis of Matrimid® at 675°C (P1-675°-CMS): Arrhenius-type plots of permeability (P), diffusivity (D) and corrected diffusivity (Đ), and van't-Hoff type plot of sorption coefficient (𝕊)

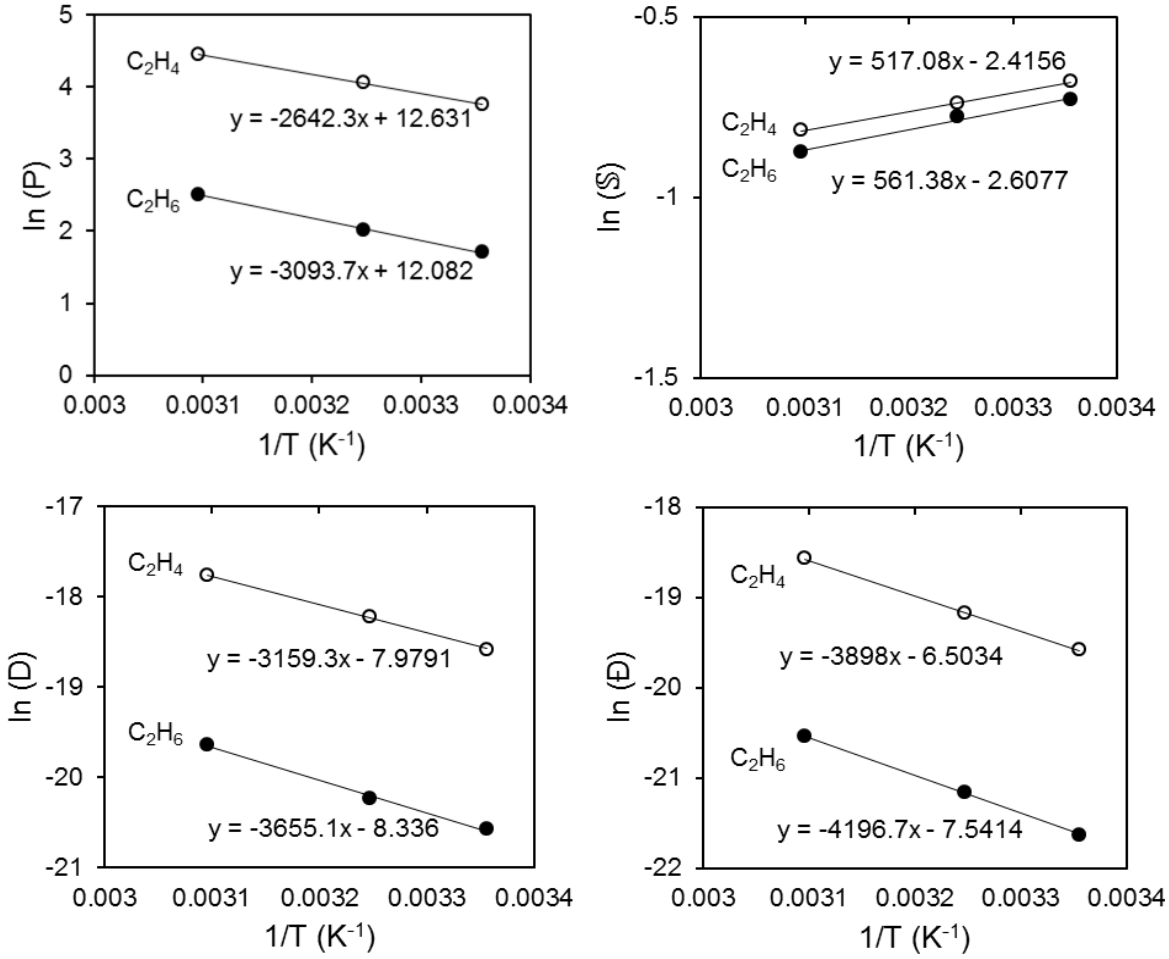

Figure 6.5: Temperature dependence of C_2H_4 and C_2H_6 transport in CMS dense film derived from UHP Ar pyrolysis of 6FDA:BPDA-DAM at 675°C (P3-675°-CMS): Arrhenius-type plots of permeability (P), diffusivity (D) and corrected diffusivity (Đ), and van't-Hoff type plot of sorption coefficient (𝕊)

Table 6.1: Summary of performance, activation energies (E_P, E_D, $E_Đ$), pre-exponential factors (P_o, D_o, $Đ_o$), and energetic and entropic contribution factors for C_2H_4/C_2H_6 separation between 25-50°C for different dense films

	P1	**P1-500°C-CMS**	**P1-550°C-CMS**	**P1-675°C-CMS**	**P3-675°C-CMS**
P_{C2H4} (Barrer)	0.4-0.6	68.1-91.2	15.1-25.3	14.1-24.2	43.1-85.4
D_{C2H4} (10^{-9} cm^2/s)	0.5-1.1	29.2-48.8	4.9-9.7	4.0-8.1	8.5-19.1
$Đ_{C2H4}$ (10^{-9} cm^2/s)	0.3-0.7	12.5-24.6	2.0-4.4	1.7-4.0	3.2-8.6
P_{C2H4}/P_{C2H6}	4.1-4.9	3.8-4.0	6.2-6.3	10.8-11.2	6.9-7.8
D_{C2H4}/D_{C2H6}	3.2-3.7	3.4-3.6	5.6-5.8	9.9-10.3	6.5-7.4
$Đ_{C2H4}/Đ_{C2H6}$	3.8-4.3	3.7-4.1	6.0-6.1	10.7-11.0	7.2-7.8
$E_{P\text{-}C2H4}$ (kJ/mol)	12.9	9.1	16.8	17.3	21.9
$E_{P\text{-}C2H6}$ (kJ/mol)	15.5	10.3	17.2	19.0	25.7
$E_{D\text{-}C2H4}$ (kJ/mol)	23.5	16.4	21.9	23.0	26.3
$E_{D\text{-}C2H6}$ (kJ/mol)	26.7	18.4	22.9	24.2	30.4
$E_{Đ\text{-}C2H4}$ (kJ/mol)	25.5	21.8	24.8	26.5	32.4
$E_{Đ\text{-}C2H6}$ (kJ/mol)	28.8	24.8	25.4	27.4	34.9
$P_{o\text{-}C2H4}$ (Barrer)	7.0E+01	2.7E+03	1.3E+04	1.5E+04	3.1E+05
$P_{o\text{-}C2H6}$ (Barrer)	4.2E+01	1.1E+03	2.5E+03	2.7E+03	1.8E+05
$D_{o\text{-}C2H4}$ (cm^2/s)	7.5E-06	2.2E-05	3.3E-05	4.3E-05	3.4E-04
$D_{o\text{-}C2H6}$ (cm^2/s)	7.3E-06	1.4E-05	8.9E-06	6.7E-06	2.4E-04
$Đ_{o\text{-}C2H4}$ (cm^2/s)	8.7E-06	8.2E-05	4.5E-05	7.8E-05	1.5E-03
$Đ_{o\text{-}C2H6}$ (cm^2/s)	7.9E-06	6.8E-05	9.3E-06	9.9E-06	5.3E-04
Energetic Factor (based on D)	3.2-3. 6	2.1-2.3	1.5-1.6	1.5-1.6	4.6-5.3
Entropic Factor (based on D)	~1.0	~1.6	~3.8	~6.4	~1.5
Energetic Factor (based on Đ)	3.5-3.9	3.0-3.3	1.2-1.3	1.4-1.5	2.5-2.7
Entropic Factor (based on Đ)	~1.1	~1.2	~4.8	~8.0	~2.9

The temperature dependences of permeability and diffusivity were fitted to Arrhenius-type equations (Equations 2.24 and 2.26 respectively), while the sorption coefficient follows a van't-Hoff-type equation (Equation 2.25). The results for the different dense film membranes are summarized in Figures 6.1-6.5. In all cases, the model equations show a very good fit to the experimental data with R^2 >0.99. The model fits were further used to estimate several parameters such as the activation energies of permeation and diffusion, the heat of sorption and the pre-exponential factors of permeation, sorption and diffusion. These results are summarized in Table 6.1 above.

As seen from Table 6.1 and Figures 6.1-6.5, in all cases, C_2H_4 permeability increases as a function of the testing temperature, while the C_2H_4/C_2H_6 selectivity decreases. Similarly, the diffusion coefficients increase with the testing temperature in all cases. The increase in the permeability is less than the increase in the diffusivity as a function of testing temperature, due to compensation from the sorption coefficients which decrease as a function of the testing temperature. In all cases, the diffusion selectivity is the main contributing factor to the overall permselectivity, while the sorption selectivity remains in the range of 1.1-1.3. For a given membrane, the activation energies of permeation and diffusion of C_2H_4 is slightly lower than C_2H_6, indicating a lower resistance to C_2H_4 transport.

6.2.2. Insight into Ethylene/Ethane Separation Performance as a Function of Pyrolysis Temperature

Consider the polymer precursor Matrimid® (P1) and the CMS dense films derived from UHP Ar pyrolysis of Matrimid® at different pyrolysis temperatures (P1-500°C-CMS, P1-550°C-CMS and P1-675°C-CMS). The reader should refer to Table 6.1 for the following discussion. The expected trends of permeability and diffusivity as a function of

the pyrolysis temperature have already been described in great detail in Chapter 5. The C_2H_4 permeability increases several orders of magnitude in going from the precursor polymer, Matrimid® to the CMS dense film, P1-500°C-CMS. The C_2H_4/C_2H_6 selectivity of the P1-500°C-CMS, however, drops below that of the precursor. As described previously, the P1-500°C-CMS is in a partially pyrolyzed state with large micropores resulting from the evolution of by-products of polymer decomposition during pyrolysis. This results in a drastic increase in the permeability in going from the precursor to P1-500°C-CMS. However, since the polymer decomposition is still ongoing at this stage, the P1-500°C-CMS contains a very open structure with large micropores that are barely selective (refer to Sections 5.2.5.6 and 5.2.5.7 for a detailed discussion). The activation energies of permeation of C_2H_4 and C_2H_6 decrease in going from the precursor to P1-500°C-CMS indicating a lower resistance to gas permeation due to the open structure of P1-500°C-CMS. This, in turn, is a result of a decrease in the activation energies of diffusion in going from the precursor to P1-500°C-CMS. The increase in permeability in going from the precursor to P1-500°C-CMS primarily results from an increase in the pre-exponential factor of permeation by two orders of magnitude. Similarly, the diffusion front factor increases over an order of magnitude in going from the precursor to P1-500°C-CMS. This increase in the diffusion front factor is presumably a result of a large increase in the diffusive jump length (λ) in going from the polymer to the CMS membrane (refer to Equation 2.29).

Comparison of the transport properties of P1-500°C-CMS, P1-550°C-CMS and P1-675°C-CMS (Table 6.1) reveals that the C_2H_4 diffusivity, and, in turn, the C_2H_4 permeability, decreases with an increase in the final pyrolysis temperature. This is a result of the condensed CMS framework and a shift to a smaller average pore size with an increase in the pyrolysis temperature (Figure 5.4). The activation energies of permeation and diffusion increase with the pyrolysis temperature, indicating greater

resistance to gas transport due to the "tighter" CMS structure. While there may be a trend in the pre-exponential factors for permeability and diffusivity of the different Matrimid® derived CMS, it may be best to avoid over-interpreting these parameters given the complex nature and effects of P_o, D_o and $Đ_o$.

6.2.3. Energetic and Entropic Contribution to Ethylene/Ethane Separation

As mentioned previously, diffusion selectivity is the main contributing factor to the overall selectivity while the sorption selectivity is between 1.1-1.3. Diffusion selectivity is mainly dominated by the size and shape of the gas molecules to be separated. This diffusion selectivity was further factored into an "energetic" contribution factor and an "entropic" contribution factor [1, 2], as described in Equation 2.30. The results are summarized in Table 6.1. Using the corrected diffusivity is a more appropriate measure of the energetic and entropic contributions since it should be independent of the gas concentration and dependent directly on the size and shape of the molecules. The energetic factor results from a difference in the activation energies of diffusion of the two penetrants being separated (Equation 2.30). The entropic factor reflects dependence of the shapes and subtle configurational differences of the molecules, resulting from several degrees of freedom of rotation and internal vibration that may be lost in transition through the diffusion-limiting ultramicropores (Equation 2.32). For C_2H_4/C_2H_6 separation, the somewhat "planar" shape of C_2H_4 may allow it to have an "entropic" advantage over the "bulkier" C_2H_6 molecule in the activated state, by having fewer constraints on the acceptable orientations, if the membrane is capable of discriminating between their subtle shape and configurational differences. Contributions resulting from the entropic factor can be shown to be significant for molecules such as C_2H_4 and C_2H_6 which are similar in size and sorption properties [3]. These effects are discussed below.

Analysis of the energetic and entropic selectivity contributions of the Matrimid® polymer precursor membrane (P1 in Table 6.1) reveals that the main contribution to the overall diffusion selectivity comes from the energetic factor, while the entropic selection factor is 1.1. This suggests that the precursor polymer membrane is not capable of discriminating between the configurational differences of C_2H_4 and C_2H_6 molecules. Polymeric membranes consist of flexible polymer chains. Gas transport mechanism through polymeric membranes is discussed in Section 2.3. As gas molecules acquire enough activation energy, they move through the polymer matrix via the random creation of transient diffusive gaps due to thermal energy. The flexible polymer chains are not capable of discriminating between subtle shape differences of similar sized molecules. As a result, the entropic selection factor for C_2H_4/C_2H_6 in the polymeric membrane is close to 1 (Table 6.1).

By comparison, molecular sieving materials like CMS have a rigid pore structure that may be capable of discrimination between different molecular configurations. This however is dependent on the limiting pore dimension and shape of the CMS material. If the CMS "slit-like" pore structure [4] is too "open", as in the case of the P1-500°C-CMS, it may not be capable of discriminating between the shape and configurational differences of C_2H_4 and C_2H_6. Analysis of the energetic and entropic contribution factors of P1-500°C-CMS (Table 6.1) shows that, similar to the polymer precursor, the main contribution to the diffusion selectivity comes from the energetic factor, while the entropic factor is ~1.2.

As the final pyrolysis temperature increases, the CMS pore structure becomes "tighter" and the diffusion-limiting ultramicropores shift to a smaller average pore size, as depicted in Figure 5.4. This allows the tight CMS slit-like pores to now discriminate between the shapes and configurational differences of the somewhat "planar" C_2H_4 and the "bulkier" C_2H_6. As seen from Table 6.1, the main contribution to the diffusion

selectivity in case of the P1-550°C-CMS and P1-675°C-CMS comes from the entropic selection factor, while the energetic selectivity remains moderate. This entropic selectivity is essentially a measure of the configurational advantage that the "slimmer" C_2H_4 molecule has over the bulkier C_2H_6 molecules in transport through the CMS "slit-shaped" pore structure. In fact, the P1-675°C-CMS is capable of such high C_2H_4/C_2H_6 selectivity ~12 due to its exceptionally high entropic selectivity, close to ~8 (Table 6.1). The high entropic selectivity factor in CMS membranes resulting from the rigid slit-shaped CMS pore structure, which is not possible in the case of flexible polymer chains, is the main reason that CMS membrane C_2H_4/C_2H_6 separation performance can surpass the polymeric upper bound.

6.2.4. Physical Interpretation of Entropic Contribution Factor

It was shown above that the somewhat planar C_2H_4 molecule may have significant configurational advantage over the bulkier C_2H_6 in passage through the activated state, despite their similar size. This reflects as an entropic selectivity factor in the overall diffusion selectivity of the CMS membrane.

Singh & Koros [1] carried out similar entropic and energetic selectivity calculations for the O_2/N_2 separation using CMS membranes. It is worth noting that while Singh & Koros [1, 5] observed a significant energetic contribution to overall diffusion selectivity for O_2/N_2 separation, such effect is not observed in case of the Matrimid® CMS, because of the similar activation energies of C_2H_4 and C_2H_6. This also leads to the fact that there is no significant decrease in the CMS C_2H_4/C_2H_6 selectivity (Table 6.1) with a small increase in permeation temperature, unlike that observed in the case of most gas separations.

Singh and Koros [1] evaluated the theoretical limits for the entropic selectivity of the O_2/N_2 gas pair in transport through a "slit-like" CMS pore structure. The entropic factor is essentially equivalent to the ratio of the partition functions in the transition state to the normal state of the two molecules $\left[\frac{(F^{\neq}/F)_A}{(F^{\neq}/F)_B}\right]$ (Equation 2.32) [1, 6], which can be determined by taking into account the degrees of freedom for the two molecules in the normal and transition state. The normal state is when a gas molecule resides in a micropore, while the transition state corresponds to the gas molecule existing in a metastable state that enables it to jump through the ultramicropore with no added free energy. This is illustrated in Figure 6.6.

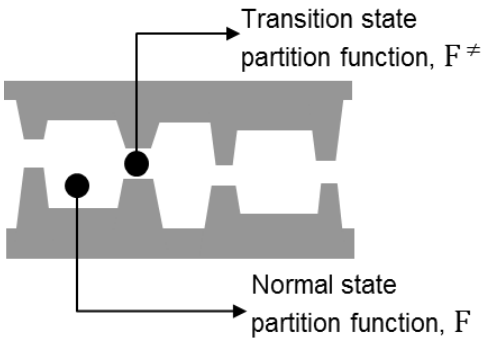

Figure 6.6: Representation of a gas molecule in the normal state (micropore) and transition state (ultramicropore) in transport through CMS

The partition function associated with each degree of translational, rotational and vibrational freedom, F_T F_R and F_V, can be calculated from Equations 6.1, 6.2 and 6.3 respectively [1, 6].

$$F_T = d_t \left(\frac{2\pi mkT}{h^2}\right)^{1/2} \quad (6.1)$$

$$F_R = \left(\frac{8\pi^2 IkT}{h^2}\right)^{1/2} \quad (6.2)$$

$$F_V = \left[\frac{\exp(-h\nu/2kt)}{1-\exp(-h\nu/kt)}\right] \quad (6.3)$$

In the above equations, m is the mass of the molecule, I is the moment of inertia, k is Boltzmann constant, h is Planck's constant, ν is the vibrational frequency and T is the absolute temperature, assumed as 300K. d_t represents the size of the cavity in which the molecules sits in the normal or transition state. The values of d_t were assumed as 11.2 Å in the normal state and 3.8 Å in the transition state in the study by Singh & Koros [1], based on zeolite 4A. In CMS membranes, by analogy to zeolites, micropores represent the normal state and ultramicropore represent the transitions state. Pore distribution analyses of CMS samples obtained from CO_2 uptake measurements using density functional theory analysis done at Micromeritics (Figures 5.16 and 5.68), show that there are hardly any pores larger than 10 Å. Hence, in the current study the values of d_t were assumed to be 8.5 Å in the normal state and 3.8 Å in the transition state. In this case, however, the entropic factor calculations are independent of the values of d_t, since it cancels off in the numerator and denominator. The partition function can then be calculated as

$$F = {F_T}^n \, {F_R}^n \, {F_V}^n \quad (6.4)$$

where, n is the number of degrees of freedom associated with each type of motion of the molecule. At ambient temperature, the degrees of freedom associated with vibrations are not considered. However, loss in a rotational degree of freedom around a given axis may manifest itself in the form of an additional vibrational mode resulting from rocking of the molecule about that axis of symmetry.

Singh and Koros [1] used the above equations to estimate the entropic contribution to O_2/N_2 separation using CMS. O_2 molecule can pass through the CMS slit-shaped pores rotating about either axis of rotation. N_2, on the other hand, may pass through rotating only about one axis as shown in Figure 6.7(i). Both O_2 and N_2 can translate along the CMS planes, transverse to the direction of diffusion. Depending on whether or not an additional vibrational degree of freedom is present for N_2, in lieu of the lost rotational degree of freedom, in the activated state, the entropic selectivity calculated is 3.7-9.0 (refer to [1] for detailed calculations). These values encompass the experimentally observed O_2/N_2 entropic selectivity range of 4.9-8.8 for CMS [1, 7, 8].

A similar analogy can be extended to the C_2H_4/C_2H_6 case as shown in Figure 6.7(ii). However, compared to the simple O_2/N_2 case where a molecule can either pass through or get rejected, the entropic selectivity for the more complex C_2H_4 and C_2H_6 molecules can be extremely complicated to predict. For these complex molecules, the entropic selection would now be dependent on the probability of many subtle configurational differences enabling a particular molecule to get through the diffusion-limiting ultramicropore. As shown in Figure 6.7(i), in a particular configuration, the 'skinnier' C_2H_4 will pass through the 'slit-shaped' CMS pores with greater ease (probability) while C_2H_6 will require greater effort (continuous rotation about an axis), if at all it can pass through in the same configuration. Computing the theoretical limits for C_2H_4/C_2H_6 entropic selectivity is thus more complex than the O_2/N_2 case, and would

require extensive modeling. Conceptually, however, the entropic factor can guide the CMS membrane optimization to tighten the slit-shaped pore dimensions.

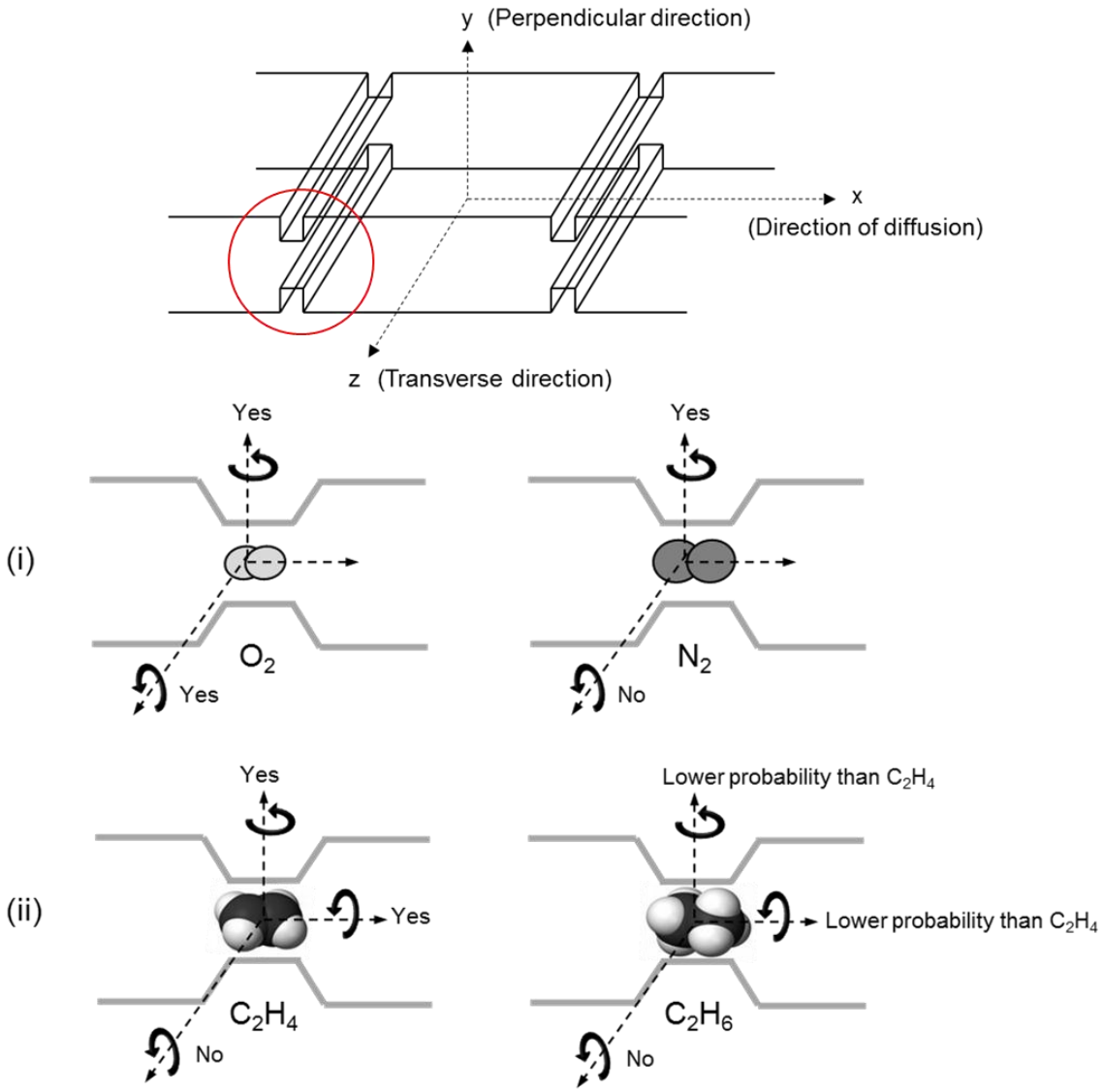

Figure 6.7: The top picture shows a 3-D representation of the CMS slit-shaped pore structure. The bottom picture shows a 2-D projected view of a CMS slit-shaped pore, in the direction of diffusion with illustration of the rotational degrees of freedom in the activated state. (i) O_2/N_2 system: O_2 can pass through rotating about both axes while N_2 can rotate only about one axis. (ii) C_2H_4/C_2H_6 system: C_2H_4 can pass through rotating about two axes with greater probability than C_2H_6. C_2H_6 may either get rejected completely at all configurations or may pass through rotating about either one axis or two axes but with a smaller probability than C_2H_4

The following "basic mapping" of the theoretical model for the O_2/N_2 case still helps reflect the contribution of entropic selectivity in C_2H_4/C_2H_6 separation using CMS. C_2H_4 and C_2H_6 molecules were considered as cuboids as shown in Figure 6.8. This model was used to calculate their moments of inertia (I) around the x, y and z axes, as shown in Figure 6.8 [9]. The partition functions associated with each degree of translational, rotational and vibrational freedom can be calculated from Equations 6.1, 6.2 and 6.3 respectively. The entropic selection factor can then be calculated as the ratio of the partition functions in the transition state to the normal state of the two molecules, $\left[\frac{(F^{\neq}/F)_A}{(F^{\neq}/F)_B}\right]$. Detailed calculations of the entropic factors can be found in Appendix D.

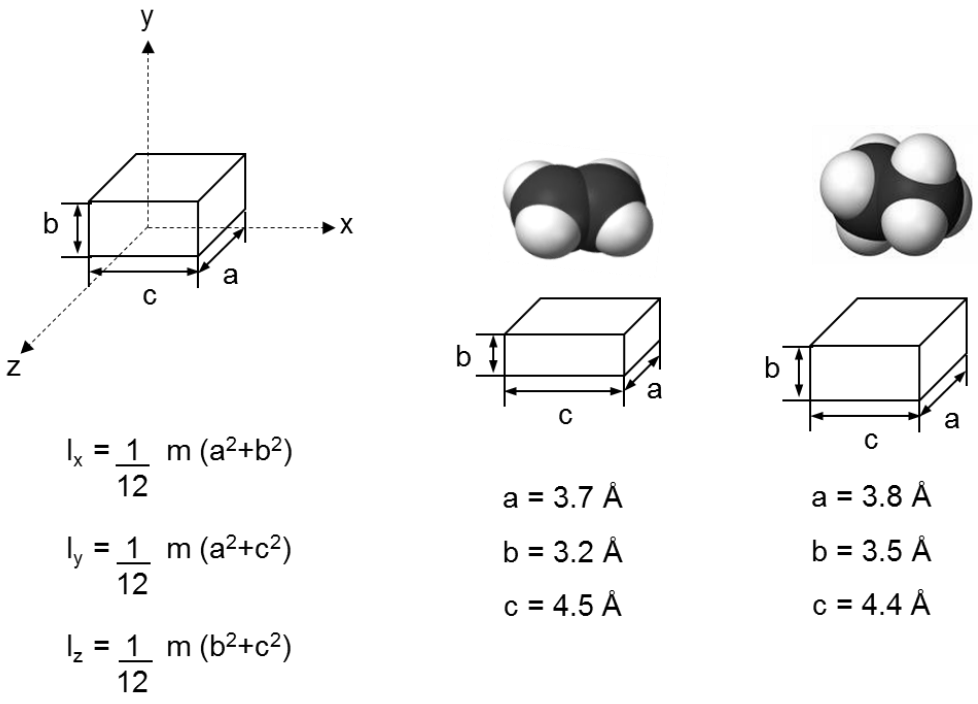

Figure 6.8: Representation of C_2H_4 and C_2H_6 based on the minimum dimensions of a cuboid that can just contain the molecules. The individual dimensions of C_2H_4 and C_2H_6 were determined using space filling CPK models

In the normal state, both C_2H_4 and C_2H_6 have 3 degrees of translation and rotation each. In the transition state, translation in the direction of diffusion (x direction) is accounted for by the factor $\left(\frac{kT}{h}\right)$ in Equation 2.29 and 2.31, to account for a vibration required to pass through the metastable state [6, 10]. If oriented along their smaller dimension ("b" in Figure 6.8), both C_2H_4 and C_2H_6 may also have translational degrees of freedom in the direction transverse (z) and perpendicular (y) to the direction of diffusion (x). In the transition state, the rotational degree of freedom along the z axis is lost for both C_2H_4 and C_2H_6 considering the lengths ("c" in Figure 6.8) of the molecules with respect to the ultramicropore dimension. Now, we may consider 2 cases in the transition state: (i) The pore structure of the CMS is "open", as in the case of P1-500°C-CMS, such that it can allow free rotation of C_2H_4 and C_2H_6 around both the x and y axes in the transition state. In this case the entropic selection factor is ~ 1.2 (see Appendix D for detailed calculations). (ii) The CMS pore structure is "tighter" (at higher pyrolysis temperatures) such that it allows rotation of C_2H_4 around the both x and y axis, but now restricts rotation of C_2H_6 around the x axis while only allowing it to rotate around the y axis. In this case, the entropic factor is ~ 31 (see Appendix D for detailed calculations). This factor may be highly exaggerated since the lost degree of rotational freedom of C_2H_6 may manifest as an additional vibrational degree of freedom resulting due to rocking of the molecule about the x axis. In addition, as described earlier and shown in Figure 6.7, due to the complicated shapes of C_2H_4 and C_2H_6, the entropic advantage may depend on many subtle configurational differences of the molecules, rather than an absolute, total loss of a degree of freedom. Detailed molecular simulations may be is necessary to theoretically assess the contribution of the entropic factor contribution to the overall C_2H_4/C_2H_6 selectivity. This is however beyond the scope of the current work, and may be considered for future studies in the field.

6.2.5. Ethylene vs. Krypton Transport

In order to gain further insight into the configurational advantage of the "planar" C_2H_4 molecule in a CMS membrane, we decided to compare C_2H_4 (3.75 Å) which possesses several configurational degrees of freedom, vs. Kr (3.7 Å), which has a similar critical diameter but no configurational degrees of freedom. The size of C_2H_4 was determined using space filling CPK models and "calibrated slits", while that of Kr was adopted from [11].

The permeability, diffusivity and sorption coefficients of C_2H_4 and Kr were obtained at 25°C, 35°C and 50°C. The corrected diffusivities were also calculated, since, as already mentioned, this is a more appropriate measure of the molecular sieving behavior of CMS based on the size and shape of the penetrants. Measurements were made on CMS dense films derived from UHP Ar pyrolysis of Matrimid® at 500°C and 675°C (P1-500°C-CMS and P1-675°C-CMS). The experimental data was fitted to Arrhenius and van't-Hoff type plots as shown in Figures 5.2 and 5.4. As in the case of C_2H_4/C_2H_6, several parameters such as the activation energies of permeation and diffusion, heats of sorption and the pre-exponential factors were calculated. These results are tabulated in Table 6.2.

Table 6.2: Summary of performance, activation energies (E_P, E_D, $E_Đ$), pre-exponential factors (P_o, D_o, $Đ_o$), and energetic and entropic contribution factors for C_2H_4 vs. Kr between 25-50°C for different CMS dense films

	P1-500°C-CMS	**P1-675°C-CMS**
P_{C2H4}/P_{Kr}	2.1-2.2	2.5-2.7
D_{C2H4}/D_{Kr}	1.1-1.3	1.9-2.1
$Đ_{C2H4}/Đ_{Kr}$	0.8-0.9	1.3-1.5
$E_{P\text{-}C2H4}$ (kJ/mol)	9.1	17.3
$E_{P\text{-}Kr}$ (kJ/mol)	10.2	17.9
$E_{D\text{-}C2H4}$ (kJ/mol)	16.4	23
$E_{D\text{-}Kr}$ (kJ/mol)	21.1	24.3
$E_{Đ\text{-}C2H4}$ (kJ/mol)	21.8	26.5
$E_{Đ\text{-}Kr}$ (kJ/mol)	22.6	26.5
$P_{o\text{-}C2H4}$ (Barrer)	2.7E+03	1.5E+04
$P_{o\text{-}Kr}$ (Barrer)	1.9E+03	7.4E+03
$D_{o\text{-}C2H4}$ (cm^2/s)	2.2E-05	4.3E-05
$D_{o\text{-}Kr}$ (cm^2/s)	1.2E-04	4.1E-05
$Đ_{o\text{-}C2H4}$ (cm^2/s)	8.2E-05	7.9E-05
$Đ_{o\text{-}Kr}$ (cm^2/s)	1.4E-04	6.1E-05
Energetic Factor (based on D)	5.8-6.7	1.6-1.7
Entropic Factor (based on D)	~0.2	~1.1
Energetic Factor (based on Đ)	1.3-1.4	~1
Entropic Factor (based on Đ)	~0.6	~1.4

Similar to the C_2H_4/C_2H_6 transport trends with the final pyrolysis temperature discussed in Section 6.2.2, the activation energies for permeation and diffusion for C_2H_4 and Kr increase in going from P1-500°C-CMS to P1-675°C-CMS, as seen from Table 6.2. This is a result of an increase in the gas transport resistance due to a "tighter" CMS morphology at higher pyrolysis temperatures.

As seen from Table 6.2, the CMS membranes show a higher permselectivity towards C_2H_4 compared to Kr. This overall selectivity is a combination of the higher sorption uptake of C_2H_4 over Kr, as well as factors relating to the size and shape considerations of the molecules. This will be discussed shortly. The P1-675°C-CMS shows a higher selectivity than P1-500°C, owing to its tighter, more selective pore structure. The concentration-dependent diffusion selectivity follows the same trend as the overall selectivity. In considering the concentration independent corrected diffusion selectivity however, it is seen that P1-500°C-CMS favors Kr while P1-675°C-CMS favors C_2H_4. This discrimination is based solely off the size and shape of the molecules. C_2H_4 and Kr are similar in size; however, C_2H_4 is a somewhat planar molecule while Kr is spherical. The "open" CMS slit-like pore structure at lower pyrolysis temperatures (P1-500°C-CMS) may not be capable of discriminating between the shape differences of C_2H_4 and Kr. As a result it does not show a preference towards C_2H_4 diffusion, and its entropic contribution is < 1. As the CMS critical pores become narrower and more restricted at higher pyrolysis temperature, the "slimmer" C_2H_4 molecule can still traverse the CMS slit-like pores relatively easily, while Kr may face significant hindrance owing to its spherical shape. Although small, this is clearly reflected in the entropic contribution factors to the C_2H_4/Kr selectivity as seen in Table 6.2. In both P1-500°C-CMS and P1-675°C-CMS, the energetic selectivity favors C_2H_4 since, being planar, it is willing to "go linear" to get through the CMS "slit", while Kr, being spherical, does not have this option, as depicted in Figure 6.9.

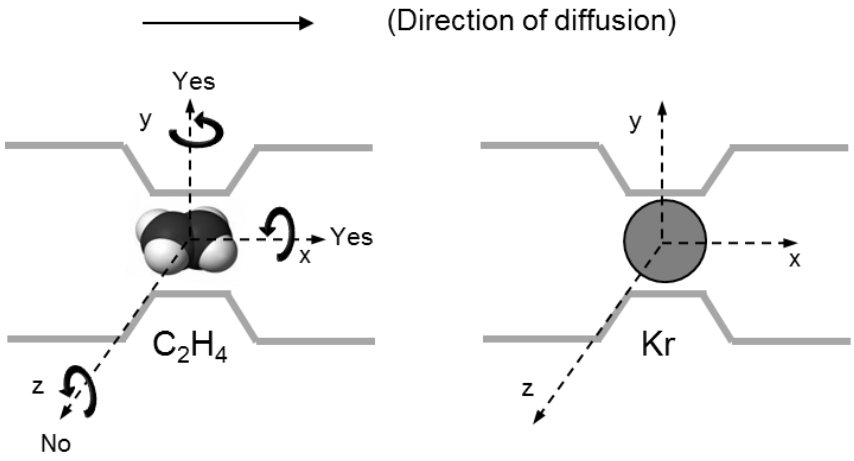

Figure 6.9: Depiction of C_2H_4 and Kr diffusion in the CMS slit in the activated state. C_2H_4 being planar can "go linear", while Kr, being spherical, does not have this option

Theoretical modeling of the C_2H_4/Kr system is much simpler than the C_2H_4/C_2H_6 case. For detailed calculations of the theoretical entropic factors, the reader may refer to Appendix D. Kr is a monoatomic spherical atom and possesses only three translational degrees of freedom. C_2H_4 on the other hand has translational, rotational and vibrational degrees of freedom. The vibrational modes of C_2H_4 will not be considered at ambient temperature. In the normal state, Kr has 3 degrees of translational freedom, while C_2H_4 has 3 degrees of translational and rotational freedom each. In the transition state, both C_2H_4 and Kr translate in the direction of diffusion (x direction), again accounted for by the factor $\left(\frac{kT}{h}\right)$ in Equation 2.29 and 2.31 [6, 10]. Both C_2H_4 and Kr can also translate along the CMS graphene-like planes, transverse (z) to the direction of diffusion (x). Additionally, in the transition state, the rotational degree of freedom along the z axis is lost for C_2H_4 considering its length ("c" in Figure 6.8) with respect to the ultramicropore dimension. Now consider two cases related to freedom to translate or not in the y-direction: (i) When the CMS pore structure is "open", as in the case of P1-500°C-CMS,

both C_2H_4 and Kr may translate along the y direction, i.e. perpendicular to the direction of diffusion. In addition, C_2H_4 can rotate around the x and y axes. This results in an entropic selection factor of ~ 0.1 (see Appendix D for details).The C_2H_4/Kr entropic factor is less than one since C_2H_4 pays a penalty by losing rotational freedom around the z axis in the transitions state, while Kr does not lose any degrees of freedom in the transition state. This loss in entropy is reflected in its energetic selectivity over Kr, as seen from Table 6.2. (ii) When the CMS slit structure is "tighter", as in the case of P1-675°C-CMS, C_2H_4 can be "slimmer" (since it loses its rotational freedom around the z axis) and can, thus, still translate in the y direction when oriented along its smaller dimension. In addition, it can rotate around the x and y axes. Kr, however, being spherical, cannot translate in the y direction and loses a degree of translational freedom. As a result, the entropic selection factor increases to ~ 2 (see Appendix D for details). The experimental entropic selectivity factor of ~ 0.6-1.4 (Table 6.2) for the C_2H_4/Kr gas pair lies within this theoretical entropic contribution range of ~ 0.1-2.0 for the CMS. Thus, the slit-shaped CMS pore structure can very effectively discriminate molecules of similar size based on their subtle shape differences.

6.2.6. Insight into Ethylene/Ethane Separation for Carbon Molecular Sieve Membranes from Different Precursors

The permeability, sorption coefficients, diffusivity and corrected diffusivity of C_2H_4 and C_2H_6 were obtained at 25°C, 35°C and 50°C for CMS dense films derived from UHP Ar pyrolysis of Matrimid® and 6FDA:BPDA-DAM at 675°C (P1-675°C-CMS and P3-675°C-CMS). The experimental data were fitted to Arrhenius and van't-Hoff type plots as shown in Figures 6.4 and 6.5. Several parameters such as the activation energies of

permeation and diffusion, heats of sorption and the pre-exponential factors were calculated. These results are summarized in Table 6.1.

A comparison of the permeation, sorption and diffusion trends for C_2H_4/C_2H_6 separation of CMS derived from Matrimid® and 6FDA:BPDA-DAM using identical pyrolysis conditions have already been discussed in great detail in Chapter 5. The 6FDA:BPDA-DAM CMS shows much higher C_2H_4 permeability, sorptivity and diffusivity compared to the Matrimid® CMS. This presumably reflects a much more open CMS framework obtained from the higher fractional free volume precursor 6FDA:BPDA-DAM which evolves bulky fluorinated by-products during pyrolysis. Figure 5.49 shows a cartoon illustration of the CMS structures believed to be obtained from 6FDA:BPDA-DAM and Matrimid®. As seen from the pore size distributions obtained from CO_2 uptake measurements (Figure 5.52) 6FDA:BPDA-DAM has a much higher pore volume compared to Matrimid®. This results in much higher sorption coefficients in the 6FDA:BPDA-DAM CMS. The average diffusion-limiting ultramicropore size of 6FDA:BPDA-DAM CMS is presumably larger compared to the Matrimid® CMS. This results in much larger diffusion coefficients in the 6FDA:BPDA-DAM CMS.

The 6FDA:BPDA-DAM CMS also shows a much greater temperature dependence for C_2H_4 permeability compared to the Matrimid® CMS. The C_2H_4 permeability from 25°C to 50°C changes ~98% for 6FDA:BPDA-DAM CMS compared to ~72% for Matrimid® CMS. The change in the corrected C_2H_4 diffusivity with the testing temperature is however comparatively similar for the 6FDA:BPDA-DAM CMS and Matrimid® CMS. The larger change in the 6FDA:BPDA-DAM CMS permeability is thus apparently an outcome of greater change in the Langmuir sorption parameters, shown in Table 6.3. The activation energies of permeation and diffusion of both C_2H_4 and C_2H_6 are also much higher for the 6FDA:BPDA-DAM CMS compared to the Matrimid® CMS. The reason for this is as follows: In case of the 6FDA:BPDA-DAM CMS, a penetrant (C_2H_4 or

C_2H_6) in the sorbed state feels a stronger "attraction" to the micropore wall, as indicated by the higher Langmuir affinity constants (b) in the 6FDA:BPDA-DAM CMS compared to Matrimid® (Table 6.3) As a result, in case of the 6FDA:BPDA-DAM CMS, a penetrant molecule requires a larger amount of energy to come out of the sorbed state in the micropore in order to make a diffusive jump through the ultramicropore. The more negative H_b for 6FDA:BPDA-DAM CMS in Table 6.3 compared to Matrimid® CMS further indicates this. As a result, the activation energy of diffusion for C_2H_4 and C_2H_6 is higher in the 6FDA:BPDA-DAM CMS. The front factors for permeation and diffusion, shown in Table 6.1, are also much higher for the 6FDA:BPDA-DAM CMS compared to the Matrimid® CMS. This is most likely a result of larger average diffusive jump length (λ) of the 6FDA:BPDA-DAM CMS.

Table 6.3: Langmuir isotherm parameters of C_2H_4 and C_2H_6 at different temperatures for CMS films derived from UHP Ar pyrolysis of Matrimid® and 6FDA:BPDA-DAM at 675°C

		P1-675°C-CMS (Matrimid®)					
		C_2H_4			C_2H_6		
		25°C	35°C	50°C	25°C	35°C	50°C
C'_H	[cm^3/cm^3]	106.9	101.9	95.2	94.0	87.6	83.4
b	[1/psia]	0.12	0.10	0.08	0.16	0.16	0.11
H_b	[kJ/mol]		-11.75			-10.80	
		P3-675°C-CMS (6FDA:BPDA-DAM)					
		C_2H_4			C_2H_6		
		25°C	35°C	50°C	25°C	35°C	50°C
C'_H	[cm^3/cm^3]	143.2	137.7	134.7	134.3	132.8	121.8
b	[1/psia]	0.22	0.18	0.11	0.25	0.18	0.16
H_b	[kJ/mol]		-17.70			-14.65	

The difference between the activation energies of permeation and diffusion for C_2H_4 and C_2H_6 is higher in case of the 6FDA:BPDA-DAM CMS compared to Matrimid® CMS, as seen from Table 6.1. As a result the energetic contribution to the overall C_2H_4/C_2H_6 selectivity is higher for the 6FDA:BPDA-DAM CMS compared to the Matrimid® CMS. The entropic contribution to the overall selectivity is lower in case of the 6FDA:BPDA-DAM CMS, indicating that its more open pore structure compared to the Matrimid® CMS shows a lower effectiveness in discrimination between the subtle shape and configurational differences of C_2H_4 and C_2H_6. A consequence of the larger dependence on the energetic factor in the 6FDA:BPDA-DAM CMS is a larger decrease in its overall C_2H_4/C_2H_6 selectivity with increasing testing temperature. This decrease in the overall C_2H_4/C_2H_6 selectivity with temperature is not seen in case of the Matrimid® CMS, owing to a dominating entropic contribution factor. This feature of the 6FDA:BPDA-DAM CMS may thus be favorable for cryogenic applications, as in the case of C_2H_4/C_2H_6 separation, since a lower testing temperature would reap a larger benefit in the C_2H_4/C_2H_6 selectivity. Thus, temperature dependence studies of C_2H_4/C_2H_6 separation also provide significant insight into the differences in the nature of CMS derived from different precursors using identical pyrolysis conditions.

6.3. Effects of Testing Pressure on Carbon Molecular Sieve Membrane Performance

Consideration of the membrane performance as a function of operating pressure conditions is important from a point of practical application since membranes are not always operated at pressures measured like those in the lab. The effects of feed

pressure for ideal downstream vacuum conditions as well as preliminary prediction of the effects of pressure ratio (feed pressure/permeate pressure) on the C_2H_4/C_2H_6 separation performance of CMS membranes were considered in this work. All measurements reported in Section 6.3 are at 35°C.

6.3.1. Effect of Feed Pressure

The effects of CMS dense film C_2H_4/C_2H_6 separation performance as a function of the feed pressure while maintaining the permeate side under vacuum were analyzed. Permeation measurements were carried out at 35°C using pure gas C_2H_4 and C_2H_6 feed pressures between 25-100 psia. The brittle nature of CMS dense films limits the highest pressure they can withstand. Hence the pressure range tested was limited to 100 psia. The CMS hollow fiber form, although more brittle compared to polymeric membranes, have been shown to withstand feed pressures up to 1000 psi in natural gas applications and are much more robust and suited for practical use [12].

The effects of feed pressure on C_2H_4 permeability is shown in Figure 6.10 for CMS dense films derived from UHP Ar pyrolysis of Matrimid® and 6FDA:BPDA-DAM at 675°C. The C_2H_4 permeability decreases ~15-25% as a function of feed pressure. The effects on sorption and diffusion as a function of feed pressure were also evaluated for CMS dense films derived from UHP Ar pyrolysis of Matrimid® and 6FDA:BPDA-DAM at 675°C. Sorption isotherms were measured up to at least 200 psia. The average transport diffusivities were back-calculated from the sorption and diffusion coefficients. The results are shown in Figure 6.11. It was found that the sorption coefficient for C_2H_4 show ~70% decrease with feed pressure in both cases. C_2H_4 diffusivity, on the other hand, shows ~60% increase with the feed pressure. The decrease in the C_2H_4 sorption

coefficient and the increase in its diffusivity offset each other to a large extent such that its permeability does not reduce significantly with the feed pressure.

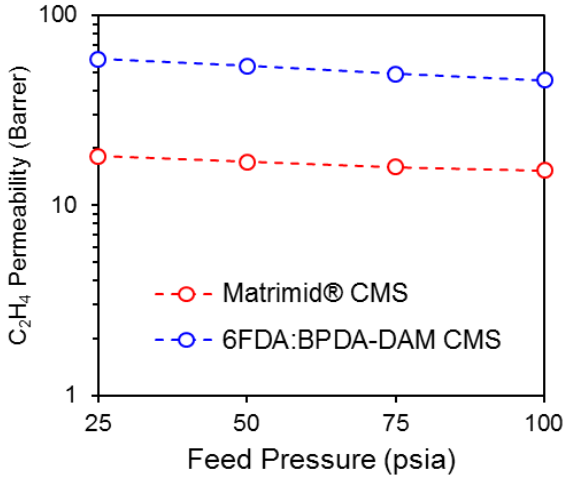

Figure 6.10: Effect of feed pressure at 35°C on C_2H_4 permeability of CMS derived from UHP Ar pyrolysis of Matrimid® and 6FDA:BPDA-DAM at 675°C

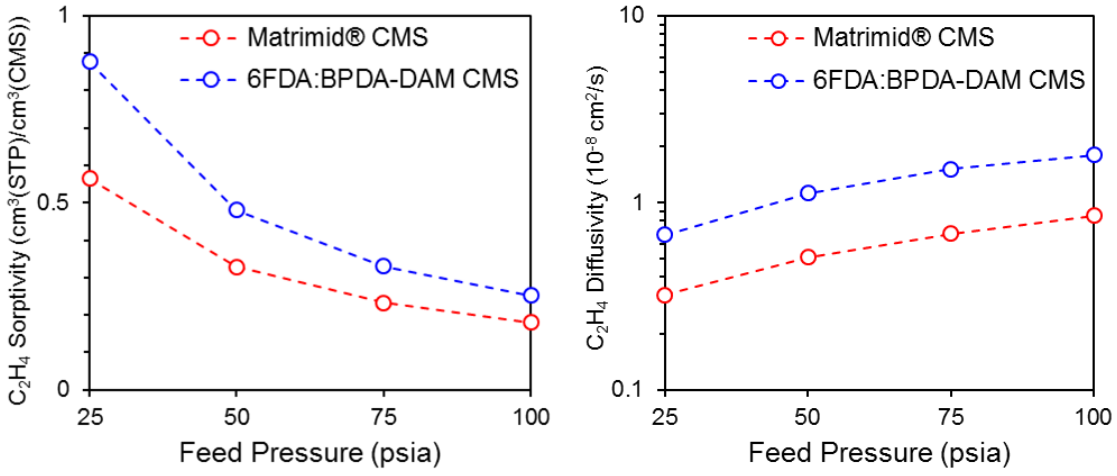

Figure 6.11: Effect of feed pressure at 35°C on C_2H_4 sorption and diffusion coefficients of CMS derived from UHP Ar pyrolysis of Matrimid® and 6FDA:BPDA-DAM at 675°C

There was some ambiguity in determining the C_2H_6 permeability trend as a function of the feed pressure. Hence the results are not reported here. The C_2H_6 trends are expected to be similar to that of C_2H_4, such that the C_2H_4/C_2H_6 selectivity may not be affected significantly with the feed pressure. This is also indicated by the mixed gas models reported in Section 6.4.

6.3.2. Effect of Pressure Ratio

The performance of a practical membrane gas separation system depends on three main factors: The membrane selectivity (α), pressure ratio (φ) and the membrane stage cut (θ) [13]. Membrane selectivity is defined as the ratio of the permeabilities of the fast gas (A) over the slow gas (B).

$$\alpha = \frac{P_A}{P_B} \tag{6.5}$$

Pressure ratio is the ratio of the feed pressure (p_o) to the permeate side pressure (p_ℓ) across the membrane.

$$\varphi = \frac{p_o}{p_\ell} \tag{6.6}$$

The membrane stage cut represents the fraction of the feed gas that permeates the membrane, and is defined as

$$\theta = \frac{\text{permeate flow}}{\text{feed flow}} \tag{6.7}$$

Consider the separation of a gas mixture at a feed pressure p_o, with component compositions x_A and x_B. The downstream is at a pressure p_ℓ, with permeate component compositions y_A and y_B. This is illustrated in Figure 6.12 for a case with zero stage cut.

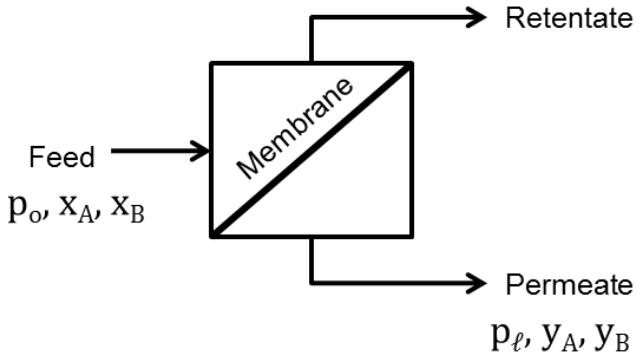

Figure 6.12: Schematic representation of membrane separation process

Flow of component A across the membrane can only occur if its partial pressure (or fugacity) on the feed side is greater than its partial pressure (or fugacity) on the permeate site. That is,

$$x_A p_o > y_A p_\ell \tag{6.8}$$

This gives

$$\frac{x_A}{y_A} \leq \frac{p_o}{p_\ell} \tag{6.9}$$

The maximum separation achieved by a membrane can thus never exceed the pressure ratio no matter how selective the membrane is.

The relationship between the membrane selectivity and pressure ratio is represented in Equation 6.10 for a case with zero stage cut. The reader may refer to [13] for a detailed derivation of the Equation 6.10.

$$y_A = \frac{\varphi}{2}\left[x_A + \frac{1}{\varphi} + \frac{1}{1-\alpha} - \sqrt{\left(x_A + \frac{1}{\varphi} + \frac{1}{1-\alpha}\right)^2 - \frac{4\alpha x_A}{(\alpha-1)\varphi}}\right] \tag{6.10}$$

There can be two limiting cases depending on the relative magnitudes of the pressure ratio and the membrane selectivity, as represented in Equations 6.11 and 6.12.

$$y_A = x_A\varphi \qquad \text{when} \quad \alpha \gg \varphi \tag{6.11}$$

This is called the pressure ratio limiting region. Membrane performance in this region is determined only by the pressure ratio across the membrane and is independent of the membrane selectivity. The second limiting case is

$$y_A = \frac{\alpha x_A}{1 - x_A(1-\alpha)} \qquad \text{when} \quad \alpha \ll \varphi \tag{6.12}$$

This is called the membrane selectivity limiting region, in which the performance is determined only by the membrane selectivity and is independent of the pressure ratio.

In the intermediate region between these two limiting cases, membrane performance depends on both the membrane selectivity and the pressure ratio. This is illustrated in Figure 6.13.

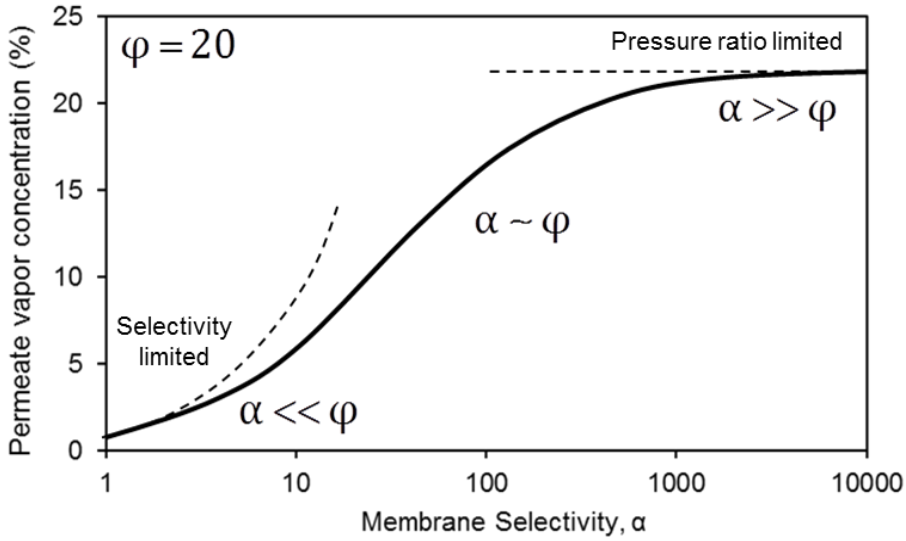

Figure 6.13: Different regions for pressure ratio and membrane selectivity dependence in membrane separation [13]

In realistic gas separation applications, there may be a limit on the practically achievable pressure ratio. Compressing the feed stream to a very high pressure or drawing a very high vacuum on the downstream to achieve large pressure ratios may not be practically or economically feasible. Typical pressure ratios are often in the range of 5-20. Because of the limit of the practically attainable pressure ratio, the benefit of very highly selective membranes may be less than one might imagine. Further, since the intrinsic membrane selectivity is based on downstream vacuum conditions, the actual separation factor may show significant deviations as the permeate side pressure increases. Separation factor is then defined as the ratio of the permeate-side mole

fractions of the fast gas over the slow gas vs. the ratio of the feed side mole fractions of the fast gas over slow gas, as represented in Equation 6.13.

$$S.F. = \frac{(y_A/y_B)_{permeate}}{(x_A/x_B)_{feed}} \quad (6.13)$$

A practical consideration of the effect of pressure ratio on CMS membrane performance for C_2H_4/C_2H_6 separation is essential for realistic application. Such studies may however be more useful if carried out in the CMS hollow fiber form which is used for practical membrane applications. In fact experimental analysis of the effects of pressure ratio using CMS dense films is limited because of their brittle nature, and was thus not considered in the current work. Preliminary predictions of the C_2H_4 permeate concentration and membrane S.F. as a function of the pressure ratio were made using Equation 6.10 and 6.13 respectively. The pressure ratio was varied from 5-20 for effectively zero stage cut. The feed gas composition is 63.2 mol% C_2H_4 and 36.8 mol% C_2H_6, which is a typical feed composition for the real application, as advised by our Dow Chemical Company collaborators. The ideal CMS membrane selectivity from the current study was used as a basis for membrane selectivity for the prediction. The ideal selectivity achievable for C_2H_4/C_2H_6 separation using 6FDA:BPDA-DAM CMS is ~7.5 while for Matrimid® CMS it is ~12. Since these are ideal selectivities at room temperature, the effects of several parameters such as the operating temperature, pressure, stage cut, presence of impurities in the feed stream etc. in realistic operations must be considered. Thus the selectivity range was chosen from 5-20, to envelope the ideal selectivities. The modeling results are shown Figure 6.14.

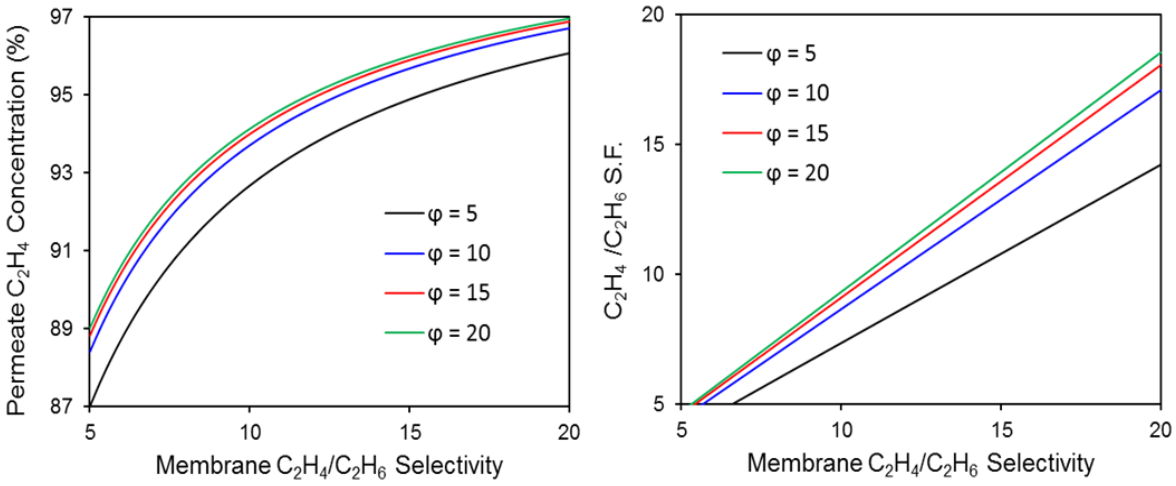

Figure 6.14: Effect of pressure ratio on C_2H_4 concentration in permeate and membrane separation factor for C_2H_4/C_2H_6 separation using CMS membranes

Higher C_2H_4 purities are achievable for higher pressure ratios, and the deviation of the actual S.F. from membrane selectivity is then smaller. As the pressure ratio decreases, the S.F. factor starts to deviate significantly from the intrinsic membrane selectivity, and low product purities are obtained. Clearly even for a CMS membrane C_2H_4/C_2H_6 selectivity of 20, the maximum achievable C_2H_4 permeate concentration may not exceed ~97%. The typical C_2H_4 purity in the petrochemical industry resulting from cryogenic distillation operations is however > 99%. Thus, unless a breakthrough membrane material is developed, the application of membranes for C_2H_4/C_2H_6 separation may be more meaningful for debottlenecking rather than as a stand-alone separation. Nevertheless, modeling predictions by several researchers have shown that hybrid membrane-distillation can still offer significant cost and energy savings [14-16]. Focus on the development of higher flux membranes is thus more crucial compared to the development of ultra-selective membrane materials. In this regard CMS membranes derived from 6FDA:BPDA-DAM may be more favorable compared to Matrimid® for C_2H_4/C_2H_6 membrane separation applications, despite its lower selectivity.

6.4. Effects of Feed Composition on Carbon Molecular Sieve Membrane Performance

Pure gas streams seldom represent the true performance of the membrane. In real membrane application, the feed gas contains multiple components, and the effects due to the presence of these components in contact with the membrane simultaneously must be considered. The feed stream composition used in this study was provided by The Dow Chemical Company. The feed stream targeted for membrane separation application is dry and relatively clean containing ~62 wt% C_2H_4 and ~38 wt% C_2H_6, along with only a few ppm of C_2H_2. All measurements in this Section 6.4 are based on measurements at 35°C.

6.4.1. Experimental Ethylene/Ethane Binary Gas Performance

The effect on CMS performance due to the presence of both C_2H_4 and C_2H_6 simultaneously in the feed gas stream was evaluated at 35°C. The specific binary gas composition used in this study contains 63.2 mol% C_2H_4 and 36.8 mol% C_2H_6. Details of mixed gas experiments can be found in Section 3.4.1. The results for C_2H_4/C_2H_6 binary gas separation using CMS dense films derived from UHP Ar pyrolysis of Matrimid® at 500°C, 550°C and 675°C and 6FDA:BPDA-DAM at 675°C are shown in Figure 6.16, along with the corresponding pure gas performances.

It was found that both C_2H_4 and C_2H_6 permeabilities decreased in the mixed gas environment compared to the pure gas permeabilities, along with a small, but not a significant, decrease in the C_2H_4/C_2H_6 selectivity. This may result from the competition effects between C_2H_4 and C_2H_6 when both the gases are present simultaneously. In the presence of a second component, the diffusion of both the gases is hindered. At the

same time, C_2H_4 and C_2H_6 compete for the limited Langmuir sorption sites present in the membrane, which brings down the sorption coefficients of the gases in the binary gas environment. As a result the permeabilities of both C_2H_4 and C_2H_6 decrease compared to the respective pure gas permeabilities. Fortunately, the C_2H_4/C_2H_6 selectivity does not decrease to any significant extent. This may be due to the similar chemical nature of C_2H_4 and C_2H_6 resulting in their similar sorption behavior, as well as the diffusive advantage of C_2H_4 despite the simultaneous presence of C_2H_6. This fact notwithstanding, pure gas measurements may give a fairly good estimate of the membrane performance for gas mixtures representative of industrial C_2H_4/C_2H_6 feeds.

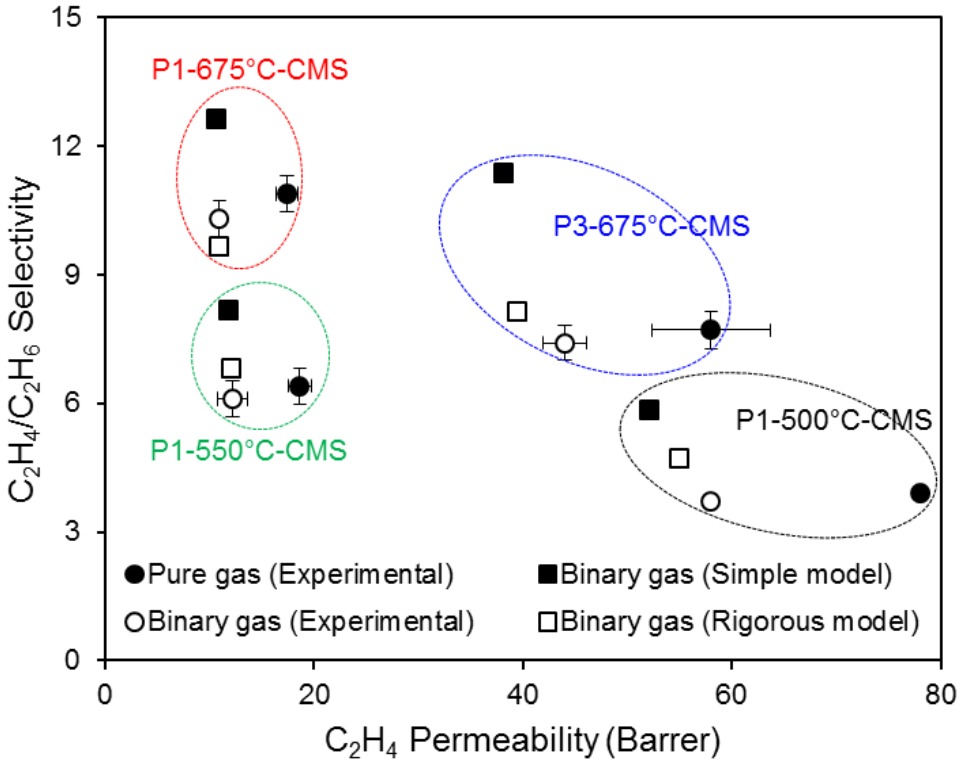

Figure 6.15: Experimental pure gas and binary gas C_2H_4/C_2H_6 separation performance of different CMS dense films, along with binary gas performance predictions using simple and rigorous models

6.4.2. Binary Component Modeling Prediction

In addition to experimental binary gas permeation analysis, modeling prediction of CMS binary gas separation was carried out based on pure gas permeation and sorption data. The details of the modeling study are described in detail in this section

Gas transport through membranes can be ideally described by Fick's first law of diffusion [17]. In describing transport processes, a frame of reference must be specified [17, 18]. In the case of membrane transport, it is often easy to use the membrane itself as the fixed frame of reference, since experimental permeation rates are measured with respect to the stationary membrane. For this static frame of reference the gas flux is a combination of two components: the bulk (convective) flux and the diffusional flux [17, 18]. Thus, in mixed gas environment, the flux of component A is comprised of the mass flux resulting from the bulk motion of each of the components of the system and the mass flux resulting from diffusion of A relative to the bulk flux.

$$n_A = n_A^{bulk} + n_A^{diffusion} \tag{6.14}$$

$$n_A^{bulk} = \left(\sum_i n_i\right)\omega_A \tag{6.15}$$

$$n_A^{diffusion} = -\rho D_{Am}\frac{d\omega_A}{dx} \tag{6.16}$$

In the case of binary gas permeation, the system comprises three components: The two gases A and B in the mixture and the membrane medium M. The flux equations for the components are then described by Equation 6.17, 6.18 and 6.19.

$$n_A = (n_A + n_B + n_M)\omega_A - \rho D_{Am} \frac{d\omega_A}{dx} \quad (6.17)$$

$$n_B = (n_A + n_B + n_M)\omega_B - \rho D_{Bm} \frac{d\omega_B}{dx} \quad (6.18)$$

$$n_M = (n_A + n_B + n_M)\omega_M - \rho D_{Mm} \frac{d\omega_M}{dx} \quad (6.19)$$

In Equations 6.14-6.19, n_i is the mass flux (g/cm^3) of component i with respect to the fixed frame of reference (membrane), ω_i is the concentration of i in the membrane (g/g), ρ is the membrane material density (g/cm^3), and D_{im} is the effective diffusivity (cm^2/s) of i. The mass flux of the membrane medium, n_M, is zero since the membrane is stationary [18].

6.4.2.1. Simple Model

In the simple model, the bulk flux contributions in Equation 6.14-6.19 are neglected under the assumption that concentrations ω_A and ω_B of the penetrants are negligible [18, 19]. As a result, the bulk flux contribution to the overall transport flux drops out and, for component A in the binary mixture, Equation 6.17 reduces to

$$n_A = -\rho D_{Am} \frac{d\omega_A}{dx} \quad (6.20)$$

This can also be represented in terms of the molar gas flux N_A with respect to the gas concentration C_A in cm^3(STP)/cm^3 as

$$N_A = -D_{Am}\frac{dC_A}{dx} \tag{6.21}$$

which is then the same as Equation 2.4.

A simplification of Equation 2.4, as shown in Section 2.3.1, results in the following expression for gas permeability (P_A) in terms of the average Fickian or transport diffusivity ($\overline{D}_{Am}$) and the average sorption coefficient ($\overline{\mathbb{S}}_A$):

$$P_A = \overline{D}_{Am}\overline{\mathbb{S}}_A \tag{6.22}$$

Now for the single component case, the sorption coefficient in CMS membranes is described by the Langmuir isotherm model as follows:

$$\overline{\mathbb{S}}_A = \frac{C_A}{p_A} = \frac{C'_{HA}b_A}{1 + b_A p_A} \tag{6.23}$$

where, C_A is the amount or concentration of gas taken up by the membrane material at a given pressure p_A at equilibrium, C'_{HA} is the Langmuir saturation constant and b_A is the Langmuir affinity constant.

Further, the Fickian or transport diffusivity D_A in highly porous materials like CMS can be strongly dependent on the concentration of the species in the membrane. Thus it is often useful to relate the concentration dependent Fickian diffusivity to a thermodynamically corrected concentration-independent diffusivity $Đ_A$ (Maxwell-Stefan diffusivity) by accounting for adsorbate loading [7, 12] as follows:

$$D_{Am} = \frac{Đ_A}{1 - \theta_A} \tag{6.24}$$

where θ_A is the fractional site saturation factor defined as

$$\theta_A = \frac{C_A}{C'_{HA}} = \frac{b_A p_A}{1 + b_A p_A} \tag{6.25}$$

Since the diffusivity obtained from experimental measurements is the average transport diffusivity (mean Fickian diffusivity), Equation 6.25 can be integrated to relate the corrected diffusivity to the average transport diffusivity as follows (see Section 2.3.3 for details):

$$\overline{D}_{Am} = \frac{Đ_A}{\theta_A} \ln\left(\frac{1}{1 - \theta_A}\right) = \frac{Đ_A (1 + b_A p_A)}{b_A p_A} \ln(1 + b_A p_A) \tag{6.26}$$

The concentration independent corrected diffusivity can then be estimated from the pure gas permeability by substituting Equations 6.23 and 6.26 in Equation 6.22 yielding Equation 6.27.

$$P_A = \frac{Đ_A C'_{HA}}{p_A} \ln(1 + b_A p_A) \tag{6.27}$$

Now for a binary mixture case, the sorption coefficients of penetrants A and B are defined as shown in Equations 6.28 and 6.29 respectively.

$$\overline{\mathbb{S}}_A = \frac{C'_{HA} b_A}{1 + b_A p_A + b_B p_B} \tag{6.28}$$

$$\overline{\mathbb{S}}_B = \frac{C'_{HB} b_B}{1 + b_A p_A + b_B p_B} \tag{6.29}$$

Further, in a binary mixture, the corrected pure component diffusivities may be used to calculate penetrant permeabilities, if the diffusion of each penetrant is assumed to be unaffected by the presence of the other penetrant (i.e. non-interacting components). Consideration of component interactions may be complicated and mathematically cumbersome, and will not be discussed here. The reader may refer to [12] for further details on transport in case of interacting components.

Thus, for the non-interacting binary gas case, the mean diffusion coefficient takes the same functional form as Equation 6.26 for both A and B, while the sorption coefficient for the binary gas case is defined by Equations 6.28 and 6.29. This yields an expression for component permeabilities in a binary, non-interacting mixture as:

$$P_A = \frac{Đ_A C'_{HA} \ln(1 + b_A p_A)}{p_A} \frac{(1 + b_A p_A)}{(1 + b_A p_A + b_B p_B)} \tag{6.30}$$

$$P_B = \frac{Đ_B C'_{HB} \ln(1 + b_B p_B)}{p_B} \frac{(1 + b_B p_B)}{(1 + b_A p_A + b_B p_B)} \tag{6.31}$$

The modeling predictions for C_2H_4/C_2H_6 binary gas separation performance using Equations 6.30 and 6.32 for CMS dense films derived from UHP Ar pyrolysis of Matrimid® at 500°C, 550°C and 675°C and 6FDA:BPDA-DAM at 675°C are shown in

Figure 6.15, along with the experimental results. Clearly, the simple model over-predicts the C_2H_4/C_2H_6 selectivity compared to the experimental selectivity in all cases.

6.4.2.2. Rigorous Model

The assumption that the concentrations, ω_A and ω_B, of the penetrants in the membrane are negligible has been casually extended to most cases. As such the bulk flux contributions to the total transport flux shown in Equation 6.14-6.19 are often neglected, as in the case of the simple model. This may however lead to significant error, since for highly condensable gases like C_2H_4 and C_2H_6 and for highly porous materials like CMS the amount of gas taken up by the membrane can be significant. Additionally, the relative contribution of the bulk flux term to the total mass flux may often be more significant in case of the slower component with respect to its diffusive component. In other words, the slow gas may get swept along with the fast gas when considering separation of a binary gas mixture. It is therefore necessary to distinguish between the permeability calculated based on the total mass flux and the permeability calculated based on the diffusive flux alone [18, 19]. Clearly, a consequence of neglecting the bulk flux term in the simple model is the over prediction of binary gas C_2H_4/C_2H_6 selectivity of the CMS membranes. It is thus essential to consider the effects of bulk flow contributions on binary gas separation performance of the CMS. This is taken into account in the rigorous model.

Considering the bulk flux terms in Equations 6.17 and 6.18 with the membrane flux (n_M) equal to zero, expressions for the mutually dependent flux of components A and B of a binary mixture are as follows:

$$n_A = -\frac{\rho D_{Am}}{[1-(1+1/r)\omega_A]}\frac{d\omega_A}{dx} \tag{6.32}$$

$$n_B = -\frac{\rho D_{Bm}}{[1-(1+r)\omega_B]}\frac{d\omega_B}{dx} \tag{6.33}$$

where,

$$r = \frac{n_A}{n_B} \quad ; (n_A > n_B) \tag{6.34}$$

Integration of Equations 6.32 and 6.33 using boundary conditions

$$x = 0; \qquad \omega_A = \omega_{Ao}\,, \qquad \omega_B = \omega_{Bo}$$

$$x = \ell; \qquad \omega_A = \omega_{A\ell}\,, \qquad \omega_B = \omega_{B\ell}$$

with, $\omega_{A\ell} = \omega_{B\ell} = 0$ for downstream under vacuum, yields the following expressions for the flux of A and B in the binary component case:

$$n_A\ell = \frac{\rho\bar{D}_{Am}}{(1+1/r)}\ln\left[\frac{1-\omega_{A\ell}(1+1/r)}{1-\omega_{Ao}(1+1/r)}\right] \approx \frac{\rho\bar{D}_{Am}}{(1+1/r)}\ln\left[\frac{1}{1-\omega_{Ao}(1+1/r)}\right] \tag{6.35}$$

$$n_B \ell = \frac{\rho \bar{D}_{Bm}}{(1+r)} \ln\left[\frac{1-\omega_{B\ell}(1+r)}{1-\omega_{Bo}(1+r)}\right] \approx \frac{\rho \bar{D}_{Bm}}{(1+r)} \ln\left[\frac{1}{1-\omega_{Bo}(1+r)}\right] \quad (6.36)$$

In the above equations, $\bar{D}_{Am}$ and $\bar{D}_{Bm}$ are defined based on Equation 6.23. The concentrations of A and B in the membrane, ω_{Ao} and ω_{Bo} can be obtained based on the Langmuir sorption model as follows:

$$\omega_{Ao} = \frac{M_A}{22400\,\rho}\left(\frac{C'_{HA} b_A p_A}{1 + b_A p_A + b_B p_B}\right) \quad (6.37)$$

$$\omega_{Bo} = \frac{M_B}{22400\,\rho}\left(\frac{C'_{HB} b_B p_B}{1 + b_A p_A + b_B p_B}\right) \quad (6.38)$$

where, M_A and M_B are the molecular weights (g/mol) of A and B.

n_A and n_B can be obtained iteratively from Equations 6.34, 6.35 and 6.36 by using an initial guess value of r. A good initial guess value for r is the ratio of n_A and n_B neglecting the r terms in Equations 6.35 and 6.36. The permeabilities of components A and B for the binary gas feed can then be obtained as follows:

$$P_A = \frac{22400\, n_A \ell}{M_A \Delta p_A} \quad (6.39)$$

$$P_B = \frac{22400\, n_B \ell}{M_B \Delta p_B} \quad (6.40)$$

where, Δp_A and Δp_B represent the partial pressure difference of A and B respectively across the membrane.

The C_2H_4/C_2H_6 binary gas separation performance predicted using the rigorous model for CMS dense films derived from UHP Ar pyrolysis of Matrimid® at 500°C, 550°C and 675°C and 6FDA:BPDA-DAM at 675°C are also shown in Figure 6.15, along with the experimental results. The rigorous binary gas model predicts the C_2H_4/C_2H_6 binary gas performance fairly well. Unlike the simple model, the C_2H_4/C_2H_6 selectivity predicted using the rigorous model is quite close to the experimental values, indicating the importance of considering bulk flux contributions to the overall transport flux for C_2H_4/C_2H_6 separation using CMS membranes.

6.5. Summary

The effects of testing conditions, i.e. the testing temperature, pressure and feed composition on C_2H_4/C_2H_6 separation performance of CMS dense films were analyzed. These studies were shown to be useful not just in predicting the membrane behavior from a practical stand point but also in a fundamental understanding of the nature of CMS membrane separation. The C_2H_4 permeability was found to increase with the permeation temperature, while the C_2H_4/C_2H_6 selectivity decreased slightly. Temperature dependence studies were useful in evaluating the transport trends of CMS membranes obtained using different precursors and processing conditions. These studies also helped elucidate the importance of entropic selection factors in advanced gas separations membranes, such as CMS, that allows them to outperform the polymeric upper bound.

The study of the pressure dependence of C_2H_4/C_2H_6 separation using CMS membranes helped gain insight into important aspects of membrane application critical for practical consideration. The feed pressure for downstream vacuum conditions was not found to significantly impact CMS transport performance. From the feed tp permeate pressure ratio modeling, it was explained that the use of membranes for C_2H_4/C_2H_6 separation may be more beneficial as a debottlenecking application in the form of a hybrid membrane-distillation operation. With current available membrane materials, consideration of the membrane flux is critical and the development of higher flux C_2H_4/C_2H_6 separation membranes may be an important factor for practical membrane area and related costs. In this regard CMS membranes derived from 6FDA:BPDA-DAM may be more favorable compared to Matrimid® for C_2H_4/C_2H_6 membrane separation applications, despite its somewhat lower selectivity.

The effect of binary gas C_2H_4/C_2H_6 on CMS performance was also evaluated. The feed mixture composition (63.2 mol% C_2H_4 and 36.8 mol% C_2H_6) was obtained from The Dow Chemical Company. It was found that both C_2H_4 and C_2H_6 permeabilities decreased in the mixed gas environment compared to the pure gas permeabilities, along with a small, but not significant, decrease in the C_2H_4/C_2H_6 selectivity. This is a result of the complicated competition effects between C_2H_4 and C_2H_6 when both gases are present simultaneously. Simple and rigorous models were used to predict binary gas C_2H_4/C_2H_6 performance of CMS membranes using pure gas permeation data. It was shown that neglecting the bulk flow contribution to the overall transport flux, as in the simple model, led to an over-prediction of the binary gas selectivity. The rigorous model on the other hand accounted for these bulk flow contributions and the predicted binary gas performance was fairly close to the experimental data.

6.6. References

[1] Singh A, Koros WJ. Significance of entropic selectivity for advanced gas separation membranes. Ind Eng Chem Res. 1996;35(4):1231-4.

[2] Singh-Ghosal A, Koros WJ. Energetic and entropic contributions to mobility selectivity in glassy polymers for gas separation membranes. Ind Eng Chem Res. 1999;38(10):3647-54.

[3] Rungta M, Xu L, Koros WJ. Carbon molecular sieve dense film membranes derived from Matrimid (R) for ethylene/ethane separation. Carbon. 2012;50(4):1488-502.

[4] Steel KM. Carbon membranes for challenging gas separations. The University of Texas at Austin, Doctor of Philosophy, 2000.

[5] Singh-Ghosal A, Koros WJ. Air separation properties of flat sheet homogeneous pyrolytic carbon membranes. J Membrane Sci. 2000;174(2):177-88.

[6] Glasstone S, Laidler KJ, Eyring H. The Theory of Rate Processes. 1st ed. New York: McGraw-Hill Book Co., Inc. 1941.

[7] Karger J, Ruthven DM. Diffusion in zeolites and other microporous solids. New York: John Wiley & Sons Inc.; 1991.

[8] Singh A. Membrane materials with enhanced selectivity: An entropic interpretation. The University of Texas at Austin, Doctor of Philosophy, 1997.

[9] McLean WG, Nelson EW. Engineering mechanics: Statistics and dynamics. 2nd ed. New York: Schaum Publishing Co.; 1962.

[10] Barrer RM. Activated diffusion in membranes. T Faraday Soc. 1939;35(1):0644-55.

[11] Reid C, Sherwood TK. The properties of gases and liquids: their estimation and correlation. New York: Mcgraw-hill; 1976.

[12] Vu DQ. Formation and characterization of asymmetric carbon molecular sieve and mixed matrix membranes for natural gas purification. The University of Texas at Austin, Doctor of Philosophy, 2001.

[13] Baker RW. Membrane technology and applications. New York: McGraw-Hill; 2000.

[14] Caballero JA, Grossmann IE, Keyvani M, Lenz ES. Design of hybrid distillation-vapor membrane separation systems. Ind Eng Chem Res. 2009;48(20):9151-62.

[15] Motelica A, Bruinsma OSL, Kreiter R, den Exter M, Vente JF. Membrane retrofit option for paraffin/olefin separation - A technoeconomic evaluation. Ind Eng Chem Res. 2012;51(19):6977-86.

[16] Humphrey JLS, A.F., Koort RA. Separation technologies: Advances and priorities; 1991. Report No.: DOE/ID/12920-1; Other: ON: DE91010024 United StatesOther: ON: DE91010024Thu Feb 07 06:01:47 EST 2008OSTI; NTIS; GPO Dep.EDB-91-063069English.

[17] Hines AL, Maddox RN. Mass transfer fundamentals and applications: Englewood Cliffs, New Jersey: Prentice Hall; 1985.

[18] Kamaruddin HD, Koros WJ. Some observations about the application of Fick's first law for membrane separation of multicomponent mixtures. J Membrane Sci. 1997;135(2):147-59.

[19] Das M, Koros WJ. Performance of 6FDA-6FpDA polyimide for propylene/propane separations. J Membrane Sci. 2010;365(1-2):399-408.

CHAPTER 7

CONCLUSIONS & RECOMMENDATION

7.1. Overview

Olefin/paraffin separations using cryogenic distillation are extremely energy and cost intensive processes in the petrochemical industry, accounting for nearly 0.15 Quads of energy consumption annually. Augmenting distillation processes with energy efficient separations using membranes, adsorption, extraction etc. have been proposed by several researchers to achieve significant cost and energy savings [1-5]. The specific focus here is on ethylene/ethane (C_2H_4/C_2H_6) separations. The low selectivity or instability of C_2H_4/C_2H_6 separation membranes reported in the literature makes them inadequate for practical consideration. Carbon molecular sieve (CMS) membranes, formed via the high temperature pyrolysis of polymeric precursor membranes, have shown potential to surpass the polymeric upper bound for gas separations such as O_2/N_2, CO_2/CH_4 etc. In addition, they have also demonstrated the ability to perform stably at high feed pressures up to 1000 psi, and do not undergo plasticization in the presence of highly condensable feeds. These combined attributes made them an interesting option to evaluate. The overarching goal of this work is to develop carbon molecular sieve (CMS) membranes for use in ethylene/ethane (C_2H_4/C_2H_6) separation.

In collaboration with The Dow Chemical Company, two projects focused on addressing the fundamental and practical aspects of CMS membrane development, primarily for supplementing the C_2-splitter (C_2H_4/C_2H_6), while also considering other potential applications in the petrochemical industry. The specific focus of the current work was to define the material science options to fabricate novel, high performing

C_2H_4/C_2H_6 separation CMS dense film membranes by identifying and optimizing key parameters to tune the CMS micro-morphology. Homogeneous dense films were used to develop fundamental and theoretical knowledge, and to extract intrinsic CMS characteristics, transport properties, and structure-performance relationships. In addition, the effects of several practical parameters such as the testing temperature, pressure and feed composition were analyzed to consider membrane behavior for use in realistic operations, as well as to gain insight into the fundamental nature of CMS separations.

The specific objectives of the current work are reiterated below for the reader's convenience:

1. Analysis of different polymers as precursors to CMS dense films for C_2H_4/C_2H_6 separation.
2. Analysis of the effects of pyrolysis parameters based on C_2H_4/C_2H_6 transport properties, and structure-performance evaluation of CMS dense films membranes.
3. Analysis of the effects of testing temperature, pressure and feed composition on C_2H_4/C_2H_6 separation performance of CMS dense film membranes.

Section 7.2 summarizes the key findings of this work and Section 7.3 proposes several areas for further research in the field.

7.2. Conclusions

The focus in this work was on developing CMS dense film membranes for ethylene/ethane (C_2H_4/C_2H_6) separation. Three polymers Matrimid®, 6FDA-DAM and

6FDA:BPDA-DAM were chosen as precursors to CMS membranes for C_2H_4/C_2H_6 separation. These precursors were chosen based on their availability, history of use in the Koros Group, and more importantly, because of the structural differences they offer in terms of chain packing, fractional free volume, glass transition temperatures etc., that offer a wide spectrum for CMS investigation. The intrinsic properties of the polymers were evaluated, as well as a polymeric C_2H_4/C_2H_6 upper bound line was established as a basis against which to compare CMS performance. Various advanced membrane types, such as facilitated transport, zeolites, CMS etc., and approaches to transcend the C_2H_4/C_2H_6 polymeric upper bound performance were discussed in detail. Preliminary fabrication of CMS membranes from the three precursors, Matrimid®, 6FDA-DAM and 6FDA:BPDA-DAM, was done using pyrolysis conditions chosen from literature. Several challenges in CMS dense film formation were also addressed. While this preliminary investigation demonstrated the viability of the precursors in forming CMS membranes capable of C_2H_4/C_2H_6 separation, it primarily illustrated that the "one size fits all" strategy cannot be applied to CMS fabrication. Extensive tuning of CMS membrane properties targeted specifically at C_2H_4/C_2H_6 separation was identified as a key aspect.

The pore structure and separation performance of CMS membranes can be tailored by controlling several pyrolysis parameters in the CMS fabrication process such as the final pyrolysis temperature, ramp rate, pyrolysis atmosphere etc. The effects of these parameters on the CMS structure and performance depend on the starting polymer material as well as the target gas separation. Detailed analyses of the effects of these parameters on C_2H_4/C_2H_6 separation performance of CMS derived from three precursors: Matrimid®, 6FDA-DAM and 6FDA:BPDA-DAM were reported. The evolution in C_2H_4/C_2H_6 separation performance with pyrolysis parameters was analyzed with respect to the CMS schematic pore structures and hypothetical critical pore distributions. It was shown that the overall permeability and selectivity trends of CMS membranes are

primarily dominated by their diffusion behavior. These insights were used to achieve optimum CMS fabrication conditions for C_2H_4/C_2H_6 separation using each precursor.

A discussion of different techniques such as TGA-FTIR and elemental analysis, Raman spectroscopy, WAXD, PALS, TEM and AFM, density and micropore volume measurements, gas transport etc. to characterize the nature and the pore structure of CMS membranes was also presented. Because of the amorphous, turbostratic nature of CMS materials, traditional characterization techniques based on spectroscopy and microscopy were not very useful in interpreting the CMS performance in relation to its pore morphology. Pore size distribution analyses from CO_2 sorption measurements were found useful in explaining the sorption behavior of CMS materials and understanding some of the gas transport trends; however, micropore distributions obtained from this analysis were found inconclusive in interpreting the CMS performance in relation to its pore morphology. In order to address these concerns, a novel method based on measuring the transport properties of different sized gases as molecular scale probes of the CMS pores was developed to infer pore structure and to construct critical diffusion limiting pore size distributions. This, in conjunction with separation performance data provided critical insights into the structure-performance relationships of the CMS materials. The semi-quantitative pores size distributions helped explain changes in the separation performance of CMS derived at different pyrolysis conditions and using different precursors.

The discovery of the presence of a physical aging effect in CMS membranes derived from certain glassy polymers was reported, and noted to complicate the results in this study. Physical aging results in a time-dependent behavior of CMS separation performance. Analogous to physical aging in glassy polymers, CMS membrane physical aging exhibit dependence on factors such as the starting precursor material, separation layer thickness, storage conditions, history etc. This finding adds another controlling

factor to CMS performance besides the CMS fabrication parameters. The effect of physical aging was most significant in CMS derived from 6FDA-DAM and makes it an unattractive precursor for C_2H_4/C_2H_6 separation. Physical aging had the least effect on Matrimid® CMS and 6FDA:BPDA-DAM CMS was intermediate. It is important to consider that the CMS membrane performance may be quite stable under active feed conditions. Thus, although the study of physical aging in CMS is important for fundamental understanding, it may not be a "show-stopper" for practical CMS application where the membrane module would be in active use after an initial stabilization period.

The effects of testing conditions, i.e. the testing temperature, pressure and feed composition on C_2H_4/C_2H_6 separation performance of CMS dense films were also analyzed. These studies were shown to be useful not just in predicting the membrane behavior from a practical stand point but also in a fundamental understanding of the nature of CMS membrane separation. The C_2H_4 permeability was found to increase with the permeation temperature, while the C_2H_4/C_2H_6 selectivity decreased slightly. Temperature dependence studies were useful in evaluating the transport trends of CMS membranes obtained using different precursors and processing conditions. These studies also helped elucidate the importance of entropic selection factors in advanced gas separations membranes, such as CMS, that allow them to outperform the polymeric upper bound.

The study of the pressure dependence of C_2H_4/C_2H_6 separation using CMS membranes helped provide insight into practical aspects of membrane application. Based on predictions of the effect of feed to permeate pressure ratio on CMS performance, it was demonstrated that the use of membranes for C_2H_4/C_2H_6 separation may be more useful as a debottlenecking application in the form of a hybrid membrane-distillation operation. With currently available membrane materials, consideration of the membrane flux is critical and development of higher flux C_2H_4/C_2H_6 separation

membranes may be an important factor for practical membrane area and related costs. In this regard CMS membranes derived from 6FDA:BPDA-DAM may be more favorable compared to Matrimid® for C_2H_4/C_2H_6 membrane separation applications, despite its somewhat lower selectivity.

The effect of binary C_2H_4/C_2H_6 feed gas on CMS performance was also evaluated. The feed mixture composition (63.2 mol% C_2H_4 and 36.8 mol% C_2H_6) was obtained from The Dow Chemical Company. It was found that both C_2H_4 and C_2H_6 permeabilities decreased in the mixed gas environment compared to the pure gas permeabilities, along with a small, but not a significant decrease in the C_2H_4/C_2H_6 selectivity. This is a result of the complicated competition effects between C_2H_4 and C_2H_6 when both gases are present simultaneously. Simple and rigorous models were used to predict binary gas C_2H_4/C_2H_6 performance of CMS membranes using pure gas permeation data. It was shown that neglecting the bulk flow contribution to the overall transport flux, as in the simple model, led to an over-prediction of the binary gas selectivity. The rigorous model on the other hand accounted for these bulk flow contributions and the predicted binary gas performance was fairly close to the experimental data.

While the current study focuses on CMS dense films owing to their simple geometry that allow fundamental analysis, considerations related to translation to the practically useful CMS hollow fiber form were also presented based on Liren Xu's work in the Koros Group. Considering the combined effects of "substructure collapse" resulting from intense heat treatment during pyrolysis, "physical aging" and CMS separation performance, 6FDA:BPDA-DAM was found to be the most preferred precursor for CMS fabrication for C_2H_4/C_2H_6 separation in this study. The current work thus establishes a framework for guiding research ultimately aimed at providing a

convenient, potentially scalable hollow fiber membrane formation technology for C_2H_4/C_2H_6 separation.

7.3. Recommendations

The research objectives of the current project have been successfully achieved. Significant contributions were made in the field of CMS membranes, not just from the point of C_2H_4/C_2H_6 separation, but overall in achieving a better understanding of the nature of CMS separation and its transport properties with respect to its microscopic morphology. There remain, however, several opportunities for further investigation and research in the field. Several potential areas for future research identified during the course of the current work are briefly outlined in this section.

7.3.1. Precursor-Carbon Molecular Sieve Structure Property Relation

In the current work, CMS derived from two different precursor materials, Matrimid® and 6FDA:BPDA-DAM, at the same pyrolysis conditions were compared in terms of their transport performance and microstructure. The diffusion limiting critical pore size distributions of CMS derived from these materials helped explain the differences in their resulting transport performance. The resulting CMS structures were also related to the starting material properties in terms of their glass transition temperatures, fractional free volume, polymer chain rigidity, by-products evolved during pyrolysis etc. The correlation between the starting precursor and the resulting CMS, however, still remains an area that is not well understood. Some studies have looked at the structure of CMS in relation to the starting material, by comparing CMS derived from

polymers having the same essential backbone but with different side groups, monomer ratios etc. [6-8]. However, to the best of our knowledge, there is no way to essentially predict or explain what the resulting CMS structure and performance would be based on the starting polymer properties. Given the amorphous nature of CMS materials that makes it extremely hard to characterize them, correlating the CMS structure to the starting polymer remains a big challenge in the CMS field. Investigating ways to do so is however extremely critical for future research in the field since there is an entire gamut of starting materials for CMS fabrication that may allow tailoring of CMS properties to specific applications. As a starting point, techniques that may allow monitoring in situ evolution of the pyrolysis by-products and microstructure evolution during pyrolysis may give some insights into correlating the resulting CMS structure to the starting polymer.

7.3.2. Detailed Investigation of Physical Aging in Carbon Molecular Sieve Membranes

In the current work, a physical aging phenomenon in CMS membranes resulting in time-dependent transport performance was reported, and noted to complicate the results in this study. Physical aging of CMS membranes adds another important controlling parameter to CMS performance besides CMS fabrication parameters such as the polymer precursor, pyrolysis conditions, pre-treatment and post-treatment conditions. The current study showed that physical aging in CMS depends on factors such as the precursor polymer, separation layer thickness, storage conditions, history etc. Since aging was discovered at a later stage during this study, only preliminary work was done to monitor aging trends in CMS. A detailed investigation of this aging behavior is critical in the future. It will be useful to investigate how and why physical aging in CMS is dependent on the polymer precursor. Several ways of stabilizing the CMS membrane

prior to testing must be explored. For example, storing the CMS in a vacuum oven prior to testing, exposing the CMS to vacuum at the end of the pyrolysis and cooling cycle in the pyrolysis furnace itself, cooling the CMS in the presence of inert gas in the pyrolysis furnace for a prolonged period prior to testing etc. It is also likely that, analogous to glassy polymers, physical aging in CMS will be temperature dependent. Thus the physical aging behavior of CMS must be investigated at different temperatures.

Physical aging in CMS seems to impact the permeabilities of other penetrants such as O_2, N_2, CO_2, CH_4 etc. as well, as seen from some preliminary measurements. However, the extent of the effect of physical aging of CMS on different penetrants was not analyzed in detail. It is anticipated that physical aging would have a smaller impact on penetrants of smaller size. It is likely that physical aging may result in a loss of the larger pores such that the effect of the tail end of the CMS pore size distribution may be more significant. This is illustrated in Figure 7.1. Thus larger gases like C_2H_4 and C_2H_6 that lie at the tail end of the distribution may be impacted more as a result of physical aging. This hypothesis must however be verified by detailed analysis of the effects of physical aging in CMS membranes on the performance of different penetrants, and may be an interesting avenue to pursue for future studies.

Investigation of ways to trap the CMS membranes in an attractive metastable state and/or ways of preventing physical aging in CMS, for example by functionalizing the CMS membranes with chemical reagents (somewhat analogous to crosslinking in glassy polymers) to stabilize it, will be beneficial in preserving high membrane flux. These directions could be of interest for pursuit in the future.

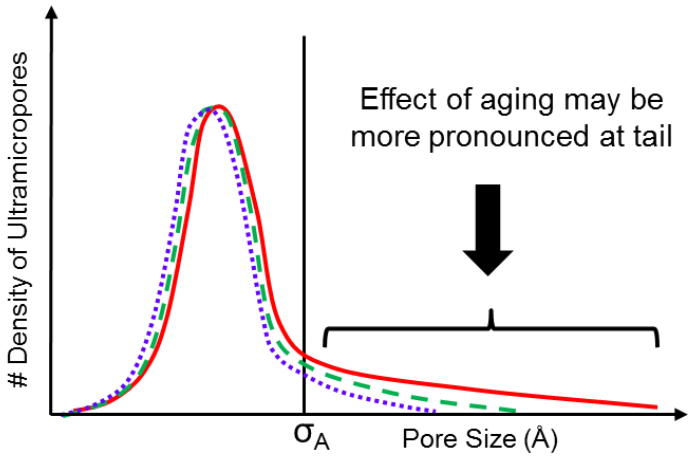

Figure 7.1: Likely effect of physical aging on the pore size distribution of CMS

7.3.3. Further Investigation of Entropic Contributions to Carbon Molecular Sieve Membrane Performance

The importance of entropic selection factors, derived from differences in the shapes and subtle configurational changes of similar sized penetrants, in molecular sieving CMS materials has been demonstrated in this work. The focus in the current work has been on C_2H_4/C_2H_6 separation. Additionally, comparison of C_2H_4, which has several degrees of rotational and vibrational freedom, against Kr, which has essentially the same critical size but lacks any configurational degrees of freedom, provided further insight into the importance of entropic factors. Singh [9] previously demonstrated the importance of entropic selection factors in O_2/N_2 separation using zeolites and CMS. Furthering the understanding of these entropic contributions to the overall CMS performance could open up a whole new area of application for CMS membranes. For example, considering differences between He and H_2, and penetrants such as C_2H_2, CH_4, C_2H_4, C_2H_6, C_3H_6, C_3H_8 etc. will be beneficial not just from an academic perspective, but also in practically applying CMS membranes to these challenging

separation areas where polymeric membranes are unable to achieve attractive separation performance.

Xu et al. [10] recently proposed the use of CMS in debottlenecking separations of olefins (C_2H_4 and C_3H_6) from paraffins (C_2H_6 and C_3H_8) in cracked gas processing. Further they discussed how CMS may be ideal candidates for various other cracked gas processing applications that involve several complex cuts between different gases such as H_2, acetylenes, olefins, paraffins etc. The "slit-shaped" pore structure of CMS membranes may allow them to effectively discriminate between linear molecules (H_2, C_2H_2, MA, PD), somewhat planar olefins (C_2H_4, C_3H_6) and bulky paraffins (CH_4, C_2H_6, C_3H_8) based on their shape differences (see Figure 7.2). In this regard, understanding the entropic contribution factors resulting from the shape and configurational differences of these molecules will be useful in applying and optimizing CMS for these complex separations. In addition to experimental and basic theoretical predictions, as was carried out in the current work, molecular simulations may allow making significant progress in better understanding the effects of entropic contributions.

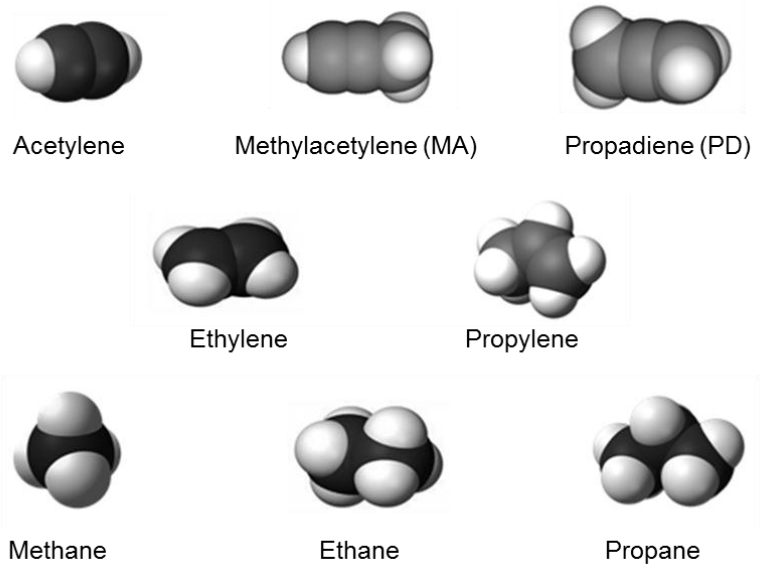

Figure 7.2: Space-filling models of C1, C2 and C3 hydrocarbons

7.3.4. Translating Promising Intrinsic Carbon Molecular Sieve Dense Film Performance to Hollow Fibers, Realistic Testing & Scale-up

In the current work CMS dense films were successfully fabricated and showed significant improvement in C_2H_4/C_2H_6 separation performance compared to the starting precursor polymer, surpassing the polymeric upper bound. A parallel project by Liren Xu in the Koros Group showed that CMS hollow fiber membranes can translate the attractive selectivity of the dense films for C_2H_4/C_2H_6 separation. However, "substructure collapse" due to intensive heat treatment during pyrolysis results in an increased separation layer thickness in the hollow fiber form, the consequence of which is a drastic loss in permeance. This is a critical challenge to address for practical CMS application, and ways to overcome substructure collapse are important for future research. Several approaches such as cross-linking and precursor modification etc. are being pursued in the Koros Group to mitigate the substructure collapse problem. Of these, the "V-modification" method developed by Nitesh Bhuwania shows a promising approach to preserve asymmetric morphology in the CMS fibers, and deserves further pursuit. In addition to finding ways of preventing substructure collapse in the hollow fiber from, it will also be useful to analyze the modification methods on the dense film form in order to develop an understanding of the effects on the intrinsic precursor and CMS properties.

Consideration of the effects of several operational parameters in practical membrane applications such as performance under cryogenic conditions, actual feed streams, pressure ratio, stage-cut etc. are also critical, as is scale-up of lab scale CMS hollow fiber production. Dr. Oguz Karvan in the Koros Group successfully demonstrated preliminary CMS scale-up to 200 fiber capacity in a large pyrolysis furnace. The impacts of scale-up on pyrolysis, CMS performance, realistic membrane module construction etc. are all important areas for future developments.

7.4. References

[1] Caballero JA, Grossmann IE, Keyvani M, Lenz ES. Design of hybrid distillation-vapor membrane separation systems. Ind Eng Chem Res. 2009;48(20):9151-62.

[2] Ozokwelu D. Hybrid separations/distillation technology: Research opportunities for energy and emissions reduction: US Department of Energy; 2005.

[3] Robinson S, Jubin R, Choate B. Materials for separation technologies: Energy and emission reduction opportunities: US Department of Energy; 2005.

[4] Gottschlich DE, Roberts DL. Energy minimization of separation processes using conventional/membrane hybrid systems: US Department of Energy; 1990.

[5] Merkel T, Blanc R, Zeid J, Suwarlim A, Firat B, Wijmans S, et al. Separation of olefin/paraffin mixtures with carrier facilitated membranes: U.S. Department of Energy; 2007.

[6] Williams PJ, Koros WJ. Gas separation by carbon membranes. In: Li NN, Fane AG, Winston Ho WS, Matsura T. Advanced membrane technology and applications. New Jersey: John Wiley & Sons Inc. 2008.

[7] Park HB, Kim YK, Lee JM, Lee SY, Lee YM. Relationship between chemical structure of aromatic polyimides and gas permeation properties of their carbon molecular sieve membranes. J Membrane Sci. 2004;229(1-2):117-27.

[8] Williams PJ. Analysis of factors influencing the performance of CMS membranes for gas separation. Georgia Institute of Technology, Doctor of Philosophy, 2006.

[9] Singh A, Koros WJ. Significance of entropic selectivity for advanced gas separation membranes. Ind Eng Chem Res. 1996;35(4):1231-4.

[10] Xu L, Rungta M, Brayden MK, Martinez MV, Stears BA, Barbay GA, et al. Olefins-selective asymmetric carbon molecular sieve hollow fiber membranes for hybrid membrane-distillation processes for olefin/paraffin separations. J Membrane Sci. 2012 (in press).

APPENDIX A

GAS COMPRESSIBILITY FACTORS

The compressibility factor (Z) is used to account for the deviance in the properties of a real gas from the ideal gas law, and is described as follows:

$$\mathrm{Z} = \frac{\mathrm{pV}}{\mathrm{RT}} \tag{A.1}$$

where, p is the gas pressure, V is the molar volume, T is the absolute temperature, and R is the universal gas constant. The deviation from ideal gas behavior is higher at higher gas pressures, and this deviation must be accounted for in the calculations.

The pressure dependent compressibility factor equations take the functional form shown in Equation A.2.

$$\mathrm{Z} = 1 + (\mathrm{A})\mathrm{p} + (\mathrm{B})\mathrm{p}^2 + (\mathrm{C})\mathrm{p}^3 + \cdots \tag{A.2}$$

where, A, B, C etc. are constants. The higher order terms in the equation are negligible and hence ignored.

The pressure dependent compressibility factor equations of pure gases were obtained from the National Institute of Standards and Technology (NIST) Software Standard Reference Database 12, Version 5.0 and NIST WebBook, Standard Reference Database Number 69. These are shown in Table A.1 below.

Table A.1: Compressibility factor equations of gases, with pressure, p in psia

Gas	Temperature	Compressibility Equation
He	35°C	$Z = 1 + (3.05E\text{-}05)p + (2.14E\text{-}10)p^2 - (4.18E\text{-}14)p^3$
Ne	35°C	$Z = 1 + (3.21E\text{-}05)p + (2.80E\text{-}10)p^2 + (2.98E\text{-}14)p^3$
Ar	35°C	$Z = 1 - (3.66E\text{-}05)p + (6.16E\text{-}09)p^2 + (8.77E\text{-}13)p^3$
Kr	25°C	$Z = 1 - (1.46E\text{-}04)p + (1.66E\text{-}08)p^2 - (1.88E\text{-}11)p^3$
Kr	35°C	$Z = 1 - (1.31E\text{-}04)p + (1.93E\text{-}08)p^2 - (1.92E\text{-}11)p^3$
Kr	50°C	$Z = 1 - (1.12E\text{-}04)p + (2.18E\text{-}08)p^2 - (1.96E\text{-}11)p^3$
Xe	35°C	$Z = 1 - (3.27E\text{-}04)p - (6.42E\text{-}08)p^2 - (5.72E\text{-}11)p^3$
H_2	35°C	$Z = 1 + (4.10E\text{-}05)p - (1.06E\text{-}10)p^2 + (1.33E\text{-}13)p^3$
O_2	35°C	$Z = 1 - (3.72E\text{-}05)p + (5.26E\text{-}09)p^2 + (1.16E\text{-}12)p^3$
N_2	35°C	$Z = 1 - (8.19E\text{-}06)p + (1.00E\text{-}08)p^2 + (2.83E\text{-}13)p^3$
CO_2	35°C	$Z = 1 - (3.07E\text{-}04)p - (5.35E\text{-}08)p^2 - (5.03E\text{-}11)p^3$
CH_4	35°C	$Z = 1 - (1.06E\text{-}04)p + (6.06E\text{-}09)p^2 + (3.28E\text{-}12)p^3$
C_2H_4	25°C	$Z = 1 - (3.91E\text{-}04)p - (7.47E\text{-}08)p^2 - (1.09E\text{-}10)p^3$
C_2H_4	35°C	$Z = 1 - (3.52E\text{-}04)p - (6.39E\text{-}08)p^2 - (5.74E\text{-}11)p^3$
C_2H_4	50°C	$Z = 1 - (3.03E\text{-}04)p - (4.60E\text{-}08)p^2 - (2.10E\text{-}11)p^3$
C_2H_6	25°C	$Z = 1 - (5.35E\text{-}04)p + (3.06E\text{-}09)p^2 - (6.25E\text{-}10)p^3$
C_2H_6	35°C	$Z = 1 - (4.73E\text{-}04)p - (7.13E\text{-}08)p^2 - (2.98E\text{-}10)p^3$
C_2H_6	50°C	$Z = 1 - (4.03E\text{-}04)p - (7.95E\text{-}08)p^2 - (1.12E\text{-}10)p^3$
SF_6	35°C	$Z = 1 - (7.47E\text{-}04)p + (3.09E\text{-}07)p^2 + (2.26E\text{-}09)p^3$

APPENDIX B

PURE GAS DATA

The pure gas permeability (P) data at 50 psia feed pressure and the dual mode/Langmuir sorption isotherm parameters of different gases are shown in Table B.1-B.5 below for different dense film membranes. In Tables B.1-B.5, k stands for Henry's law constant, C'_H stands for Langmuir hole-filling capacity or saturation capacity, and b stands for Langmuir affinity constant.

Table B.1: Permeability and dual mode sorption parameters for P1 (Matrimid® precursor)

Gas	T	P	k	C'_H	b
	°C	Barrer	cc(STP)/cc(CMS).psia	cc(STP)/cc(CMS)	1/psia
C_2H_4	25	0.38	0.18	12.0	0.059
C_2H_4	35	0.45	0.14	11.1	0.054
C_2H_4	50	0.56	0.11	10.2	0.048
C_2H_6	25	0.08	0.11	9.2	0.111
C_2H_6	35	0.10	0.09	8.2	0.104
C_2H_6	50	0.13	0.07	7.3	0.089

Table B.2: Permeability and Langmuir sorption parameters for P1-500°C-CMS_UHP Ar

Gas	T	P	C'_H	b
	°C	Barrer	cc(STP)/cc(CMS)	1/psia
He	35	600.0	6.8	0.007
Ne	35	190.0	11.9	0.011
Ar	35	67.5	30.1	0.008
Kr	25	30.5	56.0	0.031
Kr	35	34.8	50.9	0.030
Kr	50	42.0	43.0	0.026
Xe	35	7.6	76.5	0.110
H_2	35	973.5	29.5	0.031
O_2	35	180.4	57.5	0.008
N_2	35	42.5	57.1	0.007
CO_2	35	825.3	72.5	0.060
CH_4	35	37.8	52.0	0.035
C_2H_4	25	68.0	69.4	0.132
C_2H_4	35	77.1	63.5	0.114
C_2H_4	50	90.5	60.7	0.076
C_2H_6	25	17.0	60.5	0.195
C_2H_6	35	19.7	55.0	0.149
C_2H_6	50	23.5	51.2	0.100
SF_6	35	1.1	24.1	0.045

Table B.3: Permeability and Langmuir sorption parameters for P1-550°C-CMS_UHP Ar

Gas	T	P	C'_H	b
	°C	Barrer	cc(STP)/cc(CMS)	1/psia
He	35	310.0	9.4	0.005
Ne	35	130.0	13.8	0.007
Ar	35	34.0	69.8	0.007
Kr	35	9.0	86.1	0.038
Xe	35	1.9	82.1	0.089
H_2	35	652.0	24.0	0.030
O_2	35	131.3	67.2	0.009
N_2	35	18.2	53.7	0.009
CO_2	35	535.0	83.0	0.060
CH_4	35	8.2	69.9	0.048
C_2H_4	25	15.0	90.0	0.150
C_2H_4	35	18.5	85.1	0.132
C_2H_4	50	25.3	80.2	0.110
C_2H_6	25	2.4	81.1	0.184
C_2H_6	35	3.0	76.0	0.158
C_2H_6	50	4.1	69.8	0.141
SF_6	35	0.4	25.0	0.050

Table B.4: Permeability and Langmuir sorption parameters for P1-675°C-CMS_UHP Ar

Gas	T	P	C'_H	b
	°C	Barrer	cc(STP)/cc(CMS)	1/psia
He	35	220.0	9.5	0.005
Ne	35	117.0	14.5	0.008
Ar	35	26.9	76.4	0.007
Kr	25	5.3	102.6	0.032
Kr	35	7.0	94.6	0.030
Kr	50	9.4	90.0	0.026
Xe	35	0.5	95.0	0.085
H_2	35	552.9	22.0	0.038
O_2	35	128.0	90.0	0.009
N_2	35	16.5	78.0	0.007
CO_2	35	460.0	109.0	0.062
CH_4	35	6.4	89.8	0.028
C_2H_4	25	14.0	106.9	0.120
C_2H_4	35	17.7	101.9	0.101
C_2H_4	50	24.0	95.0	0.083
C_2H_6	25	1.2	94.0	0.160
C_2H_6	35	1.6	87.6	0.159
C_2H_6	50	2.3	83.4	0.115
SF_6	35	0.1	20.0	0.050

Table B.5: Permeability and Langmuir sorption parameters for P3-675°C-CMS_UHP Ar

Gas	T	P	C'_H	b
	°C	Barrer	cc(STP)/cc(CMS)	1/psia
He	35	1332.2	15.5	0.005
Ne	35	450.0	15.5	0.006
Ar	35	67.1	104.7	0.007
Kr	35	18.5	132.1	0.030
Xe	35	3.7	140.0	0.140
H_2	35	2995.0	30.1	0.030
O_2	35	250.0	110.0	0.010
N_2	35	35.3	93.3	0.010
CO_2	35	1122.0	150.0	0.059
CH_4	35	16.7	110.1	0.035
C_2H_4	25	43.1	143.2	0.217
C_2H_4	35	57.7	137.2	0.181
C_2H_4	50	85.6	134.7	0.114
C_2H_6	25	5.6	134.3	0.254
C_2H_6	35	7.6	132.8	0.170
C_2H_6	50	12.4	121.8	0.157
SF_6	35	0.4	26.0	0.050

Pure gas permeability (P) data was obtained directly from permeation measurements. Sorption isotherm parameters were obtained from direct sorption measurements. The sorption coefficient ($\overline{S}$) for polymers and CMS can be obtained using b and C'_H as shown in Equations B.1 and B.2 respectively:

$$\text{Polymers: } \overline{S}_A = k_{DA} + \frac{C'_{HA} b_A}{1 + b_A p_A} \tag{B.1}$$

$$\text{CMS: } \overline{S}_A = \frac{C'_{HA} b_A}{1 + b_A p_A} \tag{B.2}$$

Mixed gas sorption coefficients in CMS can be obtained from Equation B.3.

$$\text{CMS (Binary gas): } \overline{S}_A = \frac{C'_{HA} b_A}{1 + b_A p_A + b_B p_B} \tag{B.3}$$

Average pure gas transport (Fickian) diffusivity ($\overline{D}$) can then be obtained from pure gas permeability and sorption coefficients using Equation B.4.

$$P_A = \overline{D}_A \overline{S}_A \tag{B.4}$$

Corrected diffusivity ($Đ$), or Maxwell-Stefan diffusivity, can be obtained from the average transport diffusivity using Equation B.5.

$$\overline{D}_A = \frac{Đ_A}{\theta_A} \ln\left(\frac{1}{1-\theta_A}\right) \quad \text{(B.5)}$$

where, θ, the fractional site saturation factor, can be obtained from Langmuir isotherm parameters as follows:

$$\theta_A = \frac{C_A}{C'_{HA}} = \frac{b_A p_A}{1 + b_A p_A} \quad \text{(B.6)}$$

APPENDIX C

DIFFUSION SIZE PORE DISTRIBUTION

Carbon molecular sieve membranes consist of a "slit-like" pore structure, with larger pores called micropores (~ 6-20 Å) connected by smaller pore windows called ultramicropores (< 6-20 Å) [1]. The ultramicropores limit diffusion of gas molecules in CMS via a molecular sieving effect. It was shown in Chapter 5 that the overall permeability and selectivity trends for C_2H_4/C_2H_6 separation using CMS membranes is dominated by diffusion, while the impact due to sorption is small. It is therefore critical to characterize the diffusion-limiting ultramicropores in order to understand the CMS transport properties with regard to its structure.

It remains exceeding difficult however to characterize the CMS ultramicropores owing to the amorphous nature of the materials. A detailed discussion of this can be found in Chapter 5. In the current study, a gas probe method [2] was used to infer the CMS pores based on the transport properties of different gases as molecular size probes of the CMS pores. This was further used to establish semi-quantitative diffusion size pore distribution (DSPD) that can facilitate understanding of transport in CMS membranes in relation to their structure.

C.1. Diffusion Size Pore Distribution Construction Concept

The corrected gas diffusivities (calculated using data shown in Appendix B) were used to obtain semi-quantitative DSPDs. Gas penetrants were chosen spanning the entire size range, namely He (2.6 Å), Ne (2.8 Å), CO_2 (3.3 Å,) Ar (3.5 Å), N_2 (3.64 Å),

CH_4 (3.8 Å), Xe (4.1 Å) and SF_6 (5.5 Å). The sizes of He, Ne, Ar and Xe were taken from [3], that of CO_2, N_2 and CH_4 were taken from [4], and that of SF_6 was taken from [2]. The semi-quantitative DSPDs were constructed as illustrated by the hypothetical distribution shown in Figure C.1 below. Gas penetrants were placed by size along the x-axis spanning the CMS ultramicropore size range from 2.6 Å (the smallest penetrant tested- He) to 5.5 Å (the largest penetrant tested- SF_6). A gas penetrant may have diffusive access to all interconnected diffusive pores larger than its size. As such, the area under the DSPD curve to the right of the marked penetrant size represents the pores accessible to the gas molecule and scales with its corrected diffusivity. For example the hashed blue area under the curve in Figure C.1(i) represents the number density of diffusive pores accessible to He and scales with the He diffusivity. The area of the curve between any two gas molecules then scales with the difference of the corrected diffusivities of the two penetrants. For example the pink area under the curve in Figure C.1(i) scales with the difference of the diffusivities of He and Ne. Given the negligible diffusivity of SF_6 in all cases, it is assumed to be completely excluded from the pores such that the curve was terminated at 5.5 Å.

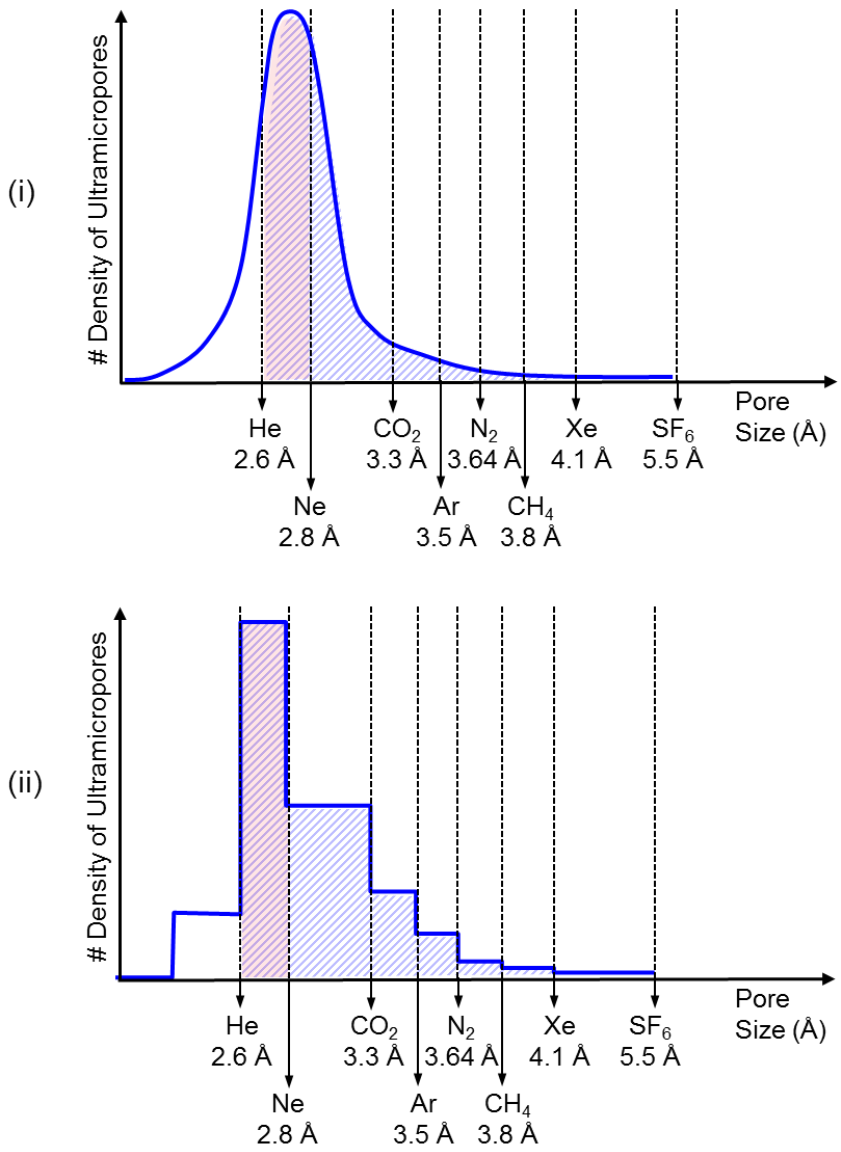

Figure C.1: Hypothetical representation of a semi-quantitative diffusion size pore distribution (DSPD) based on the diffusivities of different sized penetrants: (i) smooth distribution curve, (ii) step distribution curve

The idea in Figure C.1(i) was inspired by preliminary studies of the CMS ultramicropore distributions by Kiyono et al. [2]. Their pore size distributions are shown in Figure C.2. Kiyono et al. [2] carried out an investigation of the CMS structure, namely the applicable ultramicropore distribution, by using different sized gas molecules: He (2.6Å), CO_2 (3.3Å), O_2 (3.46Å), N_2 (3.64Å), CH_4 (3.8Å) and SF_6 (5.5Å) as probes. In their case,

average transport diffusivities were used for pore size distribution construction. The shapes of the distributions in Figure C.2 were drawn by trial and error to match the ratio of diffusion coefficients relative to the area of accessible ultramicropores for each respective molecule for gas separations among CO_2, O_2, N_2 and CH_4. In addition, the total area under the curve was adjusted to be around 2.6 times larger for 6FDA:BPDA-DAM membranes than for Matrimid® to reflect the relative diffusion coefficient of He in the two polymers. This was based on the assumption that He samples all pores accessible to any gas molecule in both cases.

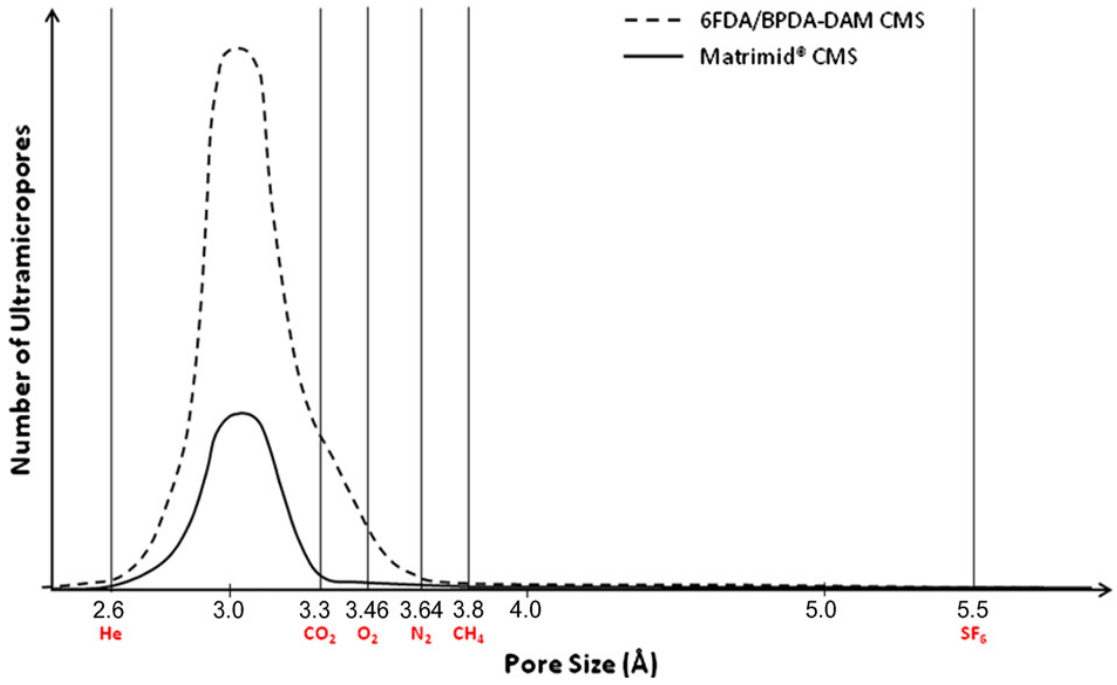

Figure C.2: Semi-quantitative critical ultramicropore distributions developed by Kiyono et al. [2] for CMS derived from pyrolysis of Matrimid® and 6FDA:BPDA-DAM at 550°C

In the current study, diffusion size pore distributions (DSPDs) were constructed as described above. Corrected diffusivities, instead of average transport diffusivities,

were used for the pore size distribution development. Corrected diffusivities, being independent of the penetrant concentration and dependent solely on the size and shapes of the penetrant gases, are a more appropriate in interpreting molecular sieving behavior. Corrected diffusivities were obtained using the data and equations shown in Appendix B. Further, instead of representing the distribution as a smooth curve shown in Figure C.1(i) the distribution was represented in step form, as shown in Figure C.1(ii) since it corresponds to discrete measurements. This was done because the shape of the curve in Figures C.1(i) and C.2 must be fit by trial and error, which can be extremely tedious and may also leave some room for ambiguity in the actual shape of the curve. The concept is however the same. As such, the cumulative area under the curve to the right of any penetrant size scales with its corrected diffusion coefficient. For example the hashed blue area under the step distribution curve in Figure C.1(ii) represents the number density of diffusion size pores accessible to He and scales with the He diffusivity. The area of the rectangle between any two gas molecules then scales with the difference of the corrected diffusivities of the two penetrants. For example the pink rectangular area in Figure C.1(i) scales with the difference of the diffusivities of He and Ne. Further, the ratio of the areas to the right of two given penetrants may represent the diffusion selectivity for the gas pair.

C.2. Diffusion Size Pore Distribution Construction Example

The construction of the semi-quantitative diffusion size pore distribution (DSPD) curve based on the concept described in C.1(ii) is shown below as an example for CMS

derived from UHP Ar pyrolysis of Matrimid® at 675°C. Table C.1 shows the calculations of the areas and heights of the rectangles between consecutive penetrants.

Table C.1: Calculations for use in the semi-quantitative diffusion size pore distribution (DSPD) for CMS derived from UHP Ar pyrolysis of Matrimid® at 675°C.
σ – penetrant size (adopted from [2-4]), Đ – corrected diffusivity (obtained from Appendix B), A – area under the curve (scales with Đ), ΔA – area difference between two neighboring penetrants i.e. area of rectangle between neighboring penetrants (scales with corrected diffusivity difference, ΔĐ of neighboring gases), w – width of rectangle (i.e. size difference, Δσ of neighboring gases), h – height of rectangle

Gas	Σ	Đ	A (~ Đ)	ΔA (~ ΔĐ)	w (~ Δσ)	h (= ΔA/w)	Scaled h
	Å	cm^2/s	Arbitrary	Arbitrary	Arbitrary	Arbitrary	Arbitrary
He	2.6	2.59E-06	2.59E-06	1.97E-06	0.2	9.87E-06	98662.72
Ne	2.8	6.14E-07	6.14E-07	5.37E-07	0.5	1.07E-06	10732.45
CO_2	3.3	7.73E-08	7.73E-08	4.63E-08	0.2	2.31E-07	2313.84
Ar	3.5	3.11E-08	3.11E-08	1.36E-08	0.14	9.69E-08	969.30
N_2	3.64	1.75E-08	1.75E-08	1.54E-08	0.16	9.63E-08	962.54
CH_4	3.8	2.09E-09	2.09E-09	2.01E-09	0.3	6.71E-09	67.06
Xe	4.1	7.88E-11	7.88E-11	6.55E-12	1.4	4.68E-12	0.05
SF_6	5.5	7.22E-11	7.22E-11				

The DSPD is then constructed using "scaled h" from Table C.1 on the ordinate and penetrant size (σ) from Table C.1 on the abscissa. Figures C.3 and C.4 show the distributions, on a normal and natural log scale respectively, constructed using the data shown in Table C.1, for CMS derived from UHP Ar pyrolysis of Matrimid® at 675°C.

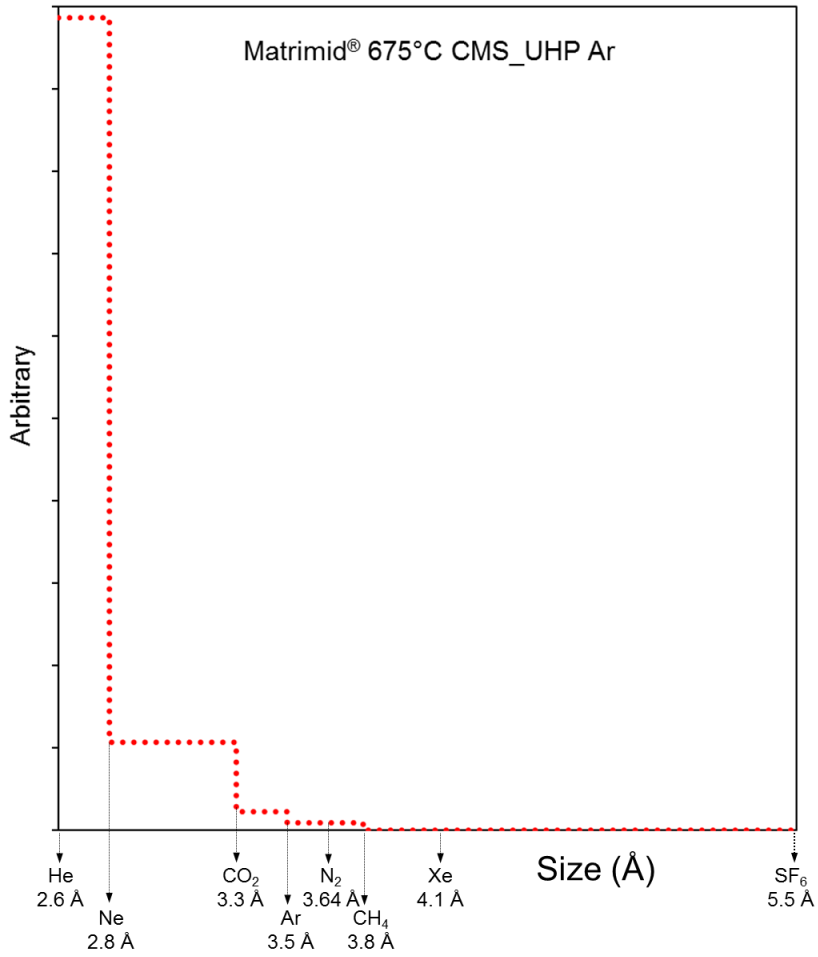

Figure C.3: Semi-quantitative diffusion size pore distribution (DSPD) on normal scale for CMS derived from UHP Ar pyrolysis of Matrimid® at 675°C

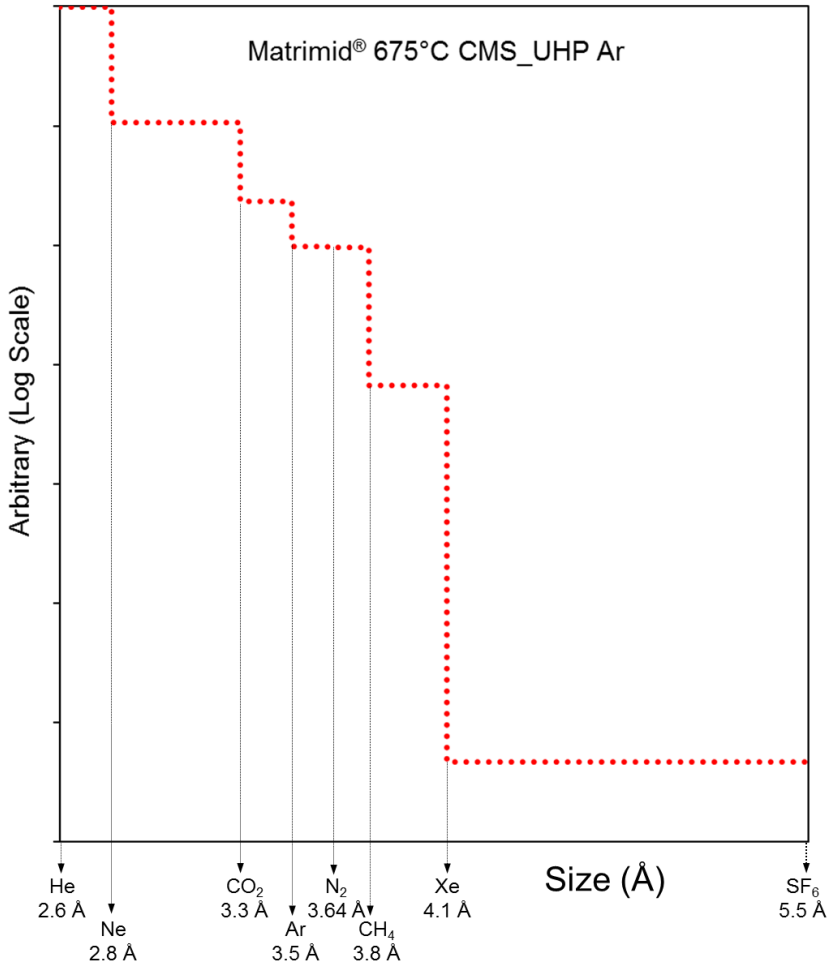

Figure C.4: Semi-quantitative diffusion size pore distribution (DSPD) on natural log scale for CMS derived from UHP Ar pyrolysis of Matrimid® at 675°C

C.3. Representation of Literature Data Using Current Semi-Quantitative Diffusion Size Pore Distribution Construction Method

The diffusion size pore distribution (DSPD) method from the current work was applied to the data from Kiyono et al. [2]. As mentioned previously, Kiyono et al. [2] used average transport diffusivity to construct their critical pore size distributions, represented in Figure C.2. Here, both average transport diffusivity and corrected diffusivity was used to build DSPDs based on the current step method using the data from Kiyono et al. [2].

The results are shown in Figures C.5 and C.6 for distributions based on average transport diffusivities and corrected diffusivities respectively.

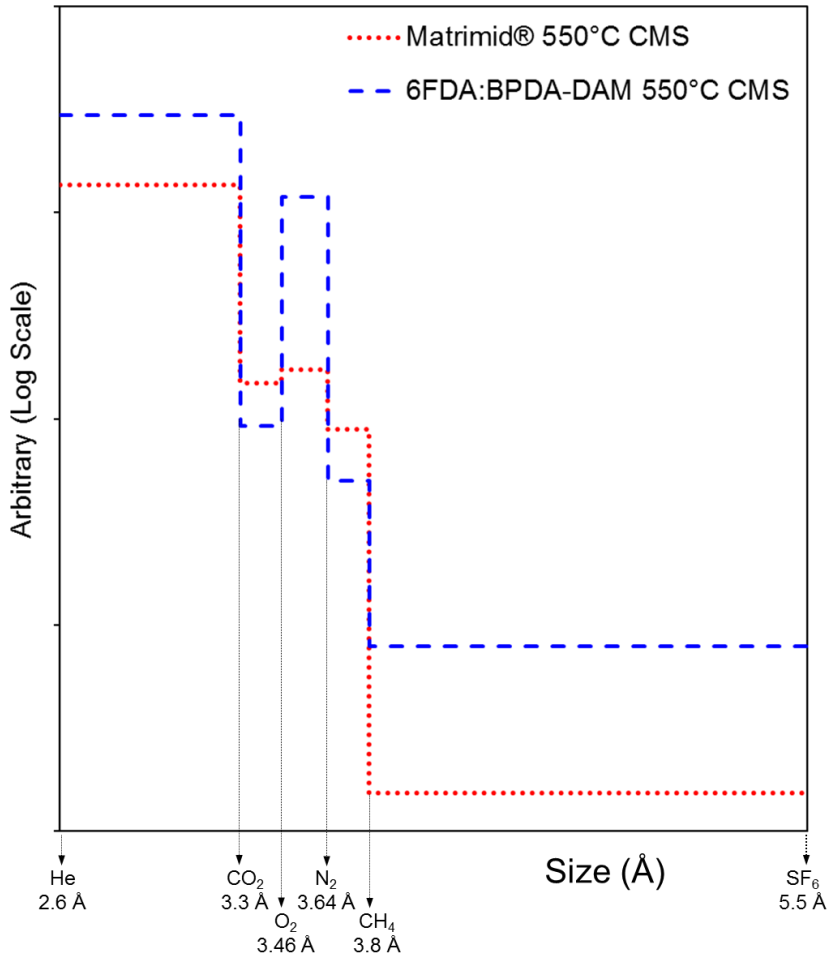

Figure C.5: Semi-quantitative diffusion-limiting ultramicropore distribution, developed using the current step method, based on average transport diffusivity data from [2]

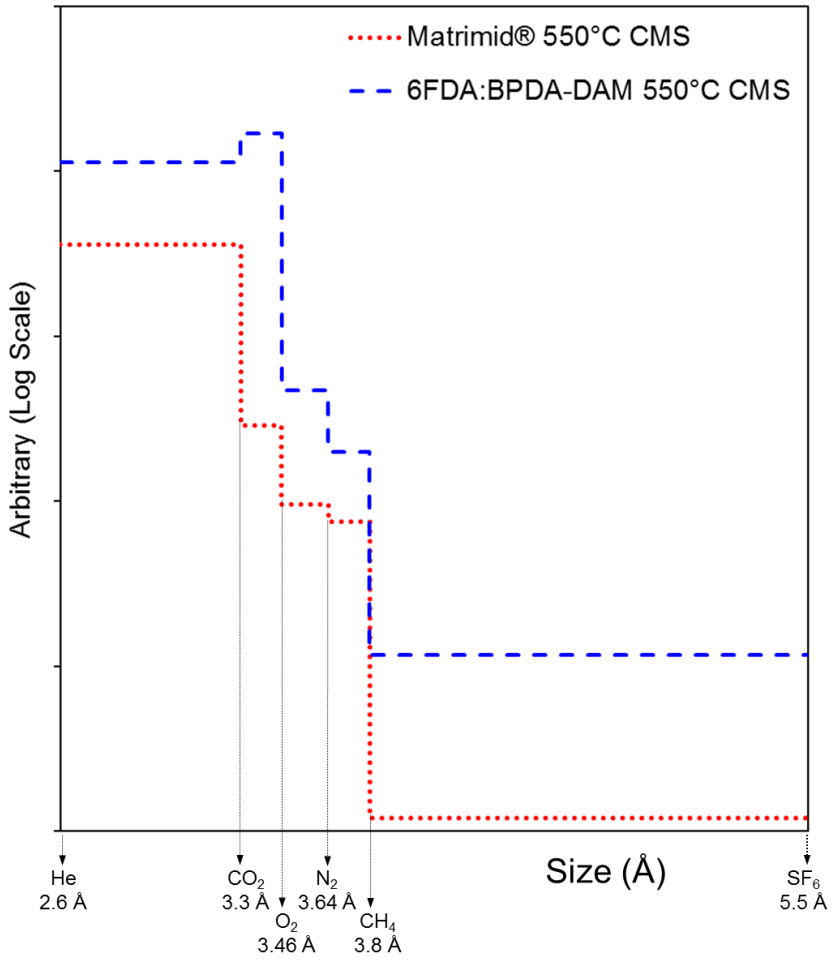

Figure C.6: Semi-quantitative diffusion size pore distribution (DSPD), developed using the current step method, based on corrected diffusivities obtained from data in [2]

A comparison of Figures C.5 and C.6 clearly shows that using corrected diffusivities is more appropriate, The distributions in Figure C.5 shows spikes which may results from concentration dependence of the average transport diffusivities. Using the corrected diffusivities in Figure C.6 however does not show this anomalous behavior resulting from penetrant concentration dependence.

C.4. References

[1] Steel KM. Carbon membranes for challenging gas separations. The University of Texas at Austin, Doctor of Philosophy, 2000.

[2] Kiyono M, Williams PJ, Koros WJ. Effect of polymer precursors on carbon molecular sieve structure and separation performance properties. Carbon. 2010;48(15):4432-41.

[3] Reid C, Sherwood TK. The properties of gases and liquids: Their estimation and correlation. New York: Mcgraw-hill; 1976.

[4] Breck DW. Zeolite molecular sieves. New York: Wiley & Sons; 1974.

APPENDIX D

THEORETICAL ENTROPIC FACTOR CALCULATIONS

Carbon molecular sieve membranes consist of a "slit-like" pore structure, with larger pores called micropores (~ 6-20 Å) connected by smaller pore windows called ultramicropores (< 6-20 Å) [1]. Figure D.1 shows a 3-D representation of a CMS pore structure. This combination of micropores and ultramicropores allows CMS membranes to achieve both high permeability and high selectivity via a molecular sieving effect. Diffusion through the critical pores requires molecules to overcome repulsion from the pore walls, and even small changes in size can result in significant differences in the activation energy required for diffusion [1, 2]. On the other hand, the rigid pore structure of CMS also allows it to effectively discriminate between the shapes and subtle configurational differences of similar sized penetrants [3].

In transport through CMS membranes, a penetrant molecule is said to be in a normal state is when it resides in a micropore, while the transition state corresponds to the gas molecule existing in a metastable state that enables it to jump through the ultramicropore with no added free energy [3], as illustrated in Figure D.1. While the molecules may translate and rotate freely in a larger micropore site, they may lose certain degrees of freedom in the restricted ultramicropore sites depending on the size and shape. This may result in shape or configurational selection, referred to as "entropic selection" of one penetrant over the other [3].

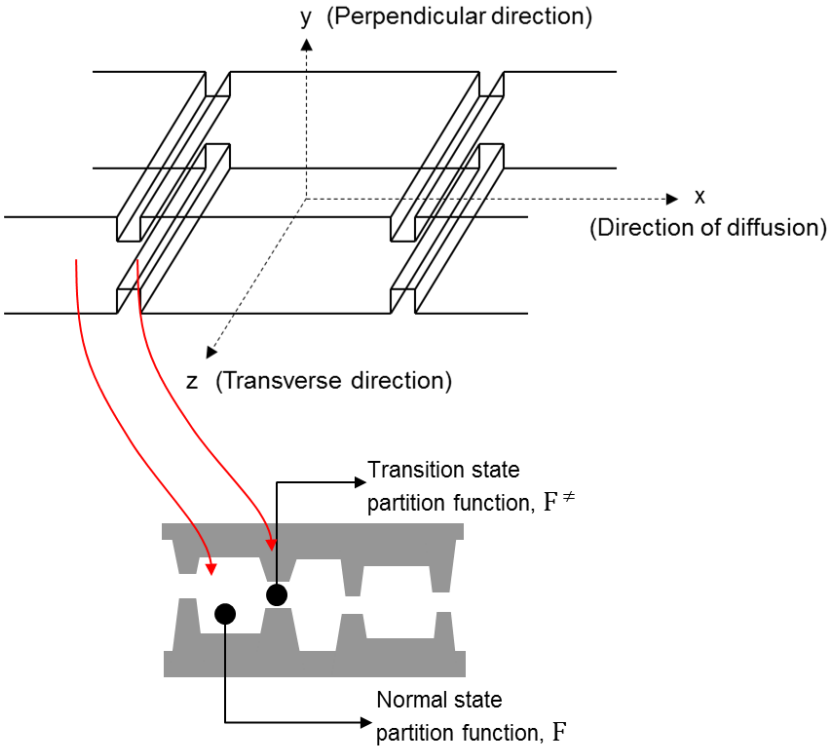

Figure D.1: 3-D representation of ideal CMS "slit-like" pore structure with micropores and micropores, and representation of normal and transition states on a penetrant in transport through CMS

The activation entropy of diffusion (S_D) can be related to the pre-exponential factor of diffusion (D_o), and further related to the partition function of the molecules in the normal and transition state, as shown in Equation D.1 [3, 4].

$$D_o = e\lambda^2 \frac{kT}{h} \exp\left(\frac{S_D}{R}\right) = e\lambda^2 \left(\frac{kT}{h}\right) \frac{F^{\neq}}{F} \tag{D.1}$$

where, λ is the average diffusive jump length, k is Boltzmann's constant, and h is Planck's constant [3-5] . F is the partition function in the normal state and $F^{\neq}$ represents partition function in the transition state.

Thus, the entropic contribution to the overall selectivity can be calculated by considering the partition function of the molecules in the transition state vs. the normal state, as follows:

$$\text{Entropic Factor} = \left[\frac{(F^{\neq}/F)_A}{(F^{\neq}/F)_B}\right] \tag{D.2}$$

The partition function associated with each degree of translational, rotational and vibrational freedom, F_T, F_R and F_V respectively, can be calculated from Equations D.3, D.4 and D.5 respectively [3, 4].

$$F_T = d_t \left(\frac{2\pi mkT}{h^2}\right)^{1/2} \tag{D.3}$$

$$F_R = \left(\frac{8\pi^2 IkT}{h^2}\right)^{1/2} \tag{D.4}$$

$$F_V = \left[\frac{\exp(-h\nu/2kt)}{1-\exp(-h\nu/kt)}\right] \tag{D.5}$$

In the above equations, m is the mass of the molecule (C_2H_4 = 28 amu, C_2H_6 = 30 amu, Kr = 84 amu), I is the moment of inertia, k is Boltzmann constant, h is Planck's constant, ν is the vibrational frequency and T is the absolute temperature, assumed as 300K. d_t represents the pore dimension in which the molecules is in the normal (micropore) or transition (ultramicropore) state. In the current study the values of

d_t were assumed to be 8.5 Å in the normal state and 3.8 Å in the transition state. The partition function can then be calculated as

$$F = {F_T}^n \, {F_R}^n \, {F_V}^n \tag{D.6}$$

where, n is the number of degrees of freedom associated with each type of motion of the molecule. At ambient temperature, the degrees of freedom associated with vibrations are not considered in the normal state [3]. However, loss in a rotational degree of freedom around a given axis may manifest itself in the form of an additional vibrational mode resulting from rocking of the molecule about that axis of symmetry.

Theoretical calculations of the entropic selection factors in the context of C_2H_4 vs. C_2H_6 and C_2H_4 vs. Kr molecules are presented in Sections D.1 and D.2 respectively.

D.1. Ethylene vs. Ethane Case

C_2H_4 and C_2H_6 molecules were considered as cuboids as shown in Figure D.2. This model was used to calculate their moments of inertia (I) along the x, y and z axes, as shown in Figure D.2 [6]. The partition function associated with each degree of translational, rotational and vibrational freedom can be calculated from Equations D.3, D.4 and D.5 respectively. The entropic selection factor can then be calculated using Equation D.2.

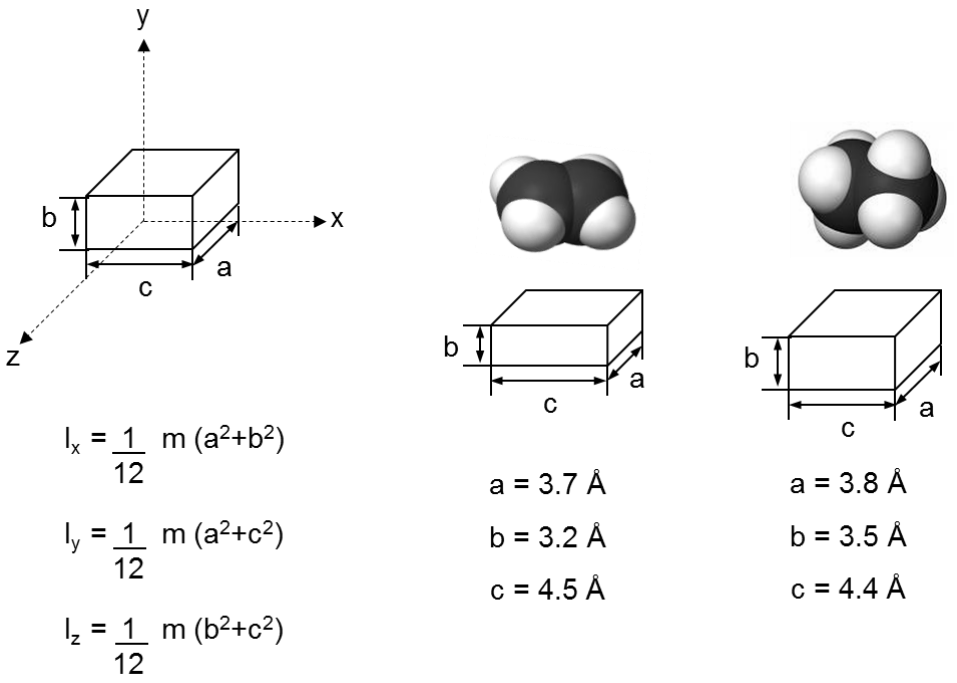

$$I_x = \frac{1}{12} m (a^2+b^2)$$

$$I_y = \frac{1}{12} m (a^2+c^2)$$

$$I_z = \frac{1}{12} m (b^2+c^2)$$

C_2H_4	C_2H_6
a = 3.7 Å	a = 3.8 Å
b = 3.2 Å	b = 3.5 Å
c = 4.5 Å	c = 4.4 Å

Figure D.2: Representation of C_2H_4 and C_2H_6 based on the minimum dimensions of a cuboid that can just contain the molecules. The dimensions of C_2H_4 and C_2H_6 were obtained using space-filling CPK models

Figure D.3 shows a representation of the degrees of freedom in the normal and transition states in case of (i) "open" slit and (ii) "tight" slit for C_2H_4 and C_2H_6 in transport through CMS.

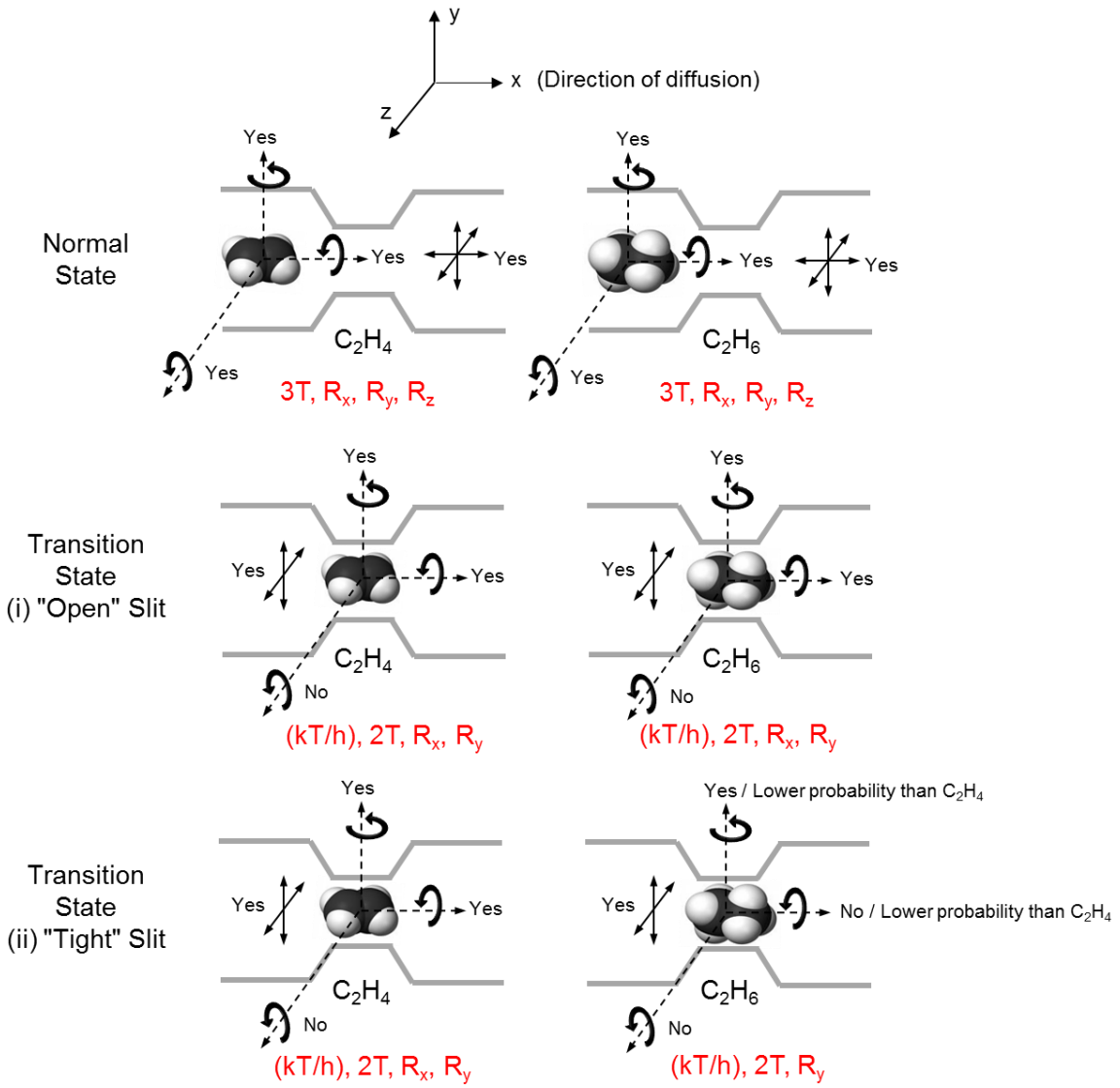

Figure D.3: Representation of the degrees of freedom in the normal and transition states in case of (i) "open" slit and (ii) "tight" slit for C_2H_4 and C_2H_6 in transport through CMS. Double sided arrows indicate translation in the x, y and z directions

In the normal state, both C_2H_4 and C_2H_6 have 3 degrees of translation and rotation each. In the transition state, translation in the direction of diffusion (x direction) is accounted for by the factor $\left(\frac{kT}{h}\right)$ in Equation D.1, to account for a vibration required to pass through the metastable state [2, 4]. If oriented along their smaller dimension ("b" in

Figure D.2), both C_2H_4 and C_2H_6 may also have translational degrees of freedom in the direction transverse (z) and perpendicular (y) to the direction of diffusion (x). In the transition state, the rotational degree of freedom along the z axis is lost for both C_2H_4 and C_2H_6 considering the length ("c" in Figure D.2) of the molecules with respect to the ultramicropore dimension. Now, we may consider 2 cases in the transition state:

(i) <u>"Open" Slit</u>

The pore structure of the CMS is "open" (at low pyrolysis temperature), such that it can allow free rotation of C_2H_4 and C_2H_6 around both the x and y axes in the transition state. The entropic factor is then represented as follows:

$$\text{Entropic Factor} = \frac{\left[\frac{(kT/h)\ F_T^{\neq 2}\ F_{Rx}^{\neq}\ F_{Ry}^{\neq}}{F_T{}^3\ F_{Rx}\ F_{Ry}\ F_{Rz}}\right]_{C_2H_4}}{\left[\frac{(kT/h)\ F_T^{\neq 2}\ F_{Rx}^{\neq}\ F_{Ry}^{\neq}}{F_T{}^3\ F_{Rx}\ F_{Ry}\ F_{Rz}}\right]_{C_2H_6}} \approx 1.2 \qquad \text{(D.7)}$$

(ii) <u>"Tight" Slit</u>

The CMS pore structure is "tighter" (at higher pyrolysis temperature) such that it allows rotation of C_2H_4 around the both x and y axis, but now restricts rotation of C_2H_6 around the x axis while only allowing it to rotate around the y axis. In this case, the entropic factor is represented as

$$\text{Entropic Factor} = \frac{\left[\frac{(kT/h)\ F_T^{\neq 2}\ F_{Rx}^{\neq}\ F_{Ry}^{\neq}}{F_T{}^3\ F_{Rx}\ F_{Ry}\ F_{Rz}}\right]_{C_2H_4}}{\left[\frac{(kT/h)\ F_T^{\neq 2}\ F_{Rx}^{\neq}}{F_T{}^3\ F_{Rx}\ F_{Ry}\ F_{Rz}}\right]_{C_2H_6}} \approx 31 \qquad \text{(D.8)}$$

This factor may be highly exaggerated since the lost degree of rotational freedom of C_2H_6 may manifest as an additional vibrational degree of freedom resulting due to rocking of the molecule about the x axis. In addition, as described earlier (Figure 6.7), due to the complicated shapes of C_2H_4 and C_2H_6, the entropic advantage may depend on many subtle configurational differences of the molecules, rather than an absolute, total loss of a degree of freedom.

D.2. Ethylene vs. Krypton Case

Figure D.4 shows a representation of the degrees of freedom in the normal and transition states in case of (i) "open" slit and (ii) "tight" slit for C_2H_4 and C_2H_6 in transport through CMS.

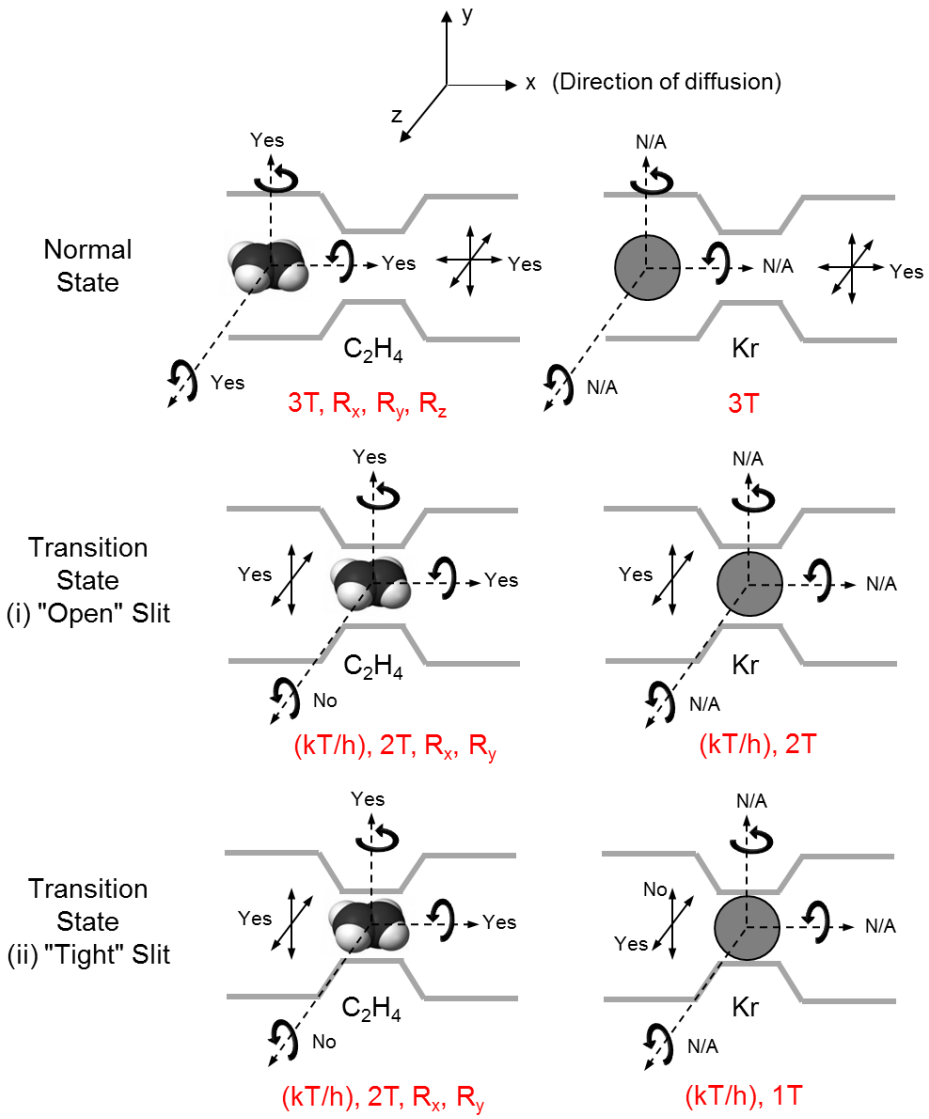

Figure D.4: Representation of the degrees of freedom in the normal and transition states in case of (i) "open" slit and (ii) "tight" slit for C_2H_4 and Kr in transport through CMS. Double sided arrows indicate translation in the x, y and z directions

In the normal state, Kr has 3 degrees of translational freedom, while C_2H_4 has 3 degrees of translational and rotational freedom each. In the transition state, both C_2H_4 and Kr translate in the direction of diffusion (x direction), again accounted for by the factor $\left(\frac{kT}{h}\right)$ in Equation D.1 [2, 4]. Both C_2H_4 and Kr can also translate along the CMS

graphene-like planes, transverse (z) to the direction of diffusion (x). Additionally, in the transition state, the rotational degree of freedom along the z axis is lost for C_2H_4 considering its length ("c" in Figure D.2) with respect to the ultramicropore dimension. Now consider two cases in the transition state:

(i) "Open" Slit

When the CMS pore structure is "open" (low pyrolysis temperature), both C_2H_4 and Kr may translate along the y direction, i.e. perpendicular to the direction of diffusion. In addition, C_2H_4 can rotate around the x and y axes. The entropic factor is then represented as follows:

$$\text{Entropic Factor} = \frac{\left[\frac{(kT/h)\ F_T^{\neq 2}\ F_{Rx}^{\neq}\ F_{Ry}^{\neq}}{F_T{}^3\ F_{Rx}\ F_{Ry}\ F_{Rz}}\right]_{C_2H_4}}{\left[\frac{(kT/h)\ F_T^{\neq 2}}{F_T{}^3}\right]_{Kr}} \approx 0.1 \qquad \text{(D.9)}$$

The C_2H_4/Kr entropic factor in this case is less than one since C_2H_4 pays a penalty by losing rotational freedom around the z axis in the transitions state, while Kr does not lose any degrees of freedom in the transition state. This loss in entropy is reflected in its energetic selectivity over Kr (Table 6.2), since the "linearly-oriented" and "slimmer" C_2H_4 molecule may require lower activation energy for diffusion compared to the round Kr molecule.

(ii) "Tight" Slit

When the CMS slit structure is "tighter" (higher pyrolysis temperature), C_2H_4 can be "slimmer" (since it loses its rotational freedom around the z axis) and can, thus, still

translate in the y direction when oriented along its smaller dimension. In addition, it can rotate around the x and y axes. Kr, however, being spherical, cannot translate in the y direction and loses a degree of translational freedom. In this case, the entropic factor is represented as

$$\text{Entropic Factor} = \frac{\left[\frac{(kT/h)\, F_T^{\neq 2}\, F_{Rx}^{\neq}\, F_{Ry}^{\neq}}{F_T{}^3\, F_{Rx}\, F_{Ry}\, F_{Rz}}\right]_{C_2H_4}}{\left[\frac{(kT/h)\, F_T^{\neq}}{F_T{}^3}\right]_{Kr}} \approx 2 \qquad \text{(D.9)}$$

Thus, in this case, since the "tighter" CMS slit can discriminate between the shapes of C_2H_4 and Kr, C_2H_4 shows an entropic advantage in transport through the CMS.

D.3. References

[1] Steel KM. Carbon membranes for challenging gas separations. The University of Texas at Austin, Doctor of Philosophy, 2000.

[2] Barrer RM. Activated diffusion in membranes. T Faraday Soc. 1939;35(1):0644-55.

[3] Singh A, Koros WJ. Significance of entropic selectivity for advanced gas separation membranes. Ind Eng Chem Res. 1996;35(4):1231-4.

[4] Glasstone S, Laidler KJ, Eyring H. The Theory of Rate Processes. 1st ed. New York: McGraw-Hill Book Co., Inc. 1941.

[5] Singh-Ghosal A, Koros WJ. Energetic and entropic contributions to mobility selectivity in glassy polymers for gas separation membranes. Ind Eng Chem Res. 1999;38(10):3647-54.

[6] McLean WG, Nelson EW. Engineering mechanics: Statistics and dynamics. 2nd ed. New York: Schaum Publishing Co.; 1962.

BIBLIOGRAPHY

Baker RW. Future directions of membrane gas separation technology. Ind Eng Chem Res. 2002;41(6):1393-411.

True WR. OGJ Focus: Global ethylene production continues advance in 2009. Oil Gas J. 2010;108(27):34-8.

http://www.dow.com/productsafety/finder/.

http://www.plastemart.com/upload/literature/Global_demand_of_ethylene.asp.

http://www.chemsystems.com/reports/search/docs/abstracts/0405-7-abs.pdf.

http://www.lyondellbasell.com/index.htm.

Abedi AA. Economic analysis of a new gas to ethylene technology. Texas A&M University, Master of Science, 2007.

Falqi FH. The miracle of petrochemicals - Olefins industry: An in-depth look at steam crackers. Boca Raton: Universal Publishers 2009.

Worrell E, Phylipsen D, Einstein D, Martin N. Energy use and energy intensity of the U.S. chemical industry. Berkeley: Ernest Orlando Lawrence Berkeley National Laboratory, University of California; 2000.

Eldridge RB. Olefin paraffin separation technology - A review. Ind Eng Chem Res. 1993;32(10):2208-12.

Gottschlich DE, Roberts DL. Energy minimization of separation processes using conventional/membrane hybrid systems: US Department of Energy; 1990.

Merkel T, Blanc R, Zeid J, Suwarlim A, Firat B, Wijmans S, et al. Separation of olefin/paraffin mixtures with carrier facilitated membranes: US Department of Energy; 2007.

Caballero JA, Grossmann IE, Keyvani M, Lenz ES. Design of hybrid distillation-vapor membrane separation systems. Ind Eng Chem Res. 2009;48(20):9151-62.

Ozokwelu D. Hybrid separations/distillation technology: Research opportunities for energy and emissions reduction: US Department of Energy; 2005.

Robinson S, Jubin R, Choate B. Materials for separation technologies: Energy and emission reduction opportunities: US Department of Energy; 2005.

Koros WJ. Evolving beyond the thermal age of separation processes: Membranes can lead the way. AIChE J. 2004;50(10):2326-34.

Vu DQ. Formation and characterization of asymmetric carbon molecular sieve and mixed matrix membranes for natural gas purification. The University of Texas at Austin, Doctor of Philosophy, 2001.

Koros WJ, Mahajan R. Pushing the limits on possibilities for large scale gas separation: Which strategies? J Membrane Sci. 2000;175(2):181-96.

Rungta M, Xu L, Koros WJ. Carbon molecular sieve dense film membranes derived from Matrimid® for ethylene/ethane separation. Carbon. 2012;50(4):1488-502.

Robeson LM. Correlation of separation factor versus permeability for polymeric membranes. J Membrane Sci. 1991;62(2):165-85.

Robeson LM. The upper bound revisited. J Membrane Sci. 2008;320(1-2):390-400.

Steel KM. Carbon membranes for challenging gas separations. The University of Texas at Austin, Doctor of Philosophy, 2000.

Xu L, Rungta M, Koros WJ. Matrimid® derived carbon molecular sieve hollow fiber membranes for ethylene/ethane separation. J Membrane Sci. 2011;380(1-2):138-47.

Vu DQ, Koros WJ, Miller SJ. High pressure CO_2/CH_4 separation using carbon molecular sieve hollow fiber membranes. Ind Eng Chem Res. 2002;41(3):367-80.

Azhin M, Kaghazchi T, Rahmani M. A review on olefin/paraffin separation using reversible chemical complexation technology. J Ind Eng Chem. 2008;14(5):622-38.

Faiz R, Li K. Olefin/paraffin separation using membrane based facilitated transport/chemical absorption techniques. Chem Eng Sci. 2012;73:261-84.

Pinnau I, Toy LG. Solid polymer electrolyte composite membranes for olefin/paraffin separation. J Membrane Sci. 2001;184(1):39-48.

Ho WS, Dalrymple DC. Facilitated transport of olefins in Ag^+-containing polymer membranes. J Membrane Sci. 1994;91(1-2):13-25.

Teramoto M, Shimizu S, Matsuyama H, Matsumiya N. Ethylene/ethane separation and concentration by hollow fiber facilitated transport membrane module with permeation of silver nitrate solution. Sep Purif Technol. 2005;44(1):19-29.

Teramoto M, Takeuchi N, Maki T, Matsuyama H. Ethylene/ethane separation by facilitated transport membrane accompanied by permeation of aqueous silver nitrate solution. Sep Purif Technol. 2002;28(2):117-24.

Singh A. Membrane materials with enhanced selectivity: An entropic interpretation. The University of Texas at Austin, Doctor of Philosophy, 1997.

Marsh H. Introduction to carbon science: Butterworths; 1989.

Pierson. Handbook of carbon, graphite, diamond, and fullerenes NY: Noyes Publication 1993.

Jenkins GM, Kawamura K. Polymeric carbons - Carbon fiber, glass and char. London: Cambridge University Press 1976.

Williams PJ. Analysis of factors influencing the performance of CMS membranes for gas separation. Georgia Institute of Technology, Doctor of Philosophy, 2006.

Ismail AF, Saufi SM. Fabrication of carbon membranes for gas separation - A review. Carbon. 2004;42(2):241-59.

Kiyono M. Carbon molecular sieve membranes for natural gas separations. Georgia Institute of Technology, Doctor of Philosophy, 2010.

Stoeckli HF. Microporous carbons and their characterization: The present state of the art. Carbon. 1990;28(1):1-6.

Breck DW. Zeolite molecular sieves. New York: Wiley & Sons; 1974.

Fu YJ, Liao KS, Hu CC, Lee KR, Lai JY. Development and characterization of micropores in carbon molecular sieve membrane for gas separation. Micropor Mesopor Mat. 2011;143(1):78-86.

Park HB, Kim YK, Lee JM, Lee SY, Lee YM. Relationship between chemical structure of aromatic polyimides and gas permeation properties of their carbon molecular sieve membranes. J Membrane Sci. 2004;229(1-2):117-27.

Suda H, Haraya K. Gas permeation through micropores of carbon molecular sieve membranes derived from Kapton polyimide. J Phys Chem B. 1997;101(20):3988-94.

Campo MC, Magalhaes FD, Mendes A. Comparative study between a CMS membrane and a CMS adsorbent: Part I-Morphology, adsorption equilibrium and kinetics. J Membrane Sci. 2010;346(1):15-25.

Chen J, Loo LS, Wang K, Do DD. The structural characterization of a CMS membrane using Ar sorption and permeation. J Membrane Sci. 2009;335(1-2):1-4.

Koros WJ. Membranes: Learning a lesson from nature. Chemical Engineering Progress. 1995;91(10):68-81.

Koros WJ, Fleming GK. Membrane-based gas separation. J Membrane Sci. 1993;83(1):1-80.

Hines AL, Maddox RN. Mass transfer fundamentals and applications: Englewood Cliffs, New Jersey: Prentice Hall; 1985.

Rao MB, Sircar S. Nanoporous carbon membranes for separation of gas-mixtures by selective surface flow. J Membrane Sci. 1993;85(3):253-64.

Rao MB, Sircar S. Nanoporous carbon membrane for gas separation. Gas Purification & Separation. 1993;7(4):279-84.

Rao MB, Sircar S. Performance and pore characterization of nanoporous carbon membranes for gas separation. J Membrane Sci. 1996;110(1):109-18.

Koros WJ. Barrier polymers and structures. Washington DC: American Chemical Society 1990.

Koros WJ. Transport properties. In: Mark HM. Encyclopedia of polymer science and technology. 3ed: Wiley-Interscience 2004.

Ismail AF, David LIB. A review on the latest development of carbon membranes for gas separation. J Membrane Sci. 2001;193(1):1-18.

Wijmans JG, Baker RW. The solution-diffusion model - A review. J Membrane Sci. 1995;107(1-2):1-21.

Baker RW. Membrane technology and applications. New York: McGraw-Hill; 2000.

van Krevelen DW. Properties of polymers. 3 ed: Elsevier Science; 1997.

Karger J, Ruthven DM. Diffusion in zeolites and other microporous solids. New York: John Wiley & Sons Inc.; 1991.

Higashi K, Ito H, Oshi J. Surface diffusion phenomena in gaseous diffusion. I. Surface diffusion of pure gas. J At Energy Soc Jpn. 1963;5:846-53.

Crank J, Park GS. Diffusion in polymers. New York: Academic Press; 1968.

Singh A, Koros WJ. Significance of entropic selectivity for advanced gas separation membranes. Ind Eng Chem Res. 1996;35(4):1231-4.

Das M. Membranes for olefin/paraffin separations. Georgia Institute of Technology, Doctor of Philosophy, 2009.

Singh-Ghosal A, Koros WJ. Energetic and entropic contributions to mobility selectivity in glassy polymers for gas separation membranes. Ind Eng Chem Res. 1999;38(10):3647-54.

Glasstone S, Laidler KJ, Eyring H. The Theory of Rate Processes. 1st ed. New York: McGraw-Hill Book Co., Inc. 1941.

Hatori H, Yamada Y, Shiraishi M, Yoshihara M, Kimura T. The mechanism of polyimide pyrolysis in the early stage. Carbon. 1996;34(2):201-8.

Ehlers GFL, Fisch KR, Powell WR. Thermal degradation of polymers with phenylene units in the chain. IV. Aromatic polyamides and polyimides. J Polymer Sci Part A: Polymer Chemistry. 1970;8(12):3511-27.

Koresh J, Soffer A. A Molecular-sieve carbon membrane for continuous process gas separation. Carbon. 1984;22(2):225-.

Centeno TA, Fuertes AB. Carbon molecular sieve gas separation membranes based on poly(vinylidene chloride-co-vinyl chloride). Carbon. 2000;38(7):1067-73.

Fuertes AB, Menendez I. Separation of hydrocarbon gas mixtures using phenolic resin-based carbon membranes. Sep Purif Technol. 2002;28(1):29-41.

Wei W, Hu HQ, You LB, Chen GH. Preparation of carbon molecular sieve membrane from phenol-formaldehyde Novolac resin. Carbon. 2002;40(3):465-7.

Centeno TA, Fuertes AB. Supported carbon molecular sieve membranes based on a phenolic resin. J Membrane Sci. 1999;160(2):201-11.

Acharya M, Foley HC. Spray-coating of nanoporous carbon membranes for air separation. J Membrane Sci. 1999;161(1-2):1-5.

Acharya M, Raich BA, Foley HC, Harold MP, Lerou JJ. Metal-supported carbogenic molecular sieve membranes: Synthesis and applications. Ind Eng Chem Res. 1997;36(8):2924-30.

Ismail AF, David LIB. Influence of the thermastabilization process and soak time during pyrolysis process on the polyacrylonitrile carbon membranes for O-2/N-2 separation. J Membrane Sci. 2003;213(1-2):285-91.

Williams PJ, Koros WJ. Gas separation by carbon membranes. In: Li NN, Fane AG, Winston Ho WS, Matsura T. Advanced membrane technology and applications. New Jersey: John Wiley & Sons Inc. 2008.

Jones CW, Koros WJ. Carbon Molecular-sieve gas separation membranes .1. Preparation and characterization based on polyimide precursors. Carbon. 1994;32(8):1419-25.

Fuertes AB, Nevskaia DM, Centeno TA. Carbon composite membranes from Matrimid (R) and Kapton (R) polyimides for gas separation. Micropor Mesopor Mat. 1999;33(1-3):115-25.

Barsema JN, Klijnstra SD, Balster JH, van der Vegt NFA, Koops GH, Wessling M. Intermediate polymer to carbon gas separation membranes based on Matrimid PI. J Membrane Sci. 2004;238(1-2):93-102.

Kim YK, Lee JM, Park HB, Lee YM. The gas separation properties of carbon molecular sieve membranes derived from polyimides having carboxylic acid groups. J Membrane Sci. 2004;235(1-2):139-46.

Kim YK, Park HB, Lee YM. Preparation and characterization of carbon molecular sieve membranes derived from BTDA-ODA polyimide and their gas separation properties. J Membrane Sci. 2005;255(1-2):265-73.

Tin PS, Chung TS, Hill AJ. Advanced fabrication of carbon molecular sieve membranes by nonsolvent pretreatment of precursor polymers. Ind Eng Chem Res. 2004;43(20):6476-83.

Kusuki Y, Shimazaki H, Tanihara N, Nakanishi S, Yoshinaga T. Gas permeation properties and characterization of asymmetric carbon membranes prepared by pyrolyzing asymmetric polyimide hollow fiber membrane. J Membrane Sci. 1997;134(2):245-53.

Okamoto K, Kawamura S, Yoshino M, Kita H, Hirayama Y, Tanihara N, et al. Olefin/paraffin separation through carbonized membranes derived from an asymmetric polyimide hollow fiber membrane. Ind Eng Chem Res. 1999;38(11):4424-32.

Tin PS, Chung TS, Kawi S, Guiver M. Novel approaches to fabricate carbon molecular sieve membranes based on chemical modified and solvent treated polyimides. Micropor Mesopor Mat. 2004;73(3).

Xiao YC, Dai Y, Chung TS, Guiver MD. Effects of brominating matrimid polyimide on the physical and gas transport properties of derived carbon membranes. Macromolecules. 2005;38(24):10042-9.

Steel KM, Koros WJ. An investigation of the effects of pyrolysis parameters on gas separation properties of carbon materials. Carbon. 2005;43(9):1843-56.

Geiszler V. Polyimide precursors for carbon molecular sieve membranes. University of Texas at Austin, Doctor of Philosophy, 1997.

Geiszler VC, Koros WJ. Effects of polyimide pyrolysis conditions on carbon molecular sieve membrane properties. Ind Eng Chem Res. 1996;35(9):2999-3003.

Grisdale RO. The properties of carbon contacts. J Appl Phys. 1953;24(10):1288-96.

Kiyono M, Williams PJ, Koros WJ. Effect of pyrolysis atmosphere on separation performance of carbon molecular sieve membranes. J Membrane Sci. 2010;359(1-2):2-10.

Kiyono M, Williams PJ, Koros WJ. Effect of polymer precursors on carbon molecular sieve structure and separation performance properties. Carbon. 2010;48(15):4432-41.

Su J, Lua AC. Influence of carbonisation parameters on the transport properties of carbon membranes by statistical analysis. J Membrane Sci. 2006;278(1-2):335-43.

Koresh JE, Soffer A. The carbon molecular-sieve membranes - General properties and the permeability of CH4/H2 mixture. Separ Sci Technol. 1987;22(2-3):973-82.

Kusakabe K, Yamamoto M, Morooka S. Gas permeation and micropore structure of carbon molecular sieving membranes modified by oxidation. J Membrane Sci. 1998;149(1):59-67.

Soffer A, Azariah M, Amar A, Cohen H, Golub D, Saguee S, et al., inventors; Rotem Industries Ltd., assignee. Method of improving the selectivity of carbon membranes by chemical vapor deposition. United States. 1997.

Hayashi J, Mizuta H, Yamamoto M, Kusakabe K, Morooka S. Pore size control of carbonized BPDA-pp'ODA polyimide membrane by chemical vapor deposition of carbon. J Membrane Sci. 1997;124(2):243-51.

Jones CW, Koros WJ. Carbon composite membranes - A solution to adverse humidity effects. Ind Eng Chem Res. 1995;34(1):164-7.

Chen CC. Thermally crosslinked polyimide hollow fiber membranes for natural gas purification. Georgia Institute of Technology, Doctor of Philosophy, 2011.

Pye DG, Hoehn HH, Panar M. Measurement of gas permeability of polymers. I. Permeabilities in constant volume/variable pressure apparatus. J Appl Polym Sci. 1976;20(7):1921-31.

Pye DG, Hoehn HH, Panar M. Measurement of gas permeability of polymers. II. Apparatus for determination of permeabilities of mixed gases and vapors. J Appl Polym Sci. 1976;20(2):287-301.

Koros WJ, Paul DR. Design considerations for measurement of gas sorption in polymers by pressure decay. J Polym Sci Pol Phys. 1976;14(10):1903-7.

Costello LM, Koros WJ. Temperature-dependence of gas sorption and transport properties in polymers - Measurement and applications. Ind Eng Chem Res. 1992;31(12):2708-14.

Guiver MD, Robertson GP, Dai Y, Bilodeau F, Kang YS, Lee KJ, et al. Structural characterization and gas-transport properties of brominated matrimid polyimide. J Polym Sci Pol Chem. 2002;40(23):4193-204.

Kim JH, Koros WJ, Paul DR. Physical aging of thin 6FDA-based polyimide membranes containing carboxyl acid groups. Part I. Transport properties. Polymer. 2006;47(9):3094-103.

Freeman BD. Basis of permeability/selectivity tradeoff relations in polymeric gas separation membranes. Macromolecules. 1999;32(2):375-80.

Haraya K, Obata K, Itoh N, Shndo Y, Hakuta T, Yoshitome H. Gas permeation and separation by an asymmetric polyimide hollow fiber membrane. J Membrane Sci. 1989;41:23-35.

Barrer RM. Activated diffusion in membranes. T Faraday Soc. 1939;35(1):0644-55.

van Amerongen GJ. The permeability of different rubbers to gases and Its relation to diffusivity and solubility. J Appl Phys. 1946;17(11):972-85.

Barrer RM, Skirrow G. Transport and equilibrium phenomena in gas elastomer systems .1. Kinetic phenomena. J Polym Sci. 1948;3(4):549-63.

Burns RL, Koros WJ. Defining the challenges for C3H6/C3H8 separation using polymeric membranes. J Membrane Sci. 2003;211(2):299-309.

Chan SS, Wang R, Chung TS, Liu Y. C-2 and C-3 hydrocarbon separations in poly(1,5-naphthalene-2,2 '-bis(3,4-phthalic) hexafluoropropane) diimide (6FDA-1,5-NDA) dense membranes. J Membrane Sci. 2002;210(1):55-64.

Chan SS, Chung T-S, Liu Y, Wang R. Gas and hydrocarbon (C2 and C3) transport properties of co-polyimides synthesized from 6FDA and 1,5-NDA (naphthalene)/Durene diamines. J Membr Sci. 2003;218(1-2):235-45.

Tanaka K, Taguchi A, Hao J, Kita H, Okamoto K. Permeation and separation properties of polyimide membranes to olefins and paraffins. J Membr Sci. 1996;121(2):197-207.

Staudt-Bickel C, Koros WJ. Olefin/paraffin gas separations with 6FDA-based polyimide membranes. J Membrane Sci. 2000;170(2):205-14.

Semenova SI. Polymer membranes for hydrocarbon separation and removal. J Membrane Sci. 2004;231(1-2):189-207.

Ilinitch OM, Semin GL, Chertova MV, Zamaraev KI. Novel polymeric membranes for separation of hydrocarbons. J Membrane Sci. 1992;66(1):1-8.

Ilinich OM, Zamaraev KI. Separation of ethylene and ethane over polyphenyleneoxides membranes: transient increase of selectivity. J Membrane Sci. 1993;82(1-2):149-55.

Teplyakov V, Meares P. Correlation aspects of the selective gas permeabilities of polymeric materials and membranes. Gas Separation & Purification. 1990;4(2):66-74.

Reid C, Sherwood TK. The properties of gases and liquids: their estimation and correlation. New York: Mcgraw-hill; 1976.

Hirschfelder, Oakland K. Molecular theory of gases and liquids. New York: Wiley Interscience; 1964.

Petropolous JH. Mechanisms and theories for sorption and diffusion of gases in polymers. In: Paul DR, Yampol'skii YP, eds. Polymeric gas separation membranes. Boca Raton: CRC Press 1994.

Koros WJ, Paul DR, Huvard GS. Energetics of gas sorption in glassy-polymers. Polymer. 1979;20(8):956-60.

Brandt WW. Model calculation of the temperature dependence of small molecule diffusion in high polymers. J Phys Chem-Us. 1959;63(7):1080-4.

Ho WSW, Doyle G, Savage DW, Pruett RL. Olefin separations via complexation with cuprous diketonate. Ind Eng Chem Res. 1988;27(2):334-7.

Teramoto M, Matsuyama H, Yamashiro T, Katayama Y. Separation of ethylene from ethane by supported liquid membranes containing silver-nitrate as a carrier. J Chem Eng Jpn. 1986;19(5):419-24.

Eriksen OI, Aksnes E, Dahl IM. Facilitated transport of ethene through Nafion membranes .1. Water Swollen Membranes. J Membrane Sci. 1993;85(1):89-97.

Tsou DT, Blachman MW, Davis JC. Silver-facilitated olefin/paraffin separation in a liquid membrane contactor system. Ind Eng Chem Res. 1994;33(12):3209-16.

Bessarabov DG, Sanderson RD, Jacobs EP, Beckman IN. High-efficiency separation of an ethylene ethane mixture by a large-scale liquid-membrane contactor containing flat-sheet nonporous polymeric gas-separation membranes and a selective flowing-liquid absorbent. Ind Eng Chem Res. 1995;34(5):1769-78.

Teramoto M, Matsuyama H, Yamashiro T, Okamoto S. Separation of ethylene from ethane by a flowing liquid membrane using silver-nitrate as a carrier. J Membrane Sci. 1989;45(1-2):115-36.

Nymeijer K, Visser T, Assen R, Wessling M. Super selective membranes in gas-liquid membrane contactors for olefin/paraffin separation. J Membrane Sci. 2004;232(1-2):107-14.

Ryu JH, Lee H, Kim YJ, Kang YS, Kim HS. Facilitated olefin transport by reversible olefin coordination to silver ions in a dry cellulose acetate membrane. Chem-Eur J. 2001;7(7):1525-9.

Kim HS, Ryu JH, Kim H, Ahn BS, Kang YS. Reversible olefin complexation by silver ions in dry poly(vinyl methyl ketone) membrane and its application to olefin/paraffin separations. Chem Commun. 2000(14):1261-2.

Ruthven DM. Molecular sieve separations. Chem-Ing-Tech. 2011;83(1-2):44-52.

Agarwal K, John M, Pai S, Newalkar BL, Bhargava R, Choudary NV. SAPO-34 assisted C3 separation: Modeling and simulation. Micropor Mesopor Mat. 2010;132(3):311-8.

Ruthven DM, Reyes SC. Adsorptive separation of light olefins from paraffins. Microporous Mesoporous Mat. 2007;104(1-3):59-66.

Bloch ED, Queen WL, Krishna R, Zadrozny JM, Brown CM, Long JR. Hydrocarbon separations in a metal-organic framework with open iron(II) coordination sites. Science. 2012;335(Copyright (C) 2012 American Chemical Society (ACS). All Rights Reserved.):1606-10.

Yang RT. Adsorbents: Fundamentals and applications: John Wiley & Sons, Inc.; 2003.

Li K, Olson DH, Seidel J, Emge TJ, Gong H, Zeng H, et al. Zeolitic imidazolate frameworks for kinetic separation of propane and propene. J Am Chem Soc. 2009;131(30):10368-9.

Zhang C, Dai Y, Johnson JR, Karvan O, Koros WJ. High performance ZIF-8/6FDA-DAM mixed matrix membrane for propylene/propane separations. J Membr Sci. 2012;389:34-42.

Zhang C, Lively RP, Zhang K, Johnson JR, Karvan O, Koros WJ. Unexpected molecular sieving properties of zeolitic imidazolate framework-8. The Journal of Physical Chemistry Letters. 2012:2130-4.

Bae T-H, Lee JS, Qiu W, Koros WJ, Jones CW, Nair S. A high-performance gas-separation membrane containing submicrometer-sized metal-organic framework crystals. Angew Chem, Int Ed. 2010;49(Copyright (C) 2012 American Chemical Society (ACS). All Rights Reserved.):9863-6, S/1-S/6.

Dai Y, Johnson JR, Karvan O, Sholl DS, Koros WJ. Ultem®/ZIF-8 mixed matrix hollow fiber membranes for CO2/N2 separations. J Membr Sci. 2012;401–402(0):76-82.

Ordonez MJC, Balkus KJ, Jr., Ferraris JP, Musselman IH. Molecular sieving realized with ZIF-8/Matrimid mixed-matrix membranes. J Membr Sci. 2010;361(Copyright (C) 2012 American Chemical Society (ACS). All Rights Reserved.):28-37.

Pan Y, Lai Z. Sharp separation of C2/C3 hydrocarbon mixtures by zeolitic imidazolate framework-8 (ZIF-8) membranes synthesized in aqueous solutions. Chem Commun. 2011;47(37):10275.

Gücüyener C, van den Bergh J, Gascon J, Kapteijn F. Ethane/ethene separation turned on its head: Selective ethane adsorption on the metal−organic framework ZIF-7 through a gate-opening mechanism. J Am Chem Soc. 2010;132(50):17704-6.

Chmelik C, Freude D, Bux H, Haase J. Ethene/ethane mixture diffusion in the MOF sieve ZIF-8 studied by MAS PFG NMR diffusometry. Microporous Mesoporous Mater. 2011;147(Copyright (C) 2012 American Chemical Society (ACS). All Rights Reserved.):135-41.

Bux H, Chmelik C, van Baten JM, Krishna R, Caro J. Novel MOF-membrane for molecular sieving predicted by IR-diffusion studies and molecular modeling. Adv Mater. 2010;22(42):4741-3.

Bux H, Chmelik C, Krishna R, Caro J. Ethene/ethane separation by the MOF membrane ZIF-8: Molecular correlation of permeation, adsorption, diffusion. J Membr Sci. 2011;369(1-2):284-9.

Chmelik C, Bux H, Voss H, Caro J. Adsorption and diffusion - Basis for molecular understanding of permeation through molecular sieve membranes. Chem-Ing-Tech. 2011;83(1-2):104-12.

Olson DH, Camblor MA, Villaescusa LA, Kuehl GH. Light hydrocarbon sorption properties of pure silica Si-CHA and ITQ-3 and high silica ZSM-58. Micropor Mesopor Mat. 2004;67(1):27-33.

Dai W, Scheibe M, Li L, Guan N, Hunger M. Effect of the methanol-to-olefin conversion on the PFG NMR self-diffusivities of ethane and ethene in large-crystalline SAPO-34. Journal of Physical Chemistry C. 2011;116(3):2469–76.

Romero-Perez A, Aguilar-Armenta G. Adsorption kinetics and equilibria of carbon dioxide, ethylene, and ethane on 4A(CECA) zeolite. J Chem Eng Data. 2010;55(9):3625-30.

Moore TT, Mahajan R, Vu DQ, Koros WJ. Hybrid membrane materials comprising organic polymers with rigid dispersed phases. AIChE J. 2004;50(Copyright (C) 2012 American Chemical Society (ACS). All Rights Reserved.):311-21.

Díaz K, López-González M, del Castillo LF, Riande E. Effect of zeolitic imidazolate frameworks on the gas transport performance of ZIF8-poly(1,4-phenylene ether-ether-sulfone) hybrid membranes. Journal of Membrane Science. 2011;383(1–2):206-13.

Singh-Ghosal A, Koros WJ. Air separation properties of flat sheet homogeneous pyrolytic carbon membranes. J Membrane Sci. 2000;174(2):177-88.

Centeno TA, Vilas JL, Fuertes AB. Effects of phenolic resin pyrolysis conditions on carbon membrane performance for gas separation. J Membrane Sci. 2004;228(1):45-54.

Suda H, Haraya K. Alkene/alkane permselectivities of a carbon molecular sieve membrane. Chem Commun. 1997(1):93-4.

Barsema JN, van der Vegt NFA, Koops GH, Wessling M. Carbon molecular sieve membranes prepared from porous fiber precursor. J Membrane Sci. 2002;205(1-2):239-46.

Steel KM, Koros WJ. Investigation of porosity of carbon materials and related effects on gas separation properties. Carbon. 2003;41(2):253-66.

Tuinstra F, Koenig JL. Raman spectrum of graphite. J Chem Phys. 1970;53(3):1126-&.

Dresselhaus MS, Jorio A, Souza AG, Saito R. Defect characterization in graphene and carbon nanotubes using Raman spectroscopy. Philos T R Soc A. 2010;368(1932):5355-77.

Lai J, Guo HJ, Wang ZX, Li XH, Zhang XP, Wu FX, et al. Preparation and characterization of flake graphite/silicon/carbon spherical composite as anode materials for lithium-ion batteries. J Alloy Compd. 2012;530:30-5.

Xu L, Rungta M, Brayden MK, Martinez MV, Stears BA, Barbay GA, et al. Olefins-selective asymmetric carbon molecular sieve hollow fiber membranes for hybrid membrane-distillation processes for olefin/paraffin separations. J Membrane Sci. 2012 (in press).

Pinnau I, Hellums MW, Koros WJ. Gas-transport through homogeneous and asymmetric polyestercarbonate membranes. Polymer. 1991;32(14):2612-7.

Pfromm PH, Pinnau I, Koros WJ. Gas-transport through integral-asymmetric membranes - A comparison to isotropic film transport-properties. J Appl Polym Sci. 1993;48(12):2161-71.

Pfromm PH, Koros WJ. Accelerated physical aging of thin glassy polymer-films - Evidence from gas-transport measurements. Polymer. 1995;36(12):2379-87.

Cui LL, Qiu WL, Paul DR, Koros WJ. Physical aging of 6FDA-based polyimide membranes monitored by gas permeability. Polymer. 2011;52(15):3374-80.

Huang Y, Paul DR. Effect of temperature on physical aging of thin glassy polymer films. Macromolecules. 2005;38(24):10148-54.

Jones CW, Koros WJ. Characterization of ultramicroporous carbon membranes with humidified feeds. Ind Eng Chem Res. 1995;34(1):158-63.

Gawrys M, Fastyn P, Gawlowski J, Gierczak T, Niedzielski J. Prevention of water vapour adsorption by carbon molecular sieves in sampling humid gases. J Chromatogr A. 2001;933(1-2):107-16.

Menendez I, Fuertes AB. Aging of carbon membranes under different environments. Carbon. 2001;39(5):733-40.

Lagorsse S, Magalhaes FD, Mendes A. Aging study of carbon molecular sieve membranes. J Membrane Sci. 2008;310(1-2):494-502.

Jones CW, Koros WJ. Carbon molecular-sieve gas separation membranes .2. Regeneration following organic exposure. Carbon. 1994;32(8):1427-32.

McLean WG, Nelson EW. Engineering mechanics: Statistics and dynamics. 2nd ed. New York: Schaum Publishing Co.; 1962.

Motelica A, Bruinsma OSL, Kreiter R, den Exter M, Vente JF. Membrane retrofit option for paraffin/olefin separation - A technoeconomic evaluation. Ind Eng Chem Res. 2012;51(19):6977-86.

Humphrey JLS, A.F., Koort RA. Separation technologies: Advances and priorities; 1991. Report No.: DOE/ID/12920-1; Other: ON: DE91010024 United StatesOther: ON: DE91010024Thu Feb 07 06:01:47 EST 2008OSTI; NTIS; GPO Dep.EDB-91-063069English.

Kamaruddin HD, Koros WJ. Some observations about the application of Fick's first law for membrane separation of multicomponent mixtures. J Membrane Sci. 1997;135(2):147-59.

Das M, Koros WJ. Performance of 6FDA-6FpDA polyimide for propylene/propane separations. J Membrane Sci. 2010;365(1-2):399-408.

S, Jubin R, Choate B. Materials for separation technologies: Energy and emission reduction opportunities: US Department of Energy; 2005.

VITA

Meha Rungta was born on October 9, 1985 in Kolkata, India, daughter of Sunil Rungta and Renu Rungta. She completed her schooling from Modern High School for Girls, Kolkata, India, after which she ventured to southern India to pursue her undergraduate studies. In August 2008, she received a Bachelor of Technology degree in Chemical Engineering from National Institute of Technology, Tiruchirappalli, India. She then enrolled in the School of Chemical & Biomolecular Engineering at Georgia Institute of Technology in August 2008, to pursue a Doctor of Philosophy in Chemical Engineering, under the guidance of Dr. William J. Koros. In August 2010 she received a Master of Science degree in Chemical Engineering, and will be completing her Doctor of Philosophy degree in Chemical Engineering from Georgia Institute of Technology in December 2012. After graduation, Meha will be starting her professional career as a Senior Research Engineer at the ExxonMobil Chemical Company, Baytown, TX.